Doctoral Dissertation
Doctoral Program in Electrical, Electronics and Communications Engineering
(32^{th} cycle)

Reconfigurable Antennas and Systems

Enrico Tolin

* * * * * *

Supervisor
Prof. Francesca Vipiana

Doctoral examination committee
Prof. Riccardo Maggiora, Politecnico di Torino
Prof. Paolo Nepa, Università degli studi di Pisa
Prof. Oscar Quevedo-Teruel, KTH - Kungl. Tekniska Hogskolan
Prof. Guido Valerio, Sorbonne Université
Prof. Werner Wiesbeck, Karlsruher Institut für Technologie

Politecnico di Torino
June 15, 2020

I hereby declare that, the contents and organisation of this dissertation constitute my own original work and does not compromise in any way the rights of third parties, including those relating to the security of personal data.

. . . . . .

Enrico Tolin

Turin, June 15, 2020

Summary

The increasing demand of compact and multi-functional antennas and RF systems is driving this research activity, where the reconfigurability concept is used to enhance the capability and performance of a rat-race coupler, an UHF RFID antenna and a phased array based on Rotman lens as beamforming network. In each of the three designs it has been considered manufacturing and component/-material costs, in order to introduce novel solutions that are ready to be applied in a "real world" scenario. In particular, a reconfigurable phase management system, superimposed to the phase distribution of a Rotman lens, has been proven to extend the scan range of a linear antenna array by factor two. Both simulations and measurements show that, by introducing a reconfigurable phase shifting system, the performance of the Rotman lens as beamformer are enhanced, resulting in a doubling of the scan range and an increase of the scanning beams, thus keeping a fine spatial resolution and very good coverage. The second research topic is focused on the development of a miniaturized and frequency reconfigurable rat-race coupler operating in two frequency bands, centered at 900 MHz and 1.7 GHz, that has been developed using the artificial transmission lines technique, employing both the right and left handed versions. In the design of the proposed reconfigurable rat-race coupler a method to efficiently manage the group delays of the rat-race branches for improving the operative bandwidth is described. Moreover, the frequency and polarization reconfigurability concept have been used to realize a compact and more efficient UHF RFID reader antenna. The frequency reconfigurability allows the antenna to operate in two UHF RFID regional bands (i.e. European and North American), while the polarization agility greatly reduces the polarization loss factor which occur between the RFID Tag (linearly polarized) and the UHF RFID reader antenna, typically circular polarized, thus removing the static three dB loss.

Above all, don't fear difficult moments. The best comes from them.

Rita Levi Montalcini

Preface

The research activities included and described in this thesis have been developed in the frame of a collaboration between Politecnico di Torino, Torino, Italy and the company IMST GmbH, based in Kamp-Lintfort, Germany.

The research projects have been supervised by Prof. Francesca Vipiana from Politecnico di Torino, and by Dr. Simona Bruni from IMST GmbH.

In particular, Oliver Litschke and Dr. Bruni technically supported the activity described in Chapter 2, while the research projects reported in Chapter 3 and 4 have been supervised by Dr. Achim Bahr and Dr. Bruni.

All the designed prototypes have been assembled and measured in IMST facility laboratories and anechoic chamber.

Contents

List of Tables

List of Figures

Abbreviations

3-D	Three Dimensional
5G	Fifth Generation
ADS	Advanced Design System
ATL	Artificial Transmission Lines
BFN	Beam Forming Network
BM	Beam Mirroring
BST	Barium Strontium Titanite
CBS	Complete Beam Shifting
CMOS	Complementary Metal Oxide Semiconductor
CP	Circular Polarization
DC	Direct Current
DoA	Direction Of Arrival
DPDT	Double Pole Double Throw
EM	Electro Magnetic
EMC	Electromagnetic Compatibility
EMI	Electromagnetic Interference
ENIG	Electroless Nickel Immersion Gold
FET	Field Effect Transistors
FHSS	Frequency Hopping Spread Spectrum
FM	Frequency Modulation
FPGA	Field Programmable Gate Array
GeTe	Germanium Tellurium
GPS	Global Positioning System
GSM	Global System for Mobile communication
HPBW	Half Power Beam Width
IoT	Internet of Things
ISM	Industrial Scientific Medical
LC	Liquid Crystal
LH	Left Hand
LHCP	Left Hand Circular Polarization

LNA	Low Noise Amplifiers
LOS	Line Of Sight
LP	Linear Polarization
LTE	Long Term Evolution
MEMS	Micro-Electro-Mechanic System
MIMO	Multiple Input Multiple Output
mm-waves	Millimiter waves
MMIC	Monolithic Microwave Integrated Circuit
NFC	Near Field Communication
PA	Power Amplifiers
PCB	Printed Circuit Board
PMU	Phase Management Unit
RH	Right Hand
RHCP	Right Hand Circular Polarization
RF	Radio Frequency
RFID	Radio Frequency IDentification
RTPS	Reflection-Type Phase Shifter
SATCOM	Satellite Communiction
SIR	Signal to Interference Ratio
SMD	Surface Mounted Devices
SP3T	Single Pole Three Throw
SP4T	Single Pole Four Throw
SPDT	Single Pole Double Throw
SRR	Short Range Radar
UHF	Ultra High Frequency
YIG	Yttrium Iron Garnet
WiMax	Worldwide Interoperability for Microwave Access
WLAN	Wireless Local Area Network

Chapter 1

Introduction

In recent years wireless systems have undoubtedly experienced an extraordinary growth, due to the multitude of applications that are adopting this technology for increasing their portability, versatility and performance. The progress in RF/mm-wave circuits and antennas in last decades has brought to a widespread of these technologies in numerous applications, e.g. mobile and satellite communication, radar sensing, biomedical, imaging, navigation systems, etc. Indeed, many different communication standards have been created for supporting the requirements of all the different applications, and the great increase in demand of frequency bands lead nowadays to a scarcity of the available RF spectrum. Moreover, following the prediction for the next future, an expansion of the market due to the advent of the Fifth Generation (5G) of mobile communication will be experienced, devoted to fulfill the requirement for the high speed connectivity. In addition, the wireless connectivity will be applied to many devices, in which many operation of various services [1] will be integrated. The latter aspect is part of the so called "Internet of Things" (IoT), which foresee the wireless connection of any kind of device, from industrial automation systems to household appliances. IoT is a very powerful technology, and it is estimated by Ericsson that 24.9 billions IoT connection will be active by year 2025. This number is not so surprising, if it is considered that IoT will also embrace vehicle-to-vehicle communications, as well as security sensors and wearable devices. In Fig. 1.1, the concept of smart home making use of IoT technology is illustrated.

In particular, wearable devices have encountered a substantial increase in few years, and they expect to be a key factor for IoT [3]. Wearables are also not only related to consumer electronic, but also to medical devices, for monitoring health parameters of patients [4]. However, even with the advent of new communication standards, the majority of smart devices will use legacy RF formats. An important market with an increasing interest in sensing and connectivity devices is the automotive one, which nowadays requires many communication (e.g. Bluetooth, FM radio, LTE), navigation (e.g. GPS) and radar sensor systems. In particular,

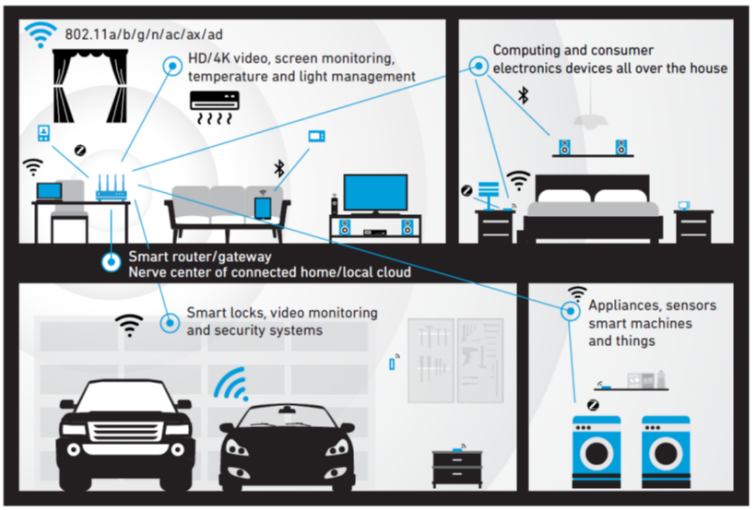

Figure 1.1: Picture showing the future application of IoT technology in a house environment [2].

lot of attention is gaining the radar technology, because it represents an enabling technology for the autonomous intelligent driving, which is expected in next years. Furthermore, the high volume of new antennas to be used in the next future, for both civilian and military purposes, will also cause Electromagnetic Interference (EMI) and Electromagnetic Compatibility (EMC) problems, which can range from a temporary failure of the service to a permanent damage of the device. The proliferation of new mobile platforms and wireless equipments establish a severe constraints on the dimensions, weight and cost issues regarding the antennas and feeding networks. Therefore, following all these great technological demands, the research is focusing on the development of high performance and miniaturized devices, which are easy to be integrated and low cost.

In this context, antenna systems are of paramount importance, since they actually characterize the transmission and reception over the wireless medium. The continuous demand for particular characteristics has driven the innovation to create many kinds of antennas (e.g. monopoles, Yagi antennas, horns, waveguide based, microstrip antennas, reflector, etc.) that can be found in literature [5], each of them presenting benefits and limitations which are suitable for specific applications. The different kind of antennas have peculiar characteristics that define their performance and usage, as radiation pattern, frequency band, polarization and shape. For this reason, antennas are typically passive devices, exhibiting fixed characteristics, and this leads to critical problems when many standards, each of them using a dedicated antenna, have to be integrated in a single device. In the case of a portable or handheld device, the difficulty is even larger: not only for the spatial allocation of the dedicated antennas, but also because of the isolation that has to be ensured for

the correct operation of the system. A typical solution employs several dedicated antennas or multiband/wideband solutions for supporting various communication standards [6–9]. Clearly, by utilizing dedicated antennas, the mentioned problems regarding integration and isolation has to be faced, while multiband and wideband antennas are more difficult to design, and an increased complexity is required from the RF front-end, especially concerning the filters and diplexers that are connected to the Low Noise Amplifiers (LNA) and the Power Amplifiers (PA). Therefore, a complete new class of antennas and RF/microwave components is needed, since the present and future wireless technologies requires antennas and circuits that can be multifunctional, covering many standards and capable to change their characteristic accordingly to adapt to the environment [10–12]. In the highlighted context, an attractive solution is represented by reconfigurable antennas, that have the capability to dynamically change one or more peculiar characteristics (i.e. radiation pattern, polarization and frequency band), in order to meet the requirements of a multi standard communication system, or to adapt to different scenarios [13]. For these reasons, great attention has been reserved to reconfigurable antennas and components in recent years due to their attractive and flexible functionality[14–17], which can allow a multiple service in a compact solution, reducing size, complexity and costs while increasing the total performance of the system. Moreover, reconfigurability enables the multi operation by properly changing the polarization, and it can maximize the connectivity while avoiding interference thanks to the shaping of the pattern. Moreover, studies have demonstrated that the utilization of reconfigurable antennas is greatly beneficial for IoT sensors networks for power saving [18], thanks to their adaptive radiation capability that supports an efficient ultra low power communication between the sensor nodes randomly spread in the space, in contrast with the typically used omnidirectional antenna, as depicted in Fig. 1.2.

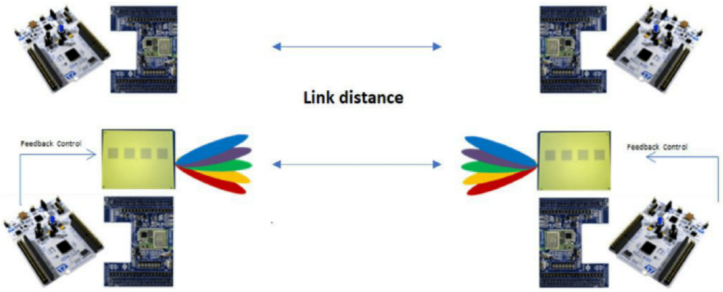

Figure 1.2: Standard versus reconfigurable pattern antenna in the communication between sensors in a IoT network [18].

Reconfigurable antennas are distinguished in four main categories, depending on the type of intrinsic property that is intentionally modified: frequency, polarization, pattern and compound reconfigurable antennas. The latter type of reconfigurable

antennas is characterized by the ability to change or tune two or more of the fundamental property of the antenna independently. The three main properties that are modified by reconfigurable antennas are depicted in Fig. 1.3.

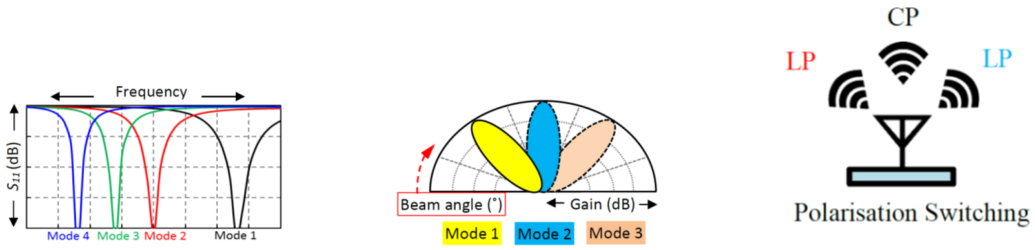

(a) (b) (c)

Figure 1.3: Illustration of the three main types of reconfigurable antennas:(a) frequency (b) pattern and (c) polarization.

Typically, the reconfiguration of the fundamental properties of the antenna is achieved by rearranging the surface currents or the electric field distribution in a reversible way, in order to adapt the functionalities of the antenna according to a special requirement. This is possible by integrating active elements (switches or tunable materials) in the antenna structure or in the feeding network. Many different reconfiguration techniques have been adopted, in order to comply with specific application and technology issues. The main techniques that enable reconfigurability are recognised as: electrical, mechanical, optical and smart material based. Moreover, it is noticed that reconfigurable antennas have gained attention not only on standard communication standards, but in almost all applications, ranging from Near Field Communication (NFC) [19] to Terahertz [20]. The great needs of systems that can dynamically change their functionality, as well as the need for multi-standard RF/mm-waves components has led to application of the reconfigurability concept to basic RF structures and component, which have been designed for operating in different frequency bands or in multiple operation states, e.g. couplers [21], filters [22–24] and absorbers [25]. In addition, the reconfigurability concept is used also for enhancing the performance of antenna arrays, by applying to the antenna elements or to the feeding network [26]. Also metamaterials have experienced a strong effort on research for applying reconfiguration, as described in [27]. However, the application of reconfigurability to an antenna brings to the consideration of new factors and challenges that have to be faced by antenna designers, such as the achievement of an adequate gain, stable radiation and proper matching throughout the different operative states. In addition, the inclusion of the switching components contributes to the evolution of antenna topologies for combining the radiative element with the switching component, typically controlled by a DC signal. As a result, parameters like switching speed, maximum power

rating and DC power consumption, which are more related to the RF/digital electronics field, have to be addressed in the design of the reconfigurable antennas. Clearly, the same considerations are applied for every reconfigurable structure under development. Therefore, the design of a reconfigurable antenna embraces the knowledge of multiple technologies, which are essential for the identification of the best reconfiguration property and technique to be involved in the design.

1.1 Review of Reconfiguration Techniques

The peculiar factor of reconfigurable antenna and components is the switching/-tuning element that allows the modification of its behaviour in a predefined and controlled way. Just considering the antennas, the three main properties (i.e. radiation pattern, polarization and frequency of operation) can be controlled in many ways by employing different reconfiguration techniques, and it is responsibility of the designer to choose the best method that efficiently realizes the intended task and that is compliant with the performance and technical constraints. The same considerations can be applied to other RF/microwave components, as for instance filters and feeding networks, where reconfigurability is typically applied to change the topology (by enabling/disabling some parts) or by tune the frequency of operation. Moreover, in all cases, cost and manufacturing issues plays an important role for the reconfigurable antennas and systems, and they have also to be considered in the development. As a matter of fact, the possibility of having a multitude of operative states involves also more design effort to ensure that the requirements are fulfilled in each of them. In the following, an overview of the main methods that enables reconfigurability are briefly described.

1.1.1 Mechanical Techniques

The mechanical tuning technique is the first method applied for the early realization of the reconfigurable antennas. By employing this technique, the intrinsic characteristics of the antenna are modified with the use of actuators, motors or other methods for moving part and/or the entire antenna, thus changing the electrical properties. More in detail, some designs are characterized by a mechanical tuning that modify the properties of the antenna substrate as in [28–30], while other solutions are focused on the changing of the antenna structure by moving some parts, resulting in a modification of the antenna radiating edges which lead to a different antenna operation, such as different bandwidth, pattern and polarization [31–33]. This technology is important solution regarding reconfigurability, since it does not rely on switching devices, that typically need biasing lines, controls and they have electrical limitations concerning power and tunability, as for instance the reconfigurable horn antenna especially designed for high power application in

[34], which uses some movable metallic flaps for modifying the antenna pattern, as shown in Fig. 1.4a.

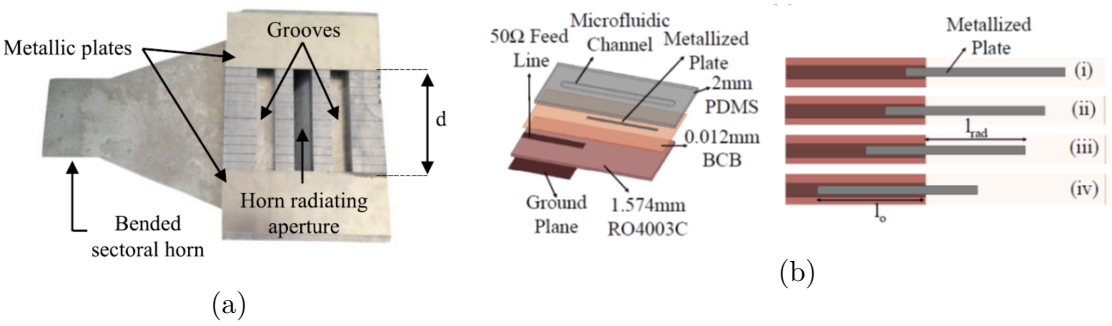

Figure 1.4: Two example of mechanical reconfigurability (a) Horn antenna using two movable metallic flaps for changing the aperture length in the H-plane direction for reconfiguring the half power beamwidth [34], (b) monopole with frequency reconfigurability achieved by microfluidically extruding or retracting a metalized plate [35].

Mechanical reconfigurability is obtained by using various actuators, that can be stepped or linear motors, ideal to move specific parts of the antenna [31, 36], as well as turning [37] and rolling motors [38]. Moreover, also electric and magnetic motors, like MEMS [39–41] and piezoelectric actuators [32] have demonstrated good performance. However, the structural modification of antennas utilizing mechanical methods presents some drawbacks, such a bulkiness, slow response time and regulation accuracy, as well as generating some concerns on the life-cycle and maintenance of some mechanical parts. Moreover, many innovative concepts have been presented for exploiting the property of mechanical reconfigurability to be low loss while ensuring high linearity and higher isolation. Some new concepts which are becoming popular in recent years are the microfluidic technology, [35], whose structure is shown in Fig. 1.4b, as well as elastomers [42] and origami antennas [43].

1.1.2 Reconfiguration Through Electrical Switches and Tuning Elements

Electrical reconfiguration is the the most widely used technique applied to achieve reconfigurability. The electrical reconfigurability mechanism is based on switches, controlled by voltages or currents, that are used to modify the antenna surface current distribution, to connect and disconnect some section of the structure and/or radiating edges as well as for altering the impedance [14, 16, 44]. An attractive feature of such components is the easy integration with the antenna

structure and planar devices, allowing the designer to place such tuning elements in the peculiar position for allow the desired reconfiguration. Two different type of electrical reconfiguration technologies can be distinguished. The first includes the switching elements, such as PIN diodes, RF-MEMS, CMOS switches, Field Effect Transistors (FET). The second category is related to the continuous tuning element, namely varactors (i.e. variable capacitor), which are diodes able to vary their junction capacitance as a function of the reverse bias voltage.

In past years, lot of attention were gained to RF-MEMS, which are micro mechanical systems that can be controlled by an applied voltage, due to their very high isolation and low loss. Many different design employed RF-MEMS as reconfigurable element [45–51], however, this component lost some interest due to its high cost, the low switching speed and for the required positive and negative control voltages, and, most importantly, for its limited life cycle.

On the other hand, PIN diodes is probably the most popular component used for applying reconfigurability. PIN diodes are cheap, low loss and fast switching component which can be modeled as a current controlled resistor: few milliamperes are enough to pass from a high impedance state to a resistance in the order of $\sim \Omega$. This component can be easily be placed in antenna structure, filters and feeding networks, due to its small form factor, ensuring a high reconfigurability dynamic [52–57]. One remarkable example of reconfigurable design employing PIN diodes is the pixel antenna [58], shown in Fig. 1.5a, which is able to reconfigure frequency, radiation pattern and polarization of a patch antenna. It is noticed that the use of PIN diode is quite simple, however a proper DC biasing network has to be designed, which is sometimes difficult since it can affect the RF performance of the device. Moreover, the DC power consumption can be an issue, since the component needs some current to be set in low loss state. The latter semiconductor component which is frequently used in many reconfigurable design is the varactor diode, which is the ideal choice when a continuous variation of a parameter is needed (e.g. continuous frequency tuning) for filters, antennas and metamaterials [44, 59–62]. As a design example, it is shown in Fig. 1.5b an example of reconfigurable filtenna, where the varactor is used to tune the frequency of the filter electronically.

The main drawback of such a component is its low tunability range and its limitation in bandwidth. In literature are also reported some designs that employs the use of both varactor and PIN diodes, for achieving reconfigurability [63, 64]. Despite their wide usage, this components exhibits some shortcomings, such as the non-linearity effects (e.g. intermodulation), the presence of the biasing and control lines placed close the RF device, RF losses and DC consumption and the sensitivity interference.

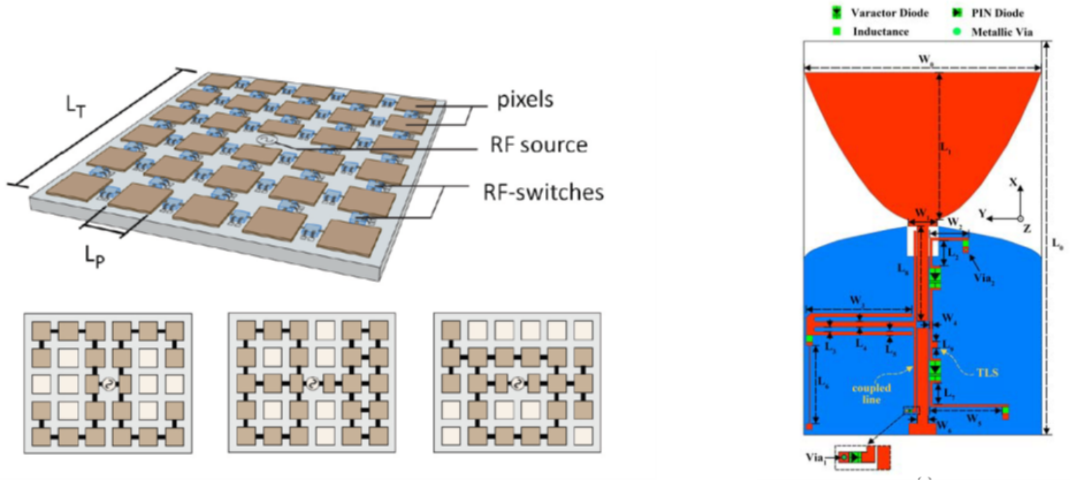

(a) (b)

Figure 1.5: Two example of electrical reconfigurability using semiconductor components (a) fully reconfigurable pixel antenna, [58], (b) reconfigurable filtenna based on varactor diodes, composed by a wideband monopole and a frequency agile filter [61].

1.1.3 Reconfiguration Through Smart Materials

In recent years, lot of attention has gained the so called "smart materials", which are materials whose characteristic can be tuned by the application of an external control, that can be represented by a voltage, a magnetic field or a thermal source. Many reconfigurable antennas, filters, phase shifters, absorbers and metamaterial components have employed such materials to properly alter their characteristic. From this reconfigurable technique, two different types can be defined: the material that can change their permittivity ϵ_r and/or permeability μ_r, and instead the ones that can modify their conductivity.

The most commonly used in reconfigurable application are the first type, which includes Liquid Crystals (LC) and ferrite materials, the most popular smart materials among all. Liquid crystal is an anisotropic material whose permittivity can be controlled by the orientation of its rod-shaped molecules, by the proper application of an electric or magnetic field. In particular, the nematic phase of the LC is the most interesting for mm-wave frequencies. Therefore, the permittivity of the LC based substrate can be altered by varying the applied voltage, in a continuous way, and this feature is used to modify the electrical length of many antennas and components [65–69], thus achieving a modification of the phase attained, frequency band, polarization etc. An example of such a design is displayed in Fig. 1.6a, where a reflectarray based on LC substrate is able to provide a sum or difference of the beam by exploiting the properties of the smart material. The main drawback of

the LC are related to their low tunable capability and the increase manufacturing complexity due to the liquid nature of such a material. Moreover, ferrite materials have also been used in many designs involving reconfigurability, due to their ability to modify the permittivity and permeability by the application of an electric and magnetic field, respectively [70–73]. Another interesting characteristic of such materials is their high intrinsic values of ϵ_r and μ_r in comparison with standard dielectric, which is interesting for miniaturization purpose. In Fig. 1.6b it is shown an example of patch antenna loaded with a ferromagnetic material, called Yttrium Iron Garnet (YIG). The displayed antenna is able to change the radiation characteristic upon a variation in the magnetic field. The typical drawbacks that are related to the utilization of this kind of material are the high thickness and the complex tunable system, which often lead to a non uniform tunability due to the non uniform field distribution.

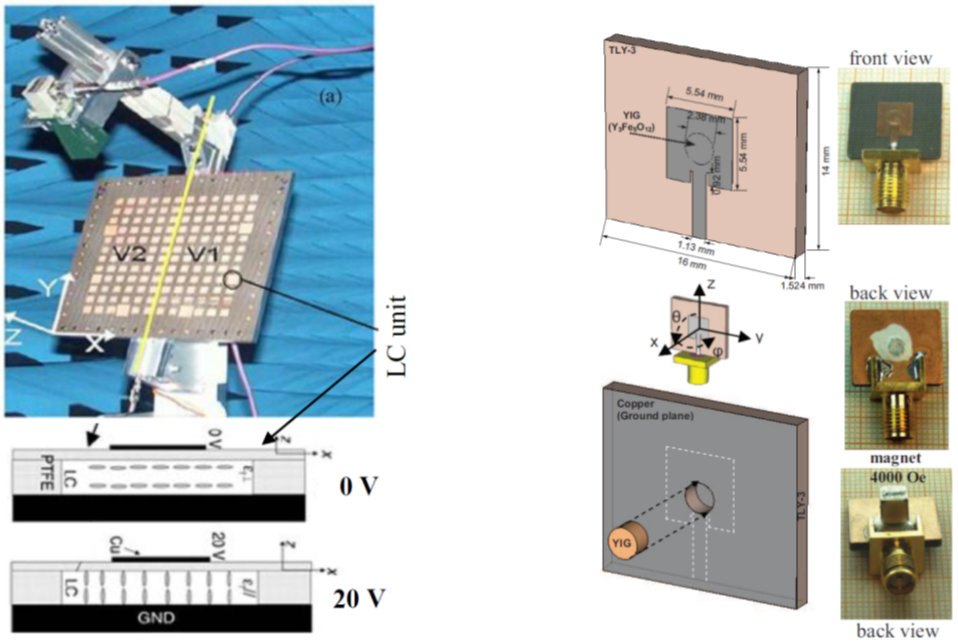

(a) (b)

Figure 1.6: Two example of reconfigurability using smart materials (a) reconfigurable reflectarray using liquid crystals [74], (b) polarization reconfigurable patch antenna employing Yttrium Iron Garnet (YIG) [75].

The second type of smart material, named phase changed materials, have the particular characteristic of change their resistivity according to some external control. This feature is particularly interesting, because the insulator-to-metal transition can is very steep, and for this reason such materials can be used to efficiently realize switches for mm-wave and Terahertz application. Some results showing the

capability of such materials are reported for Barium Strontium Titanite (BST), that can be controlled by an applied voltage [76, 77], and for Vanadium dioxide (VO_2), that can be thermally controlled [78–80]. Another important phase change material, which has attracted lot of interest, is the Graphene, that can be controlled by a DC voltage to act as a lossy dielectric or a conductor [81–83].

1.1.4 Reconfiguration Through Optically Controlled Switches

At last, it is here presented a novel technique, which has been matter of research in recent years, due to the requirements for high performance switching and tuning elements that can be used in the mm-waves and Terahertz frequency ranges. In fact, optical reconfiguration is an attractive solution since it does not require any bias or control on the active components, because this technology rely on photoconductive switches and materials. The principle of operation of such a switches uses a light source, typically a laser, to increase the conductivity through the increase of charge carrier density in the material. Clearly, some complexity is required for the arrangement of the optical fibers and laser source. Moreover, the switching speed of this components is lower than the semiconductor ones. Despite the mentioned drawbacks, mainly due to the early research stage, some interesting design have been reported employing silicon photodiodes and phototransistors [84–88]. Some promising results are obtained in the mm-wave range by the Germanium Tellurium (GeTe) phase change material, which demonstrates low loss in *ON* state and high isolation when *OFF* [89, 90]. In [91], a reconfigurable patch antenna employing GeTe switching concept was manufactured and measured. Moreover, it exhibits high power handling and low power consumption, and it can be a good candidate for future reconfigurable design.

1.2 Applications of Reconfigurable Antennas and Components

As previously discussed, reconfigurabilty represents an attractive solution to overcome many limitations of standard antenna functionalities imposed by the modern wireless communication systems. Due to their flexibility and their capability to enhance the system and channel performance, reconfigurable antennas are the best candidate for being one of the most important components in the future of communication and wireless sensors. Moreover, since this technology is very promising, many studies are also focusing on the management of reconfigurable antennas, for taking advantage of their potential in create a highly integrated and smart approach to future connectivity, by using FPGA and neural networks [92–94] or optimization algorithms (e.g. particle swarm, genetic) are employed to define the best reconfigurable architecture [95, 96]. In the following, an overview of the advantages and

perspectives of the four types of reconfigurable antennas, which involves frequency, polarization and pattern agility, are briefly given.

1.2.1 Frequency Reconfigurable Antennas and Systems

Frequency reconfigurable antennas and systems, whose functionality is shown in Fig. 1.3a, are the key element for the future multi-standards and multi-services wireless devices, as replacement of the single band or multiband components that are currently integrated in many portable and connected devices such as mobile phones, smart watches, laptops, tablets and home appliances. In fact, frequency agile devices can be used to dynamically and efficiently reallocate the used frequency spectrum: this can be done by continuously varying the frequency range [97–101] or by switching between different bands [102, 103]. This concept is the idea leading the Cognitive Radio [104], which is an intelligent system which is able to monitor the radio channel and identify the idle frequencies of the spectrum, called white spaces, and then to react and to tune its operation accordingly. In order to do so, a reconfigurable antenna is needed, for properly set the system to operate in the desired white space frequencies. In Fig. 1.7 the communication process operated by the cognitive radio is depicted.

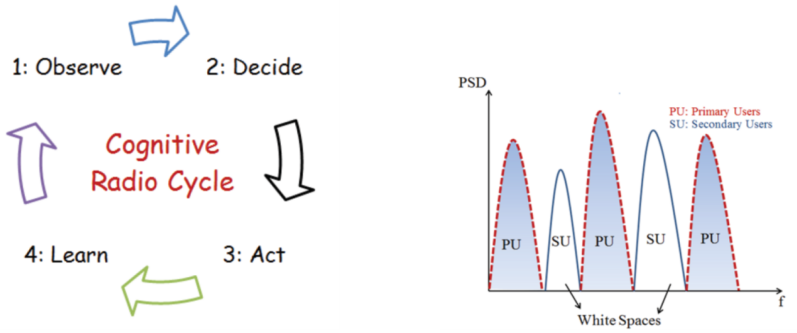

(a) (b)

Figure 1.7: Illustration of the principle of operation of the cognitive radio:(a) cognition cycle (b) the white spaces concept on the frequency spectrum [104]

Another interesting application of frequency reconfigurabilty, useful in wireless communication systems like WLAN and WiMAX, is the modification of the operational bandwidth from wideband to narrowband/multi-bands [103, 105–107]. From system point of view, frequency reconfigurable antennas shows advantages in comparison with wideband and multiband antennas in avoiding unwanted signals and interference and simplify the architecture of the RF front-end circuitry. This effect is obtained by both using a narrowband but highly tunable characteristic of the frequency agile structure, or by implementing some filtering over a wide frequency

range (e.g. notch filters) that can be dynamically adjusted for rejecting the interference or to separate several communication standards [44, 52, 108–110]. The latter kind of reconfigurable antennas are called filtennas, and they are named in this way because they combine the feature of an antenna and a filter, therefore providing high selectivity without distortions on the radiation pattern. Clearly, frequency reconfigurability is also a popular solutions for filters, for adjusting the frequency response [111–113] as well as the bandwidth or the center frequency in single [114, 115] and dual band applications [22, 116, 117]. Usually, the achievement of frequency reconfigurability is realized by modifying the electrical length employing various methods, as for instance material tuning, impedance loading, metamaterials components or by switching devices. A commonly used technique to tune the electrical length of the antenna or passive device is realized by altering the geometry of the radiating device, by connecting/disconnecting specific parts and therefore having an operating bandwidth which is accordingly reconfigured. This method is very effective to switching between lower/higher frequency bands, and it has been applied to many types of antennas, such as microstrip [102, 118–121], dipoles [86, 122], and slot type [45, 123]. Another popular method for achieving frequency reconfigurability is through reactive loading, where a tuning element is used to compensate the reactive part of the input impedance of the antenna, thus shifting the matching point [124, 125]. The last method used for the frequency variation is obtained by changing the material properties, thus producing a modification of the electrical length without altering the physical dimensions. The principle of operation exploits the different propagation constant related to the changes in the material, which induces a shift toward lower or higher frequencies as the permittivity change high to low (and vice-versa) [82, 126, 127].

1.2.2 Polarization Reconfigurable Antennas

Polarization reconfigurable antennas are an important solution for limiting multipath fading problems (as illustrated in Fig. 1.8a, for the case of in-body communication) and for reducing the polarization mismatch loss between the transmitter and receiver. The latter aspect became critical in a dynamic scenario, where the position of the transmitting or receiving device is changing in position and orientation, thus causing potential communication failure due to the polarization mismatch, as depicted in Fig. 1.8b for the case of single polarized antennas.

Moreover, a polarization reconfigurable antenna can be useful to support frequency reuse, by switching among two orthogonal polarization modes, if the communication is under Line-Of-Sight (LOS). If this is not the case, polarization reconfigurability can be used to support a diversity scheme. Further applications of this type of reconfigurable antennas can be found in SATCOM and radar applications [130, 131], as well as in MIMO systems to achieve polarization diversity [132]. In literature are found many designs concerning polarization reconfigurable antennas

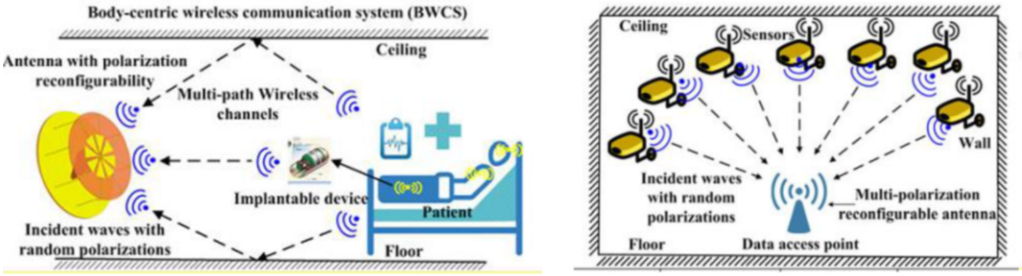

(a) (b)

Figure 1.8: Application of the reconfigurable antennas to reduce (a) the multipath effect [128] and (b) polarization mismatch due to random positioning of the receiver and transmitter devices [129].

that can switch between Right Hand Circular Polarization (RHCP) and Left Hand Circular Polarization (LHCP), or that can select between Circular and Linear Polarization (LP) states [133–137]. Another interesting implementation concern the multi-linear polarization antennas, which are able to select among two or more LP states [128, 129, 138, 139]. More in detail, polarization reconfigurability is achieved by varying the surface current flow direction of the antenna. Many techniques are used to obtain such a modification of surface currents, by employing reconfigurable feeding networks [140–143], metasurfaces [144–146], and tunable radiators [147–149].

1.2.3 Pattern Reconfigurable Antennas

Pattern reconfigurable antennas represent an important category, being a very attractive solution in applications like surveillance, tracking, vehicle-to-vehicle and satellite communication, cognitive radio, etc [150–154]. In fact, this kind of antennas have the peculiar property to alter their radiation pattern in predefined direction, for scanning the main beam or null spot in the desired directions. This is an essential feature by greatly increasing the transmission rate, by steering a high gain beam toward a target direction for maintaining the LOS, and therefore a strong communication link, between one or two moving devices [10, 152, 155]. Especially for MIMO application the pattern reconfigurability represent an interesting solution for minimizing the spatial correlation of the signals [156–158]. A significant example of pattern reconfigurable antenna in displayed in Fig. 1.9. This designed, presented in [159], employed an arc dipole radiating structure that can be modified by a reconfigurable feeding network to radiate at four different directions, as can be noticed in Fig. 1.9b.

Moreover, some designs applied the same concept to the null steering, by exploiting the Direction Of Arrival (DoA) technique to discriminate between the signal

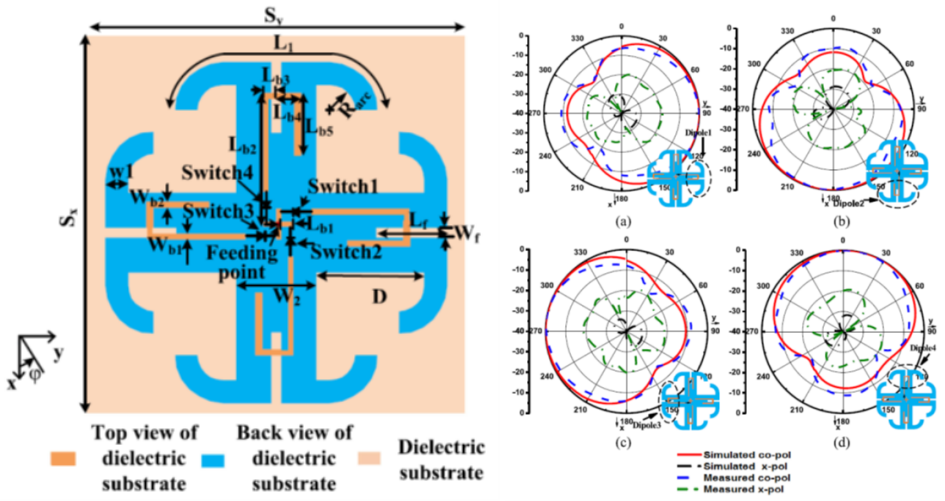

(a) (b)

Figure 1.9: Pattern reconfigurable arc dipoles antenna (a) antenna topology, (b) 90° radiation pattern rotation [159].

and the noise the antenna is able to place the null in the direction of the interference and reject it [160, 161]. Pattern reconfigurability is obtained by controlling the current distribution on the antenna, for properly modifying the radiation characteristic. The main challenge is represented by the impedance matching, that is altered by the reconfiguration process of the surface currents of the antenna. Many different methods are employed for achieving pattern reconfigurability, such as rotation [41], parasitic elements or stubs [162–168], frequency selective surfaces [169, 170], partially reflecting surfaces [171, 172], pixel antenna structure [173, 174], coplanar to slotline transitions [175], switchless method [176], multi-modal excitation [177, 178].

1.2.4 Multiple Reconfigurable Functions

Reconfigurable antennas and systems that are able to reconfigure two or more characteristic are indicated compound reconfigurable. Especially concerning antennas, the combination of multiple function is clearly an asset for some application, in particular for the development of portable devices that can use such a structure to integrate multiple functionalities, keeping the overall dimension compact. In recent years, many researches have been focused on the development of compound antenna, for combining the advantages of two or more reconfiguration techniques. Recently, many antennas with pattern and polarization reconfigurability was proposed, for improving the capacity of the communication system as in [179–183].

For example, MIMO technology can used both pattern and polarization reconfigurability to develop and adaptive system, which can improve its efficiency by applying both polarization and pattern diversity [16, 157]. Many research were investigating the concept of frequency and pattern reconfigurability [86, 93, 184–186]. Moreover, pattern and frequency reconfigurability can be applied to increase the Signal-to-Interference Ratio (SIR), as in [187]. With this approach, the combination of frequency selectivity, employed to reject the out-of-band interference, were used in combination with a high directive steering pattern for reducing the in-band interference. It is also mentioned that the multiple reconfiguration of pattern and frequency is a key technology that is required by the cognitive radio [188]. Polarization and frequency can also be simultaneously reconfigured, for enhancing capacity of the system through polarization diversity while operating in a free portion of the communication spectrum, as in [189–193]. However, the development of such a multi-functional systems has proven to be a great challenge: in fact, since the antenna characteristic properties are closely related and mutually dependent, sophisticated method to separately control the reconfiguration of each parameter has to be investigated. In order to accomplish to the multiple reconfiguration, the choice of the tuning technique is essential.

1.3 Outline of the Thesis

The Thesis structure is summarized below.

In Chapter 2, a method to extend the scan range of a phased array based on Rotman lens as beamformer is demonstrated through simulation and measurements. The scan range extension is based on a reconfigurable phase shifting architecture, named Phase Management Unit, located between the Beam Forming Network and a linear antenna array. Two different approaches for the realization of the switching phase shifters, responsible for the scanning mode selection, are described. Moreover, in the design it has been employed a novel method to efficiently illuminate the Rotman lens and, at the same time, to generate a cosine type amplitude tapering. A compact design has been manufactured and measured, employing standard PCB technology, showing an actual increase of the scan range of a factor two, in comparison with the standard approach.

In Chapter 3 a miniaturized and frequency reconfigurable rat-race coupler has been designed. The concept of artificial transmission lines is here exploited to design a very compact coupler, which can operate in two different frequency bands, by acting on switches. The reconfigurable method, based on addition and subtraction of line sections of proper length, is enhanced by a novel theory for balancing the phase characteristic of the miniaturized branches of the rat-race coupler, including also the effect of the switching elements. The measurement on the prototype have shown good agreement with both analytical and simulated results.

The frequency and polarization techniques have been applied to a UHF RFID reader antenna. Chapter 4 presents the realization of a compact antenna, with multiple reconfiguration capability, by employing the concept of the reconfigurable feeding network. In particular, it is demonstrated how the polarization reconfigurability can be a breakthrough in UHF RFID reader antenna application to overcome the polarization mismatch effect, which occur in the communication link between a circular polarized antenna and a linear RFID Tag. Based on an electrically small suspended patch antenna, several method for the application of both frequency and polarization agility are investigated, each of them focused on the optimization of a particular aspect, showing promising results.

Finally, in Chapter 5 the conclusion of this research work are drawn and, moreover, some comments on future applications and possible suitable techniques for the reconfigurable antenna technology are provided.

Chapter 2

Scan Range Extension of a Phased Array Based on Rotman Lens

The continuous evolution of communication systems is experiencing a rapid increase of the frequencies of cellular bands, driven by the demand of high data rate and fast connectivity. As a result, the communication network technology is complementing the operation frequencies in the radio spectrum from the sub-6 GHz to the mm-waves, as required by *5G* [194]. In order to meet these requirements, communication systems are evolving through beam switching or beam steering solutions in *K* bands, and moving toward the 50 – 110 GHz range. Moreover, also radar sensors are evolving towards higher frequency bands, and *E*- and *W*- bands are typical frequency ranges where radar sensor are operating in standard security application. Undoubtedly, radar technology is growing exponentially in recent years, with an increasing trend due to the technical advancement in customary markets like automotive, space or military, and the exploitation of these devices in sensors for industrial, automation and surveillance applications. A notable example of its application is the Advanced Driver Assistant System (ADAS), which represents one of the key elements that support the autonomous driving research and development, following the goal of a Highly Automated Driving (HAD) by 2020, for highway driving scenarios, and the final introduction of fully automated driving after the year 2025 [195].

In this context, phased arrays are key components for supporting the technological challenges for the future wireless systems. Their wide spreading application leads to a raise in technology development, which increased the requirement of an array antenna system with high performance, low cost and easy integration. In particular, the commitment of antenna designers is not only focused on wide band antennas and wide-angle scanning arrays, but also on the development of suitable Beam Forming Networks (BFN) for properly feeding the antenna systems and shaping the pattern in a wide angular range. Ideally, the BFN should be wide band, low

loss and it has to properly feed the antenna array with the necessary phase and amplitude distributions. The requirements are extended to solutions which are suitable for high volume production and compatible with Surface Mounted Devices (SMD) and Monolithic Microwave Integrated Circuit (MMIC) for an easy integration with the electronics. In the highlighted contexts, significant interest has gained the Rotman lens [196, 197]. In particular, this kind of BFN is very attractive because it is a True Time Delay (TTD) device (thus intrinsically broadband), in contrast to other beam forming concepts like the Butler Matrix, which is limited by the performance of the phase shifters. In addition, the Rotman lens is relatively simple to design, it supports multiple beams and, if designed properly, it exhibits low losses and an accurate progressive phase distribution over all its outputs. Moreover, its manufacturing is very convenient for most applications, due to its monolithic planar structure, which is light weight, easy to produce and low cost. Being the scan range a primary feature of many antenna array systems, this chapter focus on the description of a general method for extending the scan range of a phased array based on a reconfigurable phase shifters system. The concept for broadening the scan range is first described analytically by considering a general linear array, and afterwords, its combination with the Rotman lens for designing a 24 GHz ISM radar antenna system is investigated. Therefore, two design of a compact and wide scan range phased arrays based on Rotman lens as beamforming network will be proposed. In the first design, the reconfigurable operation related to the phase that has to be applied at antenna array input, which is necessary to extend the scan range, is realized employing a single phase shifting stage. In the second design, the phase operation is divided in a fixed and reconfigurable phase shifting stages, for improving the overall performance. Moreover, in the latter design, a novel feeding concept for the Rotman lens is applied and analyzed.

2.1 Rotman Lens

This type of beamforming network takes his name from Walter Rotman, who first developed the concept in 1963 in collaboration with Turner [198] as an improvement of the Ruze lens concept [199]. In their work Rotman and Turner derived the set of equations needed to determine the geometry of the lens, depicted in Fig. 2.1.

The Rotman-Turner lens was designed to provide 2D scan to a linear antenna array, and was characterized by two conductive parallel plates, excited by horn antennas at input side (named as *Beam Contour*) and connecting the array elements via transmission lines at its output (named as *Array Contour*). In other words the operation of a Rotman lens can be described as the transformation of the excited *Beam Contour* into a linear phase shift for the *Array Contour*, which can be directly connected to a linear array. This development was using three focal points along the beam contour that ensure theoretical zero phase error of the phase front feeding

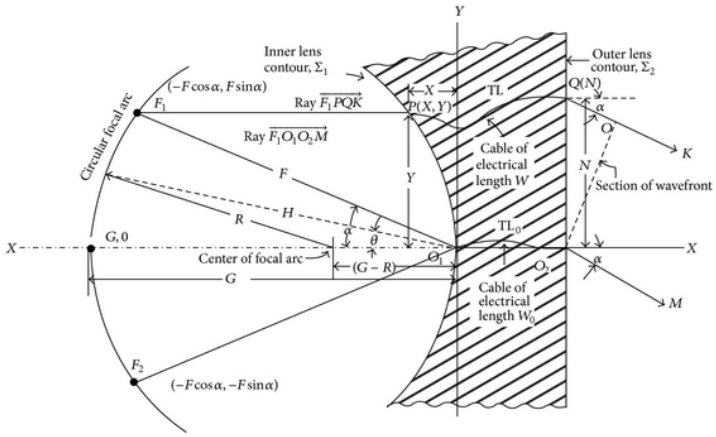

Figure 2.1: Original geometry of the Rotman lens[198].

the linear array elements. In this first version, the parallel plates were filled by air, and the contour was imposed to be circular, restricting the scan angle of the phased array to be equal to the angle subtended by the beam port position. The principle of operation of this passive beamforming network is the exploitation of the electrical length between a defined input on the beam port contour to all the ports on the array contour for creating a linear progressive phase shift across them. Therefore, the signal injected in one of the beam ports of the lens generates a cylindrical wave front that propagates in the structure and distributes evenly in all array ports outputs. The path length with which the wave is travelling in the structure defines the phase shift. This means that for each input of the Rotman lens a well defined phase shift is associated, which is therefore related to a distinct beam of the antenna array. Since this first design, many research were focused on the improvement of the concept developed by Rotman and Turner, as for instance the insertion of the *Dummy ports* for reducing the effect of the spillover and the use of a dielectric filled waveguide for reducing the size of the lens by a factor $\sqrt{\epsilon_r}$ [200]. An important advancement was introduced by Katagi [201], that defined a new variable for providing the degree of freedom of independently setting the scan angle and the angle subtended by the off-axis focal point (respectively β and α in Fig. 2.2). Therefore, referring to Fig. 2.2 and to Fig. 2.1 for comparison, it can be noticed that with the concept developed by Katagi the scan angle β is different from the angle α obtained from the inner focus axis XO_1 and the other focal points O_1F_1 (equivalently O_1F_2) where X, F_1 and F_2 are the three focal points introduced by Rotman,with G and F the respective focal length. The figures report also the beam contour, indicated with σ_1 array contour, named σ_2, as well as the transmission lines connecting the N_{max} elements of the antenna array. More in detail, Katagi demonstrated that by using the new design variable, defined as the

ratio between α and β, a new shape of contours can be calculated and, as a result of the refocusing, a lower phase error can be achieved.

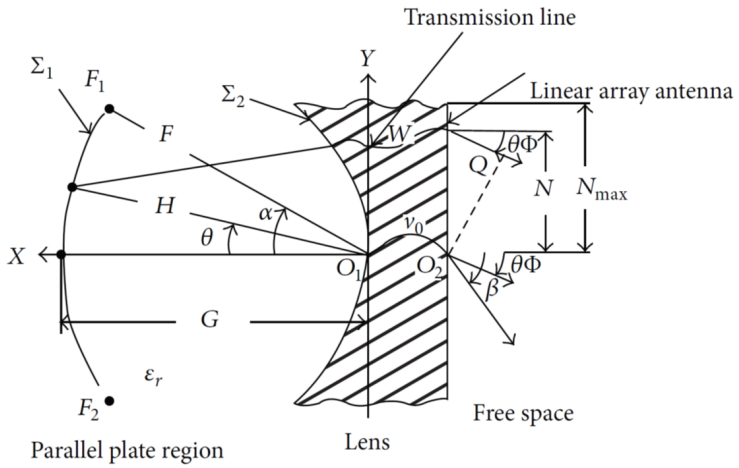

Figure 2.2: Geometry of Rotman lens proposed by Katagi [201].

The major breakthrough was introduced by Hansen in [202], who introduced the elliptic beam contour. In his work, Hansen proposed seven design parameters: focal angle, focal ratio, beam angle to ray angle ratio (i.e. β and α), maximum scan angle, focal length, array element spacing and ellipticity.

The Rotman lens designed in the presented research work follows the set of equations derived by Hansen. Despite the multitude of studies conducted in past decades, the Rotman lens is still attracting many interest in the scientific community, and many studies have been carried for improving the performance of Rotman lens, by calculating a more efficient lens geometry [203–209], or by optimizing its construction [210, 211]. Furthermore, state-of-the-art technologies have been applied to the Rotman lens design for enhancing its performance, by exploiting Substrate Integrated Waveguide (SIW) [212–214], Low Temperature Cofired Ceramic (LTCC) [215], or either introducing synthesized dielectric substrates [216], multilayer design [217] or Ridge Band Gaps (RBG) [218]. Since its first development, the Rotman lens has proven to be an interesting approach for producing 2D scanning in linear antenna array in many applications, since it is a True-Time-Delay (TTD) device, and therefore it produces beam steering independently of the frequency, and it is therefore capable of wide-band operation. In fact, as long as the path lengths exhibit constant time-delay behavior over the bandwidth, the lens is insensitive to the beam squint problems exhibited by constant phase BFNs. This is in contrast to other passive beamforming networks like Butler Matrix and discrete phase shifters. Moreover, the Rotman is relatively simple to design, it supports multiple beams and, if proper designed, it exhibits low losses and an accurate progressive phase distribution over all its outputs. Furthermore, its manufacturing is very convenient

for most applications, due to its monolithic planar structure, which is light weight, easy to produce and low cost. However, in order to have the precise progressive phase distribution, the geometry of the lens has to be carefully chosen, according to the desired maximum scan angle. Moreover, an efficient design of the lens does not consider only to pursuit the beam steering, instead the geometry is optimized for reducing the spillover losses and their impact on the BFN. In this context, the *Dummy ports* (terminated to 50 Ω) are placed between the beam and the array contours of the lens, for absorbing the power radiated at the side of the lens (i.e. power that is not coupled to the array ports), therefore avoiding internal reflections in the lens cavity. This aspect is very important in the design of the lens, and it will be discussed in more detail in the following paragraphs. Finally, Fig. 2.3 shows the propagation principle of a typical Rotman lens, where it can be distinguished the wavefront which has its origin on the excited beam port and it is then coupled to all the array ports. In Fig. 2.3, it can also be recognized the power lost in the *Dummy ports* (place on the sides) due to spillover.

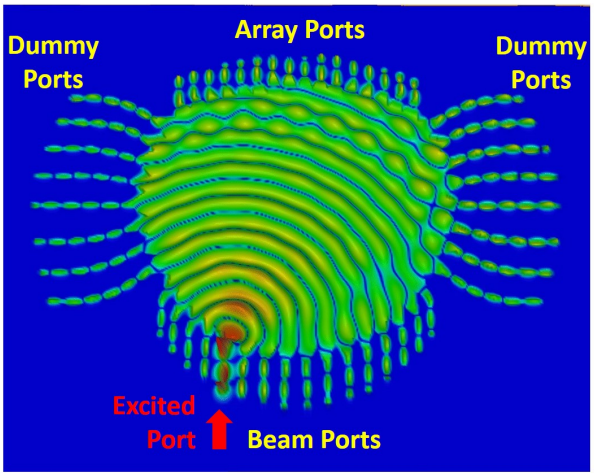

Figure 2.3: Simulated wave propagation inside the Rotman lens cavity. The excited input, positioned on the lower side, generates a wave propagating inside the lens, and reaching all the output ports, located on the top side of the figure, with equal phase. Moreover, the mutual coupling between input ports as well as the spillover effect, visible on the terminated lines in the two sides of the lens, can be observed.

As previously stated, a wide scanning range phased array is desirable in many different applications. The enormous increase of mm-wave antennas covering applications ranging from communication to surveillance estimated for the next future is setting the requirements to high performance but low cost and reliable solutions. In this chapter, a general method for increasing the scan range of a general phased array is firstly theoretically formulated, and its concept is then used together with a

Rotman lens in order to design and realize a wide scanning range radar antenna suitable to be used as a Short Range Radar (SRR) in the 24 GHz ISM band. Actually, Rotman lenses represent a key technology to develop radars for both consumer and automotive market, due to its good performance, its multi-beam capability and the favorable manufacturing considerations (i.e. planar structure and low cost). However, the design of the Rotman lens become complicated when wide scan angles are required. The reason for the high inaccuracies of this kind of BFN, concerning the phase distribution and beam level in relation to wide scan angle, is given by the intrinsic geometry of the lens, which assumes excessive and inefficient shapes. Nevertheless, few achievements have been published for improving this aspect of the Rotman lens. The most representative is found in [219], where Piezoelectric Transducer (PET) controlled phase shifters were used for increasing the steering angle by 8°, for a total scanning range of ±38°. In a similar way, in [220], Liquid Crystals (LC) phase shifters were used in combination with the Rotman lens to increase the scanning range by ±7.5°.

The scope of this research activity is to propose a method to double the Field of View (FOW) of the Rotman lens. The standard Rotman lens with wider angle will be applied to the case of a planar antenna array scanning for ±30° for validation of the proposed design method.

2.2 Extended Scan Range Method

The process of extending the scan range is related to a well defined phase shifting pattern superimposed to the phase distribution of the original BFN, which is then fed to the antenna array. This phase operations are collected in a block, represented in Fig. 2.4, named Phase Management Unit (PMU). The PMU working principle can be distinguished into two separate but concurrent operations, which have been named "Complete Beam Shifting" (CBS) and Beam Mirroring (BM).

In order to clarify the effect of the PMU on the phase distribution in the case of a generic phased array, it is considered the general equation for the array factor $AF(\theta, \varphi)$ of a $N-$elements linear array:

$$AF\left(\theta\right) = \sum_{n=1}^{N} I_n e^{j(n-1)(kd\sin\theta+\Phi)} \underbrace{e^{j\alpha_n}}_{\text{CBS}} \underbrace{e^{j\beta_n}}_{\text{BM}} \tag{2.1}$$

referring in particular to the case when the array elements are arranged along the x axis, with uniform spacing d, uniform phase gradient Φ between adjacent array elements, and the antenna radiation pattern steered in the xz plane. In (2.1), j is the imaginary unit, I_n is the amplitude of $n-th$ element excitation, and k is the wavenumber.

The two phase factors $e^{j\alpha_n}$ and $e^{j\beta_n}$ are the phase contributions of the CBS and the BM respectively; hence, as already pointed out, the extended scanning range

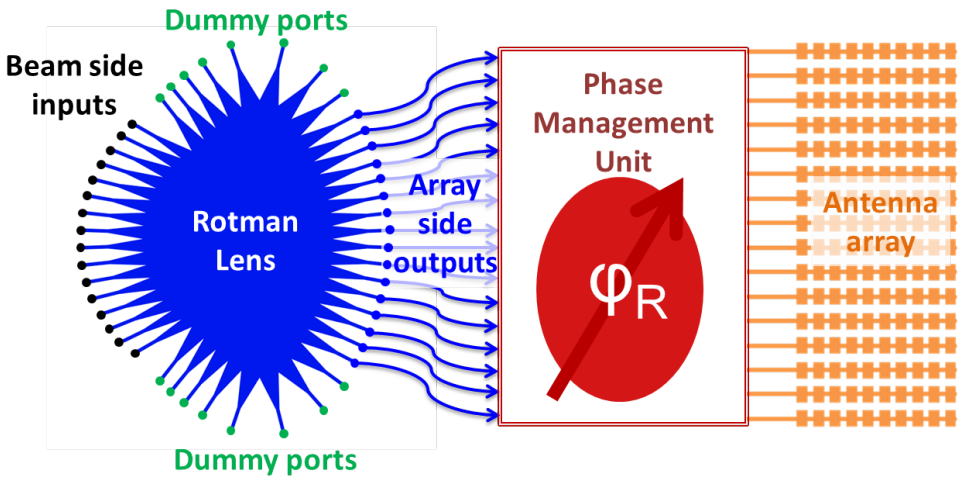

Figure 2.4: Block diagram illustrating the extended scan range Rotman lens method fundamental parts. The three elements are: Rotman lens, Phase Management Unit, that produces the increase of the scanning range, and the antenna array.

method involves two operations superimposed to the BFN phase distribution. In order to better understand the scan range extension method, the two contributions on the phase of the CBS and BM will be analysed separately.

2.2.1 Complete Beam Shifting

The Complete Beam Shifting is a general approach to move all the radiated beams in such a way that just one portion of the scan range is covered (either positive or negative). In other words, when the CBS is applied to an initial phased array scanning in the range $\pm\theta_{max}$, the out coming scan is then modified to cover the range from 0 to $2\theta_{max}$. This process is resulting by the application of a progressive phase shift superimposed to the canonical phase distribution produced by the original BFN. The additional phase term, $e^{j\alpha_n}$ in (2.1), that defines the CBS, is specified as:

$$\alpha_n = n \cdot k \cdot d \cdot \sin(\theta_{max}) \tag{2.2}$$

with $n = 1, 2, \ldots, N$ is the $n-$th array element. In Fig. 2.5 is given a graphical representation of the effect of the CBS on the initial pattern.

2.2.2 Beam Mirroring

Similar considerations discussed for the CBS are applied to the BM. Taking as reference a radiated beam, the BM operation produces a reversal of the sign of its pointing angle by the application of proper phase distribution at the array input.

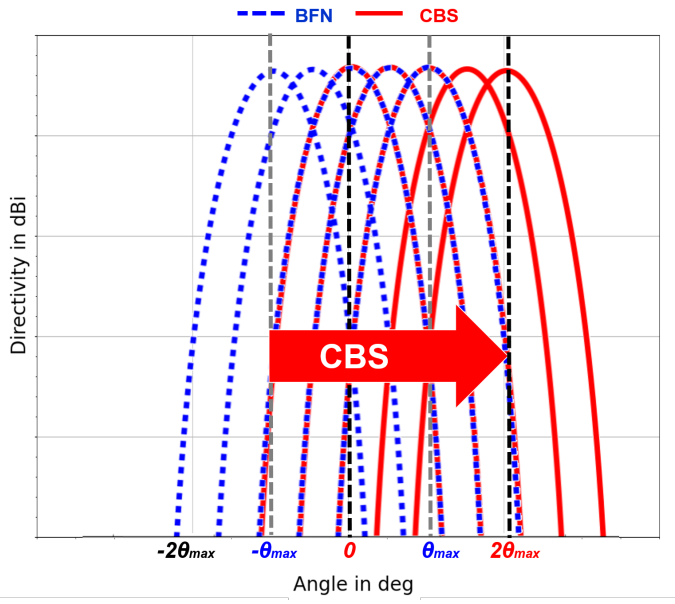

Figure 2.5: Working principle of the complete beam shifting effect. The initial beam pattern (dashed line) is shifted by θ_{max}.

This process is repeated for all the beams. Analytically, the phase term $e^{j\beta_n}$ in (2.1), that accounts for the BM, is expressed as:

$$\beta_n = -(2n-1) \cdot k \cdot d \cdot \sin(\theta_{max}) \tag{2.3}$$

with $n = 1, 2, \ldots, N$. Figure 2.6 shows the principle of operation of the BM, where the application of the term $e^{j\beta_n}$ to the considered $n-$th radiated beam introduces a movement on the opposite side of the scan range, with magnitude $2\theta_{max}$. Moreover, it can be easily verified that the beam previously pointing to θ_{max}, due to the application of the BM, is now pointing to $-\theta_{max}$, and, as a remarkable case, the beam pointing at $\theta = 0°$ will be then located at $-2\theta_{max}$.

2.2.3 Combination of CBS and BM

From the description of the PMU realized so far, it is noticed that the combination of the CBS and BM applied to the original BFN phase distribution allows to provide a doubling of the initial scanning range, as illustrated in Fig. 2.7 for a general case. In fact, at first all the beams are re-positioned in the positive portion of the scanning range by applying the CBS, and consequently they are shifted completely toward the negative side by using the BM.

However, the BM operation has to be applied only when negative angles are needed for scanning. In other words, the phase management unit (PMU) must be *reconfigurable* for adapting the system to scan either positive or negative angles.

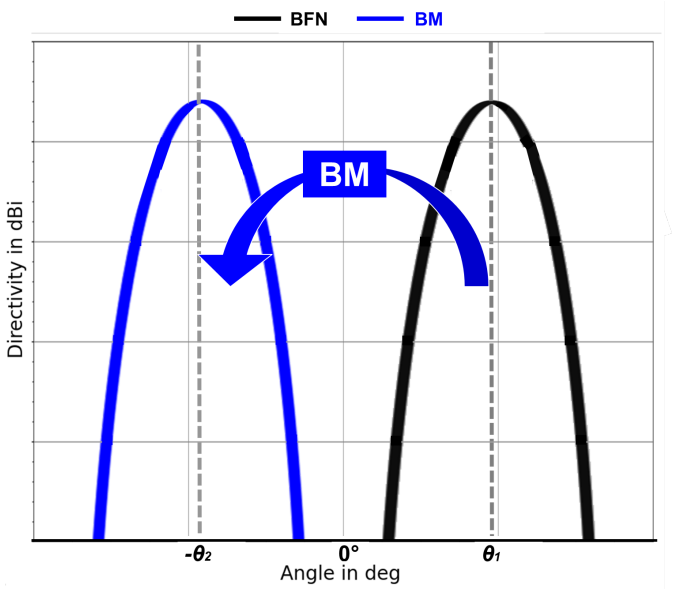

Figure 2.6: Beam mirroring operation principle: the beam is shifted by $2\theta_{max}$, thus positioning the generic beam located at θ_1 on the other side of the scan diagram, according to $\theta_1 - 2\theta_{max} = -\theta_2$.

Therefore, the extended scan range method indicates that, by properly superimposing a reconfigurable phase shifting to the phase distribution of the BFN at every element of the antenna array, the overall scan range is extended by a factor two. This implies some complexity of the PMU if a generic steering angle is considered. However, by analyzing the proposed progressive phase shifting used to extend the scanning range, a convenient case can be recognized when $\theta_{max} = 30°$ and the distance d between the antenna array elements is set as $\lambda/2$, where λ is the operation wavelength. In this way, when $\theta_{max} = 30°$, in (2.2) the phase term simplifies to $\alpha_n = n \cdot \frac{\pi}{2}$, and hence a 90° based progressive phase shift, superimposed to the BFN initial phase distribution, is needed to redefine an initial scan range of ±30° to the range 0° – 60°. On the other hand, in this case, (2.3) is also based on multiples of 90°. It can be analytically verified that the sum of the phase contributions of BM and CBS corresponds to a -90° progressive phase shifting:

$$\alpha_n + \beta_n = (1 - n) \cdot \frac{\pi}{2} \tag{2.4}$$

Figure 2.8 illustrates the described concept, considering a basic block of four multiples of 90° for the CBS (the same is repeated for all the successive ports). Therefore, it can be noticed that there is no need to change the phase shifting at every line by the application of the BM, because the half wavelength multiples can be exploited. By this simple assumption, a negative version of the odd multiples of 90° can be generated by the phase inversion at odd index of array input ports. Hence the

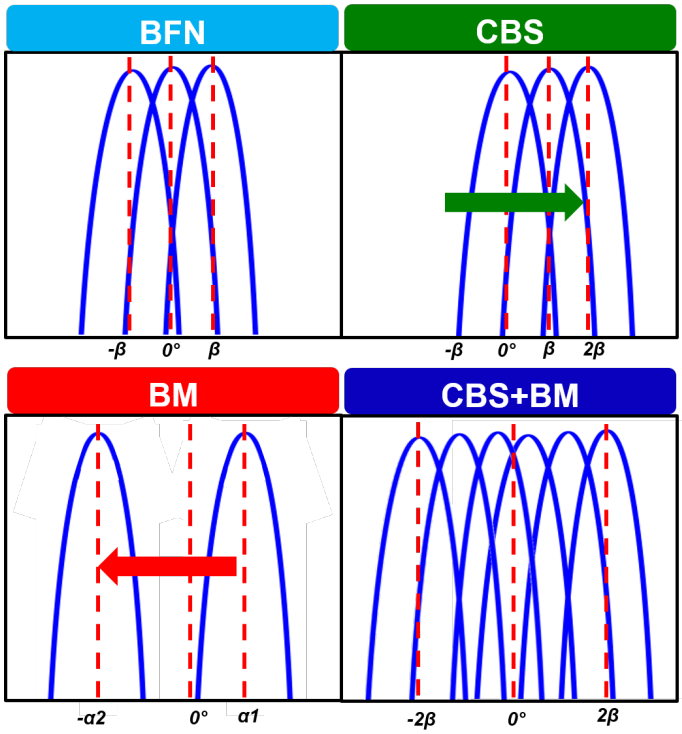

Figure 2.7: Combination of "complete beam shifting" and "beam mirroring" for scanning range extension of Rotman lenses.

PMU can be realized with a microwave circuit that combines both the CBS and BM operations through a suitable 1-bit control.

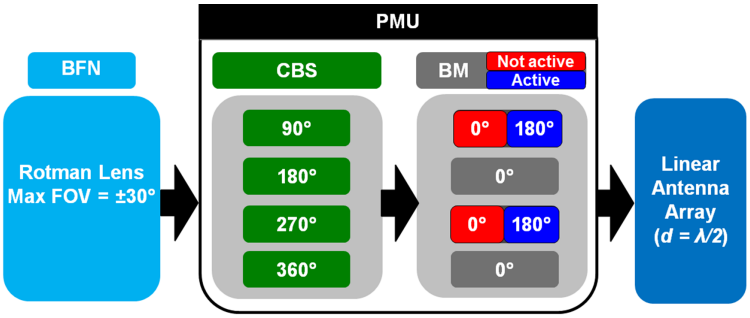

Figure 2.8: Block scheme of the basic phase distribution given by the CBS and BM in the case of an initial Rotman lens scanning between ±30° and a linear array with spacing d=$\lambda/2$.

In Fig. 2.9, the simultaneous application of the two previously described steps are depicted, where a general scan array system able to steer the beams from 30° to -30° is considered. As initially stated, highlighted in red, it is assumed that the

variable phase shifters are not providing the phase reversing (i.e. $\beta_n = 0°$). In this frame, CBS is applied, resulting in a radiation pattern covering angles from 0° to 60°. On the other hand, by taking advantage of the BM effect (with a superposition of 180° phase shifting every second line of the array input), the beam coverage will then be ranging from 0° to -60°, as highlighted in green. Thus, as expected from the theoretical analysis of the proposed method, the combination of the CBS and BM to the Rotman lens phase distribution will effectively provide a doubling of the scanning range with respect to the original phased array. As further advantage, the number of the available beams is also greatly increased, without the introduction of new beam ports that would lead to a more complicated design of the Rotman lens.

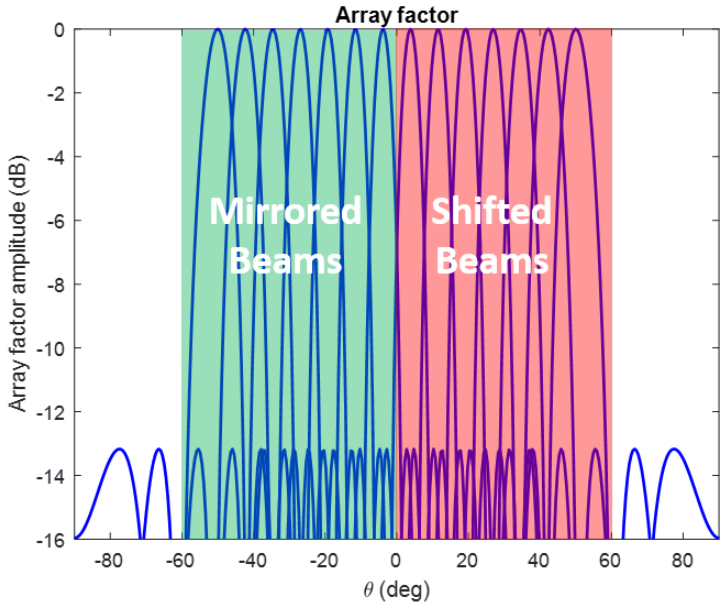

Figure 2.9: Illustration of the doubling of beam coverage with application of CBS and BM to an original phased array based on Rotman lens with initial scan range of ±30°.

2.3 Wide Range Scan Array Design

In order to validate the concept described in Sect. 2.2, in the following will be described the design of the scanning array system using the Rotman lens as beamforming network. The scope is to develop a wide scanning range 24 GHz radar (the 24 GHz ISM operational bandwidth is 24 – 24.25 GHz), based on the block diagram reported in Fig. 2.4. Moreover, it is required that the development of the extended scan range system employs a standard PCB process and materials:

therefore, standard dielectric Rogers *RO4350B* has been used, as it is a low cost and high-performance RF material. In standard PCBs used for industrial and commercial applications, the conductor is not realized as bare copper due to the high cost, instead a common surface finishing which presents good solderability of SMD and MMIC components and a fairly good conductance at low cost is the Electroless Nickel Immersion Gold (ENIG). For properly modeling the antenna system the conductivity of the ENIG was extrapolated by measurements, which is found to be $\sigma = 5.6 \cdot 10^6\ S/m$ in the range 22 — 26 GHz. Due to the complexity of the system, the full wave software EMPIRE XPU [221] has been used for modeling and optimizing all the parts of the design. It is important to remark that, since the functionality of the system is based on the path length of the travelling wave for producing the progressive phase shift, only with a full wave simulation the lens performance including losses and phase distortion can be truly evaluated, since these aspects cannot be included in the formulation based on a ray tracing concept. In the following sections, the design of the antenna array and the first version of the Rotman lens design are presented.

2.3.1 Antenna Array Design

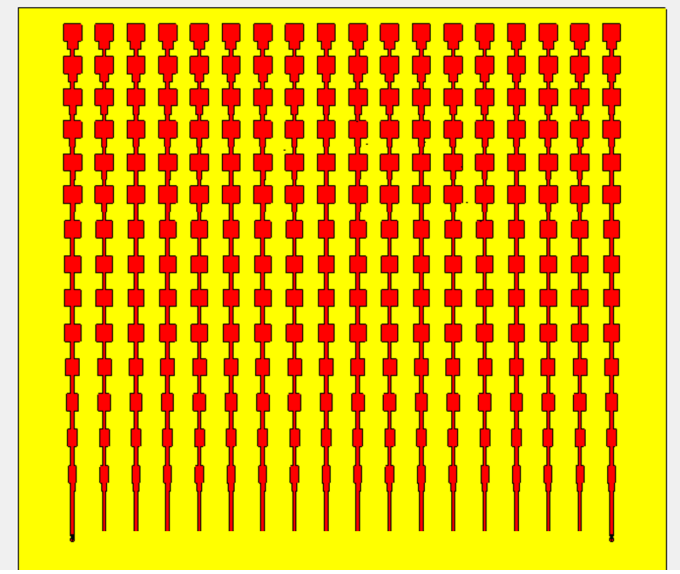

Figure 2.10: Full wave simulated model of the antenna array.

The radiating elements are an essential part of a radar system, and they qualify the range of coverage and the accuracy of detection. For these reasons, the antenna array should exhibit high directivity, small Half Power Beam Width (HPBW) and low sidelobe levels. It is also preferable to develop the antenna system in a planar structure, for best system integration and easy manufacturing, especially for the

automotive application scenario. Here, a linear array of patches with serial feed is utilized, targeted for covering the 24 GHz ISM band, designed in combination with the extended scan range Rotman lens BFN. More in detail, Fig. 2.10 reports the modeled array, which is composed by an array of 14 patches for each of the 16 channels and placed on a 508 μm *RO4350B* substrate, necessary to achieve the required matching condition for the 24 GHz ISM band. The characteristic impedance of the antenna columns have been set to 75 Ω. Moreover, it can be noticed from Fig. 2.10 that two parasitic columns, terminated to 75 Ω, are inserted on the array sides, with the purpose of limiting the effect of the finite dimension of the ground plane. The distance d between antenna columns, arranged along the x axis, is chosen equal to $\lambda/2$, which allows the 90° based phase shift for enabling the CBS and the BM to be applied. In addition, an amplitude tapering is applied across the antenna columns (along the y axis) for reducing the sidelobe levels in the $H-$plane. In Fig. 2.11 the co-polar component of the radiation pattern is presented, in both the $E-$plane and $H-$plane cuts. Moreover, in order to better evaluate the HPBW, the -3 dB level is indicated. In particular, in the $E-$plane the HPBW is found to be 6.4°, while for the $H-$plane this kind of serial feeding arrays typically present a not symmetric beam, and in this case the HPBW is equal to 8.6°.

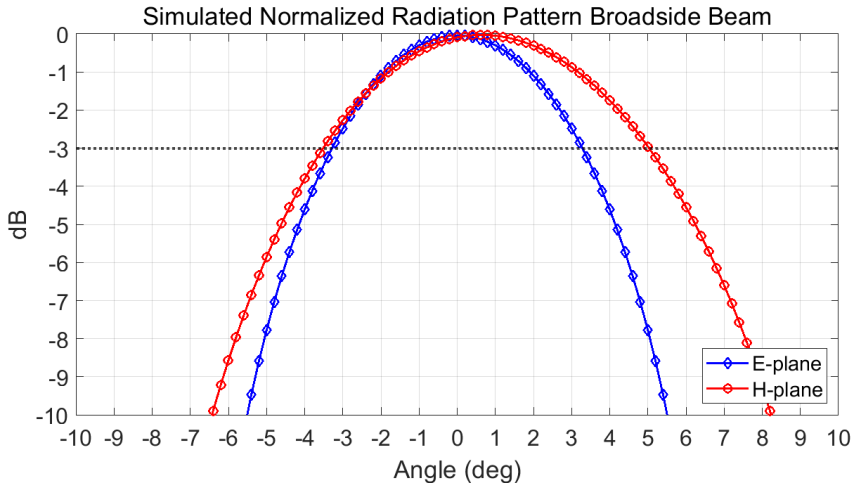

Figure 2.11: Simulated normalized $E-$plane and $H-$plane co-polar component of the radiation pattern in broadside direction at 24 GHz. The -3 dB level, corresponding to the HPBW, is also indicated.

Since the goal of this research is to reach ±60° with the extending scan range method (starting from an initial ±30° provided by the BFN), the scanning performance on the full targeted range is shown in Fig. 2.12, obtained by feeding the array with an ideal excitation (uniform amplitude with correct phase shifts). It is

noticed that at the maximum scanning angle (i.e. set to ±60°), the scanning loss is quantified to 5.3 dB, mainly due to the patch element pattern.

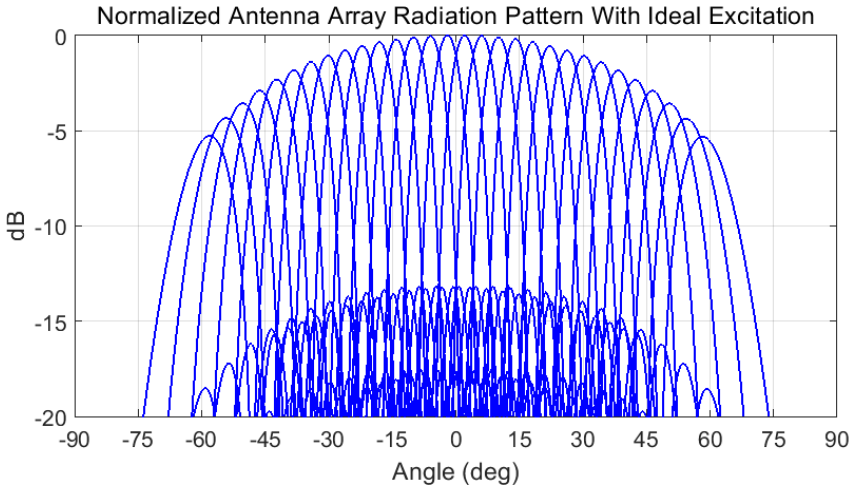

Figure 2.12: Simulated normalized antenna array radiation pattern at 24 GHz with ideal excitation, scanning at ±60°.

2.3.2 Rotman Lens Design

In Sect. 2.1, the Rotman lens has been described and its main features highlighted. In particular, it was shown that the lens is practically a waveguide in which the wave is propagating through, and by proper design of beam and array contours the desired phase distribution is generated. It is important to carefully design the Rotman lens, for having a uniform power distribution at the array ports, together with a progressive phase shift applied at the array input. Moreover, it is essential to take care of the reflections within the lens cavity (in particular at the sides) and at the array input interface: in fact these reflections will propagate in arbitrary directions inside the lens and they will cause distortions to incoming wave, thus increasing the phase and amplitude errors. Another aspect that has to be considered is the phase center of the input/output ports. In fact, any mismatch from ideality of the calculated propagation pathways introduces an error that will be translated to a degradation of the performance of the scanning array. This effect is more evident for extreme scan ranges, because of the proximity of the input ports to the dummy port sides, and for this reason the array side illumination will be less efficient compared to the central beam ports. By taking all the mentioned considerations into account, a 24 GHz tri-focal Rotman lens designed to provide steering angles between ±30° has been realized in a *RO4350B* substrate, according to the formulation described in [202] and [204] for automatic construction of the lens contours.

Moreover, in order to have a pattern suitable for radar applications (i.e. a good coverage of the azimuthal plane, good angular accuracy etc.), and considering also trade-offs with design complexity (i.e. size of the array, complexity of the electronics on beam port side), it was decided to design the Rotman lens with 18 beam ports and 16 array ports. Finally, 8 dummy ports have been placed on both sides, for ensuring a good absorption of the power that is not coupled into the array ports. The choice of the number of array ports is directly related to the antenna system that will be connected with the Rotman lens, while the number of beam ports is related to the scanning beam spacing, which will be 3.2° for the design under investigation.

Another very important part of the Rotman lens design are the transmission lines placed on the output of the beam contour side. They are used for equalizing the path length and to connect the Rotman lens with the antenna array. The latter aspect is critical, since it lead most of the times to a set of meandered lines that have to handle the curved shape of the Rotman lens and the straight interface of the array, maintaining the same length for all the lines. As a result, long lines are added to the design, bringing an increase of losses and consumption of PCB area, and they often require a long optimization time for reaching the correct phase plane. In Fig. 2.13a, where a standard design of a Rotman lens is presented, and the complicated structure needed to connect this lens BFN and the linear antenna array can be clearly recognized . A more convenient method is used here, that

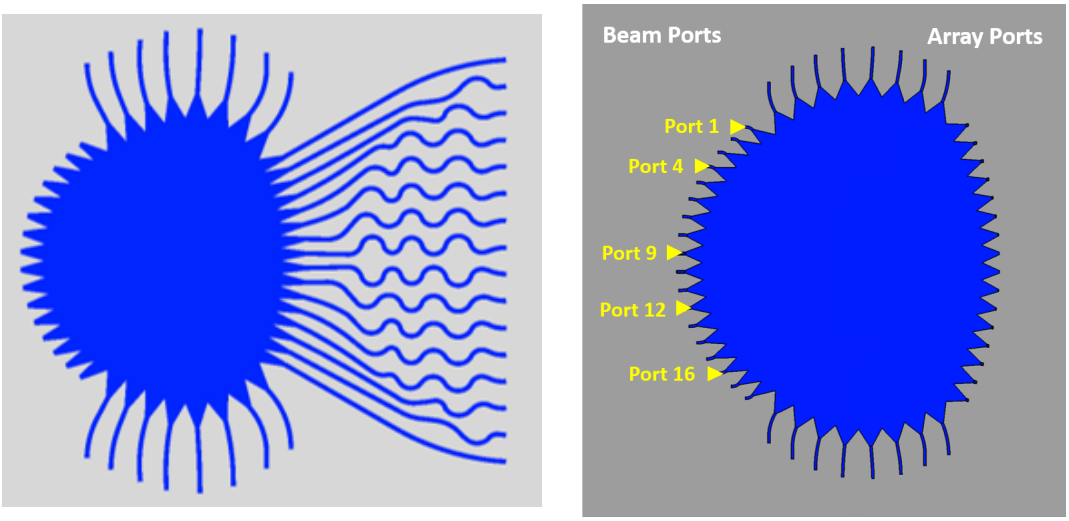

(a) (b)

Figure 2.13: Rotman lens: (a) standard design with meandered transmission lines; (b) designed Rotman lens in the 254 μm *RO4350B* substrate. Some input ports are named for reference.

exploits a multilayer design for placing the Rotman lens and the antenna array on

different layers. In this way the long meandered transmission lines can be avoided by adjusting their length among the two layers. In other words, for connecting each output of the Rotman lens to the corresponding antenna array column a variable position of the layer-to-layer transition is used, and therefore the mutual difference between each line is split among Top and Bottom layer. The outcome of this solution is a very linear and regular routing, where the line lengths are minimized with respect to the commonly adopted solution shown in Fig. 2.13a. A further advantage of the folding technique is the possibility to use a different substrate with respect to the one used for the antenna array, that is otherwise imposed in the single layer solution (for ensuring an adequate bandwidth of the patch array). Therefore, instead of using a 508 μm thick *RO4350B* substrate, a 254 μm thick laminate is utilized. For an accurate design the different relative permittivities of the two different thickness substrates are taken into account in the routing of the transmission lines. Finally, the designed Rotman is presented in Fig. 2.13b.

In Fig. 2.14 the input reflection coefficient of the Rotman lens are shown. Clearly, the choice of keeping a short taper (length of $\lambda/2$) lead to a reflection coefficient which is -10 dB in average (some oscillations are given by the propagations and reflections inside the lens cavity), with a maximum of approximately -9 dB. It is noticed that for achieving a great improvement of the reflection coefficients a much longer taper would have been needed, which is in contrast with the objective es of this research. This aspect will be taken in consideration in the outlook of the research project, where a novel feeding solution is proposed. At the contrary, the port-to-port coupling is very low, below -14 dB, as can be recognised from Fig. 2.15, where the coupling coefficients are reported for the outer (Fig. 2.15a), central (Fig. 2.15a) and mid section input ports (Fig. 2.15b) corresponding respectively to *Port1*, *Port9* and *Port4*. Being the lens a symmetrical structure, these three ports give a quite complete overview on the overall coupling performance.

2.3.3 Layer to Layer Transition

Figure 2.16 shows the realization of the layer to layer transition. This structure exploits a very convenient way for coupling a signal from a layer to another at millimeter waves: the microstrip to slotline vertical transition. This technology is well known and it has been extensively investigated [222]. In literature many researchers have been using this principle for a wide variety of applications, including phase shifters [223] and couplers [224].

As can be noticed from Fig. 2.16, the designed transition is composed by four basic elements: the feeding line located on the *Rotman lens side*, the output line on the *Array side* and the slot used to couple the energy between the two lines. The two lines and the slot are positioned orthogonally, for ensuring that the electric field is properly coupled. Due to manufacturability requirements, the PCB is constructed as a four layer PCB, with two ground planes that are positioned below

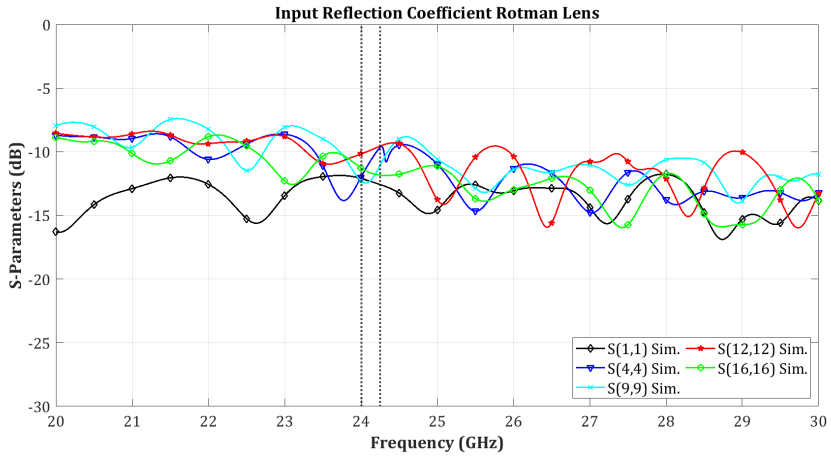

Figure 2.14: Input reflection coefficient of the modeled Rotman lens for ports *Port1*, *Port4*, *Port9*, *Port12* and *Port16*. The 24 GHz ISM band is highlighted for reference.

the BFN and the array respectively. Therefore, the slot is replicated identically in two ground plane layers, which are separated by 200 μm (*RO4450B* was used as Prepreg material). The fourth element composing the transition is the via fence that follows the contour of the slot, which ensures that the potential on the two inner metal planes is the same and it prevents the generation of surface waves that would dissipate the energy on the ground planes, thus rising the crosstalk between adjacent lines. The density of the via fence is imposed by the standard manufacturing process limits. It is noticed that by this arrangement the two slots surrounded by vias can be treated as a unique structure. Moreover, Fig. 2.16 displays the use of circular stubs for properly terminating the lines with a virtual short and, similarly, an open realized with two circular apertures is employed for terminating the slots. This type of circular stubs are widely used in literature for microstrip lines and slots, due to their very broadband behaviour [225]. Finally, as previously mentioned, the selection of different substrates leads to an optimized structure. Because of the choice to use 254 μm on the *Rotman lens side* and 508 μm on the *Array side*, the microstrip lines on the two layers have different characteristic impedance (50 Ω for the first case and 75 Ω in the latter case) but the same line width; in this way a compact and symmetric design of the microstrip-slot interface is obtained. In fact, a wider line on the array side would have required a longer slot (placed perpendicularly to the line) and a larger bending for routing the connection to the antenna column. However, the different characteristic impedance has to be taken into account in the two microstrip-slot matching conditions, as in Fig. 2.17, where the $S-$parameters relative to the designed transition are reported. Referring to

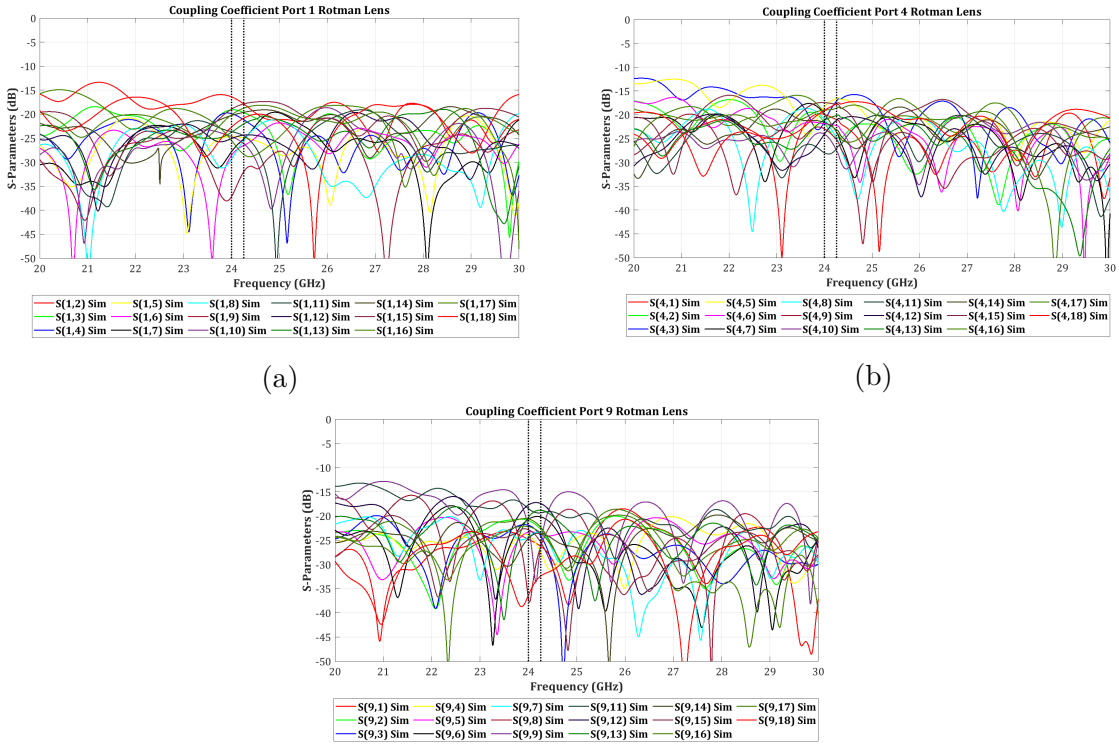

Figure 2.15: Simulated coupling coefficient of the modeled Rotman lens inputs with: (a) *Port1* (b) *Port4* and (c) *Port9* excited; 24 GHz ISM band is highlighted for reference.

the $|S_{ii}|$ coefficients, the *Input "1"* is referred to the *Array side*, with characteristic impedance of 75 Ω, while *Input "2"* is normalized to 50 Ω because it belongs to the *Rotman side*. The introduced losses are approximately 1.2 dB in the band of interest.

2.3.4 Phase Management Unit

The central part of this design is the Phase Management Unit, since it is the component responsible for the widening of the scan angle through the combination of CBS and BM. As already discussed in Sect. 2.2, the PMU has to be placed between the Rotman lens and the array antenna elements. Since the Rotman lens BFN enables a maximum scan angle $\theta_{max} = 30°$ and the antenna array columns are equispaced by $\lambda/2$, the 90° based phase shift for enabling both the CBS and the BM can be applied, as depicted in Fig. 2.8. Moreover, this means that the BM is applied just at every second antenna feeding line, involving a 0° phase addition when BM is *OFF*, and a 180° phase inversion when BM is set *ON*. Clearly, a switching device

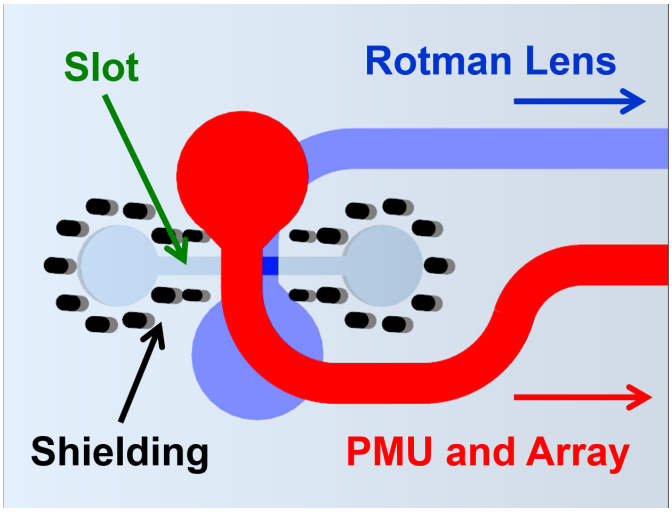

Figure 2.16: Modeled layer-layer transition (ground planes and dielectric are not shown for clarity). The energy is coupled from the Rotman lens side to the array side via the slot. Lines are terminated with a circular stub, while the slot is terminated with a circular open. The shielding surrounding the slot is also indicated.

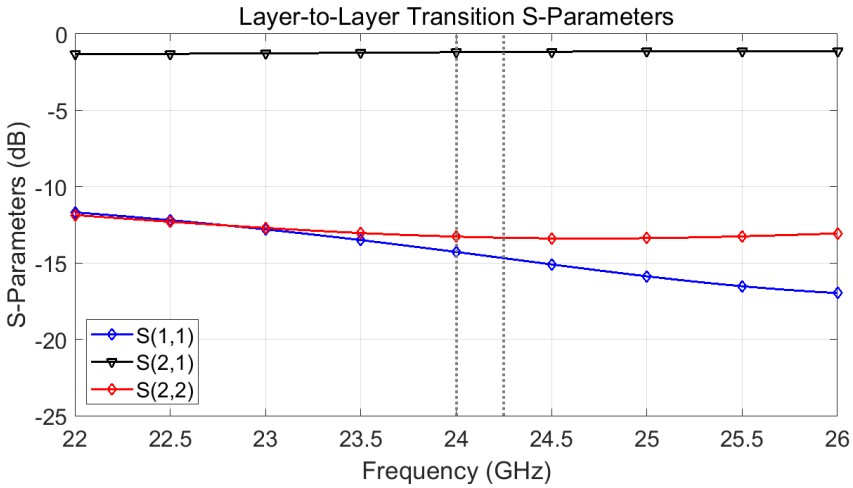

Figure 2.17: Simulated S-parameters of the layer-to-layer transition. *Input 1* is related to the *Array side* (75 Ω), while *Input 2* is related to the *Rotman side* (50 Ω). The 24 GHz ISM operative band is highlighted for reference.

has to be placed in the PMU, for the proper functionality of the BM. For this reason, the PIN diode used in this research is the flip chip *MA/COM MA4FCP200* [226], characterized by very low parasitic and low series resistance at the frequency range of interest, despite their low cost. Furthermore, the implementation of a reconfigurable phase shifter for fulfilling the widening of the scan range concept

introduces a necessary selection of the portion of scan range that will be active, while the other would be not operative. For this reason the choice of a fast switching device like PIN diodes reduces the latency time for changing the state of the BM, which is equivalent to switch between the positive and negative scan range angles.

For better integration of the PMU, the two operations CBS and BM can be combined in a single structure, including also the required switchable phase shifting operation. The rat-race coupler is a good candidate for fulfilling both these functions, used as static Reflective Type Phase Shifter (RTPS) for the CBS application, while the BM operation can be fulfilled by the integration of the PIN diodes at the terminations of the delay branches (Fig.2.18). In this way, by switching the

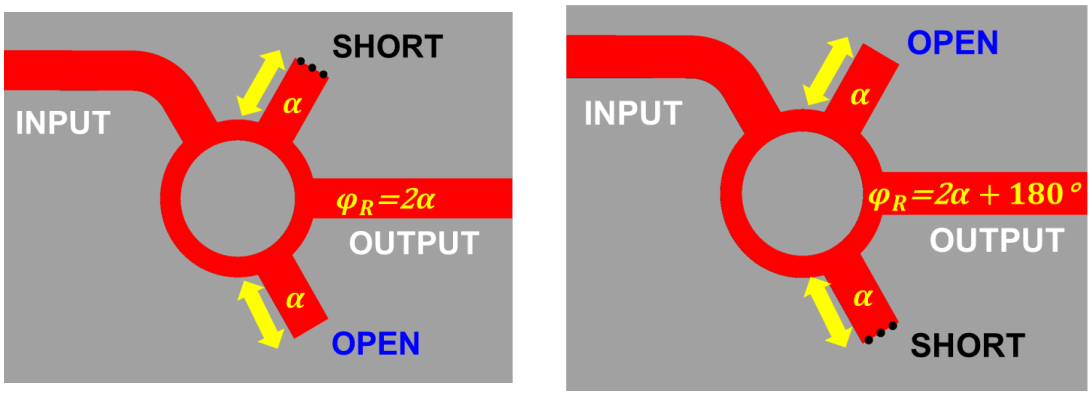

(a) (b)

Figure 2.18: Principle of operation of the Phase Management Unit circuit based on RTPS. The two different terminations corresponding to the *ON/OFF* states of the PIN diodes are shown. By switching the polarity of the termination a phase inversion is achieved.

state of the diode, it is obtained a simple and precise 180° phase difference. In fact, this type of RTPS requires two terminations that offers high reflecting coefficient, and are 180° out of phase with respect to each other (i.e. typically open and short). The output phase shift is determined by the sum of the electrical length of the two stubs with proper sign, defined by the type of termination. Therefore, by controlling the terminations, by means of reversing the polarity, a phase inversion is achieved. The described operations based on rat-race coupler and PIN diodes are depicted in Fig. 2.18.

2.3.5 PIN Diode Modelling

For a proper calculation of the phase contribution given by the PMU, a precise model of the structure used for the accomplishment of CBS and BM is essential. Moreover, the PIN diode used for switching between the two phase conditions of

the BM (i.e. 0° and 180° states) has to be accurately characterized in order to have a precise and reliable EM model. Therefore, the $S-$parameters of the component have been included in the model of the phase shifter in both *ON* and *OFF* configuration at 24 GHz. This was possible only for modeling and optimizing the phase shifter, since the use of the $S-$parameters in the complete system simulation would have required excessive computational effort. Therefore, a reduced model was extrapolated for the simulation of the complete beamforming network and antenna array, employing ideal components to characterize the two bias states of the diode. Moreover, since this component is placed directly on the EM structure, its physical dimensions cannot be neglected in the frequency range under investigation. Indeed, the physical dimensions of the *MA4FCP200* PIN diode is only 380 μm, however, this would correspond approximately to 18° at 24 GHz, considering the guided wavelength. Therefore, the *MA/COM* PIN diode is modeled as a full wave 3-D object, containing the lumped circuit elements which take into account for the electrical behaviour of the diode in its two bias conditions. In Fig. 2.19, showing

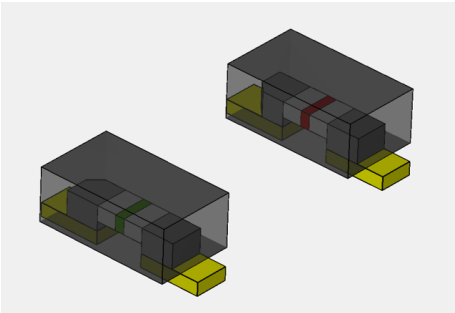

Figure 2.19: 3-D model of the PIN diodes with opposite biasing. The green box in the middle of the component contains the lumped electrical model of the *ON* condition, while the red part contains the equivalent *OFF* capacitance

the model of the diode, it can be noticed that the physical structure is maintained (i.e. soldering pads, internal metal structure and outer passivation/polymer layer) and the concentrated circuit parameters have been modeled as a 50 μm long cell, positioned in the middle, which is related to the reverse junction capacitance in *OFF* state and to the forward resistance and the equivalent inductance in *ON* state, as previously discussed. In this way, the maximum error in the determination of the component equivalent length would be equivalent to 50 μm, which is also the minimum mesh size for the simulated models. This discretization is chosen as a trade-off between accuracy and simulation time. Therefore, in order to obtain the precise electrical model of the PIN diode at the target frequency of 24 GHz, a simple 2-port simulation including the 3-D model shown in Fig. 2.19 was used to optimize the circuital parameters for matching the $S-$parameters provided by the semiconductor manufacturer, for both the *ON* and *OFF* states of the diode. Specifically, the parameters used in the *ON* state of the diode were $R_{ON} = 6.5$

Ω and $L_{ON} = 0.15\ n$H, assuming a forward current of 10 mA, while for the *OFF* configuration the equivalent capacitance of $C_{OFF} = 25\ f$F was used, assuming $5V$ reverse biasing voltage.

2.3.6 Complete Beam Shifting and Beam Mirroring: Rat-race Coupler Architecture

In the design of the PMU, based on RTPS, a priority importance has been given to the creation of an accurate but highly integrable phasing block fulfilling the operations of CBS and BM.

As first step, being applied at every antenna array input, the phase shifters reproducing the CBS operation are considered. It is noticed that a very convenient way for performing the 90° multiple based phase variation by using the RTPS is to consider a basic CBS unit, which consists of four steps performing correspondingly the 90°, 180°, 270°, 360° progressive phase shift. This set of four phase shifters are replicated four times for covering all the antenna array inputs. By the proposed arrangement of the PMU, the 90° based phase shift is fulfilled (2π multiples are subtracted from the theoretical progressive phase shifting for reducing losses and enhancing compactness). Actually, it is noticed here that the use of the rat-race coupler as component of the RTPS leads to further advantages: the 0° and 90° topologies have the same structure as the 180° and 270° ones respectively, just the stub positions are inverted with respect to the rat-race center (mirrored along the "output" line direction, as in Fig. 2.21 and Fig. 2.20).

As second step, the BM is applied to the above considerations on the RTPS arrangement. It was already clarified that the choice of the rat-race coupler is valuable for incorporating the operation of the BM together with the CBS in a single structure. Therefore, for achieving the BM effect, the switching device (i.e. the *MA4FCP200* PIN diodes) has to be connected to ground as termination of the RTPS stubs, with opposite orientation, as previously shown in Fig. 2.18. The *ON/OFF* parameters derived in Sect. 2.3.5 are then included in a detailed 3-D model of the component, for enhancing accuracy. The mutual change of the *ON/OFF* conditions of the two branches provides the switching between the *OPEN* and *SHORT* circuit accordingly, and as a result, the 180° shift is achieved. Nevertheless, if this simplified concept is directly applied, a significant phase error will occur. The reason is found on the different electrical length of the PIN diode in the *ON* and *OFF* bias conditions; in other words, when the diode is *OFF* the stub is loaded by C_{OFF}, whereas, when it is *ON*, the stub is connected to ground through the diode and its electrical length is significantly increased. Therefore, a balanced approach is used for compensating the error resulting from the line length difference during the *ON/OFF* states.

By using four diodes instead of two, it is possible to realize the required phase shift in such a way that two diodes are simultaneously conducting in the opposite

branches, thus equalizing the path length to ground. Furthermore, the *ON/OFF* impedance (including also stray capacitance and inductance of the component), influences the effective length of the stubs. Therefore, for having the correct phase difference among all the phase shifters, the proper tuning of the two stubs is very important. However, by the application of the balanced configuration, the *OPEN* termination cannot be used, since the path to ground has to be ensured for properly biasing the PIN diode. Therefore, it is implemented the $\lambda/4$ transformers in series with the PIN diode for converting the connection to ground to an *OPEN*, and then achieving the 180° phase inversion. As a result of these considerations, the PMU is designed based on a 4-cells arrangement, leading to the RTPS architectures displayed in Figs. 2.20 and 2.21, where the two *ON/OFF* operations of the BM are illustrated. Figure 2.20 gives an insight on the phase distribution in the BM

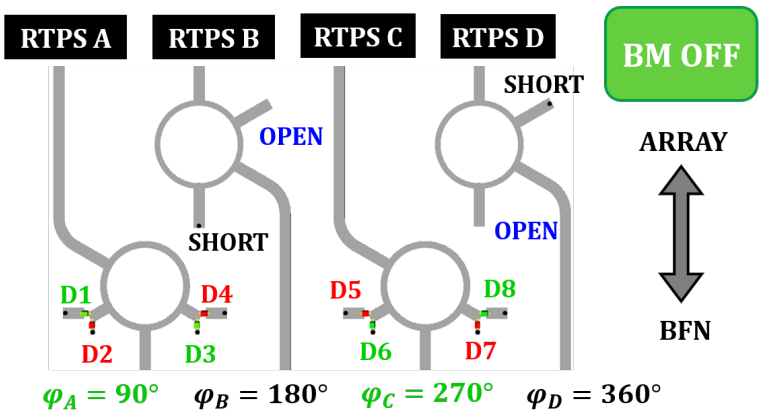

Figure 2.20: Basic PMU unit cell in BM *ON* operation. Reconfigurable *RTPS A* and *RTPS c* produce 90° and 270° phase shifting, while *RTPS B* and *RTPS D* provide a fixed 180° and 360° phase shifting, respectively.

OFF state, that is attained by each phase shifter which is composing the basic 4-cells arrangement of the PMU. The basic PMU unit cell is composed by two reconfigurable phase shifters, *RTPS A* and *RTPS C*, that are capable of switching between the two phase shifts ±90° and ±270°, respectively. The 4-cells arrangement is completed by two reflective type phase shifters, named *RTPS B* and *RTPS D*, which realizes a fixed 180° and 360° phase shift, respectively. From Fig. 2.20 it is clearly noticeable that *RTPS C* and *RTPS D* share the same design as *RTPS A* and *RTPS B* respectively, with the type of terminations and orientation of PIN diodes reversed. Referring to Fig. 2.20 and considering the switchable phase shifter *RTPS A*, when *D1* and *D3* are *ON* and *D2* and *D4* are *OFF*, a 90° phase shift is produced; for duality the 270° phase attained by *RTPS C* is obtained by imposing *D6* and *D8* *ON* and, consequently, *D5* and *D7* in *OFF* state.

The fixed phase shifter *RTPS B* and *RTPS D* provides 180° and 360° phase

shift, given by two stubs with electrical length of approximately 90° (the effective length has been optimized by simulations), terminated either by a *SHORT* or through an *OPEN*, in a dual way. Considering a similar approach, the duality of *RTPS A* and *RTPS C* consists on the inversion of the *ON/OFF* terminations (i.e. *SHORT/OPEN* are interchanged and the polarity of the diodes are reversed).

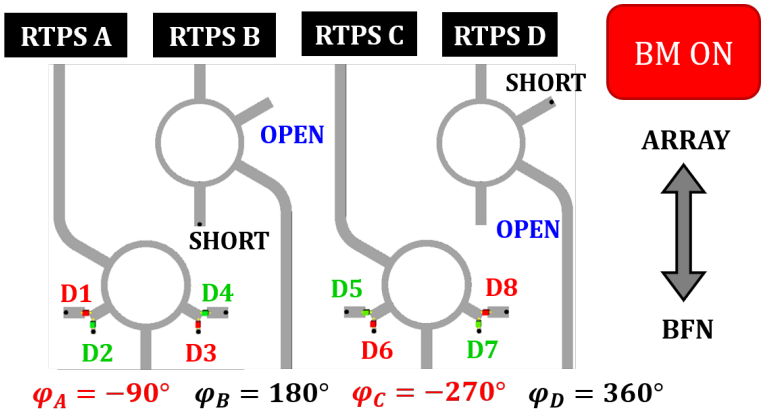

Figure 2.21: Basic PMU unit cell in BM *ON* operation. Reconfigurable *RTPS A* and *RTPS c* produce -90° and -270° phase shifting, while *RTPS B* and *RTPS D* provide a fixed 180° and 360° phase shifting, respectively.

In the second operation state shown in Fig. 2.21, indicated as BM *ON*, when *D2* and *D3* are set *ON* and the other two diodes are *OFF* the phase inversion is activated for the *RTPS A* and a -90° is applied. Similarly, *RTPS C* attains a phase shift of -270° by switching the diodes states of *D5* and *D7* to *ON* and by setting *D6* and *D8* to*OFF*. The application of the phase inversion to *RTPS A* and *RTPS C*, while keeping unchanged *RTPS B* and *RTPS D*, realized the required displacement of the beams from the positive to the negative portion of the scan range.

The RTPS have been designed on a 508 μm *RO4350B* substrate, considering 75 Ω as characteristic impedance of the rat-race based phase shifter (i.e. the four branches of the coupler are designed with a $75/\sqrt{2}\,\Omega = 106\,\Omega$) line impedance. This arrangement supposes a placement on the same side of the antenna array rather than in cascade of the Rotman lens: in this way the management of the biasing currents is much easier, taking advantage of the antenna columns which are an open in DC. The loading impedance (i.e. characteristic impedance of the stubs) has been taken to be 75 Ω, which is defined by the stub width of 500 μm, for properly accommodating the two PIN diodes.

In Fig. 2.22 and Fig. 2.23 the simulated $S-$parameters and differential phase distribution over the band 22 – 26 GHz is shown for *RTPS A* and *RTPS B* and the dual versions *RTPS C* and *RTPS D* (i.e. corresponding to progressive phase shifting of 90°, 180°, 270°° and 360°). The simulated $S-$parameters show a maximum reflection coefficient of -12.1 dB (matching to 75 Ω) in the 24 GHz ISM band,

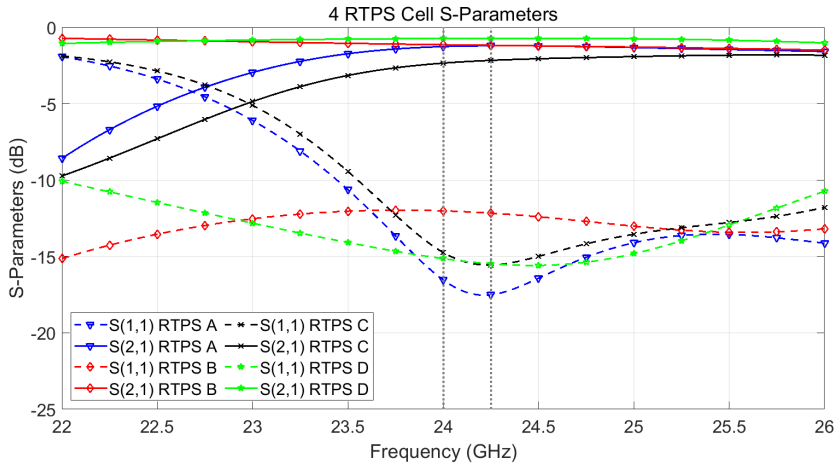

Figure 2.22: Simulated S-parameters of the four reflective type phase shifters providing 90° (black), 180° (red), -90° (blue) and -180°(green).

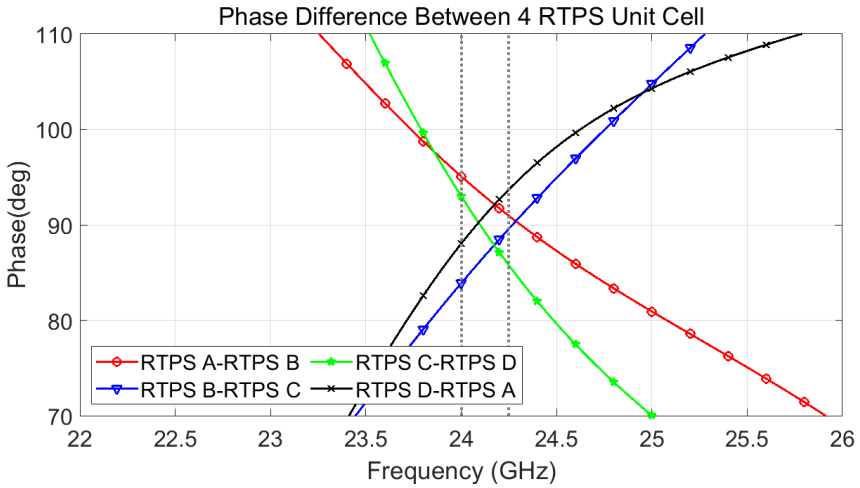

Figure 2.23: Differential phase distribution calculated at each pair of RTPS composing the basic unit cell of the PMU.

while the insertion loss is approximately 1.1 dB for the fixed type RTPS and 2.3 dB for the reconfigurable type. As expected, the RTPS which includes the PIN diodes suffer for more losses, due to the non-idealities of the active components. Nevertheless, from the simulated results reported in Fig. 2.23, the maximum phase error across the band of interest 24 — 24.25 GHz is found to be approximately 6°. It is interesting to notice the different electrical length of the branches, which leads to a very different slope of the phase. This effect is more evident in the case of the reconfigurable RTPS, due to the presence of the PIN diodes. It is noticed that the

RTPS is a simple and reliable way to realize a microwave phase shifter, however its drawback is a limited operative bandwidth, which is related to the stub lengths. Nevertheless, the use of such a structure results in a very compact definition of the PMU, and its operational bandwidth is sufficient for covering the 24 GHz ISM band.

2.3.7 Realized Extended Scan Range System

At this point, all the necessary elements to build the 24 GHz ISM band radar integrating the extending scan range method are available. According to the formulated theory, the PMU block has to be inserted between the Rotman lens and the antenna array, which are placed on the two sides of the multilayer PCB. By considering the presence of the single control line, necessary to switch between the two operative states of the BM (i.e. when *OFF* no phase inversion is applied; conversely when BM is *ON*), as already noticed it is convenient to place the PMU block on the antenna array side, which is constituted by the array columns. In this way, no in-line decoupling capacitors are needed, and the design is optimized with reduced complexity. Therefore, the bias of the PIN diodes is realized through a $\lambda/4$ line terminated on a radial stub, which is connected at its end to a resistor that defines the magnitude of the injected positive/negative current, needed to control the BM operation. It is reminded that the layer-to-layer transition performs also the impedance transformation between the 50 Ω and the 75 Ω on array side. In Fig. 2.24 the complete system is shown, and for clarification all the main components are indicated.

In the following, the simulated performance of the modeled extended scan range phased array based on Rotman lens as beamformer is reported. It can be noticed from Fig. 2.25 that the input reflection coefficient is very similar to the one displayed in Fig. 2.14. Some fluctuations of the $|S_{ii}|$, given by the internal reflections and propagation mechanism inside the lens, lead to a peak Return Loss of 9.3 dB. Moreover, Fig. 2.26 reports the input coupling coefficient $|S_{ij}|$, where the index i is related to either one of the three considered inputs (i.e. *Port1*, *Port4* and *Port9*), and the index j refers to all other input ports. Likewise to the input reflection coefficient just discussed, also in this case the same considerations already reported in 2.15 are made, where a maximum value of -15 dB is detected in this configuration. Therefore, from the comparison between the input $S-$parameters of the complete system and the stand alone Rotman lens, it is concluded that the insertion of the layer-to-layer transition and the PMU does not have a significant impact on the performance of the lens, in terms of power reflected at the array ports. If this would have not be the case, a higher variability of the input reflection coefficient and coupling would be noticed, due to the backward waves that propagate inside the lens cavity.

The resulting radiation pattern of the phased array including extended scan

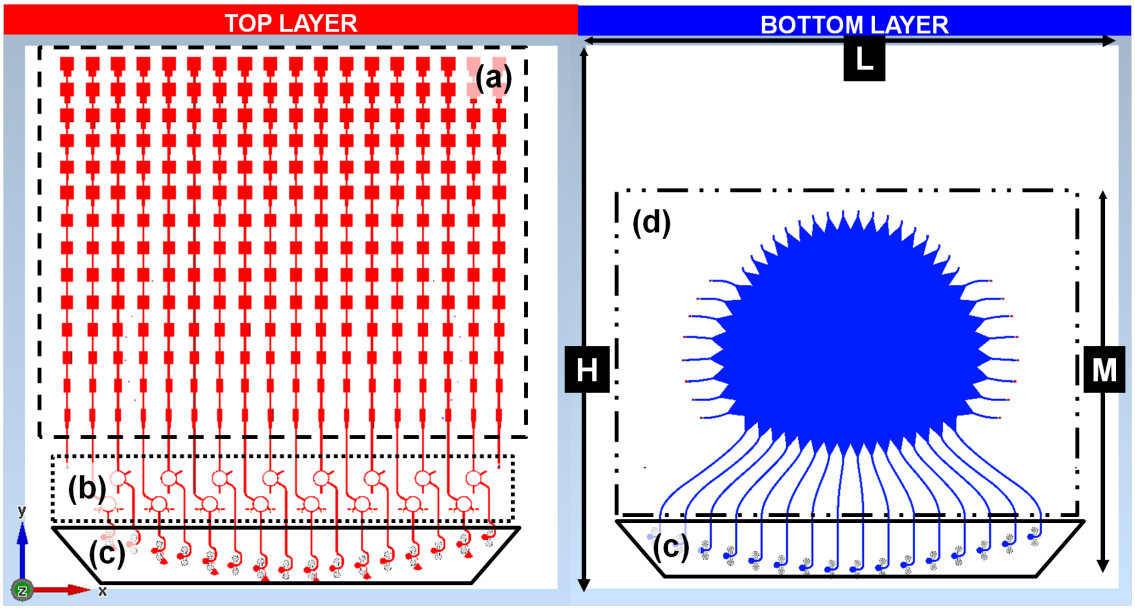

Figure 2.24: 3D model of the widen scanning range phased array: "Antenna array side" is placed on the left and "Rotman lens side" on the right. Highlighted parts: (a) linear antenna array, (b) PMU realized with fixed and reconfigurable phase shifters, (c) Rotman lens.

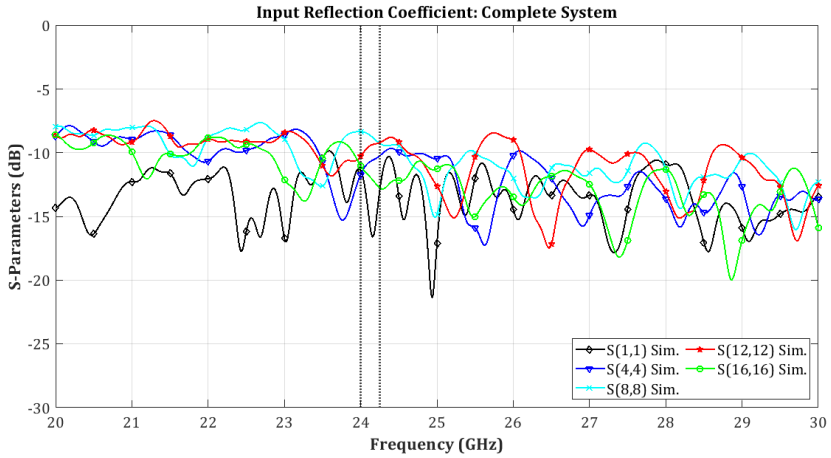

Figure 2.25: Input reflection coefficient of the complete extended scan range phased array with PMU realized with RTPS for ports *Port1*, *Port4*, *Port9*, *Port12* and *Port16*. The 24 GHz ISM band is highlighted for reference.

range method based on RTPS is shown in Fig. 2.27. In particular, Fig. 2.27

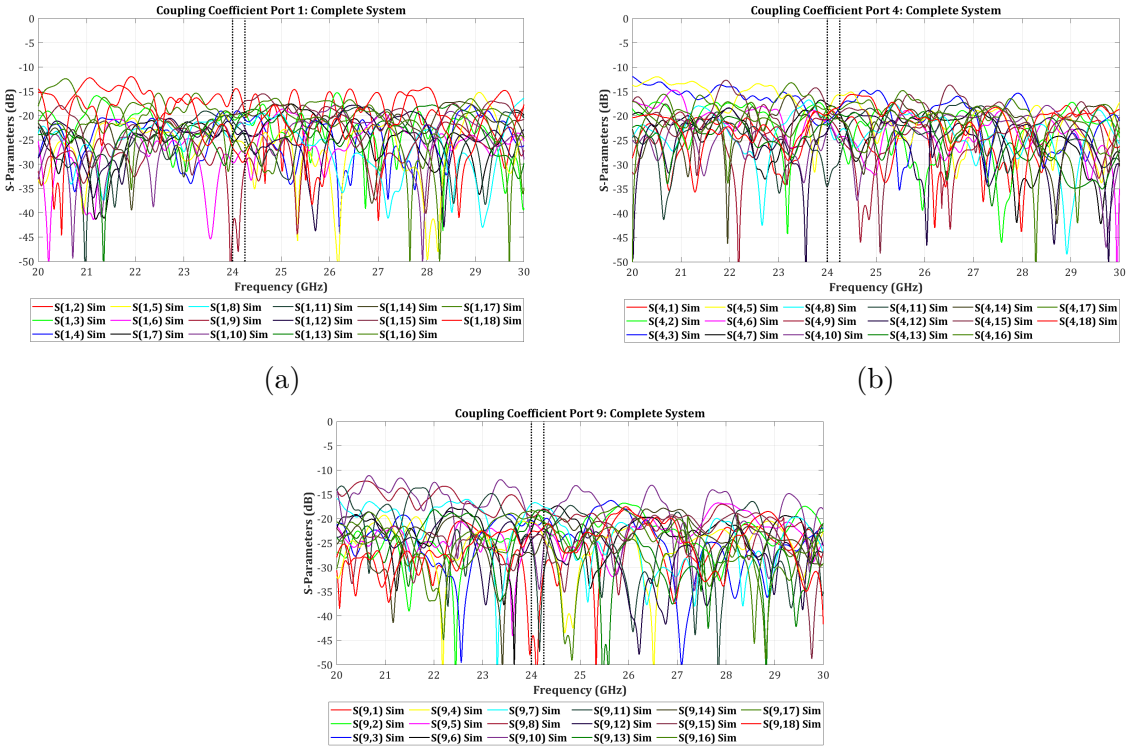

Figure 2.26: Simulated coupling coefficient of the complete extended scan range phased array EM model with PMU realized with RTPS for inputs: (a) *Port1* (b) *Port4* and (c) *Port9*; 24 GHz ISM band is highlighted for reference.

reports the co-polar component of the radiation pattern, and validates the proposed method by the consideration that the initial scan range of ±30°(related to the phase distribution of the stand alone Rotman lens) is actually doubled by considering both the effects of the CBS and BM. The maximum realized gain is 17 dB, positioned at broadside (slightly lower level of 16.9 dB is found at ±30°), while the lowest is located at 60° with the value 10.5 dB. The maximum of the beams are located at broadside and at approximately ±30°. In the latter case, the explanation lies on the better illumination of the array ports of the Rotman lens from the central ports compared to the one located at the sides that are related to the beam at broadside (because of the CBS and BM phase shifting, as discussed in Sect. 2.2.3). However, at broadside there is no reduction of the antenna gain due to scan loss. Therefore, this result demonstrates the BM is working as expected, since the beams are positioned symmetrically with respect to the azimuth, with a double beam at 0° due to the dual shifting given by the CBS and BM, as theoretically predicted in the analysis made on Sect. 2.2.3.

From the described simulated results, it can be stated that the design of the

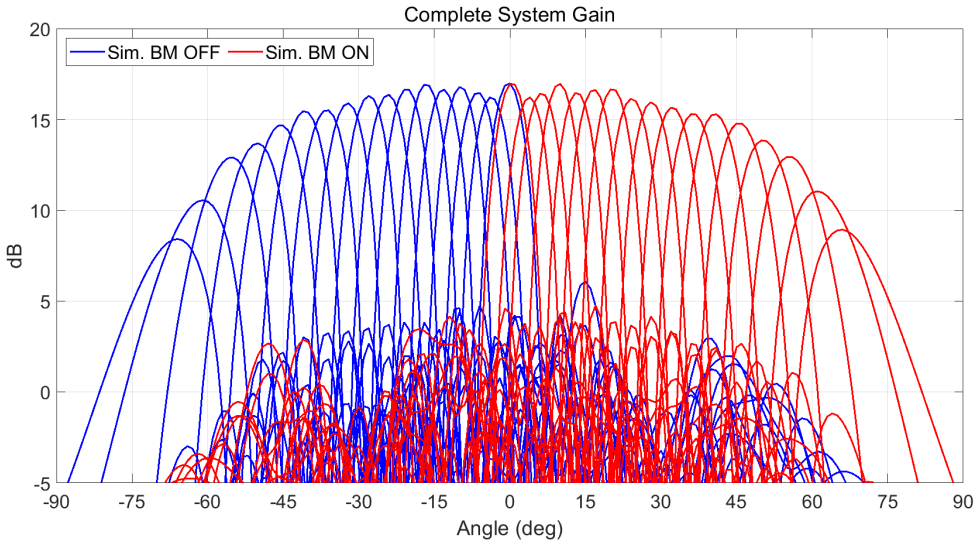

Figure 2.27: Simulated antenna gain at 24 GHz with the application of the extended scan range method. The effect of two states of the PMU are marked with blue when BM is *OFF* and with red when BM is *ON*.

phased array based on Rotman lens as beamformer, in combination with the method to widen the scan range, has shown good performance and a compact form factor. In particular, the designed PMU has demonstrated a smart approach for generating the CBS and BM effects by using only a single structure for accomplishing both functions. However, the simulated results have shown an unequal behaviour of the RTPS in the $\pm 90°$ state, probably due to the impedance of the two stubs loaded with PIN diodes, which are not exactly the same (i.e. absolute value), and which are also influenced by the two branches (i.e. $\lambda/4$ and $3\lambda/4$) of the rat-race that perform the impedance transformation. Moreover, the phase difference between the four *RTPS A-D* composing the basic unit cell (delivering $\pm 90°$ and $\pm 180°$) has proven to have a steep variation over frequency, which represents a drawback even for a narrowband system like the one considered here. Therefore, in order to overcome these limitations, an optimized concept for the PMU and the Rotman lens feeding is proposed in the following.

2.4 Optimized Wide Range Scan Array Design

Considering the limitations detected by the analysis carried on Sect. 2.3.7, an improved design for the extended scan range is provided, as an optimization of the previous architecture. The aim of the new concept is to increase the performance of the extended scan range Rotman lens by inserting a novel feeding method of the lens, and by developing a new implementation of the BM. In the following design,

the antenna array and the Rotman lens shape is maintained as already described in the previous paragraphs.

2.4.1 Multiple Feeding of Rotman Lens

Like all microwave lenses, the Rotman lens needs to be properly illuminated for ensuring good performance. Here, a novel method for improving the Rotman lens feeding is exploited [227]. The proposed illumination method of the lens uses a network of series connected Wilkinson dividers for simultaneous excitation of two consecutive Rotman lens inputs. The introduced double feeding of the Rotman lens, which employs two levels of Wilkinson dividers network, is illustrated in Fig. 2.28. For sake of clarity, in Fig. 2.28, the designators for the ports related to the complete system are identified with suffix *Port-* (i.e. when double feeding network is used), while the Rotman lens inputs are labeled with suffix *R-*.

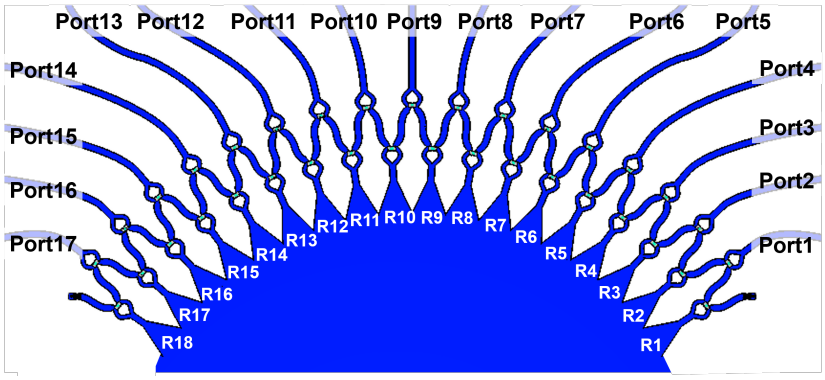

Figure 2.28: Input arrangement for the double feeding network exciting two Rotman lens ports simultaneously. The prefix *Port-* indicates the effective inputs of the phased array, while *R-* designates the Rotman lens input ports.

In order to apply the multiple feeding configuration, a different shape of the input tapers has been chosen, for allowing a regular arrangement of the Wilkinson dividers network. For this reason, the width and shape has been kept constant, and, referring to the median axis of the obtained triangular shape taper, they were orientated perpendicularly with the tangent at the beam contour. This procedure is important for easily define a precise phase center of the combined ports, that will be located at the geometrical mean between single ports centers. For example, referring to Fig. 2.28, when *Port9* is fed, the Wilkinson dividers network excites simultaneously inputs *R9* and *R10*: it is intuitive to see that the relative phase center is located in the middle (corresponding to the focal axes, in this particular case). With the proposed feeding arrangement, there will be one beam less compared to the standard case, and scan angles will be slightly shifted (by half of

spacing between beam peaks, due to the new arrangement of phase centers). Referring to the previous design, by the application of the double feeding a beam at broadside is generated, which was not possible with the stand alone Rotman lens (due to the even number of beam ports).

The principle of operation of the multiple feeding network can be explained by its analogy with the array theory: the simultaneous excitation of two elements (i.e. beam ports tapers can be considered as horns that feed the Rotman lens) leads to a more directive field distribution that illuminates the array contour on the opposite side. Clearly, the more directive illumination decreases the losses due to the leakage on the sides, where dummy ports are placed for absorbing the power spilled over. In addition, the more concentrated illumination contributes to lower the sidelobes, imposing an equivalent cosine tapering to the antenna array, without any external added component.

The explained concept are clarified by Fig. 2.29, that shows the comparison between the case when just one feeding is used to excite the lens (Fig. 2.29a), and when the double feeding concept is applied (Fig. 2.29b). It is clear that a more concentrated field distribution is present in the second case, and that almost all the power is reaching the beam contour with almost no power flowing into the Dummy loads.

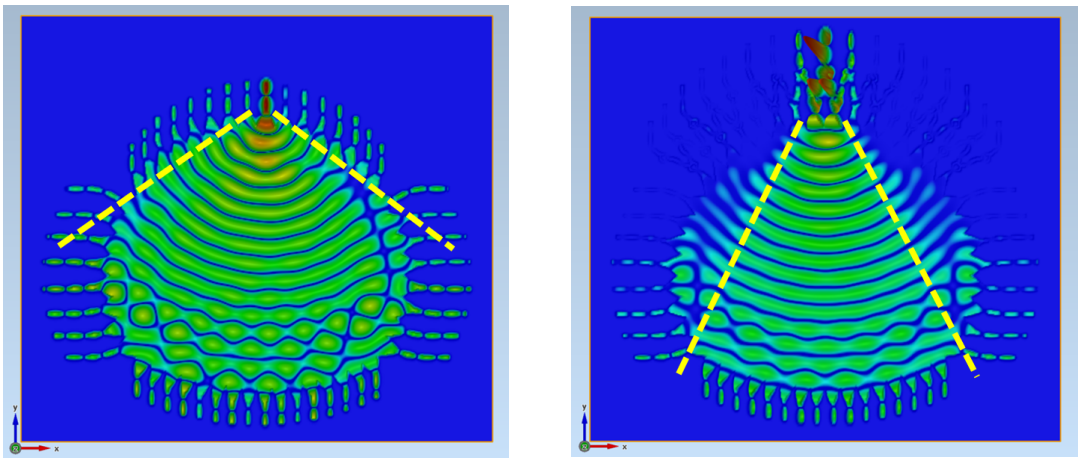

(a) (b)

Figure 2.29: Simulated wave propagation in a Rotman lens in the case of (a): standard feeding approach and (b) double feeding concept; the dashed lines enclose the area where most of the energy is present.

Beside this qualitative analysis, the improved Rotman lens efficiency can be directly estimated by comparing the power distribution with and without the employment of the double feeding concept. In order to evaluate the efficiency, the total insertion loss is calculated by considering the sum of the power at all beam

ports. The illumination loss is defined as the port-to-port integration of power coupled with the dummy ports (spillover losses) and with the unused inputs (coupling losses).

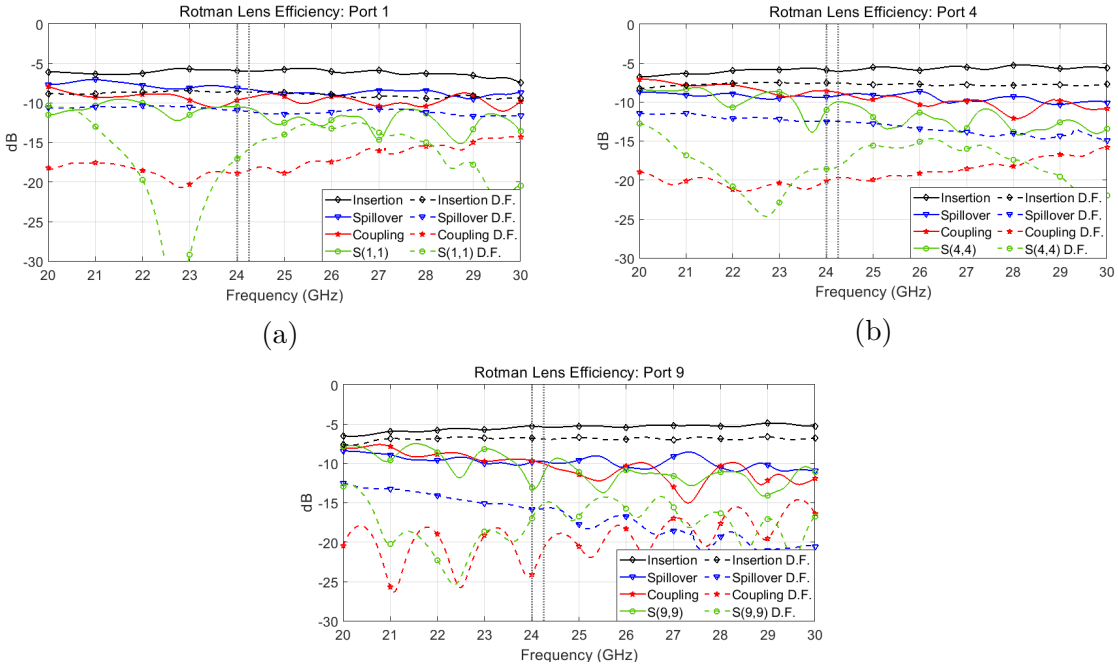

Figure 2.30: Simulated Rotman efficiency in the cases with (dashed lines) and without (solid lines) the Double Feeding (D.F.); (a) *Port1* and *R1*, (b) *Port4* and *R4* and (c) *Port9* and *R9*; 24 GHz ISM band is highlighted for reference.

Since the efficiency of the lens is strongly dependent on the position of the excited input, different ports have been assessed: ports *R1*, *R4* and *R9* (associated with the Rotman lens without double feeding), and *Port1*, *Port4* and *Port9* (related to the design including the double feeding). In this way, the worst case concerning spillover losses (i.e. most external input, Fig. 2.30a), the best case of illumination (i.e. central port,Fig. 2.30c), and an intermediate case (Fig. 2.30b) are analyzed.

The simulated parameters of the listed ports have been reported in Fig. 2.30. In order to prove the increased efficiency given by the proposed feeding method with respect to the standard approach, the total energy coupled to the dummy ports and to the array ports is analyzed. For a clear view of the improvement achieved, also the improvements on the input reflection coefficient and to the mutual coupling between adjacent ports are evaluated. Therefore, the $S-$parameters relative to inputs *Port1*, *Port4* and *Port9* (equivalently *R1*, *R4* and *R9* in the case without double feeding) have been post-processed for obtaining the total amount of power (integral) reaching the dummy ports (i.e. spillover loss is assessed), the unused

input ports (i.e. coupling loss) and the total power coupled by the output/array ports (i.e. insertion loss). By applying the double feeding, also in the worst case (*Port1*) shown in Fig. 2.30a, the spillover losses are reduced due to the more directive propagation inside the lens cavity, as graphically demonstrated in Fig. 2.29. The coupling losses are also strongly reduced (of about 10 dB in the 24 GHz ISM band) by inserting the network composed by Wilkinson dividers, due to the further increase of decoupling between adjacent ports. It is noticed here that the modification of the shape of input tapers have a negative influence on the input reflection coefficient (compared to the Rotman lens design shown in Fig. 2.14). However, the reflection coefficients are improved by the introduction of the double feeding network, from 7 dB as displayed in Fig. 2.30b to 13 dB in the case of Fig. 2.30c, in the 24 GHz ISM band. A deeper analysis is needed for the insertion loss in the two cases. Considering the Rotman lens without double feeding, the insertion loss is found to be between -6 dB and -5.3 dB in the band of interest, mostly due to illumination and conductive losses (conductivity of the surface finishing given by manufacturing process has been considered). The direct comparison with the case including the double feeding shows a lower level of the power reaching the array contour ports, despite the increased efficiency described above. This is explained by considering that the Wilkinson divider networks on the inner ring (directly connected to the Rotman lens) are excited just at one branch, while the other is just terminated to 50 Ω (considering the same return loss and coupling conditions). This leads to a theoretical loss of 3 dB with respect to the case without double feeding (considering same input matching and coupling conditions). However, because of the increased efficiency of the lens with the proposed method, the measured losses are just 2.6 dB (in the worst case of *Port1*) and 1.5 dB in the best illumination case (*Port9*). Moreover, it is underlined that, as a result of the more concentrated propagation inside the lens, a natural cosine tapering is realized in the lens structure by the application of the double feeding concept. Hence, it can be stated that the overall losses are at least comparable with the case of a typical approach including standard amplitude tapering techniques, but with the advantage of being more compact and directly integrated in the Rotman lens. By the performed analysis, it can be concluded that the proposed feeding concept is wideband in terms of efficiency and reflection coefficients.

2.4.2 Optimized Beam Mirroring Design of the PMU

In order to further optimize the implementation of the extended scan range method suitable to be used in a 24 GHz ISM radar system, a novel definition of the PMU is considered. In this new development, the unified PMU block has been removed, and the two phase effects induced by the CBS and BM are separated. In particular, it is noticed that the BM can be incorporated directly with the layer-to-layer transition from the Rotman lens to the antenna array, thus condensing in just

one element the PCB vertical transition, the impedance transformation (50 Ω to 75 Ω) and the phase inversion. It will be verified in the following that the designed structure will perform all these tasks in a very compact, but wideband and low loss structure.

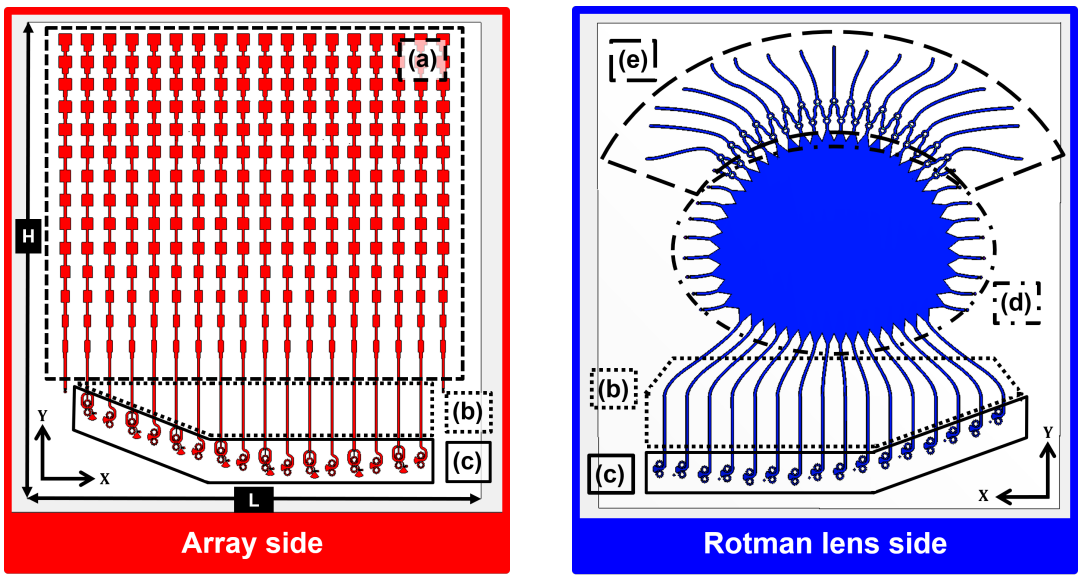

(a) (b)

Figure 2.31: Wide Range Scanning array: *"Antenna array side"*, *"Rotman lens side"*. The highlighted parts are: (a) linear antenna array, (b) CBS realized through microstrip lines, (c) BM realized with reconfigurable phase shifters and microstrip-slot transitions, (d) Rotman lens and (e) double feeding network. The names of system and Rotman lens input ports are inserted for reference.

In Fig. 2.31, the complete 3-D model is reported, where in particular the two layers named *Array side* (Fig. 2.31a) and *Rotman lens side* (Fig. 2.31b) of the complete system are shown. Each of the main parts has been enclosed by using a different line style and identifier. Referring to Fig. 2.31, the system is composed by: a) linear antenna array, b) CBS realized through microstrip lines, c) Reconfigurable phase shifters and transitions, d) Rotman lens and e) double feeding network.

CBS Realization with Transmission Lines

In the new concept, the PMU is incorporating the layer-to-layer transition for the switchable phase inversion functionality imposed by the BM, while for the CBS it is taken advantage of the flexibility to operate with the microstrip lines connecting the array and the Rotman lens. In fact, it have been already noticed that due to the multilayer design, there is no need for a well defined equal phase plane to be set as a reference for the antenna array interface (commonly realized by meandered lines),

instead, just the equality of line length has to be fulfilled. In other words, according to the axis definition in Fig. 2.31, the freedom to locate the layer transition at any position in the y coordinate (in contrast with the x direction, whose distance is set by the array spacing) allow to freely manage each line independently. Therefore, by combining the progressive phase shift imposed by the CBS and the connection lines between Rotman lens and array, the CBS is realized with a set of microstrip lines that introduces the required phase distribution while compensating the length mismatch by adding them together.

The complete length of the lines has been split between the two sides of the board for enhancing compactness, leading to an efficient and linear solution as displayed in Fig. 2.31. This arrangement greatly simplifies the routing, reducing the PCB area and the conductive losses. As a final remark, it is noticed that this solution requires almost the same area as the PMU block solution realized with RTPS.

BM Realized with Reconfigurable Layer-to-Layer Transition

In this optimized design, the microstrip to slot-line transition is used as basis for generating the BM operating principle and for coupling signals from the two sides of the board. As detailed in Sect. 2.2.3, referring in particular to Fig. 2.9, the BM is implemented with a proper arrangement of reconfigurable and fixed and reconfigurable phase shifters. In this design, the two functions are fulfilled by two specific layer-to-layer transitions, that will be referred as 0° fixed phase shifter and a specialized 0°/180° reconfigurable phase shifter.

0°/180° Reconfigurable Phase Shifter

In Fig. 2.32, the structure of the 0°/180° reconfigurable phase shifter is reported. The phase shifter shares the same layer to layer transition described in Sect. 2.3.3, but it includes four PIN diodes in the array side, devoted to produce both the two phase shifting conditions. The microwave active part has been placed on the array side, in such a way that no in-line decoupling capacitors are needed. The phase shifting takes advantage of the slot-microstrip coupling, that can be considered as a splitter, whose outputs are 180° degree out of phase. The phase selection is achieved by properly biasing the four PIN diodes, used for enabling one of the two branches (*0° path* or *180° path*) positioned at sides of the slot, for coupling the electric field with the desired polarity. In this design, the circular termination used in the previous layer-to-layer transition is here replaced by radial stubs, that have demonstrated good performance and better integration perspective, given the limitation imposed by the condensed layout and the manufacturing directives (i.e. via to via clearance and minimum copper spacing). More specifically, referring to Fig. 2.32, diodes *D1* and *D2* are placed in series, while *D3* and *D4* are connected

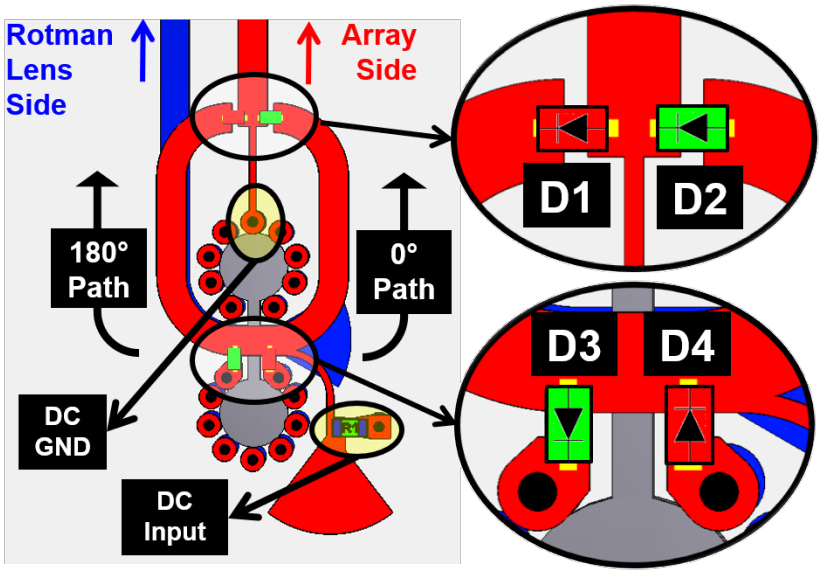

Figure 2.32: Complete model of the 0°/180° reconfigurable phase shifter, constituted by 4 PIN diodes; 0° configuration (shown in this example): *D2* and *D3* are *ON*, *D1* and *D4* are *OFF*; instead, for obtaining the 180° case, *D1* and *D4* are *ON*, and *D2* and *D3* *OFF*.

to ground, on the two sides of the slot, as closest as possible, for terminating the microstrip-to-slot transition.

The principle of operation of the reconfigurable phase shifter is the following: the configuration for achieving 0° phase shifting is obtained by direct biasing *D2* and *D3* (the *0° path* is active), while *D1* and *D4* are reverse biased. In the dual case, in which the diodes *D1* and *D4* are active while *D2* and *D3* are *OFF*, the *180° path* is selected, and the phase inversion is achieved. In principle, only two diodes can be used for achieving the same functionality, however this approach results in inadequate performance due to limited isolation in the *OFF* state of the PIN diodes at 24 GHz, that would lead to poor matching and high losses.

In Fig. 2.32, the structures developed for the correct biasing of the diodes (i.e. *DC input* and *DC GND*) are also indicated. The bias lines are fundamental for the correct operation of the PIN diodes, and they have been specifically tuned for avoiding mismatch and losses on the 0°/180° reconfigurable phase shifter. In particular, the positive/negative current is injected at *DC input*, where a $\lambda/4$ line terminated on a radial stub is used as connection with a resistor, while the *DC GND* point is used as ground reference by exploiting a $\lambda/4$ line connected directly to ground. For the biasing of the pairs of series-shunt diodes (*D1* and *D4* or *D2* and *D3*), a positive/negative voltage is used as control, specifically $V_{pos} = 5V$ and $V_{neg} = -5V$. In particular, with V_{pos} the diodes *D2*, *D3* are ON and positive angles of the scanning range are selected (i.e. BM state is *OFF*), while V_{neg} sets to *ON*

the diodes *D1* and *D4* for scanning the negative range (i.e. BM set to *ON*).

The described 0°/180° reconfigurable phase shifter is first evaluated by mean of simulation, and the $S-$parameters are displayed in Fig. 2.33.

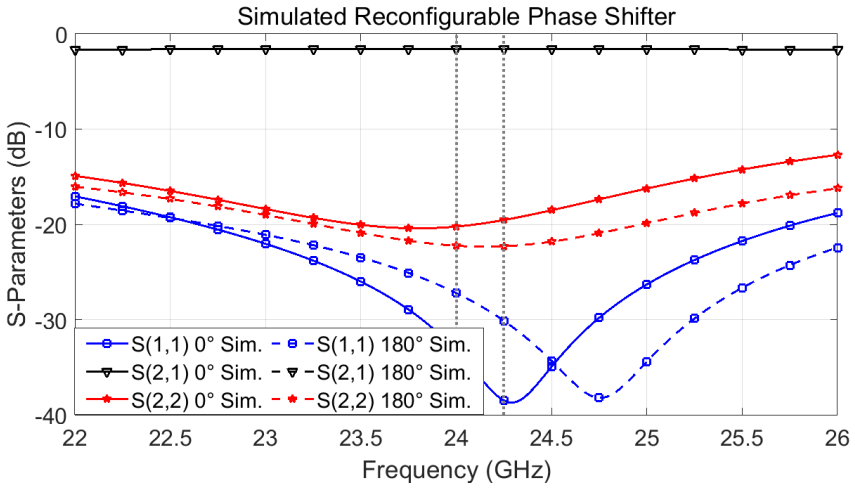

Figure 2.33: Scattering parameters of the 0°/180° reconfigurable phase shifter in both BM states; 24 GHz ISM band highlighted for reference.

It can be noticed that, from the numerical results displayed in Fig. 2.33, the insertion loss is slightly increased compared to the one calculated in Fig. 2.16: 1.9 dB for the reconfigurable phase shifter versus 1.2 dB for the simple layer-to-layer transition in the 24 GHz ISM band, where the same port termination scheme was adopted. The slightly higher losses are due to the parasitic elements of the PIN diodes, in both *ON* and *OFF* states. However, it is clear that this solution is much more efficient compared to the realization of unified PMU with RTPS. Moreover, it is recognized that $|S_{11}|$ and $|S_{22}|$ are not identical: this is due to the microwave DC decoupling which loads in a different way the active branches of the phase inverter, thus breaking its symmetry. For the same reason, the reflection coefficients $|S_{ii}|$ present a shift in frequency in the case of 0° (BM not active) with respect to the case of 180° shift (BM activated).

0° Fixed Phase Shifter

The second element of the newly developed BM is the 0° fixed phase shifter, presented in Fig. 2.34 (ground planes and dielectric are not shown). The principle of operation is the same as the one described in Sect. 2.3.3, with the only clear difference the use of radial stubs for terminating the microstrip lines connecting the Rotman lens on one side and the antenna array on the opposite side.

Moreover, the structure in Fig. 2.34 has been further optimized together with the 0°/180° reconfigurable phase shifter for achieving the best phase performance

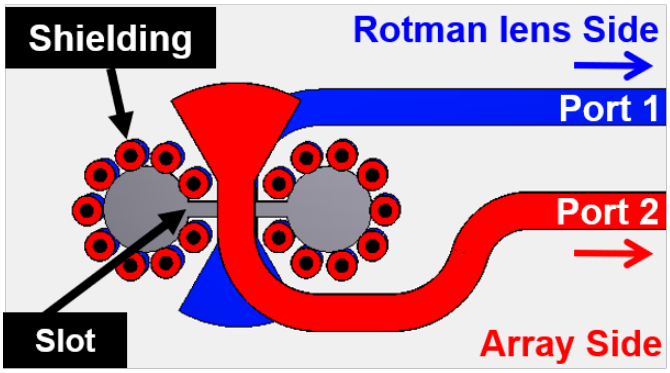

Figure 2.34: Designed model of the 0° fixed phase shifter (ground planes and dielectric are not shown). The energy is coupled from the Rotman lens side to the array side via the slot. Lines are terminated with a radial stub, while the slot is terminated with an open.

in both operative states of the BM. It can be noticed that the configuration obtained by setting the diode *D2* and *D3 ON* and *D1* and *D4 OFF* for the 0°/180° reconfigurable phase shifter is equivalent to the 0° fixed phase shifter(in first case the virtual short is fulfilled by *D3*).

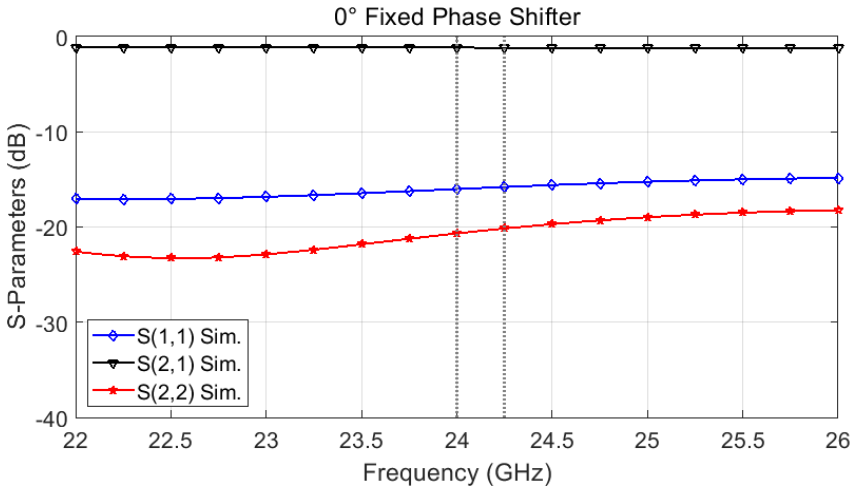

Figure 2.35: Simulated $S-$parameters of the 0° fixed phase shifter; 24 GHz ISM band is highlighted for reference.

Fig. 2.35 displays the simulated reflection coefficients of the 0° fixed phase shifter in the frequency band 22 GHz to 26 GHz. It is reminded that the $S-$parameters reported in this case are calculated considering a characteristic impedance of 50 Ω for the input at the Rotman lens side and 75 Ω for the one placed on the array

side. The analysis of the $S-$parameter of the fixed phase shifter reveals a good performance in the frequency range of interest, where the introduced losses are less than 1.3 dB. This result is similar to the one displayed in Fig. 2.16. It can be noticed that one source for the losses are relative to the actual conductivity of the ENIG finishing, which is much lower compared to solid copper, and therefore leads to increased resistive losses in the structure.

The fundamental aspect of the two phase shifters here described is related to the phase difference between the two structure in the case of BM *ON* and *OFF*, which is corresponding to a differential phase of 180° and 0° respectively. From the simulated results reported in Fig. 2.36, it is recognized that the phase error is very low in the frequency of interest, especially if it is related to the phase variation shown in Fig. 2.23. Therefore, it is verified that the proposed concept is much more wideband than the previously designed one, based on RTPS, as theoretically expected.

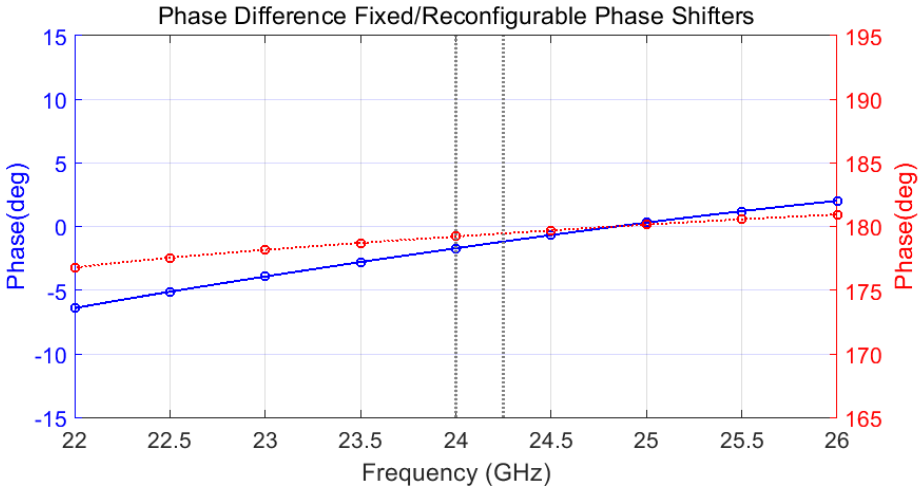

Figure 2.36: Simulated phase difference between the 0° fixed phase shifter and the reconfigurable phase shifter in the 0° (blue line) and 180°(red line) states respectively; 24 GHz ISM band is highlighted for reference.

2.4.3 Manufacturing and Experimental Validation

The extended scan range method applied to the Rotman lens as beamformer has been validated by fabricating and testing the complete described system, which is reported in Fig. 2.37, where all the main elements composing the systems are indicated. Moreover, in Fig. 2.38 the build-up of the multilayer PCB is reported for clarity.

According to Fig. 2.37, the overall dimensions of the PCB are $L = 130$ mm and $H = 140$ mm, thanks to the folding technique allowed by the layer-to-layer

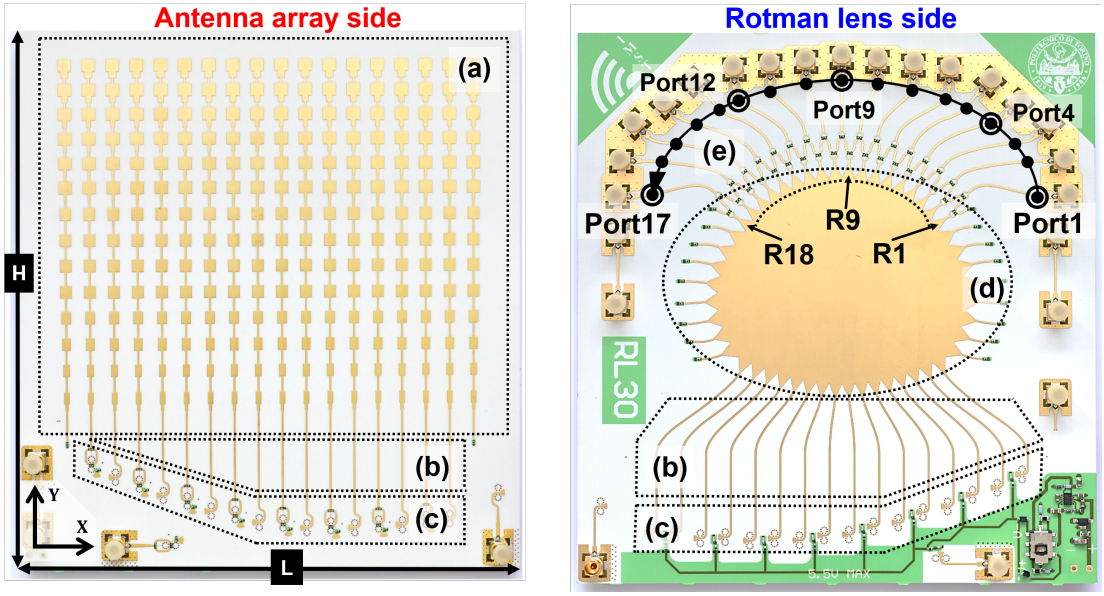

(a) (b)

Figure 2.37: Manufactured antenna array system based on Rotman lens as BFN featuring the extending scan range method. At left side (a) the antenna array and the active part of the reconfigurable phase shifter is shown, while at right side (b) the Rotman lens and the overall connections are presented. Names of input ports of Rotman lens and for the complete system are indicated for clarity.

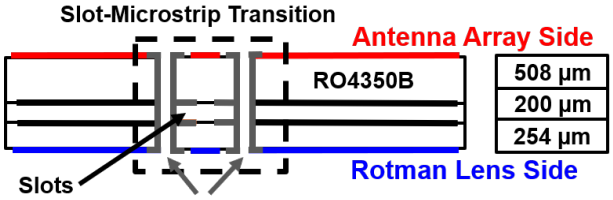

Figure 2.38: Drawing of the PCB structure, with the thicknesses of the three substrates. Cross section of the microstrip-slotline transition is also depicted.

transition. Being manufacturing and cost issues an important aspect, a standard fabrication process has been used. Therefore, according to the initial considerations on material usage, the standard Electroless Nickel Immersion Gold (ENIG) has been adopted as copper finishing for ensuring a cost effective and reliable soldering process of the components, especially for the tiny dimensions (380 μm x 230 μm) of PIN diodes. However, it is noticed here that other options could have been selected as surface finishing (e.g. solid copper, Organic Solderability Preservative), but the cost factor would have been increased sensibly. Moreover, by considering

the high number of inputs, SMP connectors have been selected as a low-cost alternative to the 2.92 mm connectors, being suitable for high density surface mount interconnections and, then, contributing also to the reduction of the form factor of the PCB. In fact, SMP connectors have the advantage of being compact, requiring very little space for positioning adjacent connections, thanks to their snap-on coupling. This feature allows to arrange the input lines in a radial pattern, thus keeping an almost constant length, as can be observed in Fig. 2.37b. Nevertheless, care must be taken when performing measurements with SMP, due to the mechanically fickle connection, as detailed in the following.

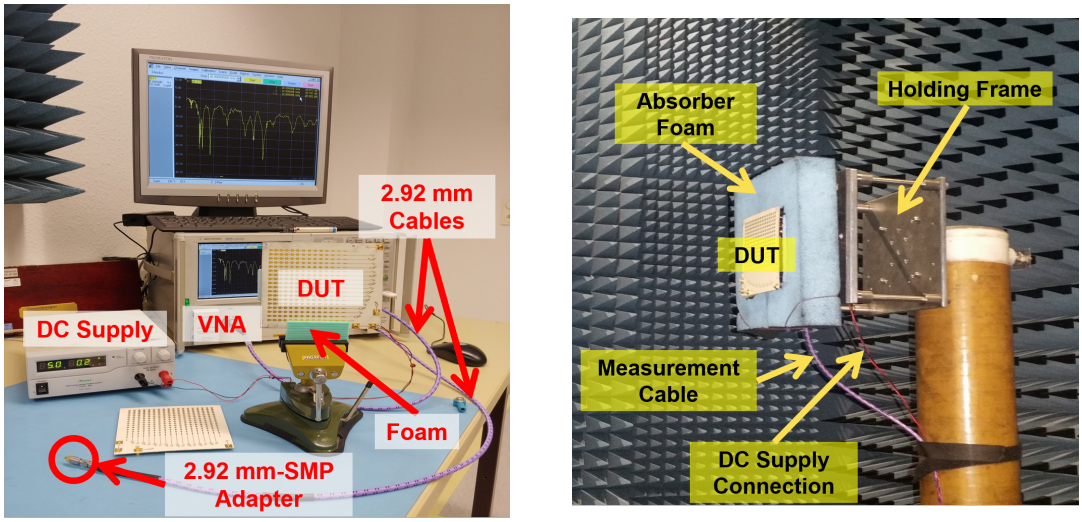

(a) (b)

Figure 2.39: Measurement test setups: in (a) the Vector Network Analyzer is employed for measurement of S-parameters, while in (b) the antenna pattern measurement setup in the anechoic chamber is shown. Main components of the two test benches are indicated.

The overall performance of the extended scan range array based on Rotman lens and the fixed/reconfigurable phase shifters have been characterized in terms of $S-$parameters by using an Agilent E8363B Vector Network Analyzer (VNA). Furthermore, the radiation pattern of the complete scanning array system has been tested in the anechoic chamber. The calibration standard used was the Through-Open-Short-Match ($TOSM$) with the 2.92 mm calibration kit, according to the type of cables required for connecting the DUT with the VNA. For both characterizations a 2.92 mm to SMP adapter has been introduced for interfacing the device under test with the VNA. Moreover, 50 Ω SMP terminations have been plugged on all the unused ports in both S-parameters and radiation measurements. In Fig. 2.39a the test setup used for the measurements of the scattering matrix is shown, while in Fig. 2.39b the picture for the far field measurement setup is presented. More

in detail, the radiation pattern has been measured in the anechoic chamber, in far field regime. The PCB has been fixed to the rotating column (aligned to the *H plane*) with a holding frame. Absorbing material has been placed for avoiding unwanted radiation to be reflected by the test fixture. A horn antenna has been used as transmit antenna. The SMP input connectors that were not connected to the measurement system were terminated with 50 Ω SMP. During measurements, the BM operative state is selected by acting on a sliding switch, connected at the outputs of a dual linear dropout regulator able to provide V_{pos} and V_{neg} (i.e. ±5 V, thanks to a regulated charge pump configuration), located on Rotman lens side (visible in Fig. 2.37 on bottom right corner), and delivering a total of 220 mA for biasing the PIN diodes. This easy way of controlling the BM greatly simplifies the measurement process: for instance, the measurement of the radiation pattern associated with one input can be performed in both states by positioning the switch for selecting the positive/negative voltage (i.e. directly related to positive/negative scan angles).

2.4.4 Manufactured Phase Shifters Analysis

The designed phase shifters have been realized and tested by means of a separate test structure, since they are the most challenging part of the overall system. In particular, Fig. 2.40b shows the measured phase shifters, in comparison with the 3D models used in simulation, reported in Fig. 2.40a. Specifically, in Fig. 2.40, the array side part of the fixed phase shifter is displayed, (i.e. the parts indicated with *1a* and *1b*) while the parts of Fig. 2.40 designated by *2a* and *2b* indicate the reconfigurable phase shifter. Finally, with *3a* and *3b* are named the modeled and fabricated part of the phase shifters etched on Rotman lens side, which is common for both designs.

In order to avoid errors due to bad soldering of the tiny PIN diodes, all the components have been tested by using a thermocamera, for checking the temperature increase given by the current flowing (either positive or negative), as shown in Fig. 2.41a. Clearly, a not correctly connected/broken diode will not be polarized, and it will appear as "cold", as demonstrated from Fig. 2.41b.

Unfortunately, for measuring such devices, the TRL method cannot be used, since the input and output ports have different characteristic impedances (i.e. dissimilar substrate thickness and consequently different tuning of the SMP-microstrip transition, as shown in Fig. 2.38). Moreover, also the time gating technique can not be used, because the resolution for differentiating the effects of the connector and the phase shifters is insufficient, due to the small physical size of the structure. For characterization purposes, a three stage quarter wavelength impedance transformer was added on the array side part of both phase shifters as can be recognized in Fig. 2.40, for performing the 75 Ω to 50 Ω transition and establishing a proper connection with the VNA.

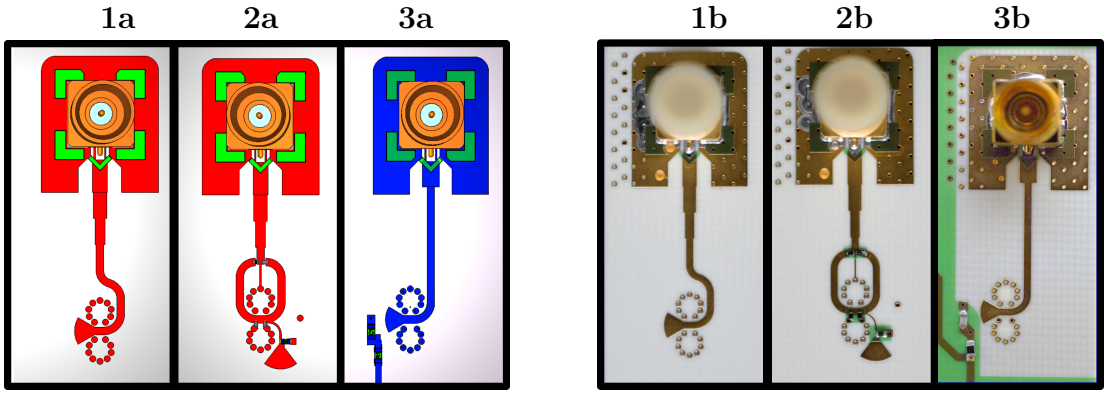

(a) (b)

Figure 2.40: Simulation models (a) and prototypes (b) of phase shifters, including the SMP connector; (1a-1b) 0° fixed phase shifter, array side; (2a-2b) 0°/180° reconfigurable phase shifter, array side; (3a-3b) 0° fixed and 0°/180° reconfigurable phase shifter, Rotman lens side (identical for the two types of phase shifters).

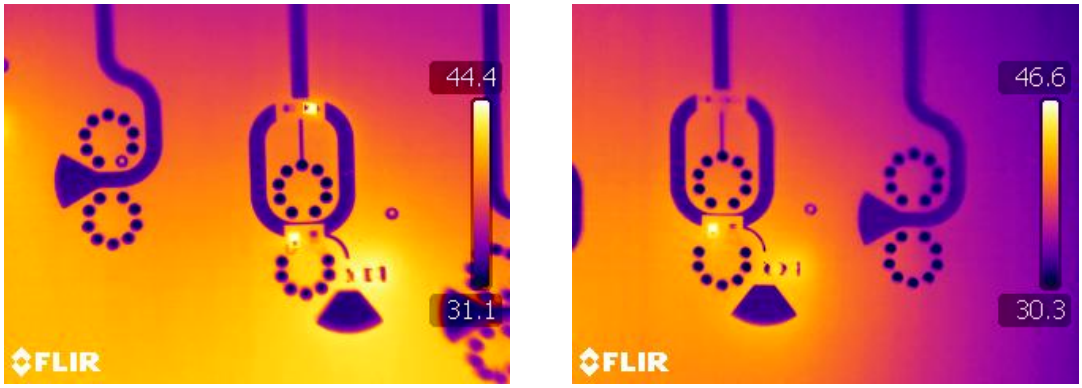

(a) (b)

Figure 2.41: Infrared pictures of the biased PIN diodes in the reconfigurable phase shifter used for functional testing. In (a) all diodes are working while in (b) one diode is damaged.

In order to make a complete analysis of this important component, three concurrent evaluations are performed. At first, the two phase shifters are characterized through numerical simulations, without the presence of the SMP connectors and the three stages impedance transformer, thus employing the same model described in Fig. 2.32 and Fig. 2.34. In addition, the measurements and the simulated model are directly compared, by embedding the model of the connector and the three stages impedance transformer in the simulation, in order to have the same configuration, therefore employing the same structures already shown in Fig. 2.40. By this procedure, a clearer and reliable comparison between the simulated and measured

results are possible, and the model used in the simulation can be validated.

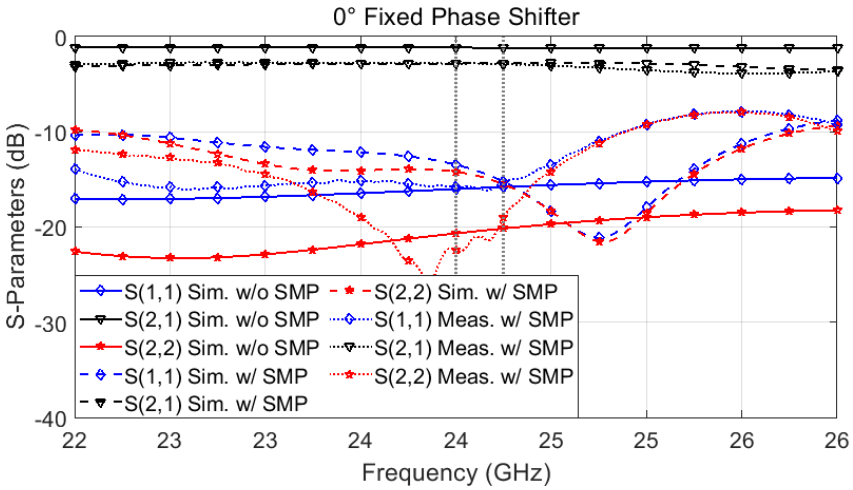

Figure 2.42: Simulated S-parameters of the 0° fixed phase shifter without the SMP connector (solid lines) and comparison between simulation and measurements including the connector (respectively dashed and dotted lines); 24 GHz ISM band highlighted for reference.

Figure 2.42 displays the reflection coefficients of the 0° fixed phase shifter in the frequency band 22 GHz to 26 GHz in the cases with SMP connectors included (through simulation and measurements, as in figures 2.40a and 2.40b parts *1x-3x*) and without (only simulated results, same as Fig. 2.35), included for reference purpose. Similarly to previous cases, the reported $S-$parameters consider the characteristic impedance of 75 Ω for the array side and 50 Ω for the Rotman lens side. The simulated results without SMP have already been described in Sect. 2.4.2. However, in the second case, where SMP connectors and the three stage impedance transformer are both included, a direct comparison between simulated and measured results can be performed. Clearly, the introduction of these components causes a degradation of the overall performance, as noticed in both measured and calculated values of the scattering parameters reported in Fig. 2.42. Nevertheless, a good agreement between the two results is recognized, where the shift to lower frequency of the $|S_{11}|$ and $|S_{22}|$ can be explained by the presence of the 2.92 mm to SMP adapter used during the measurement process that was not included in the VNA calibration.

In Fig. 2.43, the reconfigurable phase shifter is analyzed. For better comparison, Fig. 2.43a reports again the case with and without SMP connector, which is available just through simulation. More interesting at this stage are the results shown in Fig. 2.43b, where some small discrepancies between the simulated and measured amplitude of the reflection coefficients $|S_{11}|$ and $|S_{22}|$ are detected, in contrast with the characterization of the same results done for the fixed phase shifter.

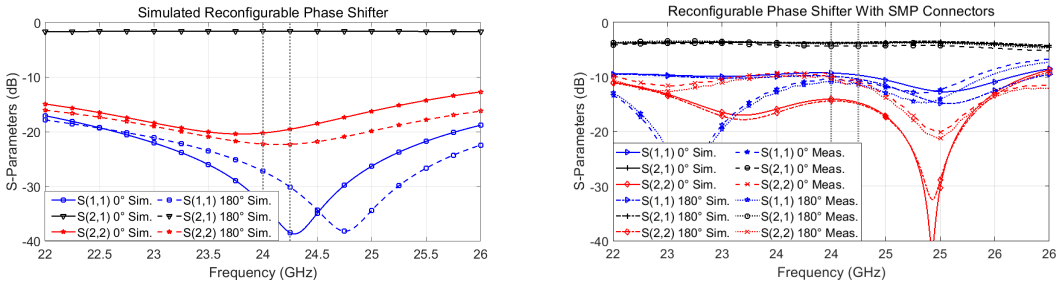

(a) (b)

Figure 2.43: Scattering parameters of the 0°/180° reconfigurable phase shifter in both BM states; (a) simulated without the SMP connector; (b) measured and simulated including the SMP connector; 24 GHz ISM band highlighted.

This can be explained with a not perfect equivalent electric modelling of the PIN diodes, in particular the values of C_{OFF} and L_{ON} reported in Sect. 2.3.5. In fact, these two equivalent electrical components are affecting mostly the reflection coefficients, rather than the losses that are typically driven by the resistive part of the model (denoted as R_{ON}), which instead show a good agreement between the two displayed curves of $|S_{12}|$ thanks to the previously measured value of conductivity of the ENIG copper finishing.

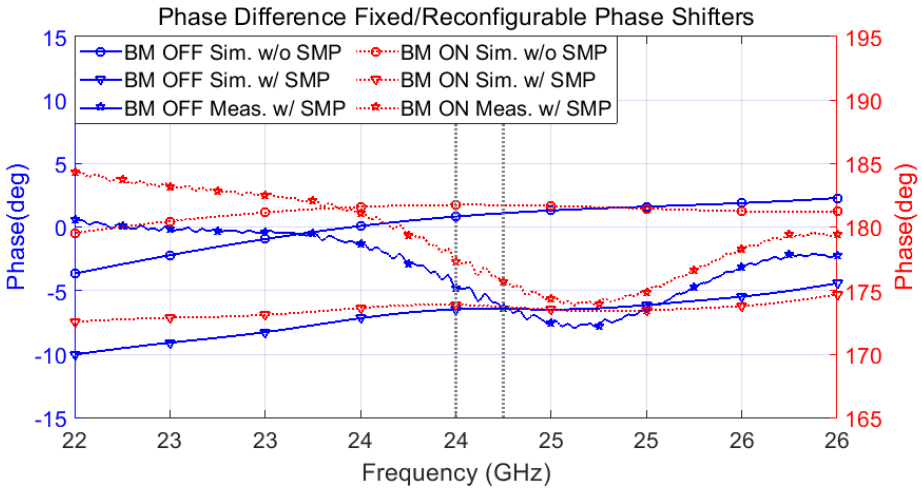

Figure 2.44: Differential phase between the reference (0° fixed phase shifter) and the 0°/180° reconfigurable phase shifter in the case BM *OFF* (solid lines, left y axis) and BM *ON* (dotted lines, right y axis); 24 GHz ISM highlighted for reference.

In analogy with the evaluation carried for the magnitude of the $S-$parameters, the phase is analyzed. In particular, Fig. 2.44 displays the differential phase relative to the S_{12} parameter between the fixed phase shifter and the reconfigurable

Table 2.1: Maximum Differential Phase Error

Bandwidth	**BM Status**					
	Sim. w/o SMP		**Sim. w/ SMP**		**Meas. w/ SMP**	
	0°	**180°**	**0°**	**180°**	**0°**	**180°**
24 – 24.25 (GHz)	0.9°	1.7°	6.4°	6.3°	6.4°	4.2°
22 – 26 (GHz)	3.6°	1.8°	10°	7.4°	7.9°	5.9°

phase shifter in the BM inactive state (i.e. 0° phase is added to the line), and the BM active state (i.e. 180° phase inversion superimposed to the phase distribution). Referring to the simulated results of the model without the SMP connectors, already displayed in Fig. 2.36, it can be observed that in the 24 GHz ISM band the phase error is very limited in both BM operative states, and the designed system has potentially more than 6 GHz bandwidth following the ±5° error criterion (from 21.55 GHz to 27.65 GHz). Instead, in the cases where the SMP connectors are included, the measured phase difference is consistent with the corresponding simulated results in both BM states, even if the measured ones are affected by some fluctuation, probably derived from the fickle mechanical contact. According to Table 2.1, which summarizes the phase errors in the examined cases, a measured maximum deviation from the theoretical values of 6.4° in the 24 GHz operative band is recognized. Moreover, the comparison with the case without SMP confirms that the transition microstrip-connector introduces a discontinuity that causes a mismatch.

Similarly to the analysis carried out for the magnitude of the scattering parameters, also in this case the discrepancies found in the simulated and measured phase errors can be explained with inaccuracies in the equivalent electrical model of the PIN diode. Finally, by considering the good agreement of the simulated and measured results including SMP, it can be assumed that the performance of the phase shifters is reasonably close to the one displayed in the simulations without connectors.

2.4.5 Complete System Characterization and Measurements

In Fig. 2.45, input reflection coefficients of the complete system, shown in Fig. 2.37, are evaluated by means of simulations and measurements. At first, in Fig. 2.45a the measurement and simulations including SMP are compared. However, in this structure, the effect of the SMP connector to microstrip transition can be excluded from the measurements by applying the time gating technique. In fact, in this case the reflections at the connector interface are clearly discriminated from the others relative to the Wilkinson dividers due to the long input lines, and they can be eliminated accordingly. Specifically, only $S-$parameters relative to the case of BM not activated (i.e. for positive bias voltage of PIN diodes) are displayed in

Fig. 2.45, because the other case is completely analogous. For a better analysis the wider frequency band of 20 — 30 GHz is considered, and the 24 GHz ISM band is indicated for reference.

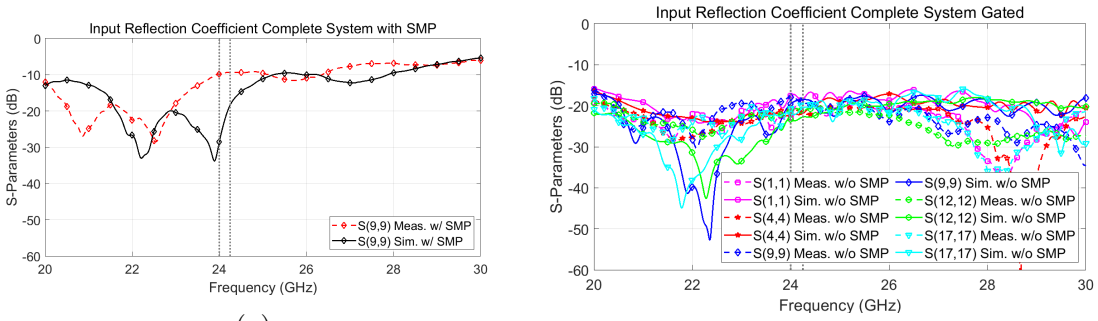

(a) (b)

Figure 2.45: Simulated (continuous line) and measured (dashed line) reflection coefficients of Ports 1, 4, 9, 12 and 17 relative to the complete system with BM not activated; (a) SMP is included in both measurements and simulations; (b) time gated measurements compared with simulations without SMP; the 24 GHz ISM band is highlighted.

The results in Fig. 2.45 exhibit a variability of the reflection coefficient across the input ports, mostly due to the asymmetry of the system (given by the CBS and the BM arrangements). However, the predicted reflection coefficient is found to be consistent with the performed measurements with time gating, even if the simulated values in *Port9*, *Port12* and *Port17* denote a better matching level at lower frequencies (with minimum at 22 GHz) with respect to measurements. By considering as reference the central port in Figs. 2.45a and 2.45b (i.e. *Port9* indicated with the diamond marker), in both cases where the SMP connectors are included or removed by applying the time gating technique, a good agreement between measured and corresponding numerical results is observed. In particular, the curves relative to simulations and measurements with connectors clearly show the degradation due to the SMP to microstrip transition, in comparison with the equivalent cases without connector. This is due to the SMP to microstrip transition, which has been optimized for the 24 GHz ISM band, and therefore is intrinsically narrowband. The shift in frequency between the ungated measurement and the simulated $S-$parameters can be explained by the SMP to 2.92 mm adapter used during measurements, and not included in the simulation. Nevertheless, it can be stated that even with SMP connectors, the extended scan range phased array is well matched in the 24 GHz ISM band (minimum measured value is 9.85 dB).

In the following, the radiation pattern of the antenna array is assessed, for validating the scan range extension method. Figure 2.46 shows the simulated and

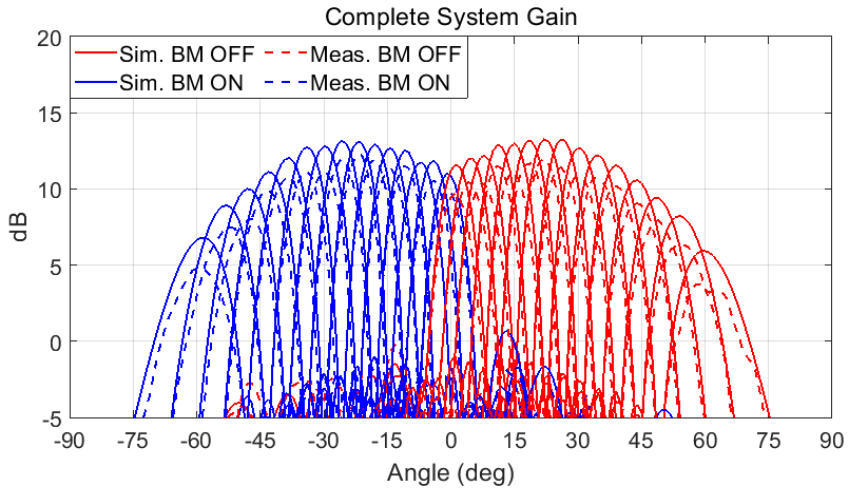

Figure 2.46: Simulated (continuous line) and measured (dashed line) gain of the realized extended scan range array at 24 GHz; different colours are used to distinguish between the case of BM activated (negative scanning angles, blue lines) and BM not activated (positive scanning angles, red lines).

measured gain pattern at 24 GHz in the *xz* plane (refer to Fig. 2.37 for axes definition). Considering the overall scanning range, it is noticed that the results obtained by measurements are in good agreement with the simulated ones, confirming that the described method is actually able to almost double the FOV of a scanning array using a Rotman lens as beamformer. In fact, the peak of the last beam is detected at 58.7°, which is close to the theoretical value of 60°. The difference of 1.3° can be attributed to many factors, and they are mainly due to tolerances in the fabrication of the prototype. For a clearer overview of the performance of the extended scan range antenna system, the main parameters displayed in Fig. 2.46 are summarized in Table 2.2, where the measured realized gain and HPBW are reported for each beam (associated with a scanning angle). The two measured quantities are also compared with the results obtained by simulation. The difference between the simulated and measured gain pattern, quantified to be between 0.7 dB and 2.2 dB, is explained by considering the losses of the SMP connectors (estimated to be about 0.7 dB at 24 GHz), inaccuracies in the modeling of components (e.g. PIN diodes) and the conductivity of the ENIG finishing. It is interesting to notice that the maximum values of the gain are not located at broadside; instead, they are located at angles in proximity of ±30° (corresponding to the initial maximum FOV of the Rotman lens). This can be explained by considering that the central input ports realize a more efficient illumination of the array contour of the Rotman lens, compared to ports placed on the sides, where a larger amount of power is coupled to the dummy ports due to the geometry of the lens (see Sect. 2.4.1). However, the peak of the gain is not associated with the beam positioned at ±30°: this is

because of the scan loss at these angles (numerically estimated to be approximately 1 dB). In fact, this characteristic shape of the gain pattern having the highest values at approximately ±25° and reducing at lower and higher angles is the sum of two different effects: the scan loss and the illumination loss. The illumination loss concerns both the beams positioned at widest and lowest scan angles, and its effect has been estimated to be 1.2 dB, by comparing the level of beam at broadside (scan loss at low scan angles is negligible) with respect to the beam at ±30° that represent the cases with best illumination of the lens (scan loss associated with this angle is considered in the calculation). Moreover, at extreme angles of the scanning range, illumination loss causes the same amount of gain reduction discussed for the broadside case, but at increasing scan angles the effects of the scan loss became dominant, as recognized in Fig. 2.12, where the reduction was estimated to be 5.3 dB at ±60°. Furthermore, from both measured and simulated antenna gains reported in Table 2.2, an asymmetry of the levels of the beams is recognized for opposite angles of the scan range. This difference can be explained by the overall insertion loss among each column of antenna array, caused by the CBS structure (i.e. longer lines used for generating the required phase distribution are intrinsically asymmetric), and by the amplitude mismatch that appears at each column due to the alternation of fixed and reconfigurable phase shifters (the last are more lossy, because of the presence of PIN diodes). This fact also explains the slightly uneven levels of some adjacent beams (e.g. beam at 11.3° compared to beam at 15°), as can be recognized from the values reported in Table 2.2. Nevertheless, it can be noticed that the performance of the designed prototype exhibits a reduction of the realized gain of maximum 3 dB, in the scanning range ±45°. In addition, it can be also observed that the spatial coverage of the beams is ensured by their tight overlapping, as a result of the BM application. In fact, not only the scan range is doubled, but also the number of available beams, which introduces the possibility to use a Rotman lens with half of beam ports compared to standard designs.

Finally, Fig. 2.47 shows the normalized amplitude of the co- and cross- components of the radiated field relative to *Port11* (as indicated in Fig. 2.37(e) enclosure), proving that the measured radiation patterns are correctly predicted by the numerical modelling. This result verifies also that the analysis carried out in Sect. 2.4.4 on phase shifters performance is consistent, and it confirms the accurate phase distribution obtained by simulation for the models without SMP connectors.

This aspect is particularly important for radar applications, and it is considered a parameter that qualifies the designed phased array. In addition, it is observed that the sidelobe level is below 10 dB in any condition (worst case), without any additional amplitude tapering at antenna inputs, thanks to the proposed double feeding structure of the Rotman lens (see Sect. 2.4.1). Furthermore, it is noticed that the double feeding concept allows to further decrease the sidelobe level by combining more inputs to be simultaneously excited: this is possible by adding an additional level of Wilkinson dividers (e.g. three stages of Wilkinson dividers

Table 2.2: Simulated And Measured Array Performance Comparison

BM ON				
Scan Angles (°)	**Gain Sim.(dB)**	**Gain Meas.(dB)**	**HPBW Sim. (°)**	**HPBW Meas. (°)**
-58.7	6.8	4.8	12.9	13.3
-52.8	8.9	7.5	10.9	10.7
-47.8	10.0	8.0	9.9	10.0
-42.9	11.1	9.9	9.1	8.9
-38.4	12.0	10.7	8.5	8.6
-33.7	12.7	11.1	8.0	7.6
-29.5	12.8	11.1	7.7	7.2
-25.5	13.1	11.9	7.4	7.2
-21.5	13.0	12.3	7.1	6.7
-17.6	12.8	11.9	7.0	7.0
-14	12.7	11.3	7.0	7.2
-10.5	12.5	10.5	6.8	6.8
-7.2	11.7	10.3	7.1	7.3
-4.1	11.8	10.5	7.1	6.8
-0.8	11.0	9.9	6.9	6.8
BM OFF				
Scan Angles (°)	**Gain Sim.(dB)**	**Gain Meas.(dB)**	**HPBW Sim. (°)**	**HPBW Meas. (°)**
1.3	11.5	9.7	7.0	7.1
4.8	12.0	10.4	7.0	7.0
8.0	12.2	10.3	7.1	7.2
11.3	12.8	11.5	6.9	6.8
15.0	12.9	11.0	6.9	7.0
18.6	13.1	11.6	7.2	7.3
22.2	13.2	12.0	7.3	7.1
26.3	13.2	11.4	7.4	7.3
30.4	12.6	10.8	7.7	7.8
34.3	12.2	10.7	8.0	7.9
39.2	11.5	10.2	8.5	8.4
43.8	10.5	9.0	9.2	9.5
48.6	9.4	7.9	10.0	10.0
54.0	8.2	6.3	11.0	11.4
59.6	5.9	3.7	13.1	13.3

instead of two as developed in this work). Table 2.3 provides a comparison among wide scan angles designs of phased arrays based on Rotman lens as beamformer

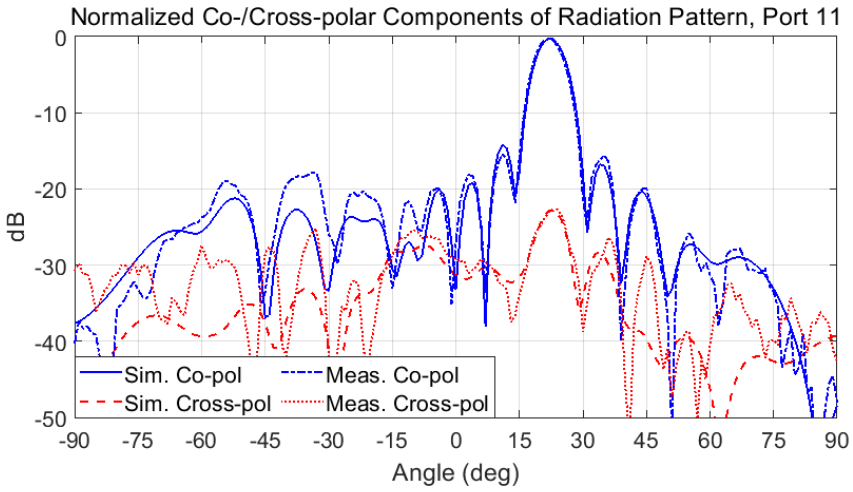

Figure 2.47: Comparison of the normalized co-polar and cross-polar components of the radiation pattern for *Port11* at 24 GHz obtained through simulation and measurement in case of BM *OFF*.

available in literature, where [219] and [220] are considered in particular, as previous examples of widening scan range researches. Finally, the cross-polar component of the radiation pattern is found to be lower than -15 dB with respect to the measured co-polar field pattern, as shown for *Port11* in Fig. 2.47.

Table 2.3: Comparison Among Rotman Lens Based Scanning Arrays

References	**Center Frequency (GHz)**	**Technology**	**Scan Range**	**Scan Extension**	**SLL (dB)**
[**219**]	24	PET	±38°	8°	10
[**220**]	9	LC phase shifters	±37.5°	7.5°	12*
[**212**]	24	SIW	±48°	-	10*
[**213**]	60	LTCC	±30°	-	12
[**215**]	10	Synthesized dielectric	±33°	-	10
This work	24	PIN diodes	±60°	30°	10

(*) Estimated graphically.

2.4.6 Conclusion and Perspectives

An innovative method for extending the scanning range of a phased array based on the concepts of Complete Beam Shifting and Beam Mirroring is here demonstrated first with a theoretical analysis, and subsequently the proposed technique has been demonstrated and validated in combination with a Rotman lens, by employing both numerical tools and measurements. As a result, by considering an initial 24 GHz trifocal Rotman lens able to achieve a FOV of $\pm 30°$, a compact and cost-effective design of a 24 GHz ISM scanning array radar was implemented, demonstrating a doubled maximum steering angle of about $\pm 60°$. Moreover, for achieving the BM, a proper reconfigurable phase shifter has been developed and realized, showing good performance and simple control requirements. The overall performance of the phased array based on Rotman lens as beamformer has been enhanced by a novel multiple feeding concept, that improves the illumination of the antenna side contour of the lens, thus decreasing the losses due to spillover and generating a cosine tapering. Finally, the purpose of building a low-cost prototype has driven the design to use solutions (e.g. use of SMP connectors and ENIG copper finishing) that have caused a decrease in the system efficiency. Hence, to overcome the limitations of the current design, an improvement on the manufacturing (i.e. connectors and surface finishing) will be considered in further designs.

As future perspective, this concept can be used for radar and communication systems operating in *E*- and *W*- bands. However, the increase of frequency will require a novel definition of the reconfigurable phase shifter, due to the fact that the use of PIN diodes becomes critical at these bands. Therefore, new switching methods have to be investigated for the application in such frequency bands. Promising results in the mm-wave range are given by new types of materials, like phase change materials, which can be used to operate as a conductor or an insulator (therefore working as a switch) by the application of an electrical or optical power signal.

Chapter 3

Frequency Reconfigurable Rat-Race Coupler

With the increase of multi-functional devices and integration of several wireless standards in a single system, nowadays several researches are focused on multi-band and miniaturized RF components (e.g. couplers, filters, phase shifters). The great demand of system integration is driven by the evidence that the size of RF passive components has experienced a limited reduction with respect to semiconductor wafer packaged components (e.g. chips). In fact, it well known from theory [228] that the physical dimensions of many aforementioned RF components, widely used in many antenna and RF circuits designs, is proportional to the wavelength, or more precisely, to the electrical length. In recent years, in most wireless applications the tendency is to move towards higher frequency bands (e.g. $5G$ communication systems for increasing the data-rate in mobile applications or the 77 GHz radar systems that are replacing the 24 GHz ISM band in automotive industry), thus leading to a reduction of the sizes of the passive components. Nevertheless, many essential and widespread applications are based on standards using frequencies below 2 GHz, that cannot benefit from the shift to higher frequency bands. Therefore, great attention is given to the realization of high performance and compact passive RF devices from the research community.

In this context, hybrid and rat-race couplers are essentials components, used in almost any application including RF circuits and antennas. They are conventionally composed by several sections of quarter wavelength transmission lines, and they are among the most demanding components in terms of PCB area. In particular, due to its planar structure, the rat-race coupler is a fundamental element in RF and microwave circuits, such as balanced mixers, power amplifiers and antenna feeding networks, offering the unique possibility to be used as in-phase or out-of-phase combiner. However, this coupler also exhibits well-known drawbacks, such as its large area and narrow bandwidth [229]. For these reasons, several studies have been focused on the size reduction, employing techniques such as slow wave structures,

metamaterials and folding technology (see e.g. [230–233]). Some research also focused on the long 270° branch, for reducing its impact on the overall dimensions [234–236]. Moreover, another important topic is represented by the design of multi-band and dual-mode rat-race couplers [237–239]. Typically, the dual band design shows a narrow fractional bandwidth and a limited size reduction. Nevertheless, despite the continuous request of reconfigurable components for supporting multiple frequency bands and different communication standards, limited effort was spent to introduce frequency reconfigurability on the rat-race coupler [240, 241].

The scope of this chapter is to propose a miniaturized and frequency agile rat-race coupler, that can be implemented in a single layer PCB and employing standard and inexpensive components and manufacturing processes. The reconfigurable operation is set at the two center frequencies of 900 MHz and 1.7 GHz, for including important industrial (e.g. RFID), satellite (e.g. GPS, Iridium) and mobile communication standards (e.g. GSM 900 and 1800 in both uplink and downlink) in the portion of the frequency spectrum below 2 GHz. Moreover, one of the targets driving this work is the introduction of a flexible design that can be suitable for low frequencies, potentially lower than the one proposed here (i.e. 900 MHz). For this reason, it has been considered the use of Artificial Transmission Lines (ATL) technique as slow wave structure, which are based on discrete components. In this way, any relation with physical and electrical length is removed, and a very compact and flexible design can be realized. As described in the chapter, the proposed method [242], represents a powerful solution to realize a transmission line with an almost arbitrary electrical length, based on a cascade of several metamaterial unit cells.

3.1 Artificial Transmission Lines

Slow wave structures are the key technique for achieving size reduction and/or multi-band operation [242, 243]. In general, the slow wave factor is designated as the ratio between the free space wavelength and the guided wave, therefore an enhancement of the slow wave factor is the key to miniaturize distributed RF components (e.g. antennas, filters, couplers). Taking into consideration RF passive components based on planar transmission lines, the size reduction is usually achieved by employing high dielectric constant materials [244] or by exploiting metamaterials [245–247] and/or periodic structures [246, 248]. In this research activity, for reducing the dimensions of the rat-race coupler, the four branches of the rat-race coupler are replaced by Artificial Transmission Lines.

In particular, the Artificial Transmission Line (ATL) is a periodic structure able to synthesize a transmission line, by reproducing the electrical length and the characteristic impedance which intrinsically characterize the transmission line. The unique feature of ATLs is the capability of realizing lines with almost arbitrary

electrical length, independently from the physical dimensions, based on the cascade of many unit cells. Therefore, the total phase incurred (or equivalently the electrical length) is controlled by the contribution of a single unit cell, multiplied by the total number of unit cells. In other words, a given transmission line with a specified electrical length can be synthesized by an ATL by setting a total number of unit cells and by defining the phase contribution for each cell, in such a way that the cascade of all cells is equivalent to the electrical length of the original transmission line. In Fig. 3.1 are depicted the two different types of ATLs elementary unit cells that will be used in the proposed design: the Right Handed Artificial Transmission Line (RH-ATL) and the Left Handed Artificial Transmission Line (LH-ATL). In particular, it is noticed from Fig. 3.1b that the RH-ATL basic unit cell is the conventional distribute equivalent circuit representation of a transmission line that can be found e.g. [228], with the difference that instead of distribute capacitance and inductance the lumped components will be used, and therefore a periodic analysis on this structure will be needed, in contrast with the commonly used transmission lines formulas. On the other hand, Fig. 3.1a displays the LH-ATL unit cell, which is the dual version of the RH-ATL unit cell.

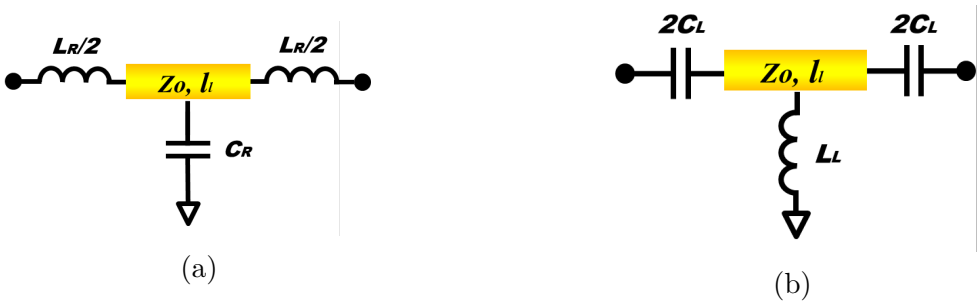

(a) (b)

Figure 3.1: Basic unit cells of the ATL periodic structure for (a) RH-ATLs and (b) LH-ATLs.

The LH-ATLs are metamaterial lines [242, 243], thus exhibiting a negative refractive index effect. Being both intrinsically dispersive transmission lines, they are characterized by different phase and propagation behaviour. Since it is a crucial point for the present work, the main phase and propagation parameters are first listed for purely Right Handed and Left Handed materials.

$$\beta_{RH} = \omega\sqrt{\mathcal{LC}} \tag{3.1}$$

$$\phi_{RH} = -\beta_{RH} l_{RH} = -\omega\sqrt{\mathcal{LC}} l_{RH} = -\theta_{RH} \tag{3.2}$$

$$\nu_{\phi,RH} = \frac{\omega}{\beta_{RH}} = \frac{1}{\sqrt{\mathcal{LC}}} \tag{3.3}$$

$$\nu_{g,RH} = \frac{d\omega}{d\beta_{RH}} = \frac{1}{\sqrt{\mathcal{LC}}} \qquad d_{g,RH} = \frac{1}{\nu_{g,RH}} = \frac{d\beta_{RH}}{d\omega} = \sqrt{\mathcal{LC}} \tag{3.4}$$

$$\beta_{LH} = \frac{-1}{\omega\sqrt{\mathcal{LC}}} \tag{3.5}$$

$$\phi_{LH} = -\beta_{LH} l_{LH} = \frac{1}{\omega\sqrt{\mathcal{LC}}} l_{LH} = -\theta_{LH} \tag{3.6}$$

$$\nu_{\phi,LH} = \frac{\omega}{\beta_{LH}} = -\omega^2\sqrt{\mathcal{LC}} \tag{3.7}$$

$$\nu_{g,LH} = \frac{d\omega}{d\beta_{LH}} = \omega^2\sqrt{\mathcal{LC}} \qquad d_{g,LH} = \frac{1}{\nu_{g,LH}} = \frac{d\beta_{LH}}{d\omega} = \frac{1}{\omega^2\sqrt{\mathcal{LC}}} \tag{3.8}$$

In particular, being $\omega = 2\pi f$ the angular frequency, and considering $\mathcal{L}$ and $\mathcal{C}$ a generic distribute inductance and capacitance, (3.1) expresses the propagation constant for the RH lines, while (3.5) defines the LH case. The phase attained by a section of transmission line can be calculated multiplying the propagation constant with the respective physical length (l_{RH} and l_{LH} in (3.2) and (3.6)). Another very important parameter of the transmission lines is their electrical length, which has the same magnitude as the phase, but it has opposite sign. Therefore, the total phase incurred by a RH line will be negative (see (3.2)), while it will be positive for LH structures, as in (3.6). From the comparison between (3.2) and (3.6), it is also observed that in the RH case the phase increases linearly with frequency, while for the LH case the phase is inversely proportional to frequency. Moreover, being a negative refractive index material, the LH line also exhibit negative phase velocity, in contrast with its counterpart, that has a positive phase velocity, as can be noticed from (3.7) and (3.3) respectively. For this reason the RH lines are also referred as forward-traveling wave lines and the LH are also called backward-traveling wave lines.

Regarding the behaviour in frequency, it is clear that RH lines have a constant phase velocity, while the LH lines have a strong variation in frequency, which is squared ($\sim \omega^2$). The same consideration for the behaviour over frequency of group velocity (inverse as group delay) can be made by analysing (3.4) and (3.8) for the RH and LH cases respectively. The aforementioned analysis on the main phase parameters of RH and LH lines is fundamental to understand the corresponding ATL versions, which share the same principal characteristics, but their dispersion relation has to be calculated using the periodic Bloch-Floquet analysis since they are realized by a cascade of unit cells made with lumped components. Moreover, as depicted in Fig. 3.1a, the LH-ATL is realized with series capacitors and shunt inductors (as purely LH line) embedded in a transmission line, which is inherently a RH element. Therefore, in the LH-ATL both the backward and forward wave behaviour are combined in the same structure.

The dispersion relation is a fundamental tool for understanding how the phase behaviour of a periodic structure is varying over frequency. Again, two different cases have to be distinguished, depending on the type of ATL that is considered.

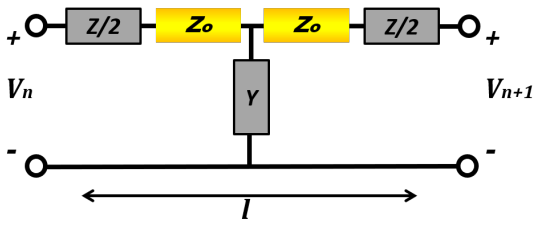

Figure 3.2: Generic $T-$type unit cell of a periodic artificial transmission line

For the calculation of the dispersion relation, an infinite periodic structure based on a generic T-type unit cell displayed in Fig. 3.2 is considered. The generic impedance Z and admittance Y are dependent on the type of unit cell (i.e. RH or LH), and they are realized by lumped components. The transmission lines connecting the lumped impedances have same characteristic impedance Z_0 and electrical length $\theta_l/2$, and the length of the cell (i.e. periodicity) is equal to l. The transfer function of such a circuit is found from the $ABCD$ matrix of the generic unit cell, treated as a two port network, which is calculated as the product of the $ABCD$ matrices of all single elements composing the unit cell. The $ABCD$ matrix relates the voltage and current at the input terminals of the $n-th$ unit cell to the same quantities at its output, which in turn are related to the adjacent unit cell $(n+1)-th$. Moreover, Floquet theorem states that a wave propagating along the periodic structure is modified after one cell (i.e. period) by the propagation factor $e^{-j\beta_c l}$, where β_c is the Bloch propagation constant relative to the unit cell. Therefore it is found in (3.9) that the propagation constant can be related to the $ABCD$ matrix through a linear system of equations in terms of V_{n+1} and I_{n+1}:

$$\begin{bmatrix} V_n \\ I_n \end{bmatrix} = \begin{bmatrix} A & B \\ C & D \end{bmatrix} \begin{bmatrix} V_{n+1} \\ I_{n+1} \end{bmatrix} = e^{-j\beta_c l} \begin{bmatrix} V_{n+1} \\ I_{n+1} \end{bmatrix} \tag{3.9}$$

By calculating the determinant of the ABCD matrix and considering just the non-trivial solutions, it is found the dispersion relation of the $T-$type unit cell is expressed as:

$$\cos(\beta_c l) = \left(1 + \frac{Z\ Y}{4}\right) cos(\theta_l) + \frac{j}{2}\left(\frac{Z}{Z_0} + Y\ Z_0\right) sin(\theta_l) + \frac{Z\ Y}{4} \tag{3.10}$$

In (3.10), the symmetry of the unit cell is exploited leading to the equality $A = D$. As suggested in [242], the characteristic impedance of the ATL is set equal to the Bloch impedance Z_{BL}. This is done in order to avoid stopbands as found in the ideal case, for the LH case. With this background, the dispersion relation for the RH $T-$type unit cell is found by substituting the inductor L and capacitor C to the generic impedances Z and Y respectively, according to Fig. 3.1b. Conversely, for an LH-ATL the definition is dual, and therefore the impedance Z corresponds

to the capacitor C and the admittance Y to the inductor L, as in Fig. 3.1a. The aforementioned description is summarized in the following Table 3.1, for clarity:

Table 3.1: Circuital Definition of the ATL $T-$type Unit Cell

RH-ATL	**LH-ATL**
$Z = j\omega L$	$Z = \dfrac{1}{j\omega C}$
$Y = j\omega C$	$Y = \dfrac{1}{j\omega L}$

3.2 Miniaturized Rat-Race Design Concept

As anticipated in Sect. 3.1, the dual periodic artificial transmission lines RH-ATLs and LH-ATLs are exploited for considerably reducing the overall dimensions of the rat-race coupler.

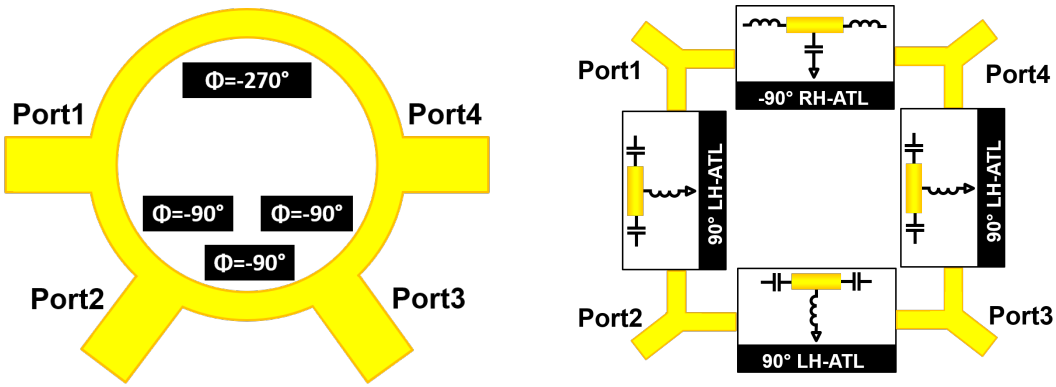

(a) (b)

Figure 3.3: Schematic representation of the (a) standard and (b) proposed rat-race design.

Figure 3.3b illustrates the concept leading the design of the miniaturized rat-race coupler, comparing it with the standard design, shown in 3.3a. For better understanding, the electrical length of the four branches, for both cases, has been reported. Moreover, Fig. 3.3b indicates also the type of ATL unit cells (i.e. either RH or LH) composing the branches of the proposed structure. According to Fig. 3.3b, it is here proposed to synthesize the +90° branches of the rat-race coupler by means of LH-ATLs, and, by exploiting the duality between the phase contributions of RH-ATLs and LH-ATLs (which are opposite in sign, as seen by comparing (3.2) and (3.6)), the -90° RH-ATL is used instead of the long 270° branch. Thus, by

exploiting the opposite phase advancing of RH-ATL and LH-ATL, the intrinsic 180° phase difference is obtained, and therefore a quarter wave line is sufficient to compose the rat-race coupler. By this assumption, it is possible to avoid the use of a high number of unit cells that would increase losses and reduce the bandwidth. It is noticed that the 270° branch is crucial for achieving the 50 Ω condition in all ports and for realizing the sum/differential feature of this particular coupler.

Many publications already focused on reducing the physical dimensions of the 270° branch, mostly employing phase inversion [236]. In particular, in [234], a similar approach was used, but it results on a moderate size reduction of the rat-race. The proposed concept, instead, will achieve a remarkable miniaturization of the rat-race coupler. Moreover, another important aspect is the range of frequencies at which this concept can be used. It is noticed that the use of lumped components makes it potentially easier to be applied at low frequencies rather than higher ones, where distributed components and structures can be easily implemented. However, this is in line with the scope of the present research.

3.3 Frequency Reconfigurability

In the previous paragraph, the method employed to reduce the size of the rat-race coupler has been discussed, however, the main goal of this research is related to the application of the frequency reconfigurability. Therefore, in the proposed design, the combination of LH-ATLs and RH-ATLs is used as basis for applying the frequency agility. The key principle consists of inserting or removing LH/RH unit cells for attaining the desired electrical length at the specific design frequency. In fact, compared to standard microstrip delay line solutions, the periodic composition of ATLs offers an easy way to define and control the attained phase, realizing a very flexible and simple structure where cells can be used to add/remove a well defined phase quantity, releasing the design to any concern about physical size. Moreover, the cell can have same physical dimension, but attaining different phase values, either positive or negative. Then, again the opposite sign of the phase contributions related to LH-ATLs and RH-ATLs can easily introduce consistent manipulation of the overall electrical length of the transmission line, as demonstrated for the 270° line replacement. As a result, the proposed method allows to theoretically synthesize a multi-band rat-race with arbitrary frequency ratio, in contrast with dual-band solutions which have a ratio between the two operative center frequencies of ~ 2. It is noticed that a particular case occurs when one center frequency is the double of the other: in this special case the phase per unit cell is the same in both cases, just the total number of unit cell is doubled. However, in the proposed design, a two band operation is realized by selecting two unrelated center frequencies.

3.3.1 Switches as Reconfigurability Element

The described method allows to theoretically synthesize a multiband rat-race whose two or more center frequencies can be independently selected. The reconfigurability of the rat-race coupler is realized by using reflective type CMOS switches. These components represent a very convenient solution for many applications, including industrial and measurement equipment ones, due to their digital controls and their very low current consumption, while operating at high maximum power rates. The latter aspect is a clear advantage compared to other silicon based solutions, as varactors and PIN diodes. As a remark, the switches impose a scheme on the possible arrangement/reconfiguration that can be achieved, so particular care has to be taken on their usage. However, the massive request of integrated RF systems from the market (especially regarding antenna switching for 5G carrier aggregation, for MIMO applications and for aperture/matching tuning) has contributed to the developments of novel solutions which are moving from the common $SPXT$ type to a $DPXT$ or even $X \times SPST$, thus being more similar to integrated switching matrices. For the implementation of the reconfigurable rat-race coupler two different types of switches are needed: with reference to Fig. 3.3b on the three +90° branches (based on LH-ATLs) a Double-Pole Double-Throw ($DPDT$) transfer switch is needed, while for the -90° branch (based on RH-ATLs) a synchronous $2\times SPDT$ switch is required. Unfortunately, these kinds of switches that are available on the market are intended for 50 Ω applications only. Therefore, it is expected an impedance discontinuity in the rat-race branches since their impedance is well known to be $\sqrt{2} \cdot Z_0$, which is approximately equal to 70.7 Ω with $Z_0 = 50\,\Omega$ the characteristic impedance of the system. Moreover, as the frequency increases, the effect of the impedance discontinuity become more dominant, and, for this reason, in this realization the maximum working frequency is limited at around 2 GHz, where the impedance discontinuity is still acceptable.

3.4 Design of the Reconfigurable ATL Based Branches

The designs of the +90° branch and -90° branch of the rat-race coupler are here described. According to the scheme reported in Fig. 3.3b, the +90° branch is realized as a cascade of LH-ATL unit cell, while in the dual case of the -90° branch the RH-ATL unit cells are used. Moreover, switches are embedded in the periodic network for increasing/decreasing the electrical length, in order to select between the two operative bands, with center frequencies f_1 and f_2, with $f_2 > f_1$. The aforementioned configurations are analyzed in detail in the following.

3.4.1 Reconfigurable +90° Branch based on LH-ATL

The miniaturization through ATLs imposes to establish a number of cells to be used, for calculating the required phase per unit cell from the dispersion relation reported in (3.10). Therefore, for enhancing miniaturization, the minimum number of unit cells used is set to $n = 2$. It is noticed that the analysis previously made for the periodic lines still holds in this case, even if just two unit cells are used. In fact, due to the definition of the $ABCD$ matrix found following the Bloch analysis described in Sect. 3.1, from which the dispersion relation is then calculated, the ATL is completely specified in terms of loading components (i.e. capacitors C and inductor L), length and characteristic impedance (equal to Bloch impedance) of the microstrip line and the total number of unit cells. In Fig. 3.4 it is illustrated the principle of operation of the frequency reconfigurable +90° branch based on LH-ATLs when the f_1 center frequency band is selected. The internal connections realized by the switch in this configuration are also depicted, highlighting that for operating in the f_1 frequency band a direct connection is used to bypass the unused cells, and reach the branch termination.

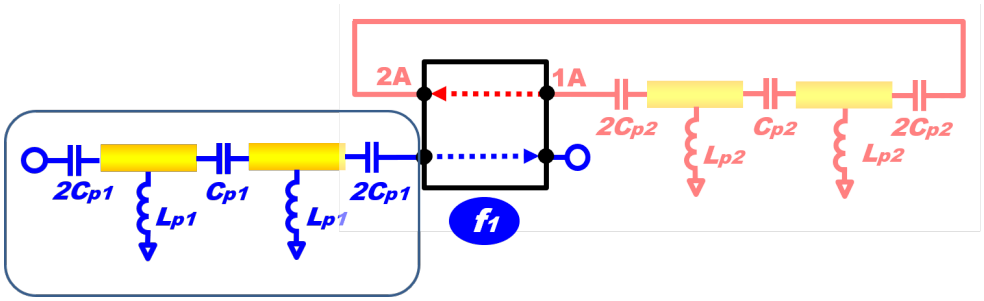

Figure 3.4: Configurations of the +90° frequency reconfigurable branch in the cases of f_1 center frequency band. The unit cells which are set inactive by the switch are shadowed.

The choice of setting as basis for the reconfigurability the configuration at lower frequency f_1 has its reason on the high-pass nature of the LH-ATL: in fact, it is assumed that the cut-off frequency for the LH-ATL designed at f_2 is above the frequency f_1, and therefore high losses can occur. The inner capacitor C_2 has a value of C_{p1} which is half of the capacitance positioned at the extremes of the realized LH-ATL structure; this is congruent with the analysis performed in Sect. 3.1 for the determination of the dispersion relation, and it can be easily proven by introducing the correct definition of the Z and Y in the generic unit cell depicted in Fig. 3.2, following the indications listed in Table 3.1. Therefore, the phase equation needed for calculating the required phase per unit cell is found by adding all the phase contributions on the highlighted branch in Fig. 3.4, including the switch, and by imposing the 90° condition at frequency f_1, as accomplished in (3.12).

In order to count for all the terms for the center frequency f_1, the phase delay (with negative sign) attained by the switch is defined to be equivalent to a 50 Ω line with phase constant $\beta_s(f_1)$ and physical length l_s. Similarly, the phase induced by the microstrip lines hosting the components are expressed through the phase constant $\beta_l(f_1)$ and by the physical length l_l (this terms corresponds to θ_l in (3.10)). The phase per unit cell $\varphi_1^+(f_1)$ for the operative frequency f_1 is reported in (3.11), where the effect on the phase given by the line (negative) and by the LH cells, composed by inductors L_{p1} and capacitors C_{p1}, (positive) can be distinguished. Clearly, $\varphi_1^+(f_1)$ corresponds to the term $\beta_c l$ in (3.10), where β_c is the propagation constant (i.e. Bloch propagation constant) of the LH-ATL unit cell.

$$\varphi_1^+(f_1) = \frac{1}{\omega_1\sqrt{L_{p1}C_{p1}}} - \beta_l(f_1)\ l_l \tag{3.11}$$

$$n\ \varphi_1^+(f_1) - \beta_s(f_1)\ l_s = \frac{\pi}{2} \tag{3.12}$$

The phase per unit cell is found after straightforward manipulations, reported in the Appendix A, and it is declared in (3.12), where the values of components C_{p1} and L_{p1} are derived by replacing the aforementioned quantities $Z = 1/j\omega C_{p1}$, $Y = 1/j\omega L_{p1}$ and $\beta_c l = \varphi_1^+(f_1)$ in (3.10). Again, in the calculation it is used the condition $L_{p1} = C_{p1} \cdot Z_{BL}^2$ with Z_{BL} Bloch impedance, equal to the characteristic impedance of the line.

The frequency agility is achieved by adding further LH-ATL unit cells, operated by changing the state of the *DPDT* transfer switch, as shown in Fig. 3.5, where the switch is functioning in crossing mode.

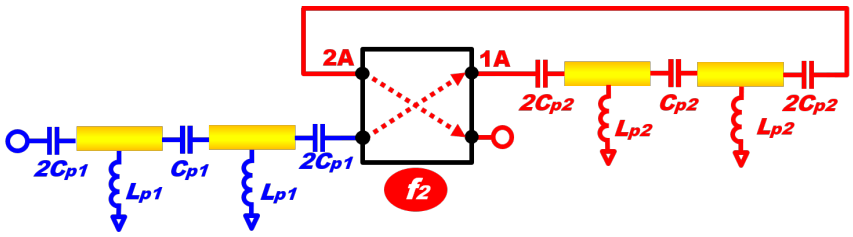

Figure 3.5: Configurations of the +90° frequency reconfigurable branch in the cases of f_2 center frequency band.

The introduced cells are required to achieve the 90° phase condition at the higher frequency f_2. It is noticed that this aspect is in contrast with standard RH lines approach, where electrical length increases linearly with frequency, and its explanation derives from the theory of the LH lines. In fact, the phase contribution of the RH lines is proportional to the angular frequency ω, whereas for LH lines, it is inversely proportional (i.e. $\sim 1/\omega$). This leads to the conclusion that, as the frequency increases, a smaller $\sqrt{L_x C_x}$ factor or equivalently more unit cells

are needed for restoring the 90° condition. Furthermore, in the case under study m_1 =2 unit cells are added to the n =2 cells already constructed. Therefore, similarly to the procedure elucidated in the case of the 90° branch at f_1, all the phase contributions are summed, leading to the equation shown in (3.13):

$$m_1\ \varphi_2^+(f_2) - 2\ \beta_s\,(f_2)\ \ l_s + n\ \varphi_1^+\,(f_2) = \frac{\pi}{2} \tag{3.13}$$

where

$$\varphi_2^+(f_2) = \frac{1}{\omega_2\sqrt{L_{p2}C_{p2}}} - \beta_l(f_2)\ l_l \tag{3.14}$$

is the phase per unit cell of the added section, composed by the microstrip line and the purely LH term, composed by the lumped components L_{p2} and C_{p2}. It is noticed that in this case the delay caused by the transfer switch, operating in crossing mode, is multiplied by two, due to the crossing configuration of the *DPDT* transfer switch, as illustrated in Fig. 3.5. The phase delay introduced by the switch has to be compensated, since it has a negative phase advancement. This also means that as the frequency increases, more phase contribution from the LH-ATLs is required. Clearly, in the case of an electrically long switch, the mentioned aspect can negatively affect the overall performance.

The procedure for calculating L_{p2} and C_{p2} is similar to the previous case at f_1. The required phase per unit cell $\varphi_2^+\,(f_2)$ needed to fulfill the phase condition is found from (3.13) and, by using the dispersion relation in (3.10) and the Bloch impedance condition, the newly introduced unit cell is fully specified.

3.4.2 Reconfigurable -90° Branch based on RH-ATL

A different procedure is applied for the design of the -90° branch that replaces the long 270° section of the rat-race coupler. Being this the dual version of the +90° branch, due to the usage of the RH-ATLs instead of LH-ATLs, more cells are needed to achieve -90° phase condition at f_1. In order to avoid the cut-off, the f_2 operation is considered first as basis line. However, before proceeding with the application of the phase condition for achieving the -90° phase of the RH-ATL, an analysis of the group delay (or equivalently the group velocity) is required. It has already been stated in Sect. 3.1 that the group velocities, reported in (3.4) for the RH case and in (3.8) for the LH lines, exhibit a very different characteristic over frequency. As can be noticed from the formulation displayed in the previous sections, for the RH line the group delay $d_{g,RH}$ is constant, while its dual version $d_{g,LH}$ is squared with respect to the inverse of frequency (i.e. $\sim 1/\omega^2$). This highly dispersive behaviour of the LH lines, and similarly for the LH-ATLs, is responsible for the narrowband behaviour of the rat-race coupler (i.e. the phase variation as a function of frequency between the +90° and -90° branch is very steep). In order to mitigate this effect, and ensuring a wide band characteristic, the group delay of the -90° RH-ATL branch

has to be as close as possible to the one given by the +90° LH-ATL branch designed in Sect. 3.4.1, leading to the condition $d_{g,RH-ATL}(f_2) = d_{g,LH-ATL}(f_2)$. As already noticed, for RH-ATL the derivative of the total phase condition is constant with respect to $\omega_2 = 2\pi f_2$ (i.e. $d_{g,RH-ATL}(f_2) = const$), therefore the only way to reach the same variation of $d_{g,LH-ATL}$ over frequency is to introduce an LH-ATL contribution, named as Phase Balancing Term (PBT). The PBT can modify the group delay of the RH-ATL for being conformal with the LH-ATL branch at the frequency of interest. Therefore, $\varphi_2^C(f_2)$ is the phase contribution of the newly introduced PBT, specified in (3.15).

$$\varphi_2^C(f_2) = \frac{1}{\omega_2\sqrt{L_{p3}C_{p3}}} - \beta_l(f_2)\, l_l \tag{3.15}$$

According to Fig. 3.6, the PBT is composed of m_2 =1 cell and it is connected to $n = 2$ RH-ATL unit cells (same as the +90°, for symmetry) through the synchronous $2\times SPDT$ switch. Due to the particular use of the switch, which can be considered as a "cell selector", the delay caused by this component is multiplied by two.

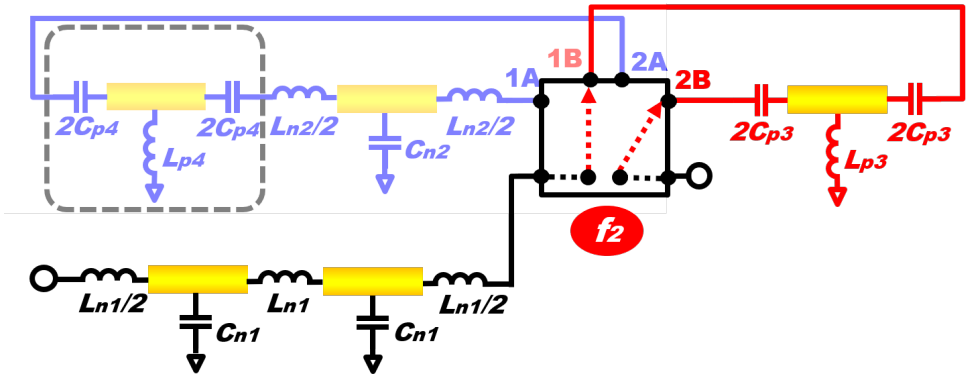

Figure 3.6: Configurations of the -90° frequency reconfigurable branch in the cases of f_2 center frequency band,including also the Phase Balancing Term. The unit cells which are set inactive by the switch are shadowed.

The phase per unit cell for the RH-ATL at frequency f_2 is indicated with $\varphi_2^-(f_2)$ and it is defined in (3.16):

$$\varphi_2^-(f_2) = -\beta_l(f_2)\, l_l - \sqrt{L_{n1}C_{n1}} \tag{3.16}$$

The total phase condition for the -90° branch is reported in the following equation:

$$n\ \varphi_2^-(f_2) - 2\,\beta_s(f_2)\, l_s + m_2\ \varphi_2^C(f_2) = -\frac{\pi}{2} \tag{3.17}$$

The PBT term is evaluated by imposing the equality on the derivatives with respect to ω_2 of the total phase conditions (3.13) and (3.17), which is equivalent to impose

the group delay equality at f_2 of the +90° and -90° branches. After some manipulations, reported in Appendix A, the phase per unit cell required for imposing the phase balancing is given by (3.18):

$$\varphi_2^C(f_2) = \frac{1}{m_2}\left[2\ \beta_s(f_2)\ \ l_s + (m_1 + n - m_2)\ \ \beta_l(f_2)\ l_l\right] \tag{3.18}$$

After having specified the phase contribution per unit cell of the PBT $\varphi_2^C(f_2)$, the values of C_{p3} and L_{p3} are calculated via (3.10) as for the cases of LH-ATL branches described in Sect. 3.4.1. By introducing the phase value of $\varphi_2^C(f_2)$ in the -90° phase condition at f_2 reported in (3.17), the required phase per unit cell $\varphi_2^-(f_2)$ is calculated and, finally, L_{n1} and C_{n1} are computed using again (3.10). During the last operation, the proper impedance and admittance are inserted as specified in Table 3.1 (i.e. $Z = j\omega L_{n1}$, $Y = j\omega C_{n1}$).

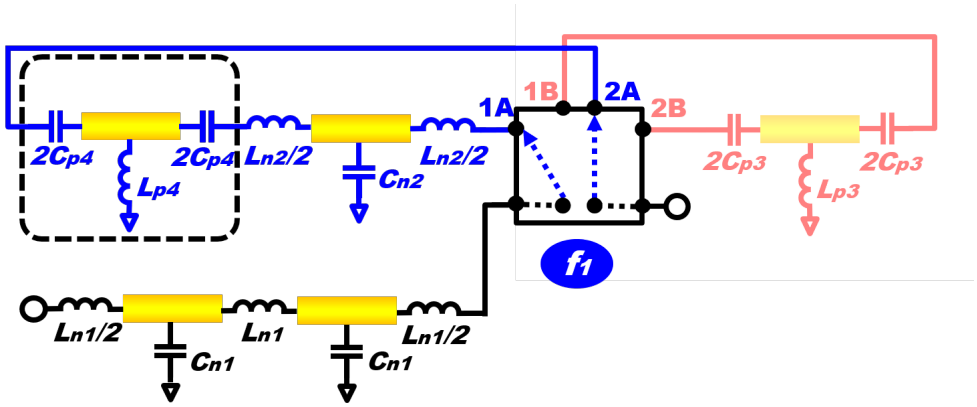

Figure 3.7: Configurations of the -90° frequency reconfigurable branch in the cases of f_1 center frequency band. The Phase Balancing Term is enclosed by a dashed line box. The unit cells which are set inactive by the switch are shadowed.

The second state of the switch inserted in the -90° RH-ATL branch is devoted to achieve the required phase condition (i.e. -90°) at lower frequency f_1. As already mentioned, this operation involves the addition of more RH-ATL unit cells, since these terms are linearly dependent with frequency (i.e. $\sim \omega$). Therefore, as clarified in Fig. 3.7, the switch is used here to introduce further RH unit cells for compensating the gap given by the lower frequency operation of the fixed RH-ATL unit cell previously designed (i.e. $\varphi_2^-(f_1)$). Likewise to the previous analysis, the total phase condition for the -90° branch at f_1 is specified in (3.19),

$$-n\,\varphi_2^-(f_1) - 2\,\beta_s(f_1)\,l_s + m_3\,\varphi_1^-(f_1) + m_4\,\varphi_1^C(f_1) = -\frac{\pi}{2} \tag{3.19}$$

$$\varphi_1^-(f_1) = -\beta_l(f_1)\ \ l_l - \omega_1\sqrt{L_{n2}C_{n2}} \tag{3.20}$$

where $\varphi_1^-(f_1)$ is the phase of a single cell. In this case, only one unit cell is added for reaching the desired condition, thus imposing m_3 =1.

By considering a very general approach, the PBT has been inserted in (3.19), even if it is expected that at the lower frequency band the group delay difference is less critical. In this case the PBT is specified by (3.21), and it is enclosed in a dashed line box in Fig. 3.7. As can be noticed from both (3.19) and Fig. 3.7, the number of unit cells for the PBT at f_1 is chosen to be m_4 =1.

$$\varphi_1^C(f_1) = \frac{1}{\omega_1\sqrt{L_{p4}C_{p4}}} - \beta_l(f_1)\ l_l \tag{3.21}$$

The calculation involving the group delays equality at center frequency f_1 are reported in Appendix A, leading to the expression of the phase $\varphi_1^C(f_1)$ required by the PBT cell (3.22).

$$\varphi_1^C(f_1) = \frac{1}{m_4}\left[\beta_s\,(f_2)\,l_s + (n{-}m_4)\,\beta_l(f_1)l_l\right] \tag{3.22}$$

At this stage, the inductors L_{n2}, L_{p4} and capacitors C_{n2}, C_{p4} loading the RH-ATL and PBT cells respectively, are calculated by applying (3.10) with the proper phases per unit cell and impedances as reported in Table 3.1.

3.5 Manufactured and Measured Reconfigurable Rat-race Coupler

A frequency reconfigurable rat-race coupler has been manufactured by employing the method described in Sect. 3.4 for the design of the two types of branches.

The two operative frequency bands have been chosen to be f_1 = 900 MHz and f_2 = 1.7 GHz, therefore including many important industrial standards (e.g. RFID, LoRA), satellite (e.g. GPS, Iridium) and mobile communication standards (e.g. LTE 900 and 1800 in both uplink and downlink). It is noticed that almost all of these applications requires a high degree of integration and a cost-effective solution. It is also remarked that the switching system is advantageous even for two different applications, like RFID and LoRA: for the first case, the high power transmission is allowed by most CMOS switches available on the market, while for the Internet of Thing application, the power consumption is a critical aspect, and again CMOS switches exhibit a low power consumption (typically current consumption on the order of $\sim$1μA). Another important aspect for the targeted applications is related to the fabrication process: the proposed method, based on planar transmission lines, can be realized in a standard PCB with single layer process, potentially using any dielectric material.

The general guideline imposed by theory, that recommends $\beta_l l_l \ll 1$, is truly an advantage here, and furthermore by keeping the electrical length of the microstrip

line small also the effect of substrate become less important. With the goal of obtaining a very compact design, the sections of microstrip line loading the SMD components have length $l_l = 2.5$ mm, which also satisfy the $\beta_l l_l \ll 1$ condition. As crucial part of the design, two switches from *Qorvo* have been selected for operating the frequency reconfigurability. The *QPC6222* Double-Pole Double-Throw transfer switch [249] is embedded in the +90° branch, while the *RFSW6232* synchronous $2\times SP3T$ switch [250] is used in the -90° branch of the coupler. The choice of using the latter switch is due to the favourable position of the input pins, with respect to the $2\times SPDT$ version of the same component family (i.e. *RFSW6222*), which allow to greatly optimize the final layout of the reconfigurable rat-race coupler, even if one switching position remains unused. Both switches can withstand quite high power (up to 35 dBm) in a small 2×2 mm plastic package.

An important asset of the proposed design includes the use of just one control signal (i.e. 1-bit for controlling the two bands operation). According to the analysis performed in Sect. 3.4, the phase incurred by the switches has been characterized through measurements, and for both components has been found to be equivalent to a 50 Ω line with length $l_s = 5.6$ mm. In the circuital simulation model of the rat-race, the losses of the switch have been considered as equivalent to an attenuator (magnitude 0.27 dB for the *QPC6222* and 0.33 dB for the *RFSW6232*). It is noticed that the chosen switches have a very good return loss (better than 25 dB) and an isolation of more than 23 dB in the two frequency bands of operation, therefore the choice of modelling these components as a transmission line does not introduce critical errors in the model, while preserving a simple definition.

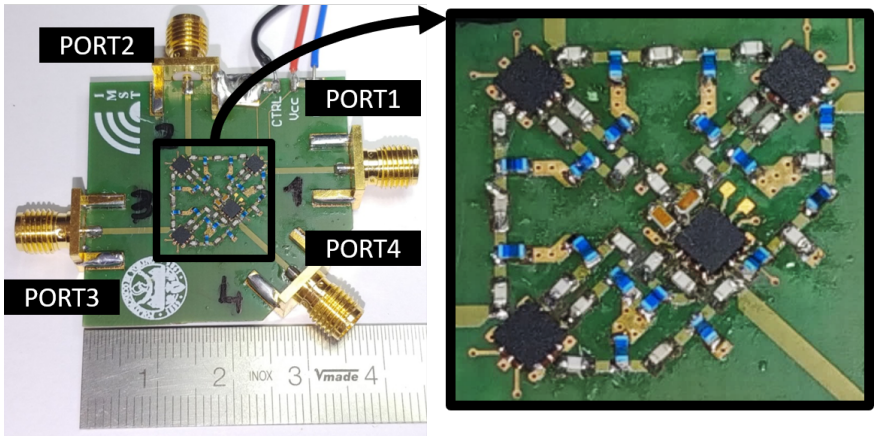

Figure 3.8: Manufactured and assembled reconfigurable rat-race coupler; an enlargement of the RH-ATL and LH-ATL with switches is provided on the right side.

Moreover, the application of the equation (3.22) with $f_1 = 900$ MHz confirms that the PBT in this frequency band (enclosed by dashed line in Fig. 3.7) can be neglected, thus allowing a more compact design. As a result, in the -90° branch

the switch selects either the PBT unit cell for the 1.7 GHz center frequency band or the RH-ATL cell for achieving the 90° phase condition at 900 MHz. Therefore, the proposed solution has been manufactured on inexpensive 0.5 mm thick FR4 substrate, characterized by $\varepsilon_r = 4.4$ and $\tan\delta = 0.02$. The manufactured and measured compact frequency-agile rat-race coupler for the frequencies $f_1 = 900$ MHz and $f_2 = 1.7$ GHz is shown in Fig. 3.8 where also an enlargement of the final structure is provided.

3.5.1 Reconfigurable Branch Based on ATL

As first step, the performance of the two branches are evaluated in both the $f_1 = 900$ MHz and $f_2 = 1.7$ GHz configurations, reported in Fig. 3.9.

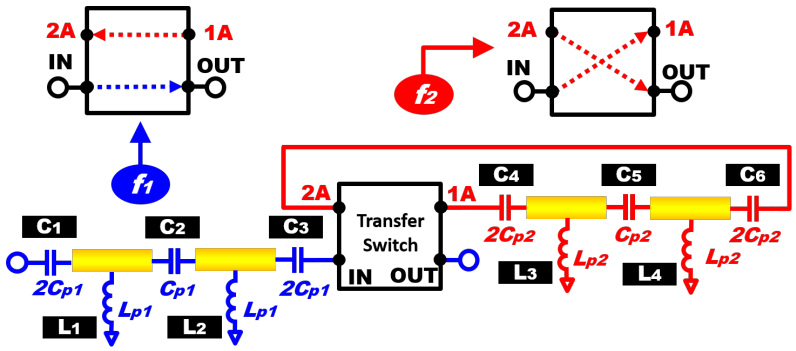

(a)

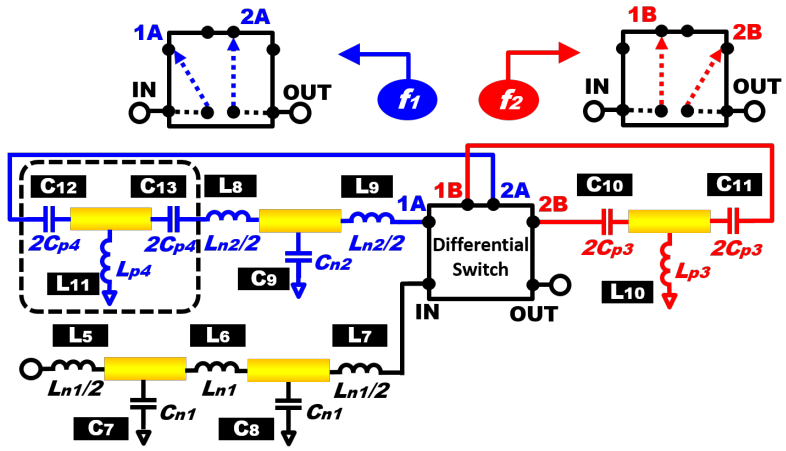

(b)

Figure 3.9: Both the frequency agile +90° and -90° branches in both configurations are reported, including the identifier of each component. The topology of connections is also reported for the two switches.

The procedure for the determination of the inductors and capacitors loading the

microstrip lines described in Sect. 3.4 has been employed, and the theoretical values found have been rounded and adjusted in order to meet commercial components availability. This aspect is more critical for inductors, which have a coarser range of available values. Moreover, the *muRata* component library has been used in the circuit simulation, performed using Advanced Design System (ADS). Furthermore, high quality wire wound inductors series *LQW15* (*LQP15* are also used, but only for values of inductance below 2.2 nH) and multilayer high-Q capacitors *GJM15* have been included in the simulations.

In order to test and validate the proposed method concerning the phase characteristics in both frequency states, a separate test board including the two reconfigurable branches of the rat-race coupler (i.e. the +90 and -90° branches depicted in Fig. 3.9) was manufactured and measured. Thank to this board, the phase and impedance matching conditions of the two branches in the two operative states were evaluated and further optimized by fine tuning the values of components. This process was necessary for covering the inaccuracies of the model of the discrete components, which have the well known drawbacks of value tolerances and non-idealities that introduces errors in the final development of the rat-race coupler. As final remark, according to availability, tight tolerance components were used, in order to reduce the uncertainty of the designed structures and being stable over manufacturing. Referring to the notation reported in Fig. 3.9, Table 3.2 displays the final values assembled in the manufactured reconfigurable rat-race coupler.

Table 3.2: Values of Components Loading the RH-ATLs and LH-ATLs

<table>
<tr><th>Frequency</th><th>90° Branch</th><th colspan="2">-90° Branch</th></tr>
<tr><td rowspan="2">900 MHz</td><td rowspan="2">$C_1 = C_3 = 4.7\,pF$
$C_2 = 2.5\,pF$
$L_1 = L_2 = 13\,nH$</td><td rowspan="3">$L_5 = L_7 =$
$2.7\,nH$
$C_7 = C_8 = 1\,pF$
$L_6 = 5.6\,nH$</td><td>$L_8 = L_9 = 1\,nH$
$C9 = 0.3\,pF$</td></tr>
<tr><td rowspan="2">1.7 GHz</td><td rowspan="2">$C_4 = C_6 = 2.5\,pF$
$C_5 = 1.2\,pF$
$L_3 = L_4 = 6.8\,nH$</td><td>$C_{10} = C_{11} =$
$2.3\,pF$
$L_{10} = 5.1\,nH$</td></tr>
</table>

In the following, the results of the simulated phase and amplitude difference, obtained in ADS including the available component libraries, are compared with the respective measurements of the reconfigurable lines including the switch. In particular, the phase and amplitude differences are defined as the magnitude and phase ratio of the $S-$parameters related to the +90° and -90° branch respectively. The phase difference is an important result since it gives an insight on how the solution employing the LH-ATLs and RH-ATLs represents a good replacement for the 270° branch, which is responsible for the "difference" operation of the rat-race coupler. Moreover, it gives a good estimation of the bandwidth, by evaluating in which frequencies the phase difference is close to the theoretical value of 180°.

On the other hand the amplitude difference is also an important parameter to be checked, because it shows the different losses associated with the two branches in the two states. In the results displayed in Fig. 3.10 for the lower frequency state of 900 MHz, a very good agreement of the simulated and measured results is noticed for the magnitude difference between the two branches.

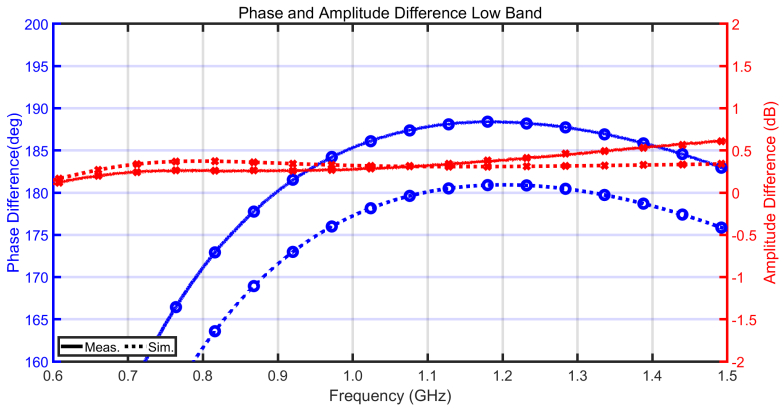

Figure 3.10: Measured and simulated amplitude and phase imbalance (solid and dashed lines respectively) related to the +90° and -90° branches operating at center frequency of 900 MHz.

From this result it can be noticed that the LH-ATL is slightly more lossy than the RH-ATL, since in the latter case the loss of the switch is counted twice (see Sect. 3.4.2). The phase error among simulated and measured phase is quite constant and approximately equal to 8°. It can also be recognized that in the measured phase difference the perfect 180° condition is obtained at the single frequency of 900 MHz (center band).

Figure 3.11 displays the case of the higher frequency band, centered at 1.7 GHz, where the amplitude error is more evident and mostly driven by the losses of the components and the switch crossing path in the LH-ATL (linearly increasing with frequency). However, the phase difference shows a large ±5° band, ranging from 1.4 GHz to approximately 2.17 GHz. This result is due to the application of the PBT unit cell, which demonstrates the efficacy of the proposed method.

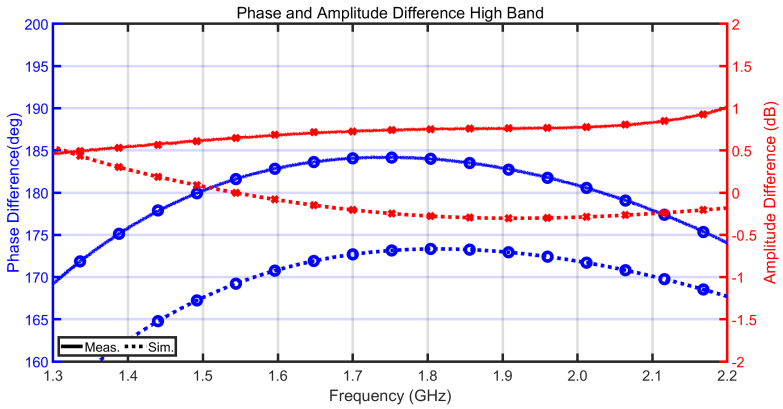

Figure 3.11: Measured and simulated amplitude and phase imbalance (solid and dashed lines respectively) related to the +90° and -90° branches operating at center frequency of 1.7 GHz.

3.5.2 Frequency Reconfigurable Rat-Race Coupler

The $S-$parameters of the complete reconfigurable rat-race coupler, in the two frequency bands, are evaluated in out-of-phase operation (*Port1* excited, referring to the nomenclature of Fig. 3.8). Moreover, the phase and amplitude difference are also calculated, for a better characterization of the proposed solution. From Fig. 3.12, a good agreement between measured and simulated $S-$parameters is observed for the 900 MHz band, with a maximum deviation of 0.38 dB in the entire band. The measured reflection coefficient is slightly higher than the simulated one, while the opposite consideration is made for the port-to-port isolation.

The phase and amplitude difference for the complete system is shown in Fig. 3.13, where the simulated results are confirmed by the measurements. However, compared to the results displayed in Fig. 3.10, in this case the total phase error is quite low, with a maximum deviation of 3.5°, while the error in magnitude has a maximum of 0.5 dB at 1.2 GHz. Nevertheless, the operative bandwidth, estimated following both the ±0.5 dB and the ±5° criterions indicate a quite wide band behaviour of the realized rat-race, even without the use of the phase balancing term.

Similarly, the same analysis is made for the case of the rat-race reconfigured to operate at the higher frequency band (center frequency 1.7 GHz). Therefore, as reported in Fig. 3.14, the discrepancies between simulated and measured quantities are more prominent, and a slight shift of the measured $S-$parameters toward lower frequencies is found. The out-of-band operation, located at frequencies below 1.4 GHz, indicates that the main source of error between simulation and measurement is due to the model of the components, which are probably less accurate for lower

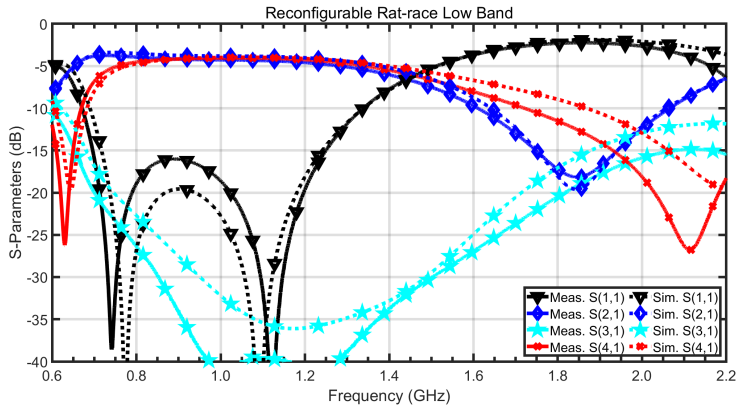

Figure 3.12: Measured and simulated (solid and dashed lines respectively) phase/amplitude imbalance with *Port1* excited for the lower frequency band centered at 900 MHz.

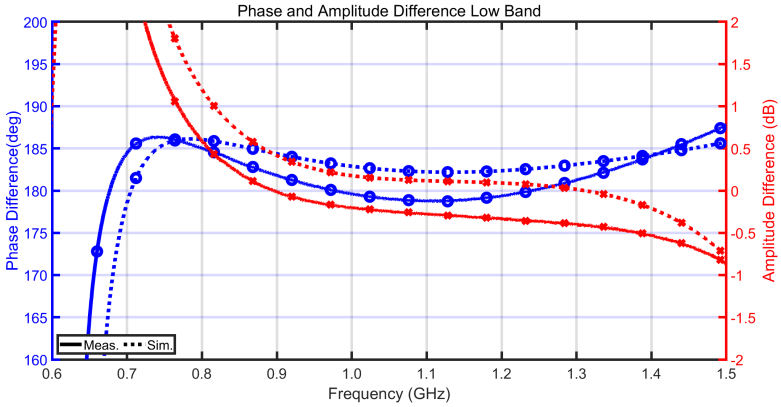

Figure 3.13: Measured and simulated (solid and dashed lines respectively) phase/amplitude imbalance with *Port1* excited for the lower frequency band centered at 900 MHz.

values of inductance and capacitance (used in the higher band configuration).

Furthermore, in Fig. 3.15, a wideband behavior of the phase imbalance $\angle S_{12} - \angle S_{14}$ are reported for the 1.7 GHz band, with an absolute error between measurement and simulation of 6.2°. However, it is noticed that the bandwidth at 1.7 GHz is narrower than the 900 MHz case reported in Fig. 3.13: this is mostly due to the effect of the switches, which are directly related to the phase contribution of the PBT, as revealed by the formulas (3.22) and (3.18). Moreover, the flattening

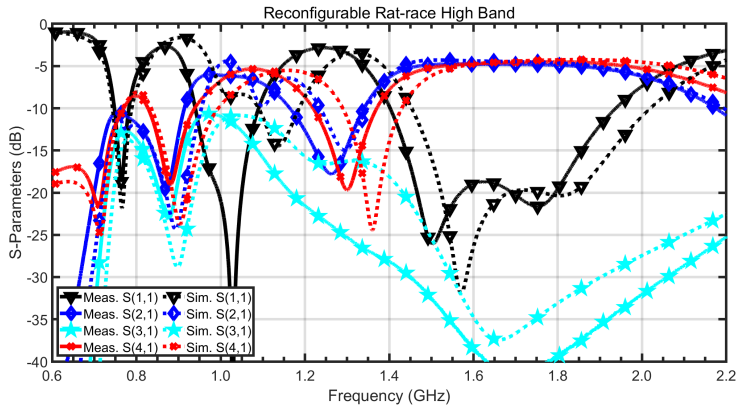

Figure 3.14: Measured and simulated (solid and dashed lines respectively) phase/amplitude imbalance with *Port1* excited for the higher frequency band centered at 1.7 GHz.

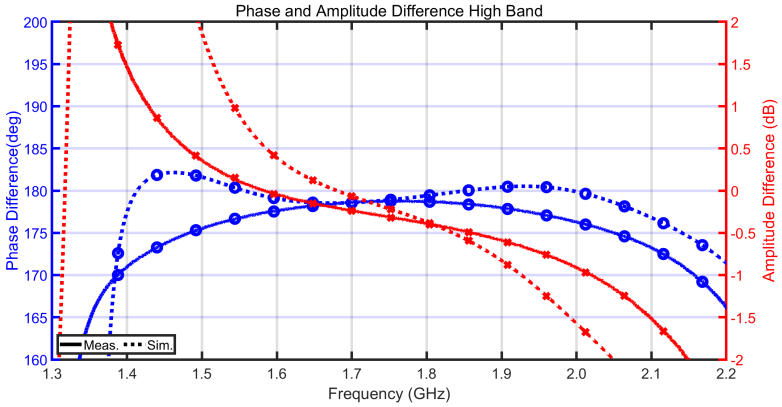

Figure 3.15: Measured and simulated (solid and dashed lines respectively) phase/amplitude imbalance with *Port1* excited for the higher frequency band centered at 1.7 GHz.

effect of the phase due to the PBT is evident in this case, according to the characterization of the rat-race reconfigurable branches operating at 1.7 GHz performed in Sect. 3.5.1. By considering the differential amplitude between $|S_{12}|$ and $|S_{14}|$, shown in Fig. 3.15, a quite high deviation between measurement and simulation is noticed, especially considering the lowest part of the 1.7 GHz operative band. This is mainly due to the shifting in frequency already mentioned by considering the $S-$parameters, which causes a steep increase of the error between the measured and simulated results. It can be concluded that the described discrepancies

between measured and simulated results have origin in the inaccuracy of the model of the components available in the *muRata* ADS library, including also tolerances of the components, and the imprecision introduced by the mounting of all the components. Moreover, it has to be considered also the effect of the switch, which is described in a simple and effective model. It is also observed that the choice of the 50 Ω switches does not compromise the overall performance, in all the working frequencies.

As a remark, in this first work, the objective was to realize a frequency agile rat-race operating in two contiguous frequency bands, without a particular attention on the cross-isolation. However, this aspect is important for some applications, for limiting the filtering in the receiver input path. Therefore, in next designs this aspect will be investigated. In this perspective, it is noticed that the nature of the proposed structure theoretically supports out-of-band suppression, since ATLs are intrinsically frequency selective structures (LH-ATL have high-pass behavior, while RH-ATL have low-pass characteristic). However, it is foreseen that more unit cells would be needed in order to account for this feature, thus increasing the final dimensions. A more deep analysis concerning the phase behaviour of the rat-race can be made by considering that the ATLs are an intrinsically frequency selective network, and therefore the group delay represents a key parameter for characterizing such a structure. This is the reason of using this specific parameter for equalizing the phase variation of the +90° and -90° branches of the rat-race coupler in the two frequency bands under investigation, as proposed in Sect. 3.4.2. Moreover, the achieved frequency bandwidths centered at 900 MHz and 1.7 GHz can be evaluated through the group delay. First of all, referring to figures 3.13 and 3.15, two effects limiting the bandwidth in both frequency states can be distinguished: one is related to the contribution of the LH-ATL (high-pass frequency selective network) and the other to the RH-ATL (low-pass frequency selective network).

The LH-ATL that realizes the +90° branches of the designed structure is the main reason of limitation in the lower side of the considered operative band. The explanation is given by considering that the LH-ATL are highly dispersive as frequency approaches the cut-off, located at low frequencies, where the group delay variation is maximum. Otherwise, the +90° branch exhibits a slow variation of group delay as frequency increases. Instead, the highest part of the operative frequency bands is dominated by the phase characteristic of the -90° branch, realized with RH-ATLs. This is the result of the increasing dispersion as frequency approaches the cut-off imposed by the low pass network, hence setting the operative highest frequency limit. Therefore, for stabilizing the two opposite contributions, the phase balancing term is needed, especially for the higher band case, with center frequency of 1.7 GHz.

The performed analysis explains the behavior of the measured phase imbalance, where a quite flat phase characteristic is observed in the proximity of center frequencies, while, in the extreme portions of the operative bands, the derivative

of the phase over frequency (i.e. group delay) has a steep variation. As already mentioned, the presence of the switches has an impact on the overall coupler performance, including an effect on the group delay. This is due to the increase of the attained phase with respect to the theoretical value of +90°, that shifts over higher frequencies the lower operative frequencies of the +90° branches (realized with LH-ATLs), where the highest group delay is present (as can be noticed from the formulas (3.12) and (3.13)). Therefore, the effect is to shift above the lowest frequency in the considered bands. Moreover, since the phase delay related to the switch has an almost linear characteristic over frequency, its effect is more pronounced in the 1.7 GHz operative frequency band, where it is also multiplied by two (the transfer switch operates in crossing mode). This condition is numerically expressed by (3.17) and (3.19).

Table 3.3: Comparison of Rat-Race Couplers Performance

Ref.	Center Frequency (MHz)	Band-Width*	Insertion Loss (dB)	Return Loss (dB)	Isolation (dB)	Relative Area** (%)
[230]	900	34%	3.5	10	9	3.9
[251]	1440	10.5%	N/A	15	20	8
[232]	900	57.5%	3.5	16	35	5.28
[241]	840 - 2480	50 MHz	4.7 - 4.9	15	20	15.92
This Work	900	64%	3.9	10	26	3.03
	1700	24%	4.3	15	30	10.42

(*) ±0.5 dB amplitude variation and 10 dB return loss criterion. In [241] the bandwidth is reported in MHz because the central frequency varies continuously.
(**) Compared to standard designs at the same frequency.

Finally, Table 3.3 summarizes the measured performance of the proposed rat-race coupler, including a comparison with other designs concerning miniaturization and frequency agility, developed in microstrip technology and in a similar frequency range. It is noticed that the proposed realization at 900 MHz is the most compact at this frequency, to the author's best knowledge.

3.6 Conclusion and Perspectives

In this chapter, a novel frequency agile rat-race coupler based on standard and inexpensive PCB technology has been designed and experimentally validated. The design exhibits an outstanding miniaturization by exploiting the LH-ATL and RH-ATL techniques, while introducing a frequency agile network in the rat-race branches for operating in the 900 MHz or 1.7 GHz bands, with an available bandwidth of 64% and 24% respectively. The frequency reconfigurability is obtained by

acting on a single control. Furthermore, a method for maintaining a broadband behaviour of the device is here described, by introducing a well defined LH-ATL phase advance on the -90° branch. The method is validated through measurement on the manufactured reconfigurable rat-race coupler.

As further perspective, a multiband rat-race coupler with three bands can be designed, by employing the theory developed here. Moreover, an improvement in cross-isolation among the two bands can be investigated for a more reliable application in real-life receivers.

Chapter 4

Frequency and Polarization Reconfigurable Antenna for UHF RFID Reader Application

Radio Frequency Identification (RFID) is one of the most widespread and important wireless standard currently used in many applications, such as transportation management system, access control, item identification and tracking [252]. Moreover, in the next future it is expected a further increase of the usage of this technology for supporting Internet of Things [253] and Industry 4.0 [254].

In order to cover all the functions in the different application scenarios, RFID comprises of many sub-types, differing in the frequency bands of use, ranging from hundred of kHz (i.e. Low Frequency, 125/134 kHz) to 5.8 GHz (Super High Frequencies RFID). Among all, the Ultra High Frequency (UHF) RFID is the most interesting technology, since it has the advantage of ensuring high reliability, relative long range of communication and fast identification of the tags. The UHF RFID is a typical example of back scattering communication system, and it is composed by the reader, the reader antenna and the tag, which is most cases passive. Typically, the reader antenna should exhibit high gain, wide bandwidth, and a polarization suitable to match the tag orientation and to ensure a proper communication. In most cases, the reader has to deal with a random orientation of the tags, therefore circular polarization (CP) is used for avoiding critical polarization mismatch. In fact, the widespread use of the UHF RFID technology imposes the passive tags to be small and cheap, while the reader is the key element that determines the performance of the complete system. Moreover, although UHF RFID is widespread all over the world, the operating bandwidth for different regions and countries are not the same: in Europe it is used the 865 – 868 MHz band, in North America the 902 – 928 MHz band, in Japan the 852 – 855 MHz and 950 – 956 MHz bands, while in China the two bands 840.5 – 844.5 MHz and 920.5 – 924.5 MHz are authorized. Figure 4.1 shows an insight of the different frequency UHF RFID

bands corresponding to specific countries/regions. It is also interesting to see the different power levels for the displayed regions.

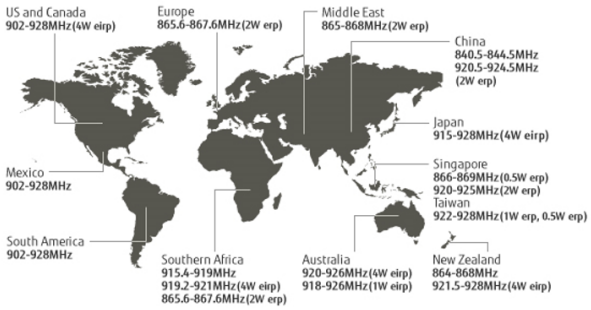

Figure 4.1: UHF RFID frequency bands and maximum power set by the standards of the main regions/countries.

For RFID system manufacturers, this aspect is undesirable because it implies a distinct hardware for each country, increasing costs and complexity. This is particularly critical for the reader antenna design, and therefore in recent years the research has been focused on the development of wideband antennas covering the whole UHF RFID band in order to overcome this problem. Many antenna engineers have studied new wideband antenna concepts, designed to provide full coverage of the UHF RFID band in the band 840 – 960 MHz in terms of matching and circular polarization (i.e. axial ratio), by mainly using stacked patches or 3-D antenna structures [255–257] which are somewhat bulky and not easily manufacturable. Therefore, great attention has been invested in compact and wideband solutions, covering all or many regional frequency bands, avoiding the use of several antenna layers [258–260]. Although these antennas seem to provide a solution to the general problem, the achievement of a broadband CP band is difficult, and furthermore the overlap between the matching and CP bands has to be established. However, the use of circular polarization does not represent the optimum solution for the typical RFID application due to the fact that the tag is linear polarized, and therefore the circular polarization leads to a constant loss of 3 dB. This consideration suggests that the only way to overcome this loss is to use a reconfigurable system that adapts to the different orientation of the tags without losing polarization efficiency. Nevertheless, the application of reconfigurability to UHF RFID reader antenna was used for controlling the pattern [261, 262] and/or polarization [183, 263]. However, in the latter case, the antenna is able to switch between Left and Right handed circular polarization, or between one linear and circular polarizations, therefore not solving the polarization loss problem.

In this chapter, the reconfigurability principle is used to overcome the limitation imposed by the use of circular polarization and, by introducing the frequency agility,

two UHF RFID regional standards are covered by using the same antenna structure. In particular, in order to accomplish the polarization and frequency agility, a reconfigurable feeding network is used. In this research activity, several topologies allowing to independently select both the frequency band and the polarization are investigated, in order to improve some design parameters. Therefore, new concept for employing the multiple reconfiguration by using a flexible design are explored, and the resulted architectures can be adopted with various antenna architectures. Moreover, it is noticed that feeding networks as reconfigurability element represent a very interesting technique, already employed in some designs for achieving polarization reconfigurability by providing the correct phase and amplitude at antenna feeding points, [140, 142, 264, 265]. However, the reconfigurable feeding networks described so far are related only to the selection of the two circular polarization (i.e. right and left handed) and two linear polarizations (i.e. horizontal and vertical). Moreover, the realization of such a feeding network is mostly based on the use of many couplers (e.g. quadrature and rat-race couplers), and for this reason the feeding network is complicated and requires lot of PCB area. Here, it is provided a compact solution based on only a single coupler for achieving the required polarization states. Moreover, being the antenna size an important aspect to be addressed, in this work the advantages given by the reconfigurability are exploited for reducing the size of the antenna, without great loss in overall performance.

In this chapter, as first step, the method for reducing the size of the antenna will be clarified, describing and comparing two different approaches for obtaining the small for form factor. Therefore, taking as basis the best antenna with reduced form factor, the frequency reconfigurability is applied. The polarization reconfigurability, that gives an essential improvement to the RFID reader application, is first theoretically explained. Then, five methods are proposed for applying the simultaneous frequency and polarization agility to the antenna. Beside the integration of the frequency and polarization selection mechanisms, the two operation can be independently operated for all the reported solutions. Furthermore, each method is characterized, comparing also the performance and design complexity of the designed solutions, highlighting benefits and limitations.

4.1 Frequency and Polarization Agility Applied to UHF RFID Antenna

In this research activity, the reconfigurability is applied to an RFID reader antennas for improving the read-write performance and to overcome limitations related to standards imposed by different countries. Considering the latter aspect, here the use frequency agility is proposed as solution to cover the EU (865.6 – 867.6 MHz) and US (902 – 928 MHz) frequency bands in a single design. This would bring many advantages from an industrial perspective, by unifying the design

of the reader antenna, therefore reducing development and manufacturing costs. Furthermore, it is proposed a method to greatly improve the overall performance of the UHF RFID antenna system by exploiting the polarization reconfigurability. In fact, it is well-known that almost all UHF RFID passive tags are extremely simple and low cost antennas, and they are typically linear polarized. In the general application environment, the tag is randomly oriented, and for this reason the solution adopted from ensuring the proper communication between tag and reader is to exploit Circular Polarization (CP). However, this polarization-free condition cause a great limitation on the total efficiency of the system: in fact the circularly polarized RFID antenna exhibits a loss of 3 dB when receiving linearly polarized waves. Being the UHF RFID based on backscattering, the polarization mismatch is even more critical, because it is firstly involved in the reader-tag link, where the power and the data are transmitted to the tag, and then also in the modulated signal backscatter from the tag to the reader antenna, thus counting twice in the full communication process.

In order to describe the loss of power due to polarization mismatch, the *Polarization Loss Factor* (PLF) is defined in (4.1):

$$PLF = |\widehat{\rho_r} \cdot \widehat{\rho_t}|^2 = |\cos(\varphi_p)|^2 \tag{4.1}$$

where $\widehat{\rho_r}$ is the polarization unit vector of the reader antenna, and $\widehat{\rho_t}$ is the unit vector of the incoming wave impinging the antenna. The quantity φ_p represents the angle between the two unit vectors. This aspect drives the necessity of having high gain circularly polarized antennas, which are often complex and difficult to design (e.g. [255, 259]), where main limitation is related to the CP bandwidth. On the other hand polarization reconfigurability can offer great benefits to the system, by extremely reducing the PLF by exploiting a switchable linear polarization system. This approach drastically increase the total efficiency of the antenna system, theoretically giving the same performance of a CP antenna with 3 dB more gain. Therefore, based on the premises just described, and by also considering manufacturing and system integration aspects, the development of a reconfigurable UHF RFID antenna will be reported in the following paragraphs.

4.2 Reduced Size Antenna

Due to the great diffusion of the RFID technology in many different applications, antenna size and manufacturing cost are of prominent importance, and they actually drive many UHF antenna reader designs. Clearly, the main drawback of an electrically small antenna is the maximum achievable gain, which is in most cases not sufficient to guarantee the communication with all tags, due to the reduced spatial coverage. On the other hand, the use of complicated antenna topologies or

the use of high permittivity materials leads to cost issues. Nevertheless, by considering the virtual 3 dB increase given by the polarization reconfigurability approach, a reduced size antenna can be developed, taking advantage of the improved polarization matching to supply at the maximum gain reduction, related to the limited antenna effective area.

In the frame of the development and testing the proposed concept of the reconfigurable UHF RFID antenna, while keeping a simple and cost-effective design, a suspended patch antenna is considered as radiating element. This is a promising option, being simple to manufacture in standard PCB technology, which lead to low cost and easy integration with the electronics and the RFID reader assembly. Moreover, the polarization control can be realized by operating on the input feeding points instead of acting on the suspended patch, thus keeping a simple architecture. A further advantage of this antenna structure is given by the uncomplicated feeding network required to feed the patch antenna, compared with other popular antenna solutions (i.e. dipoles). In this work, a method to increment the electrical dimensions of the antenna by placing loading elements at its boundaries is also exploited.

The radiating element is realized as a square patch with side dimension of 60 mm, etched in standard 0.5 mm thick FR4 dielectric material, characterized by $\epsilon_r = 4.4$ and $\tan\delta = 0.02$. The patch antenna is suspended over an electrically small ground plane, with dimension 95 × 95 mm, which is equal to 0.274 $\lambda\times$ 0.274 λ in terms of wavelength calculated in free space at 865 MHz (i.e. at minimum operative frequency). Due to the electrically small form factor of the overall system, a dual pin feeding solution is used, by placing the feeding points along the mid axes in orthogonal configuration, corresponding to the Vertical and Horizontal polarizations.

In order to achieve the considerable size reduction with respect to the $\lambda/2$ side length (according to basic antenna theory [5]), reaching the 0.175 $\lambda\times$ 0.175 λ area proposed here, four metal posts are used for both elevating the radiating element at proper distance from the ground plane and for connecting the antenna to four loading capacitors. In this way, the electrical length of the patch antenna is increased and the resonance frequency can be adjusted by increasing/decreasing the four capacitance values. This conceptual architecture implies that the four posts are made of metal, thus employing the same material and dimensions of the feeding pins are used for easing the manufacturing. Therefore, all pins are realized with 1 mm thick copper wire, and they are connected to the antenna by four holes located in the four edges of the patch. In Fig. 4.2, the dimensions of the square patch antenna and the ground plane are shown, together with the two feeding pins and the four metal posts. In the presented design, the height of the patch antenna has been set to 17 mm, as illustrated in Fig. 4.2.

Two different options arises concerning the implementation of the loading capacitors. In the first option, four commercially available SMD capacitors can be

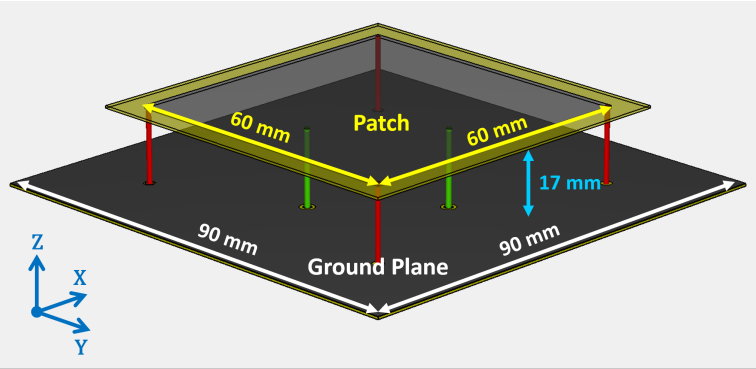

Figure 4.2: 3-D model of the proposed reduced size patch antenna. Dimensions and reference axes are also reported.

used, providing high Q-factor and flexibility (both on substrate materials and on antenna height/dimensions). However, as drawback, this solution carries the general problems concerning lumped components, as for instance the discrete values that can be used, the tolerances and parasitics. The second option uses instead distributed capacitors, that can be directly realized on PCB without any extra costs, and they can be fine tuned for ensuring the best value of capacitance to be attained. Nevertheless, this solution exhibits as drawbacks the lack of flexibility (it is fixed with the antenna design) and it is strongly dependent on the dielectric material, concerning Q-factor and tolerance. In order to provide the best solution, the two design options will be assessed.

4.2.1 RFID Antenna with SMD Loading Capacitors

In Fig. 4.3, the Empire XPU [221] model of the reduced size suspended patch antenna is illustrated, where the loading capacitors connected to the ground plane are also highlighted.

By employing this solution, 0.5 pF capacitors are used in combination with a height of 17 mm for the suspended patch. In the circuital model of the lumped capacitor it is also inserted a resistance of 0.125 Ω, compatible with the ESR of a High-Q capacitor available on the market, calculated in the frequency range of operation. Due to this arrangement, the resonance of the antenna is set to a frequency between the EU and US frequency bands, at approximately 900 MHz. In the antenna model are included four vias with a hole diameter of 1.1 mm and soldering pads with diameter of 1.7 mm on top and bottom layer of the main PCB, provided for the placement of the four metal posts. The clearance of the soldering pads with the antenna ground plane has been tuned, since it affects the resonance frequency, and then a distance of 1.15 mm has been taken from soldering pad and ground metallization. Therefore, the loading *0402* SMD capacitors are inserted in

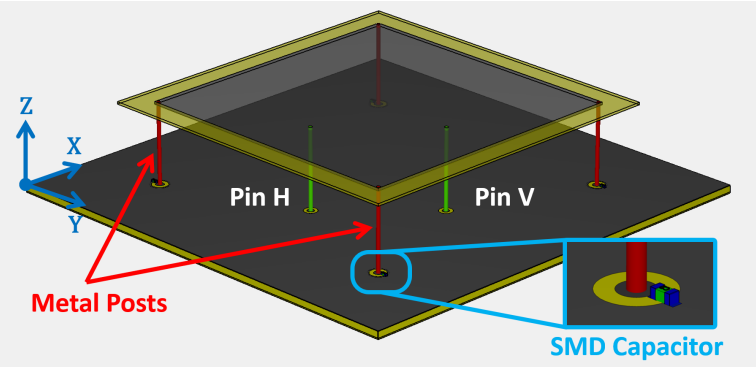

Figure 4.3: 3-D model of the proposed suspended patch antenna with double pin feeding. In the box is shown one of the end capacitor, connected to ground.

this space. With this approach, inexpensive FR4 can be used as dielectric material, which is specified by the parameters $\epsilon_r = 4.4$ and $\tan\delta = 0.02$.

The $S-$parameters and the radiation pattern at 902 MHz of the complete antenna are shown in 4.4 and 4.5 respectively. Referring to Fig. 4.4, it is noticed that the antenna resonance, identical for both inputs *Pin H* and *Pin V*, is located at approximately 901 MHz, while the -10 dB bandwidth is equal to 15.1 MHz, despite the reduced size of the patch antenna. The isolation between *Pin H* and *Pin V* is quite high, and better than -20 dB.

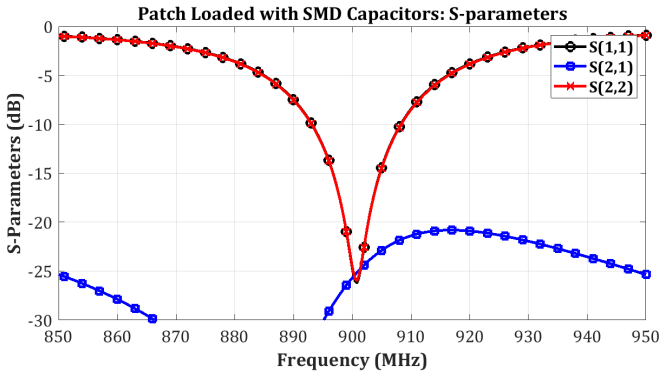

Figure 4.4: Simulated $S-$parameters of the modeled suspended patch with SMD loading capacitors.

Similar considerations on antenna size can be observed for the antenna gain reported in Fig. 4.5, where the maximum of the co-polar component is 3.9 dBi, while the maximum for the cross-polar is -16.7 dBi. The field components reported in Fig. 4.5 for the $E-$plane and $H-$plane are in accordance to the considered electric field polarization given by the the excitation of *Pin H* (corresponding to the Horizontal polarization) and the *Pin V* (corresponding to the Vertical polarization). Finally,

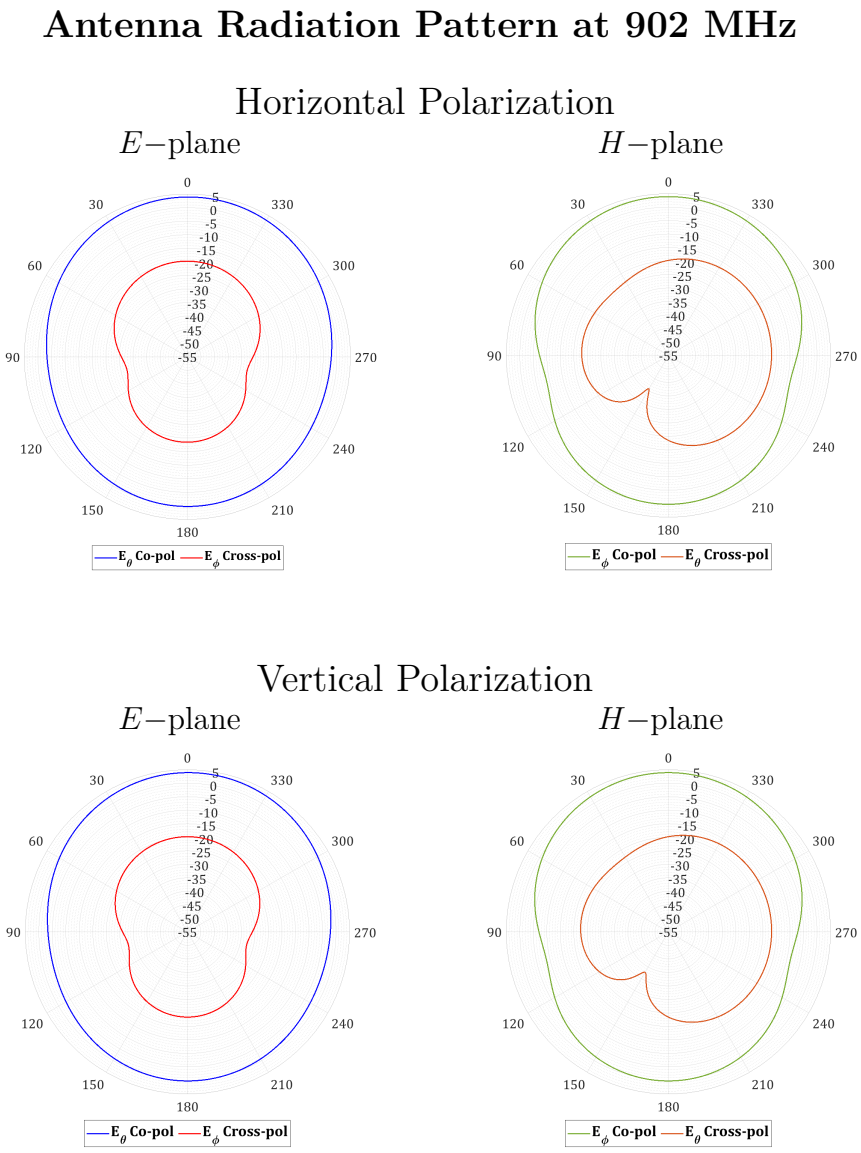

Figure 4.5: Simulated radiation pattern at 902 MHz of the modeled suspended patch with SMD loading capacitors for the *Horizontal* and *Vertical* polarizations. In agreement with the considered polarization, the $E-$plane and $H-$plane components of the electric fields are reported.

the antenna is completely symmetric with respect to the x and y axes, referring to the coordinate system in Fig. 4.3, where *Pin V* and *Pin V* are also inserted. Moreover, as important parameters for the UHF RFID application, and in general also for electrically small antennas, the radiation efficiency is reported in Fig. 4.6.

From Fig. 4.6, the total radiated efficiency results to be higher than 70% across

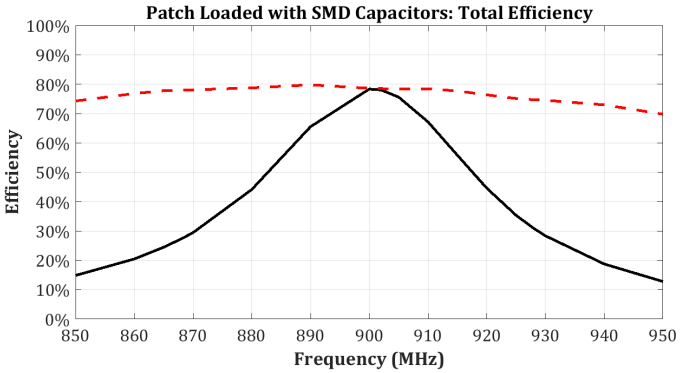

Figure 4.6: Simulated total efficiency (solid line) for the UHF patch antenna with SMD loading capacitors. For reference purpose, it is also reported the ideal radiated efficiency (dashed line) without matching and material losses.

the matching band. Moreover, the ideal radiated efficiency (i.e. radiated efficiency with no matching and resistive losses) is reported, showing that the patch antenna can potentially radiate with a very good efficiency also in all the UHF RFID bands. In other words, Fig. 4.6 demonstrates that a patch antenna has a radiation bandwidth much higher than the matching bandwidth, and this aspect will be taken as basis for the application of frequency reconfigurability.

4.2.2 RFID Antenna with Distributed Loading Capacitors

The second method analyzed for increasing the electrical length of the UHF RFID suspended patch is realized by using distributed loading capacitors. A similar configuration as the one in Fig. 4.5 is employed. In this design, the SMD capacitors have been replaced by circular pads, positioned on the same layer as the feeding lines and directly connected to the metal posts. The resulting configuration is depicted in Fig. 4.7.

It is noticed that the choice of the material to be used is very important in case of distributed component. In fact, by selecting a low cost material, like standard FR4, it is expected a high variability or inaccuracy of the reference dielectric constant, leading to unacceptable variation of the expected center frequency. Moreover, the high loss tangent would cause a low Q-factor, which would directly affect the antenna gain and efficiency. Following the goal of proving the described concept, and for having a reliable and reasonably high Q-factor of the distributed capacitor, it is chosen to utilize a 0.5 mm thick Rogers *RO4350B* dielectric, characterized by $\epsilon_r = 3.66$ and $\tan\delta = 0.004$. In principle, a high quality FR4 can be also used, after having characterized the material (many datasheets specify the dielectric constant just up to 1 MHz). On the other hand, *RO4350B* is a relatively low cost RF dielectric material, with very good and stable performance.

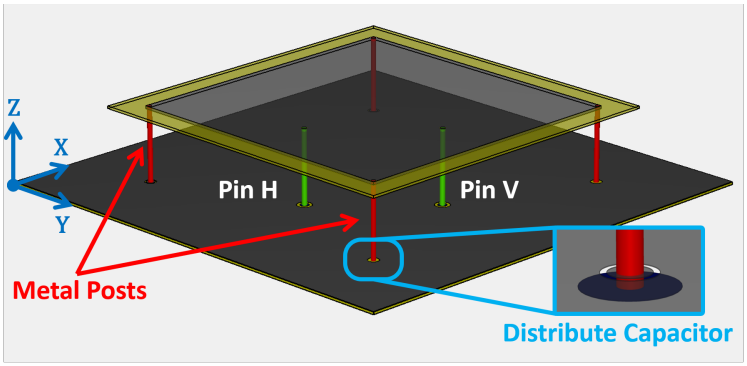

Figure 4.7: 3-D model of the antenna with double pin feeding suspended patch. Enclosed in the box is shown the detail of the modeled loading distribute capacitors, positioned on the opposite side of the ground plane, and realized with planar PCB technology. For a clearer view, the substrate is removed and the ground plane is transparent.

The circular pads that realize the distributed capacitor are shown in Fig. 4.7. As can be seen from Fig. 4.7, the pads are placed on the bottom side, and they have been tuned to adjust the resonance of the patch to approximately 900 MHz, similarly to the process described for the case of the SMD capacitors. The distributed capacitors are then realized with pads with a diameter of 3.8 mm. During the tuning phase, the diameter of the pad is varied with steps of 0.1 mm, which is the minimum recommended resolution for the standard PCB manufacturing suppliers. On top side of the main PCB, the soldering pad of the metal post is kept at the same size as previously done (diameter of 1.7 mm), while the ground clearance is now reduced to 0.25 mm. Similarly to the previous case using SMD components, the height of 17 mm has been considered for the suspended patch. In this case, the resonance of the patch loaded with the distributed capacitors is measured at about 903 MHz, with a bandwidth of 13.5 MHz, as can be noticed from Fig. 4.8, where the $S-$parameters of the complete antenna are shown. The antenna symmetry with respect to the two orthogonal planes in which the *Pin H* and *Pin V* are located can also be noticed from Fig. 4.8, where also a decoupling better than 18.7 dB is found. The realized antenna gain is also displayed in Fig. 4.9, showing a maximum peak level of 4.2 dBi in the co-polar component cuts, which is slightly higher than the lumped SMD case. Moreover, also in this case, the cross-polar is below -15 dB, with a more consistent magnitude observed in the $H-$plane cut.

Indeed, as in the case with SMD loading capacitors, the frequency reconfigurability is justified by the radiation efficiency shown Fig. 4.10 (indicated with the red dashed line), where a radiation bandwidth much wider than the matching bandwidth can be observed. Moreover, from Fig. 4.10 it can be noticed that, despite the very small electrical length and without the use of high ϵ_r materials, the antenna

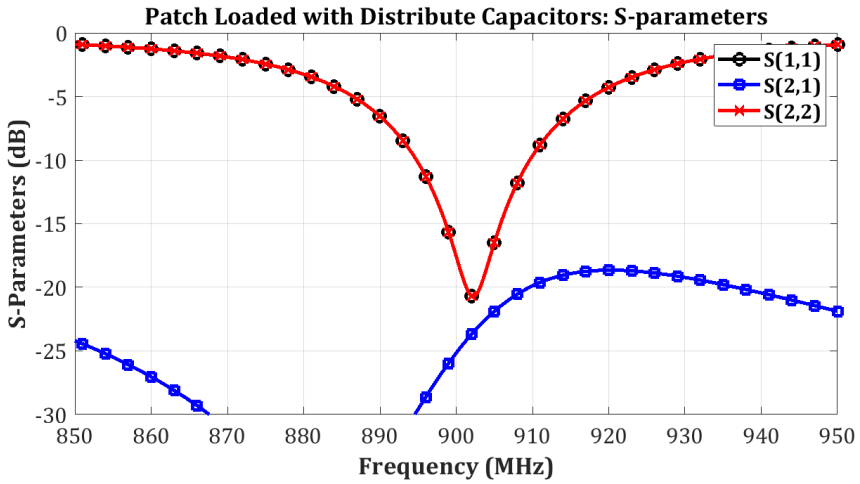

Figure 4.8: Simulated $S-$parameters of the modeled suspended patch with distribute loading capacitors.

demonstrates a total efficiency of more than 80% in the -10 dB matching band.

For the reconfigurable system, the suspended patch loaded with distributed capacitors will be used, due to the slightly better antenna performance and due to the advantage of having no extra SMD components mounted on the ground plane of the patch, which reduces cost and complexity. Moreover, the tolerance of standard 0.5 pF high-Q capacitors is quite high in relation to their small value (0.1 pF typically), and the difference in loading each side of the patch antenna could lead to undefined conditions due to the broken symmetry of the squared patch, and therefore of the H_{pol} and V_{pol} linear polarizations. On the other hand, the distributed capacitors rely on the accuracy of the fabrication process, which is the same for all of them. Therefore, the symmetry concept is preserved between the two orthogonal linear polarizations H_{pol} and V_{pol}, as recognized from Fig. 4.9. An additional advantage of the solution employing distributed capacitors with respect to the solution with SMD components, is noticed by comparing the total and radiated efficiencies, where a better performance was found. In fact, with the chosen solution, the efficiency peak is about 88%, in contrast with the 79% detected in the other solution. Moreover, a slightly higher antenna gain is achieved by using the distribute components. Finally, it is noticed a wider matching band of the reduced size antenna with SMD loading capacitors, (considering the -10 dB criterion), however, this aspect is not considered of primary importance since the frequency reconfigurable matching network will be applied to the original antenna for properly tuning the frequency band.

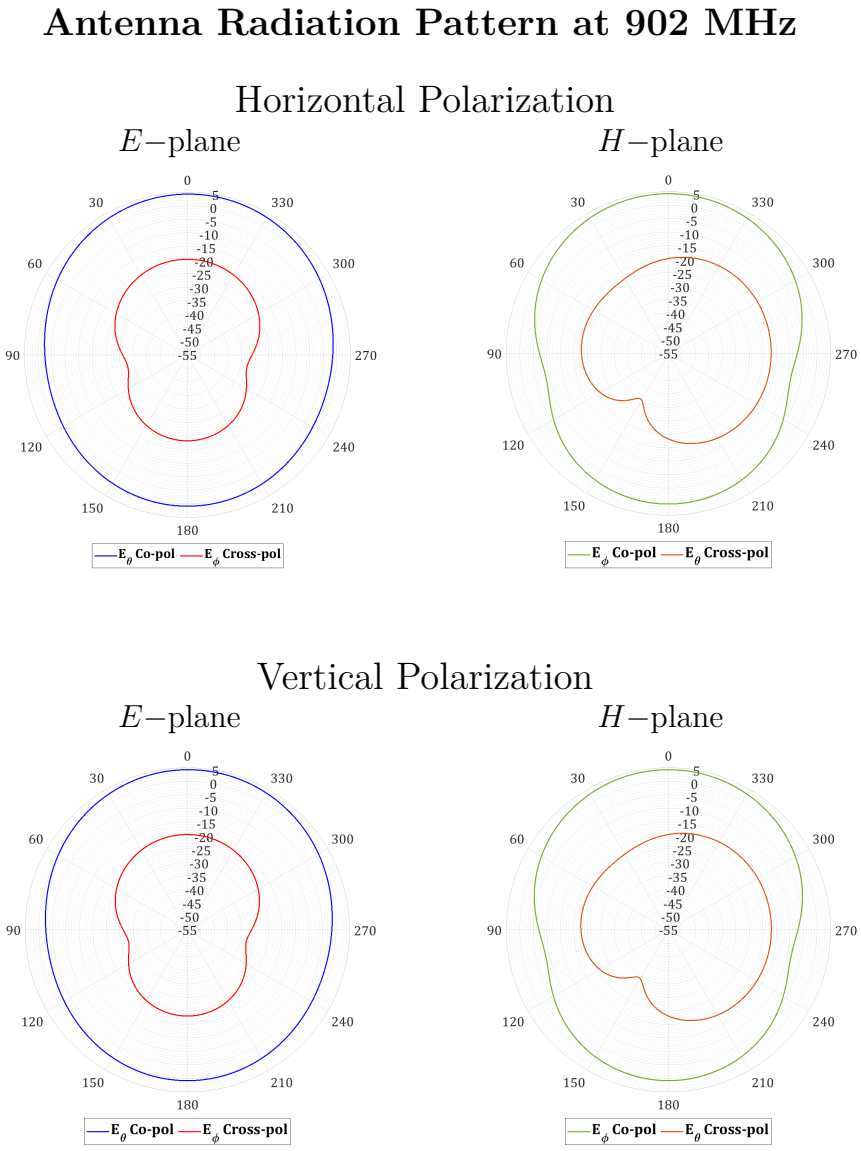

Figure 4.9: Simulated radiation pattern at 902 MHz of the modeled suspended patch with distribute loading capacitors for the *Horizontal* and *Vertical* polarizations. In agreement with the considered polarization, the $E-$plane and $H-$plane components of the electric fields are reported.

4.3 Frequency Reconfigurability

By considering the results described in Sect. 4.2.2, the frequency reconfigurability concept is here employed for covering the two UHF bands, relative to the European area (i.e. EU band, frequency range 865 – 868 MHz) and the North

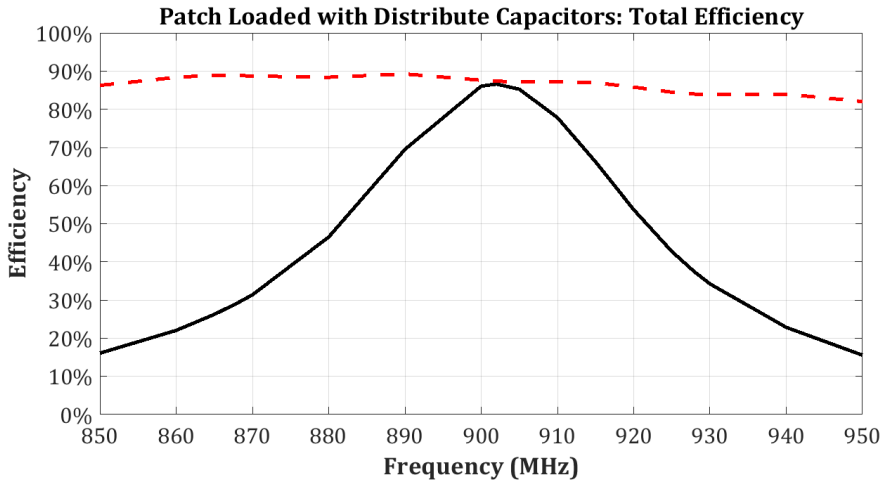

Figure 4.10: Simulated total efficiency (solid line) for the UHF patch antenna with distribute loading capacitors. For reference purpose, it is also reported the radiated efficiency (dashed line) without matching and material losses.

American (i.e. US band, frequency range 902 – 928 MHz) with a single antenna topology. In this research activity, a reconfigurable feeding network is used to modify the input impedance of the antennas. This function is fulfilled by placing a reconfigurable matching network at the two feeding pins, named *Pin H* and *Pin V*. The purpose driving the choice of the reconfigurable feeding network is the possibility to develop a flexible structure, that can be applied also to other antennas, ensuring an easy integration of the switching elements, without the introduction of further components on the antenna that can limit the efficiency and increase the assembly complexity. Since the antenna is well matched at a frequency in between the two extremes of the EU and US frequency bands, it will be beneficial to use two matching networks with similar topologies. Moreover, with the purpose of applying frequency reconfigurability, the switching elements have to be integrated in the matching structure. These matching structures have to employ the least number of switches and they have to be realized in a compact structure, that can easily be integrated with the polarization agile feeding network. Therefore, by carefully analyzing the suitable network topologies required to fulfill the matching condition in all frequency bands, it is possible to use only one switching element to cover all the states. The latter aspect is very important, since it reduces the overall complexity in terms of number of components and digital controls to be used, and furthermore it optimizes the costs and compactness of the reconfigurable structure.

The topology used in this work is the $L-$type matching network that provides the matching condition to virtually any generic impedance, named here as Z_A. The reconfigurability principle can be applied also to more complex matching networks, like π-type, $T-$type or even ladder networks, which are capable to provide broader

bandwidth, at the expense of a much higher complexity, along with an increase of losses due to the amount of components used. For clarification, a general concept of a fully reconfigurable $L-$type matching network is illustrated in Fig. 4.11, where two complementary topologies using two switches are depicted.

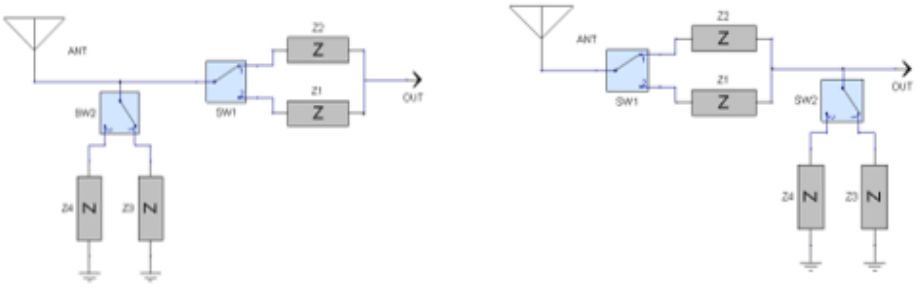

Figure 4.11: Two examples of switchable $L-$type matching network topologies. For simplicity $SPDT$ is represented, however a generic $n-$way switches can be applied.

Nevertheless, it is possible to define the optimized matching network (i.e. using only one switch) by the analysis of the Smith Chart. The concept is clarified in Fig. 4.12 where the two impedances $Z_A(f_{EU})$ and $Z_A(f_{US})$, belonging to the same antenna but measured at the two frequencies f_{EU} and f_{US} (related to the center frequencies of the EU and US UHF RFID band), are first located on Smith Chart. Then, by considering all the possible impedance transitions (i.e. along the constant $|\Gamma|$ circles, realized with ideal reactive elements) of both $Z_A(f_{EU})$ and $Z_A(f_{US})$, it can be identified the $L-$type networks that can fulfill the matching condition.

As described from the general theory of matching networks (see e.g. [266]), typically for one frequency there are two possible configurations for the $L-$type matching network. According to the goal of this work, the considered solutions are the one that shares the same network topology and that can have one matching element (i.e. impedance transition) in common. The procedure to identify the requested condition is illustrated in Fig. 4.12, where the two possible matching combinations that shares both topology and an element in common (indicated in green) are shown in Figs 4.12a, 4.12b. More in detail, after having identified the matching network topology, it is checked which component is able to provide the transition for crossing the 50 Ω constant circle (as in Fig. 4.12a) or, instead, to compensate the reactive part and fulfill the ideal match to 50 Ω (see Fig. 4.12b). The first case in Fig. 4.12a, related to the impedance of the EU center frequency band $Z_A(f_{EU})$, shows a matching network in which a shunt inductor (indicated in blue) is used for reaching the constant 50 Ω circle, while the series capacitor (indicated in green) compensates the reactive part and reaches the 50 Ω point. Conversely, starting from the impedance related to the US center frequency band (i.e. $Z_A(f_{US})$)

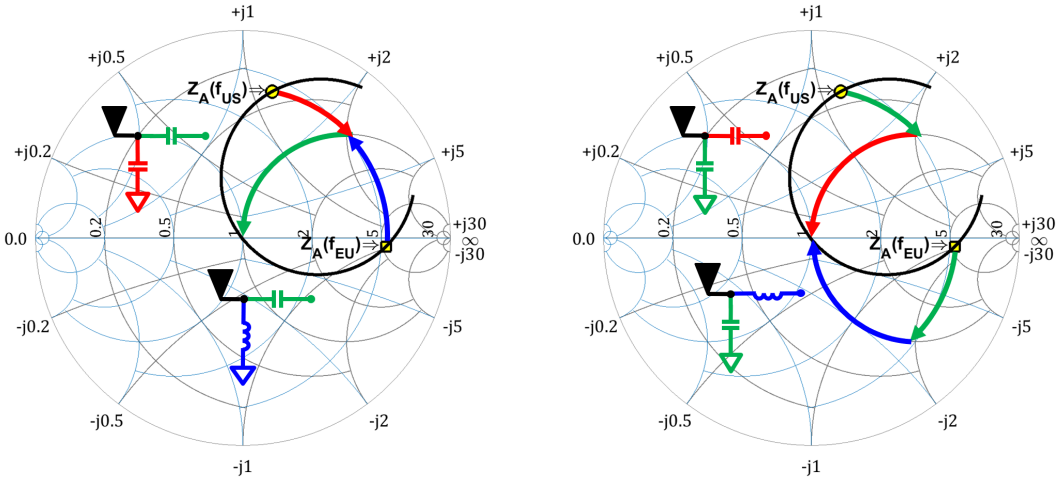

Figure 4.12: Principle of operation of the optimized $L-$type matching network employing just one switching element. Two possible cases: with respect to the common component (coloured in green) the switch can be set to (a) the first or (b) the second element of the matching network.

reported in Fig. 4.12a, the transition to the 50 Ω circle is provided by a shunt capacitor, coloured in red. From this point, the series capacitor (indicated in green) perfectly matches the impedance $Z_A(f_{US})$ to 50 Ω. By applying the reconfigurabilty approach to these configurations, the series capacitor is kept fixed, since the required values is approximately the same for the two cases, while a switch will be placed to select either the shunt inductor or capacitor. Clearly, by selecting one of the two shunt component, the corresponding frequency band will be matched. However, Fig. 4.12b presents a slightly different approach. In this case, the first reactive element placed after the antenna is a shunt capacitor, indicated in green, which is executing the transition to the constant 50 Ω circle. Then, two different reactive elements are used for completing the matching of $Z_A(f_{EU})$ and $Z_A(f_{US})$, which are one series inductor (in blue) and a series capacitor (in red), respectively. This matching network topology can be made reconfigurable by maintaining the shunt capacitor fixed, and then switch between the series inductor and capacitor to match the two corresponding bands: this is possible because the capacitance needed to fulfill the first impedance transition is approximately the same in the two cases. It is observed that the presented scenario can reasonably be applied to many other antenna matching cases, if the antenna presents a resonance located between the two extreme frequencies that have to be matched. In fact, due to this condition, it is assured that the impedance mapped in the Smith chart has a segment which is crossing the 50 Ω point (or it will be sufficiently close), and for this reason the

two impedances to be matched are also disposed in the vicinity of the normalized unitary impedance and/or conductance circles. Therefore, in the highlighted procedure, it is first evaluated the type of impedance transition, which is corresponding to a well defined circuital element (inductor or capacitor placed either in shunt or series configuration) and then, its value is assessed. For practical situations, small deviations on the alignment to the 50 Ω constant circle are tolerated, since they still provide a matching condition which is adequate for the considered application. Clearly, this is true for just one frequency, because the $L-$type matching network is notoriously narrowband [266]. Nevertheless, the compact and optimized design related to the $L-$type matching network can be maintained by noticing that the EU band is very narrow (i.e. 3 MHz bandwidth) and that the 26 MHz US band can be split in sub-bands, and then use the several outputs of the switch to properly match each of them: this operation can be done without losing system functionality because a US UHF RFID reader adopts the Frequency Hopping Spread Spectrum modulation scheme (FHSS). Actually, by using the FHSS protocol, the reader controls the channel to be used for communication, and therefore the band can be changed accordingly.

Using the consideration mentioned above, a reconfigurable matching networks for covering EU band (865 – 869 MHz) and the two US sub-bands, (902 – 915 MHz and 915 – 928 MHz) have been designed. As extensively discussed in Sect. 3.3.1, for the RFID application, PIN diodes and varactors are not suitable as switching devices because of the high power delivered by the reader front-end, (i.e. the EU standard the effective radiated power is set to 2 W, while in the US standard the limit is 4 W); at the contrary, reflective type CMOS switches can handle this power and they are easier to be integrated and controlled with digital signals. In particular, *BGSA13GN10* from Infineon [267] has been selected, which is specifically designed for antenna tuning purposes. The *BGSA13GN10* is a *SP3T* switch [267] characterized by a very low R_{ON} and C_{OFF}.

The small signal model of the *BGSA13GN10* is shown in Fig. 4.13, where the values for R_{ON} and C_{OFF} are represented for different switching states. They are respectively equal to 0.8 Ω and 300 fF when output *RF1* is enabled, while for the *RF2* case $R_{ON} = 1.4$ Ω and $C_{OFF} = 160$ fF. Finally, for *RF3*, the two values are $R_{ON} = 1.6$ Ω and $C_{OFF} = 120$ fF. The latter aspect is important from a system point of view, because it allows a good approximation of the ideal *OPEN*, in the frequency band of interest. Moreover, the datasheet also specify $C_{pad} = 42$ fF, relative to the capacitance of the soldering pads, along with the switch equivalent series inductance $L_{SER} = 0.1$ nH. However, even if the small signal model of the switch (Fig. 4.13) is theoretically sufficient for defining the behaviour of the switch, the switch has been characterized through measurements. In order to ensure a reliable EM model of the complete system, the $S-$parameters of the *BGSA13GN10* has been included in the simulations.

In this research project, a three states switch (*SP3T*) has been used for the

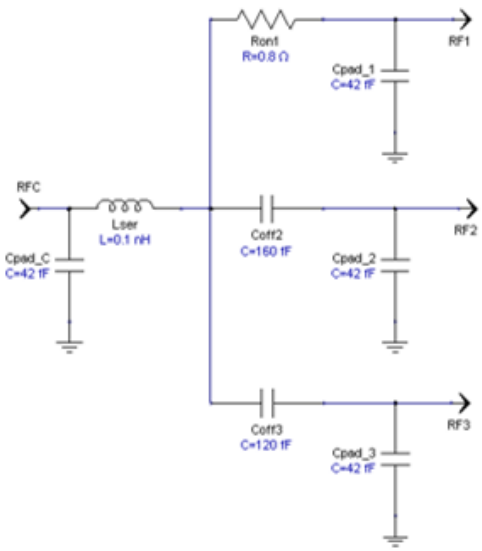

Figure 4.13: Small signal model of the *BGSA13GN10* switch in the case of *RF1* path active.

fulfillment of the targeted reconfigurability. However, it is noticed that. by considering the switches available on the market, the increased number of outputs of the switch does not lead to a more expensive design, but only to a slightly more complex management of the control signals. Moreover, for the purpose of this research, only switches based on GPIO (i.e. General Purpose Input/Output) interface are considered for simplicity, in contrast with more complex protocols as MIPI RF Front-End Control Interface (MIPI RFFE).

Therefore, by considering the input impedance of the reduced size RFID patch employing the distribute loading capacitors, obtained by the EM simulation, by following the procedure previously described the frequency agile matching network was designed using the circuit simulator Advanced Design System (ADS), keeping the goal of using only one switch. Then, the three impedances that have to be matched, related to the EU band and the two US sub-bands, (whose center frequencies are set to $f_{EU} = 867$ MHz, $f_{US1} = 910$ MHz and $f_{US2} = 920$ MHz), are corresponding to $z_A(f_{EU}) = 1.77 + j3.77$, $z_A(f_{US1}) = 0.54 + j0.24$ and $z_A(f_{US2}) = 0.33 + j0.59$. However, this process is not straightforward as depicted in Fig. 4.12, due to the presence of the switch, which introduces impedance transitions that deviates from the constant resistance/admittance circles due to the R_{ON} and the finite isolation with the other outputs. Therefore, the determination of the exact values of components loading the matching network have to be found by optimization, rather than with analytical methods. As a starting point, the theoretical matching without the switch and by using ideal component was used, in order to determine the

best topology overcoming to the complexity of the problem. During this stage, in a similar way as depicted in Fig. 4.12, two possible configurations arises, that are characterized for the position of the switchable element. If just the frequency reconfigurability is applied, the best choice would be the solution that place the switch in shunt configuration (as typically done in most antenna tuning applications); however, in this research activity also a polarization reconfigurability is targeted, so the configuration employing the switch as second element is considered.

After having established the matching network topology, the values of the components have been adjusted with the complete structure including $S-$parameters of the switch, in order to consider all the contributions of parasitics, that cannot be included in the simplified model. The fully optimized matching network is found by substituting the ideal inductor and capacitors with the $S-$parameters of the actual component used, provided in the *muRata* library of the selected inductors *LQW15* and capacitors *GRM15*, and by including in the model the connection lines between the switch and the components. In particular, for taking realistic lengths and widths of the transmission lines connecting the switch to the components, it has been taken as reference the layout shown in Fig. 4.14. It is noticed that the latter procedure is very important, and brings to important deviations to the theoretical values calculated in the previous step, due to the inclusion of parasitics of the real components and the effect of the transmission lines arranged in the matching network, which provide further small deviations to the presumed transition.

The resulting reconfigurable $L-$type matching network is reported in Fig. 4.14, where it can be noticed that the shunt capacitor $C_c = 1.2$ pF is common to all the three switchable components; in particular $L_1 = 26$ nH is used to match the lower EU band, while the series inductor $L_2 = 3.3$ nH and capacitor $C_1 = 4.7$ pF, are used to match the first and second US sub-band respectively. In the figure is also shown the layout used to define the component and switch connections, which are then included in the simulation.

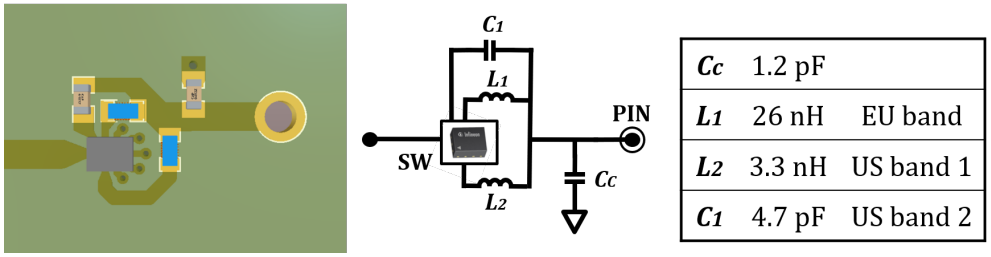

Cc	1.2 pF	
L1	26 nH	EU band
L2	3.3 nH	US band 1
C1	4.7 pF	US band 2

Figure 4.14: Complete definition of the reconfigurable $L-$type matching network employed in the design of the feeding network. On the left side is reported the layout including the switch, in the center the resulted schematic is shown while on the right the component values are listed.

Finally, the calculated switchable matching network of Fig. 4.14 has been inserted in the full EM simulation tool, for the evaluation of all the antenna parameters. The resulting reflection coefficient for the three matching bands, referred to *Pin H* excitation is reported in Fig. 4.15 (for *Pin V* the result is clearly the same).

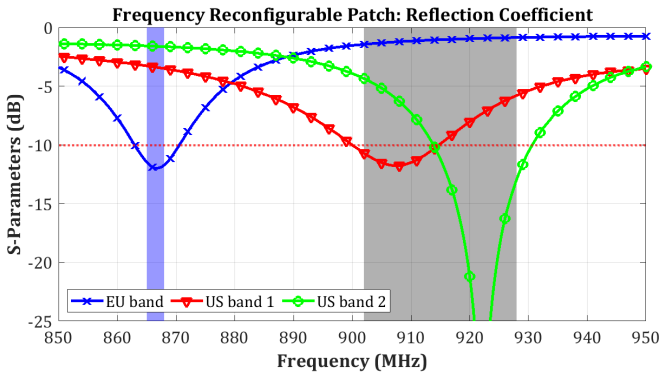

Figure 4.15: Simulated reflection coefficient for the three switching states of the reconfigurable matching network, corresponding to the EU band and the two US sub-bands, indicated for reference.

From Fig. 4.15, it can be verified that all the three bands are matched according to a -10 dB criterion and, in particular, in the US band the two sub-bands are correctly overlapping. Moreover, some interesting information are deduced from the plot of the reflection coefficient: it is clearly visible that the upper US sub-band is better matched compared to the lower. The explanation is found in relation to the analysis previously made regarding the matching network topology, described by Fig. 4.12b, by considering that the common shunt capacitor is actually moving away the already matched frequencies from the 50 Ω point. However, the switch and component non idealities are playing an important role in the resulting reflection coefficient.

The simulated antenna gain with the reconfigurable matching network included, calculated by exciting *Pin H* and keeping *Pin V* terminated on 50 Ω, is reported in Fig. 4.16 for the 867 MHz frequency case (EU band selected), and in Fig. 4.17 are displayed the gain cuts related to the US band center frequency 915 MHz (upper US sub-band matching state selected). The maximum gain measured in Fig. 4.16 at 867 MHz is equal to 2.1 dBi, while the cross-polar peak is measured to be -17.8 dBi. By considering the upper US band, the maximum of co-polar component is found to be 3.2 dBi and the cross-polar component is below -15 dB (worst case in the $H-$plane). In the case shown here, the patch is excited on the *Pin H*, knowing that in the dual case, with *Pin V* excited, the result would be the same due to antenna symmetry.

In order to have a complete overview of the designed antenna performance with the introduce circuitry, the total antenna efficiency has been evaluated in the three

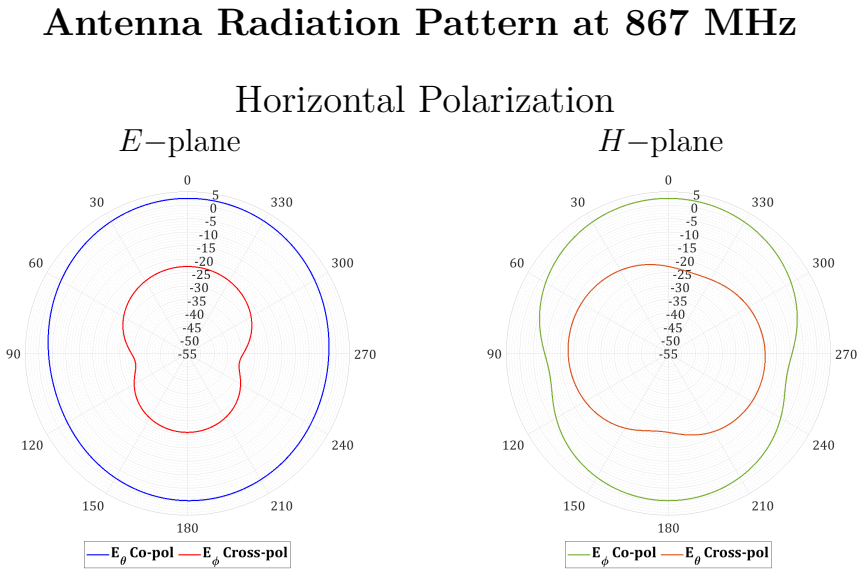

Figure 4.16: Simulated radiation at 867 MHz of the UHF RFID patch with reconfigurable matching applied and *Pin H* excited. In agreement with the considered polarization, the $E-$plane and $H-$plane components of the electric fields are reported.

matching states, as shown in Fig. 4.18. The reported radiated efficiency is quite high, and greater than 60% in the entire frequency band of operation. More in detail, in the US band the efficiency is almost entirely above 70%, while in the EU band the combination of antenna and reconfigurable matching network presents a reduction of almost 10% with respect to the upper band. This is probably due to a more lossy matching state in relation to the EU frequency band. Moreover, a reduction of the realized gain and efficiency is expected in the lower frequency band, since the antenna is electrically smaller. It is reminded that this result is related to the true power delivered to the tags, without the 3 dB loss due to polarization mismatch which is obtained by a standard CP antennas approach. In Fig. 4.18 the 50% limit, related to the real efficiency in the case of ideal CP antenna (i.e. with perfect match and no losses), is also reported for reference. This limit, that will be further proposed in all the total efficiencies plots, is the upper boundary of the radiated efficiency achievable by using a standard CP reader antenna approach, however, in practical designs, the total efficiency is below this limit. In fact, for realizing circular polarization a branch line coupler is commonly used, which introduces losses, design complexity and extra costs. This is aspect is even more critical in the UHF RFID scenario, where special components, using high permittivity or ceramic materials, are required for keeping the dimension of this component sufficiently small for being integrated in the antenna feeding. Moreover, in literature

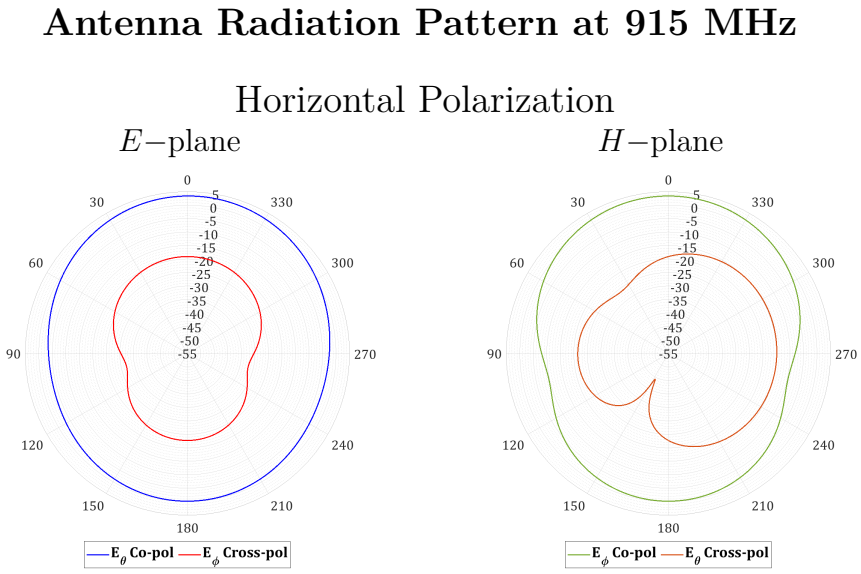

Figure 4.17: Simulated radiation pattern at 915 MHz (related to the upper US frequency band state) of the UHF RFID patch with reconfigurable matching applied and *Pin H* excited. In agreement with the considered polarization, the $E-$plane and $H-$plane components of the electric fields are reported.

are reported antenna solutions which realizes the circular polarization without external components, however, they are typically bigger in size, and its design is not straightforward. In fact, the realization of CP is not easy to be implemented, requiring also some effort to make the axial ratio and the matching bandwidth to overlap correctly. Clearly, in all the mentioned cases, the total efficiency is below 100%, which correspond to the 50% limit displayed here, upon the assumptions previously described.

4.4 Polarization Reconfigurability

As already mentioned in section 4.1, the application of polarization reconfigurability to UHF RFID reader antenna opens new perspectives on antenna designs and system development. The main reason is that the flexible polarization is able to adapt to the particular orientation of the tag, thus ensuring a proper connectivity. Moreover, it is noticed that this aspect it is even more important for ensuring an efficient data transmission between the tag and the UHF RFID reader, since it is based on a backscattering. Therefore, the more efficiently management of the communication mechanism between tag and reader is exploited to achieve the remarkable size reduction proposed here, then compensating for the relative lower

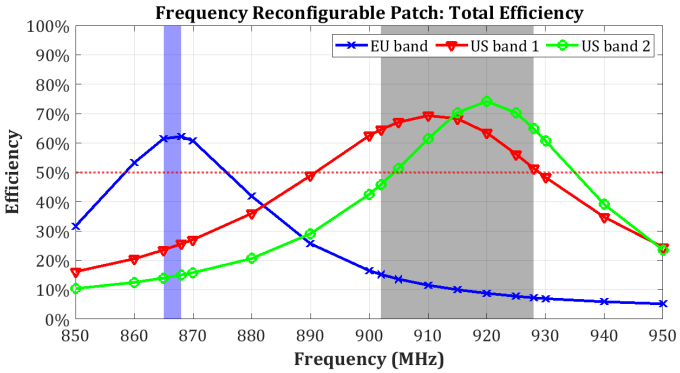

Figure 4.18: Simulated antenna total efficiency in the three switching states of the reconfigurable matching network, corresponding to the EU band and the two US sub-bands, indicated for reference. The 50% limit, related to an ideal antenna with CP approach, is also shown.

gain which is typical of electrically small antennas. In this way, the system functionality is preserved and a simple and inexpensive antenna topology and materials can be used in the design. Furthermore, the realization of polarization agility towards the feeding network allows to basically "decouple" the design of the reconfigurable network to the antenna, giving also the flexibility to use such a concept with other antenna types.

The scope of this research includes the application of frequency and polarization reconfigurability in a single structure. In the previous section a reconfigurable $L-$type matching network with the switch located as last element (placed in series configuration) has been chosen. This supports the possibility to connect directly the feeding network for polarization reconfigurability. In this way, a more compact and optimized design is obtained. Actually, the application of reconfigurability brings the advantage of more flexible antenna characteristics, but at the expense of a more complex system. Therefore, it is important to allocate properly the resources needed for the improved system (e.g. control signals, number of switch, etc.) and by assessing the performance increase given by the new concept against the losses due to the integration of the components (e.g. losses introduced by the switch versus increase of efficiency).

An important indication of the system performance is given by (4.1). In particular, by investigating the relation between the PLF and φ_p (i.e. angle between the two polarization vectors), it is found that the adoption of a four state polarization scheme greatly reduces the maximum PLF. This is obtained by considering the two orthogonal polarizations horizontal (H_{pol}) and vertical (V_{pol}), related to $Pin\ H$ and $Pin\ V$, with the addition of the two diagonal polarizations 45_{pol} and -45_{pol}. In this way, a great reduction of the PLF with respect to CP can be obtained, giving a theoretical maximum value of $PLF_{max} = 0.69$ dB as formulated in (4.2).

This result is found by applying (4.1) and by considering that, with the four 45° equispaced linear polarizations, the maximum of polarization mismatch is found at 22.5°, corresponding to the case of a tag oriented exactly in the middle of two polarization vectors, for instance H_{pol} and 45_{pol}, as depicted in Fig. 4.19.

$$PLF_{Max} = |\widehat{\rho_r} \cdot \widehat{\rho_t}|^2 = |\cos(22.5°)|^2 \,|_{dB} = 0.69dB \tag{4.2}$$

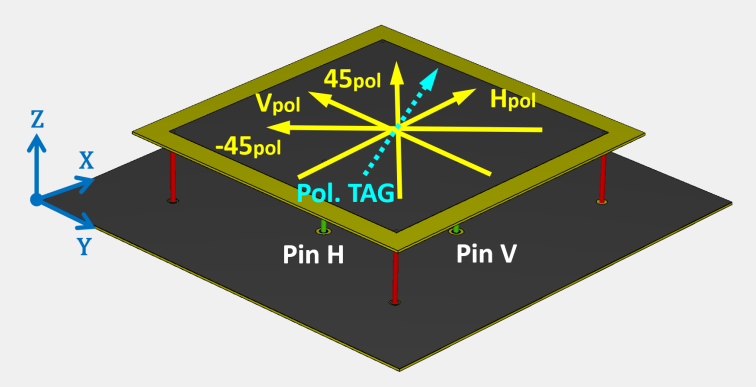

Figure 4.19: The four polarization axes related to the polarizations H_{pol}, V_{pol}, 45_{pol} and -45_{pol} are displayed. The worst case scenario for tag orientation is also depicted.

The reconfigurability concept proposed here is based on the manipulation of the feeding network for properly exciting the two antenna inputs *Pin H* and *Pin V*, corresponding to the two linear polarizations, for obtaining the desired pattern response. In this way, not only the H_{pol} and V_{pol} can be selected independently, but also the two diagonal polarizations 45_{pol} and -45_{pol} are added, by means of synchronously combining the two orthogonal feedings and by applying the correct phase difference, as illustrated also in Fig. 4.19. Hence, 45_{pol} is obtained by exciting *Pin H* and *Pin V* with exactly the same phase, while for obtaining the -45_{pol} a phase difference of 180° between the two inputs is needed.

4.4.1 Effect of the Feeding on Antenna Input Impedance

After having presented the basic concepts leading the frequency and polarization reconfigurability, a deeper characterization of the antenna is required when both approaches are applied. In this paragraph, the variation of the antenna input impedance in relation to the type of excitation that is applied to *Pin H* and *Pin V* of the suspended patch antenna will be analyzed in deep. In relation to the four switchable polarizations, three different types of excitation can be distinguished: the single pin feeding and the in-phase or out-of-phase simultaneous excitation. The first type is related to the two linear polarization H_{pol} and V_{pol}, that are obtained by exciting either *Pin H* or *Pin V*. According to the procedure described

in Sect. 4.4, the simultaneous excitation of the two antenna input pins is the key for realizing the two linear diagonal polarizations: when the two signals are in phase, the 45_{pol} is attained, conversely, when a 180° phase difference is imposed on the two inputs, the -45_{pol} is established. For the latter two feeding configurations, involving both antenna feeding pins, the concept of active impedance has to be applied. In fact, in the analysis carried out for the design of the reconfigurable matching network (see Sect. 4.3), it was considered for simplicity that just one input of the patch antenna was actually excited and the other input was terminated with 50 Ω; however, due to the coupling between the two feeding points, the input impedance of the antenna presents noticeably differences when the simultaneous excitation is applied, with considerable variation in relation to the phase difference at the feeding ports. The impact of the excitation on the input impedance is shown in Fig. 4.20, where the three types of excitations are reported. Moreover, in order to model the simultaneous excitation case (i.e. active impedance), it is used an ideal coupler for the in-phase case, while an ideal 180° phase shifter is added for the evaluation of the out-of-phase case. In Fig. 4.20, the center frequencies of the two UHF RFID bands f_{EU} and f_{US} under investigation are inserted for reference. From the figure it is clearly observed that the effect is more significant in the US band, exhibiting the worst case scenario for the in-phase excitation.

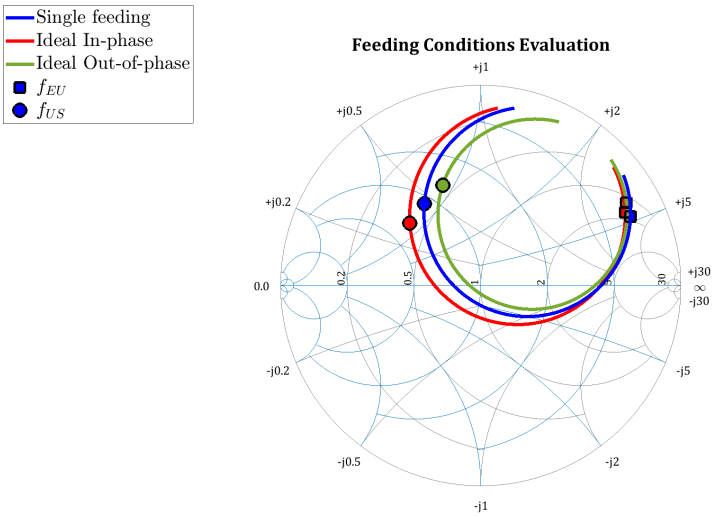

Figure 4.20: Smith chart mapping of antenna input impedance in relation to the single feeding, in comparison with the two active impedances related to the simultaneous in-phase and out-of-phase feeding. EU and US bands center frequencies are reported for all cases.

As a matter of fact, the impedances mapped on the Smith Chart in Fig. 4.20 are calculated including ideal mathematical models instead of real components (e.g.

the 180° condition is verified only at one frequency in reality). Nevertheless, they are useful to understand the behaviour of the antenna system, which is important for the definition of the reconfigurable matching network, as will be demonstrated in the following.

4.5 Frequency and Polarization Reconfigurable Systems

In this section, five different methods for realizing the reconfigurable feeding network, based on different complexity and performance levels are presented. Reflective type CMOS switches are used also in this case for enabling the polarization agility, following the considerations described in Sect.3.3.1.

4.5.1 Reconfigurable Feeding Network Based on Switched Delay Lines

In this first design, the matching network for the polarization reconfigurability is realized switching between different branch that provide different phases at the input of the frequency reconfigurability network. These delay lines are realized using microstrip lines with well-defined electrical length. In total for this configuration, four switches (*SP3T* Infineon *BGSA13GN10*) are used for the polarization reconfigurability. Two switches for each polarization branch (H_{pol} and V_{pol}) are needed for ensuring a good isolation between the active and the idle paths. Two more switches of the same type are used for enabling the frequency reconfigurability. The schematic drawing of this first design is shown in Fig. 4.21.

The feeding network is then composed by a $T-$junction at input side (whose branches are kept as shorter as possible), that connects two switches used to select among the H_{pol} and V_{pol} feeding lines constructed with correct length and impedance. Moreover, the capability of the switch to operate in *"all-OFF"* state is used to terminate the unused branches and input pins, by setting in a high impedance state all the connections (i.e. equal to the corresponding C_{OFF}).

Referring to Fig. 4.21, the four linear polarizations are obtained in the following way:

- V_{pol} is selected when *SW1* and *SW3* enable *Line A*, while *SW2* and *SW4* are set in the *"all-OFF"* state for disabling the connection with feeding lines in the H_{pol} branch;
- H_{pol} is set active by selecting *line B* through *SW2* and *SW4*, whereas the others are set to *"all-OFF"*;

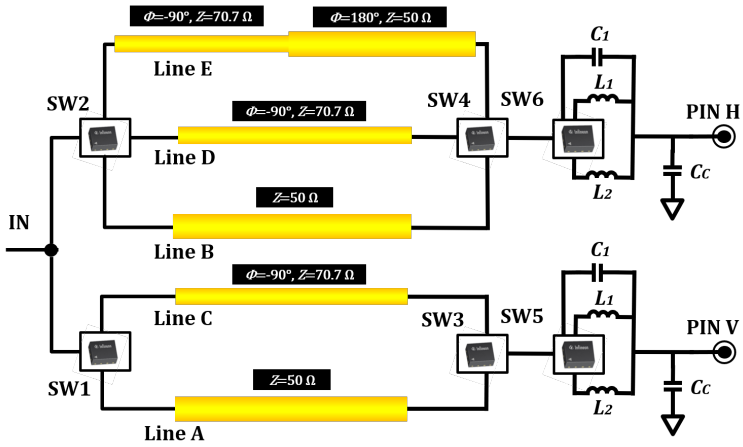

Figure 4.21: Modeled reconfigurable feeding network, including the five feeding lines that are combined to give polarization agility. Components and main elements are named for clarity.

- 45_{pol} linear polarization is obtained by feeding both the *Pin H* and *Pin V* of the patch with the same phase, imposing the 50 Ω condition at the input terminal through an impedance transformer. This is achieved through *line C* and *line D*, that are quarter wave transformers at 900 MHz (characteristic impedance $50 \cdot \sqrt{2}\,\Omega$);

- -45_{pol} linear polarization is realized in a similar way as the case 45_{pol} by selecting *line C* and *line E*. The 180° phase difference is given by *line E* that is composed by a 90°transformer and a 180° delay line (total length of 270° at middle frequency band of 900 MHz).

Concerning the two switches devoted to change the operative frequency band, named *SW5* and *SW6*, they are set as *"all-OFF"* when the corresponding branch is not enabled (thus reducing the loading effect on the antenna). Conversely, in all other cases, they are activated independently for applying frequency agility by performing the correct matching.

Similarly to the procedure used for the determination of the reconfigurable matching network, (described in Sect. 4.3), the complete feeding network is first simulated and optimized with ADS. The feeding network includes the $S-$parameter (i.e. Touchstone files) of the switches in all the configurations required for generating the four polarizations in the three frequency band states. After this optimization, the designed reconfigurable matching network is inserted in the complete 3-D model of the reduced size patch antenna loaded by distributed capacitors and simulated with Empire XPU [221] for the evaluation of the antenna parameters. With respect to the matching network defined in Fig. 4.14, a tuning was necessary for adjusting the three selectable resonances for accounting for the newly introduced

feeding structure, and in particular to the loading effect of the unused lines caused by the finite isolation of the switch. The resulting reconfigurable matching network is reported in Table 4.1.

Table 4.1: Values of Matching Network for the Switched Line Feeding

Matching Network	Values
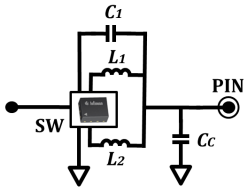	$C_c = 1.1\,pF$ $L_1 = 26\,nH$ $L_2 = 1\,nH$ $C_1 = 3.6\,pF$

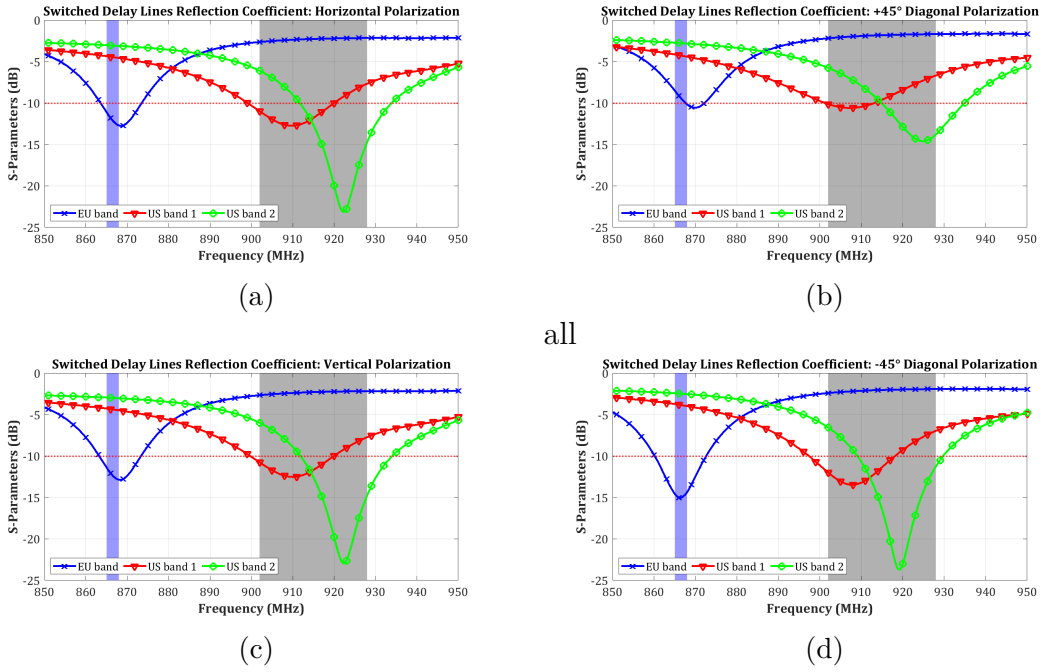

Figure 4.22: Simulated reflection coefficient for the reconfigurable feeding network antenna system based on delay lines. The frequency states corresponding to the EU band and the two US sub-bands are reported and indicated for reference. The evaluation includes the four polarization:(a) *Horizontal*, (b) *+45°* diagonal, (c) *Vertical* and (d) *-45°* diagonal.

Fig. 4.22 presents the simulated reflection coefficients for the EU and US bands in the four considered polarization states, (i.e. H_{pol}, V_{pol}, 45_{pol} and -45_{pol}). From the results reported in Fig. 4.22, it is recognized that the three bands are matched

and compliant with the -10 dB criterion, with the exception of the 45_{pol} case where the EU band is reaching the maximum reflection coefficient at 865 MHz, equal to -8.7 dB. For this case, the -10 dB matching condition is met at 867.5 MHz. A slight deviation is also detected in the US band coverage, since the overlapping is not perfect, and a maximum reflection coefficient of -9.7 dB is measured at 914.3 MHz.

For proving the analysis on the different input impedance in relation to the type of feeding (i.e. single or synchronous with 0°/180° phase difference), it is worth to display the reflection coefficients previously reported in Fig. 4.22 in a single plot, thus obtaining Fig. 4.23. From the analysis of Fig. 4.23 it is noticed that the shift in frequency in the three bands has the same trend in relation to the different polarization states, that is directly related to the results displayed in Fig. 4.20. In particular, the matching for H_{pol} and V_{pol} is almost identical (small difference is given from the different feeding path topology), while for -45_{pol} a slight frequency shift is detected, along with an overall improved matching condition in all bands, given by a more effective matching provided by the common shunt capacitor with the new impedance mapping (referring to the description of the matching network in Sect. 4.3). In contrast, for the 45_{pol} a degradation of the overall matching is recognized, which imply that the common shunt capacitor is not providing the necessary impedance transition for the alignment to the constant 50 Ω circle, as in the other cases (see Fig. 4.12b). This is in line with the theoretical results displayed in Fig. 4.20 and the characterization made so far for the H_{pol}/V_{pol} and the -45_{pol}, since the resulted impedance has an inverse trend with respect to the -45_{pol} case (best scenario). Moreover, from this analysis is it demonstrated that the final composition of the matching network has to be finalized by considering the complete model, including the switches and the SMD components, as well as the patch antenna and feeding network, for counting for all the effects. Clearly, the analysis made for the switchable delay lines case can be applied also to the other designs, that will be discussed in the following.

The full wave simulation model provides also the antenna realized gain, reported for the two center frequencies of 867 MHz for the EU band in Figs. 4.24 and 4.25, while 915 MHz is used for the US band (associated with the upper US band frequency state), corresponding to Figs. 4.26, 4.27. For all the considered frequencies, the measured $E-$ and $H-$ planes of the radiation patterns are consistent with the related polarization state. In particular, for the EU band, shown in Fig. 4.24 and Fig. 4.25, the realized gain is stable in the four polarization cases, with a maximum co-polar gain of 2 dBi. Moreover, in all the gain plots, the cross-polar component is below -15 dB (maximum measured at -17.1 dBi). Analysing the co-polar component of the radiated electric field in at 915 MHz, reported in Fig. 4.26 and Fig. 4.27, it is found that the maximum gain is realized in the -45° diagonal polarization state, with a value of 3.2 dBi, while the minimum is corresponding to the 45° polarization case, with a value of 2.6 dBi. The maximum gain in the other two configurations is

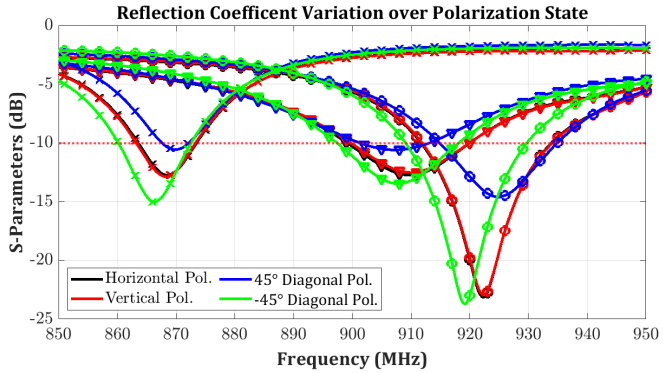

Figure 4.23: Variation of the simulated reflection coefficient in the different polarization states provided by the reconfigurable delay lines feeding network. Line markers are related to the considered matching band.

slightly higher, and equal to 2.7 dBi. Moreover, a very good polarization purity is found for the -45$_{pol}$ case, with a cross-polar component level below -28.8 dBi. The same low level of cross-polar component is noticed for the 45$_{pol}$ case, but only in the $E-$plane cut. However, in all cases the cross-polar component is below -15 dBi.

As a general comment, it is observed that the maximum gain of the suspended patch antenna is limited by the electrically small dimension of the ground plane and antenna itself, in addition to the losses introduced by the cascade of three switches, whose insertion loss is found to be approximately 0.3 dB at 900 MHz. Moreover, the latter aspect has also an impact on the total efficiency, reported in Fig. 4.28 for the four polarizations H_{pol}, V_{pol}, 45$_{pol}$ and -45$_{pol}$. From Fig. 4.28 it can be noticed that in all cases the resulted efficiency is above the theoretical 50% limit (related to and idealize CP approach), in particular improving the efficiency of almost the complete US band by 10%.

The solution reported here, although simple to realize, shows some limitations in terms of the number of switches required (i.e 6 switches are needed for the complete reconfigurability), and concerning the amount of occupied PCB area, as shown in Fig. 4.29, where the proposed solution is translated into a PCB layout. In particular, the high number of switches involved causes a decrease of total efficiency and a limitation of peak gain. In the following, more optimized solutions are adopted for the realization of the frequency and polarization reconfigurable antenna in a more compact and component-effective way.

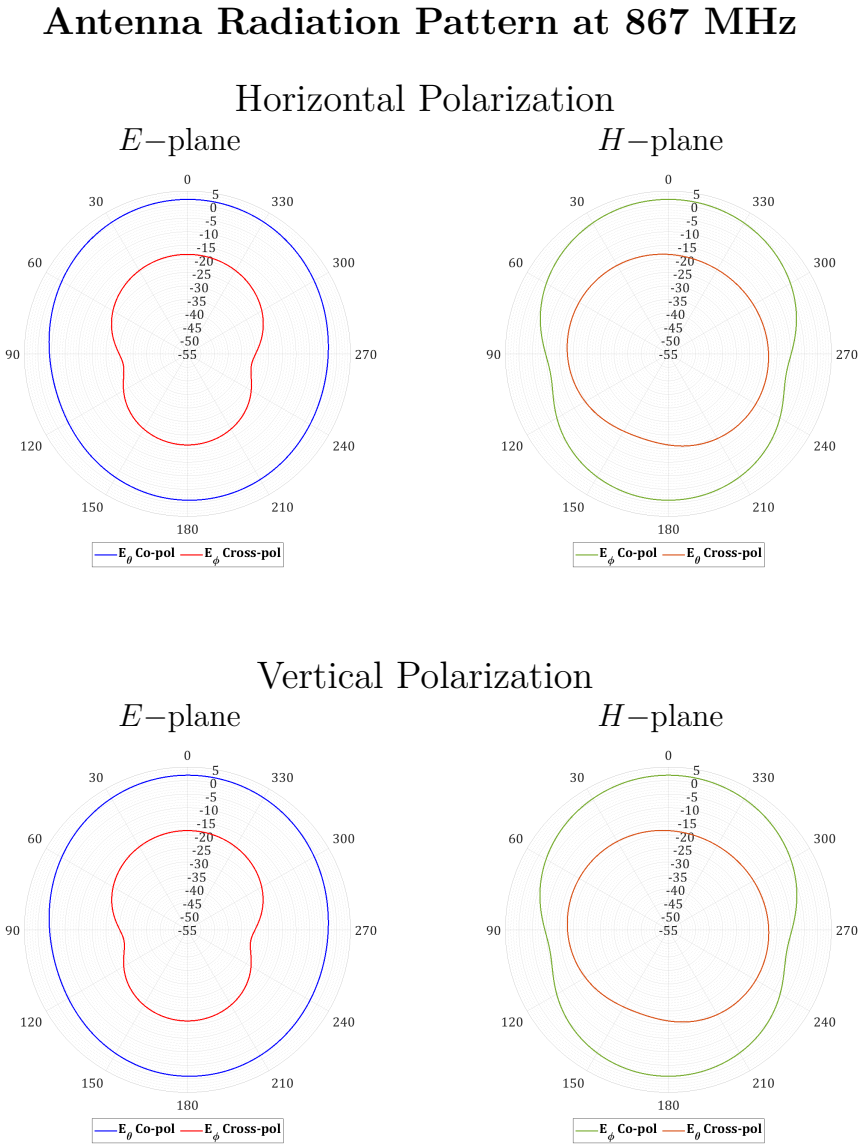

Figure 4.24: Simulated radiation patterns at 867 MHz, relative to the EU band frequency state, of the antenna with reconfigurable delay lines feeding network, in the *Horizontal* and *Vertical* polarization states. In agreement with the considered polarization, the $E-$plane and $H-$plane components of the electric fields are reported.

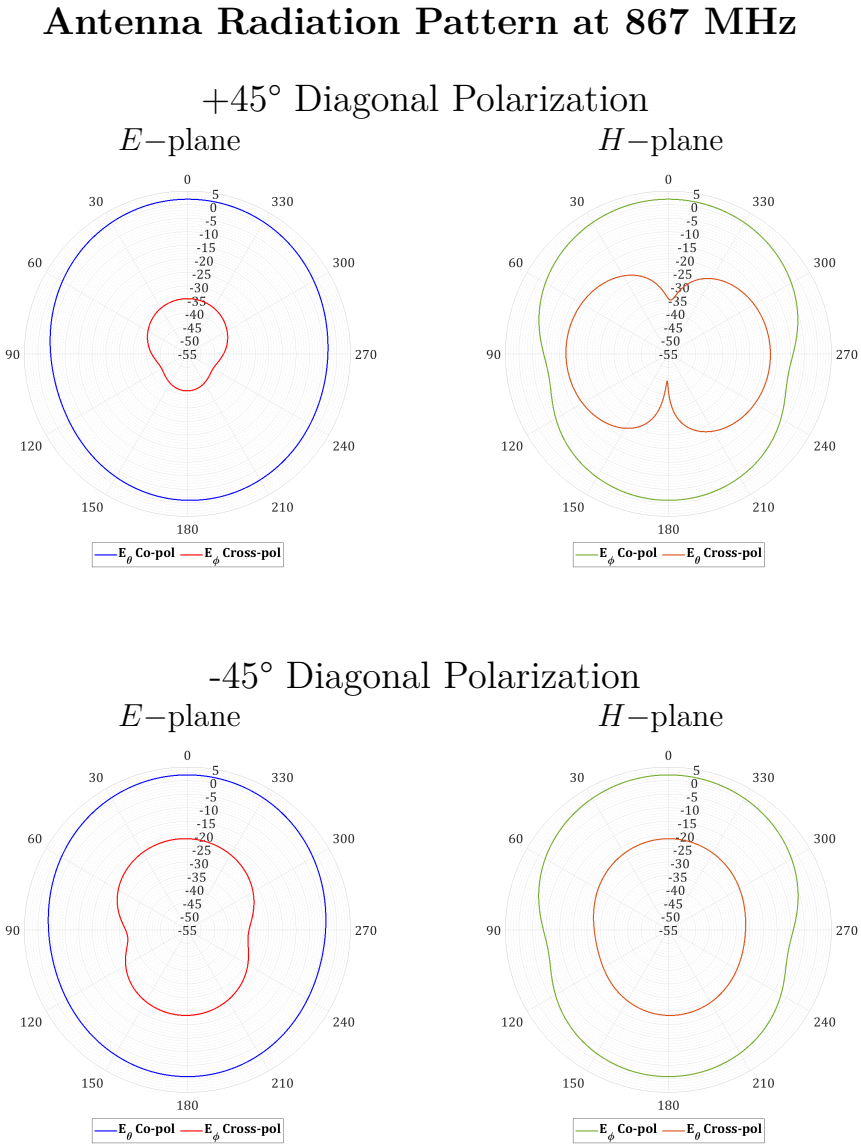

Figure 4.25: Simulated radiation patterns at 867 MHz, relative to the EU band frequency state of the antenna with reconfigurable delay lines feeding network, in the two diagonal *+45°* and *-45°* polarization states. In agreement with the considered polarization, the $E-$plane and $H-$plane components of the electric fields are reported.

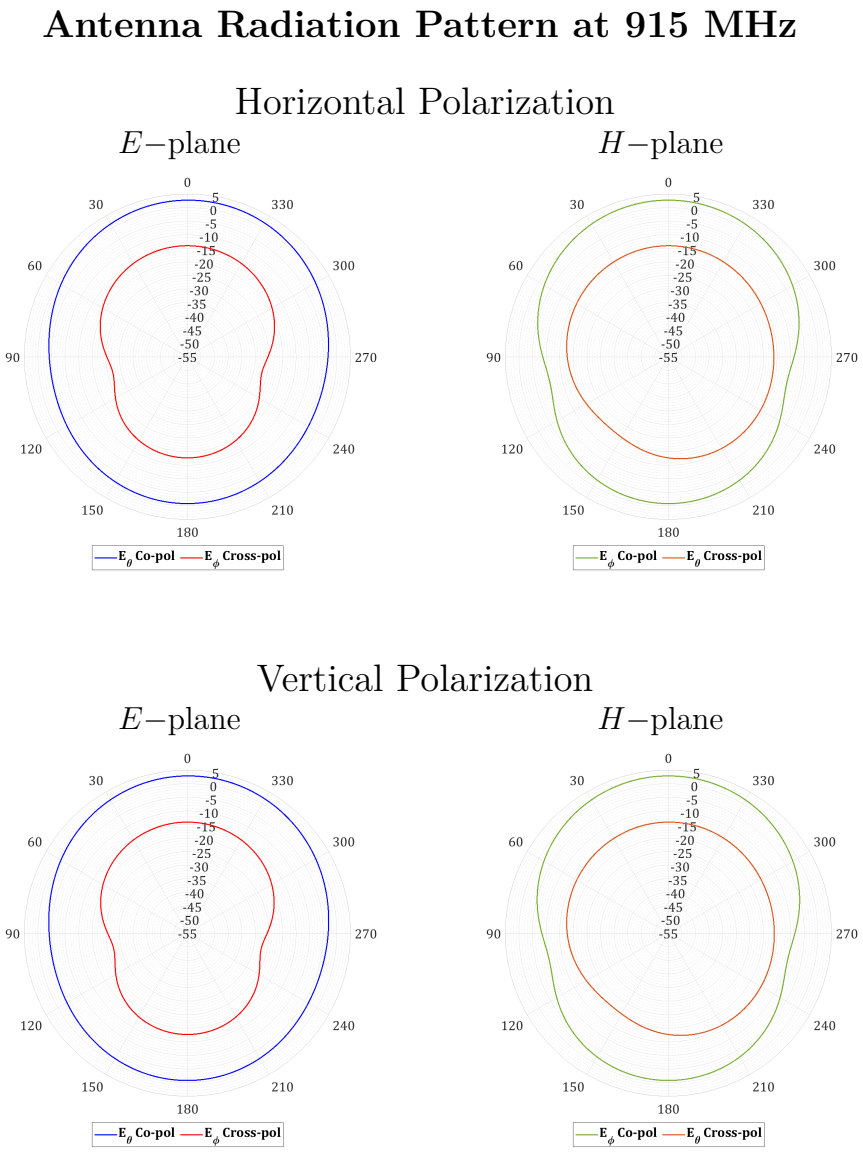

Figure 4.26: Simulated radiation pattern at 915 MHz (related to the upper US band) of the antenna with reconfigurable delay lines feeding network, in the *Horizontal* and *Vertical* polarization states. In agreement with the considered polarization, the $E-$plane and $H-$plane components of the electric fields are reported.

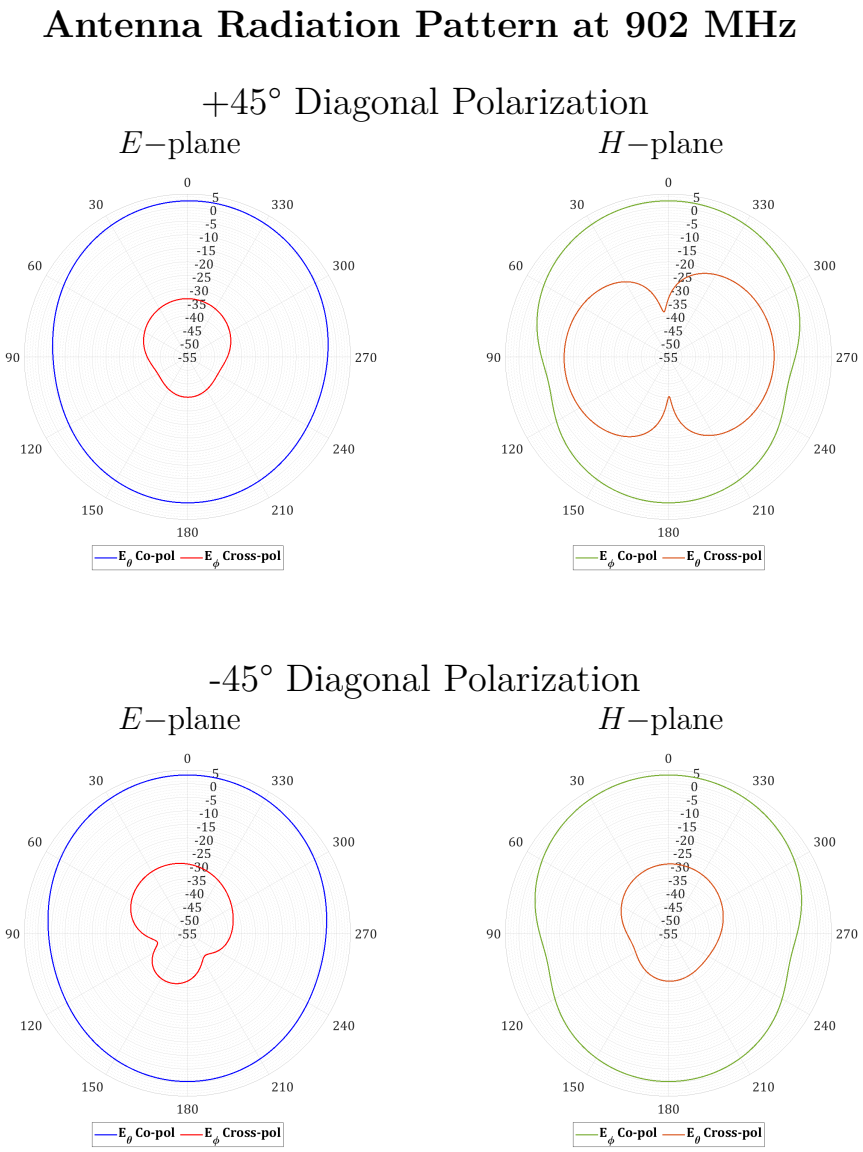

Figure 4.27: Simulated radiation pattern at 915 MHz (related to the upper US band) of the antenna with reconfigurable delay lines feeding network, in the two diagonal *+45°* and *-45°* polarization states. In agreement with the considered polarization, the $E-$plane and $H-$plane components of the electric fields are reported.

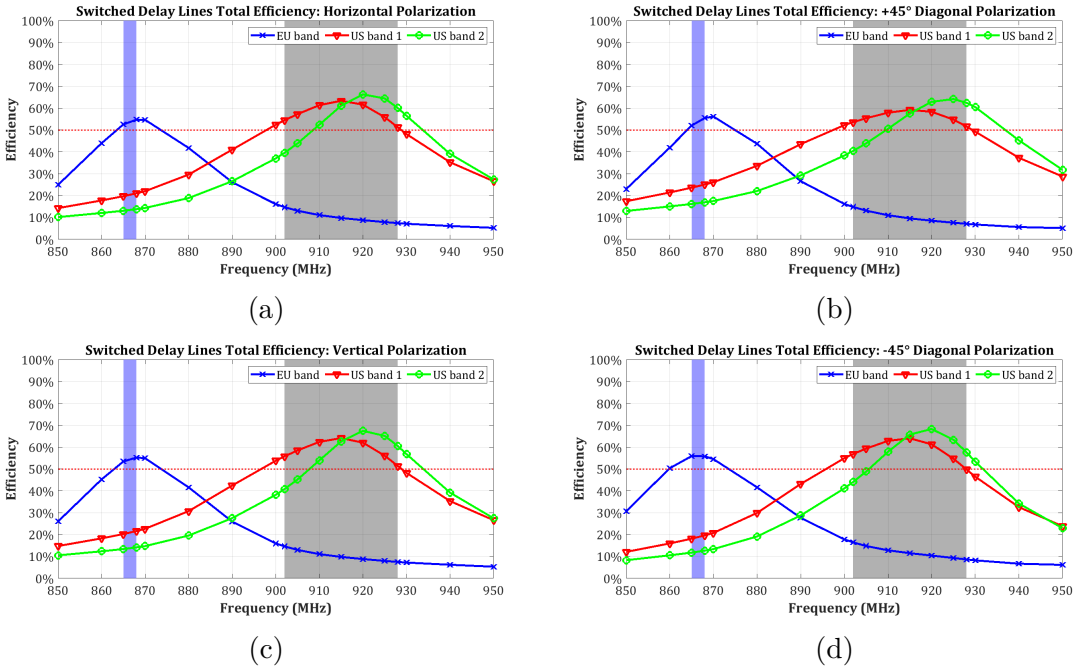

Figure 4.28: Simulated antenna total efficiency for the reconfigurable feeding network antenna system based on delay lines. The frequency states corresponding to the EU band and the two US sub-bands are reported and indicated for reference. The evaluation includes the four polarizations:(a) *Horizontal*, (b) *+45°* diagonal, (c) *Vertical* and (d) *-45°* diagonal. The 50% limit, related to an ideal CP antenna, is also shown.

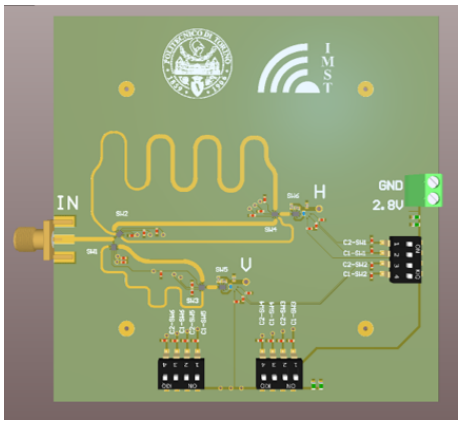

Figure 4.29: Preliminary PCB layout of the proposed reconfigurable feeding network allowing frequency and polarization agility to the reduced size patch antenna.

4.5.2 Compact Reconfigurable Feeding Network Based on Artificial Transmission Lines

A more compact solution compared to the microstrip based concept described in the previous paragraph (i.e. 4.5.1) is to replace the standard transmission lines with Artificial Transmission Lines [243], already described in 3.2. Then, with ATLs, a fixed length transmission line can be synthesized by a periodic structure whose phase is controlled by the number of $T-$shaped unit cells and the phase contribution for each of them. Therefore, the total electrical length of such a structure is almost independent from its physical size. This is especially beneficial for replacing the long 270° line used in the previous design. Moreover, by adopting this solution, not only the transmission lines can be realized in a more compact way, but also it is possible to construct 0° lines, simply balancing the negative phase attained by the RH lines (both microstrip and ATLs) and the positive phase advance introduced by the LH-ATLs. Therefore, this feature can be exploited for optimizing the design: by using 0° lines for connecting the orthogonal feeding pins of the patch in the polarization states H_{pol}, V_{pol}, and 45_{pol}, the 270° lines is no more necessary in the -45_{pol} case, since it can be replaced by a 180° line. The working principle of this solution is similar to the one discussed in 4.5.1, however the definition of the reconfigurable feeding network can be further improved by considering that the small C_{OFF} of the switches is a good approximation of an *OPEN* at 900 MHz, and by employing just 0° and 180° lines, the *OPEN* is ideally transferred to the opposite terminal of the ATL. This means that only one switch is needed for selecting the correct line in order to produce the requested polarization state, without the needs of a second one for decoupling it to the other lines. Clearly, this solution can be applied due to the narrowband UHF RFID standard for both EU and US bands.

As illustrated in Fig. 4.30, the feeding network comprises a $T-$junction at input side that connects two *SP3T* switches used to select among the H_{pol} and V_{pol} feeding lines, designed with the combination of the dual RH and LH ATLs concept. Referring to Fig. 4.30, all the *Lines A-E* are based on unit cells with a transmission line length of 2.5 mm. The method for realizing the four polarization states is detailed in the following. The V_{pol} is selected by enabling *Line A* through *SW1*, while *SW2* and *SW4* are set in *"all-OFF"*. *Line A* is a 0° phase 50 Ω line constructed of two LH-ATL unit cells with an attained phase calculated to compensate a 17 mm long microstrip transmission line. Similarly, H_{pol} is active by selecting *Line B* through *SW2*, while *SW1* and *SW3* are set to *"all-OFF"*. It is noticed here that *Line B* uses the same design as *Line A*. The 45_{pol} linear polarization is obtained by simultaneously connecting *Pin H* and *Pin V* with equal phase, through *Line C* and *Line D*, characterized by an electrical length of 0° (at center frequency of 900 MHz). *Line C* and *Line D* are composed by a superposition of two 50 Ω RH-ATL unit cells for attaining the phase of -90°, and two LH-ATLs with Bloch impedance of 70.7 Ω (i.e. $50 \cdot \sqrt{2}\,\Omega$) with +90° phase contribution. This solution

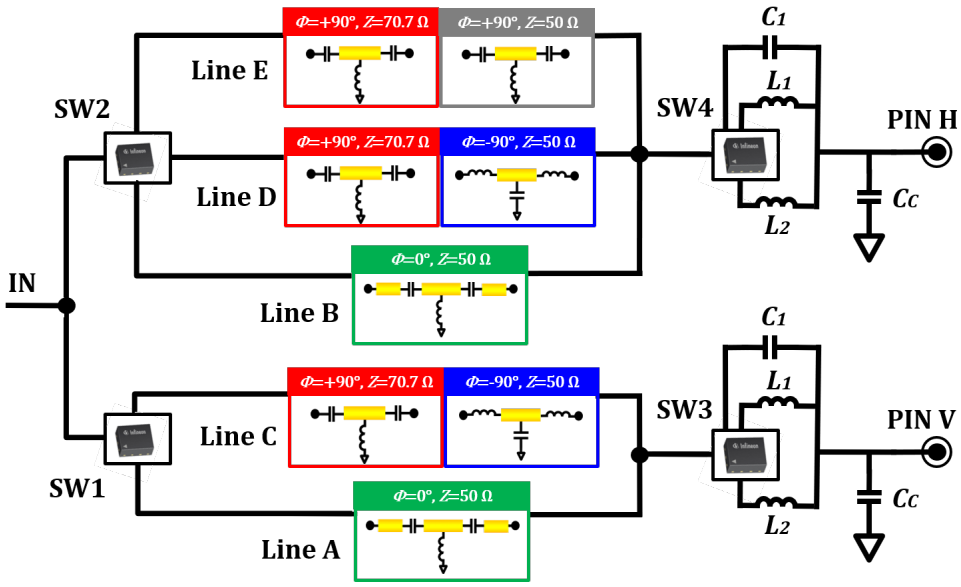

Figure 4.30: Block scheme of the reconfigurable feeding network based on ATLs. Switches, matching components and the employed ATL structures are depicted and named for clarity.

is necessary in order to have the correct 50 Ω matching condition at the system input. Finally, -45$_{pol}$ is achieved in a similar way as the 45$_{pol}$ diagonal case, by selecting *Line C* and *Line E*. In this case, *Line E* is a 180° ATL composed by two sections of LH-ATL, each of them composed of two unit cells and realizing a +90° phase shift, but differing for the Bloch impedance of the ATL periodic structure. The first section, closer to the antenna feed, has an impedance of 50 Ω, while the latter has a characteristic impedance of 70.7 Ω, for performing the 50 Ω to 100 Ω transformation. By using the theory of LH and RH lines, extensively described in [243] and [242], the five types of ATL sections necessary to complete the feeding network are derived. According to Fig. 4.30, *Lines C,D* and *Line E* are composed by two separate sections. In particular, *Lines C* and *Lines D* share the same design, and they are build as a cascade of two RH (50 Ω) and two LH (∼ 70.7 Ω) unit cells, for enhancing compactness. Similarly, *Line E* consists of four LH unit cells, having both an attained phase of 90° but with different characteristic impedance (50 Ω and (∼ 70.7 Ω)), as previously stated. The expressions for the determination of the loading capacitors C and inductors L of the four sections composing *Lines C,D* and *Line E* are straightforward, since each section is composed by $n = 2$ unit cells and it has to realize a phase of 90°, with the correct sign. Therefore, the reactive elements composing either the RH or LH artificial transmission lines are calculated from the dispersion relation of the generic $T-$type unit cells reported in (3.10) in Sect. 3.1. Moreover, together with the dispersion relation (3.10), it is fundamental to use the

Bloch impedance Z_{BL}, which is set equal to the characteristic impedance of the line. In this way, the two values of capacitors C and inductors L are obtained by using the condition $L = C \cdot Z_{BL}^2$. Then, the phase delay of the microstrip lines that will be employed in the phase calculations of the ATLs is defined as $\phi_l^x = \beta_l^x l_l = \omega\sqrt{\mathcal{L}^x \mathcal{C}^x} l_l$, where $\omega = 2\pi f$ is the angular frequency, β_l^x is the phase constant of the specific line (with characteristic impedance Z^x depending on the line type) and $l_l = 2.5$ mm its length, which is equal for all the considered ATLs. Finally, $\mathcal{C}^x$ and $\mathcal{L}^x$ are the distributed capacitance and inductance of the specific microstrip line used in the definition of the $T-$type unit cell. More in detail, the two phase delays ϕ_l^{70} and ϕ_l^{50} respectively related to the $50 \cdot \sqrt{2}\,\Omega$ and $50\ \Omega$ transmission lines, are used in the following analytical formulation. Therefore, in 4.3 the two equations that completely specify the respective ATL sections are reported, where the two corresponding impedance (named I and II) composing *Line C* and *Line D* are reported for clarity:

$$\textbf{Line C, D} \begin{cases} Z_{LH}^{I} \approx 70.7\,\Omega & \Longrightarrow n\left(\dfrac{1}{\omega\sqrt{L_{p1}C_{p1}}} - \phi_l^{70}\right) = \dfrac{\pi}{2} \\ Z_{RH}^{II} = 50\,\Omega & \Longrightarrow n\left(-\omega\sqrt{L_{n1}C_{n1}} - \phi_l^{50}\right) = -\dfrac{\pi}{2} \end{cases} \tag{4.3}$$

Similarly, *Line E* is specified as a cascade of two LH-ATLs, both with total phase contribution of 90° but different characteristic impedance, as clarified in (4.4).

$$\textbf{Line E} \begin{cases} Z_{LH}^{I} \approx 70.7\,\Omega & \Longrightarrow n\left(\dfrac{1}{\omega\sqrt{L_{p2}C_{p2}}} - \phi_l^{70}\right) = \dfrac{\pi}{2} \\ Z_{LH}^{II} = 50\,\Omega & \Longrightarrow n\left(\dfrac{1}{\omega\sqrt{L_{p3}C_{p3}}} - \phi_l^{50}\right) = \dfrac{\pi}{2} \end{cases} \tag{4.4}$$

The two 0° lines *Line A* and *Line B* are realized with $n = 2$ unit cells which are used to compensate the negative phase contribution of a 17 mm long transmission line with characteristic impedance of 50 Ω. This transmission line is divided into two section, located at the sides of the LH-ATLs, which is here indicated as ϕ_l^0. At the mid frequency of 900 MHz, the phase contribution of the 17 mm line is equal to approximately 30°. Therefore, the *Line A* and *Line B* are determined by (4.5):

$$\textbf{Line A, B} \quad \Longrightarrow \quad n\left(\frac{1}{\omega\sqrt{L_{p4}C_{p4}}} - \phi_l^{50}\right) = \phi_l^0 \tag{4.5}$$

The reconfigurable concept described so far has been evaluated through simulations, by combining the work in ADS for the definition of the ATL lines, and lately

by using the EM solver for the complete antenna characterization. More specifically, in the circuital model of the reconfigurable feeding network it is included the measured $S-$parameters of the *BGSA13GN10* switches and of the employed *muRata* inductor and capacitor families, by using the *LQW15* and *GRM15* libraries available online. In this way, a reliable model of the LH and RH artificial transmission lines is achieved and all the frequency/polarization switching states can be assessed. From the circuit simulations, the maximum insertion loss of the ATL feeding line is expected to be 0.7 dB (including the contribution of *SW1,SW2*), while the maximum phase error with respect to the theoretical 0° and 180° values in the whole EU and US bands is 4.7° and 3° respectively.

The final component definition of the reconfigurable feeding network is displayed in Table 4.2, where also the tuned components of the reconfigurable matching network were reported. It is noticed that the value of C_{L4} is resulting from the series of two capacitors, which belongs to two adjacent LH-ATls. It is here noticed that, by previously setting the length of the $T-$type unit cell of the ATLs, the overall design results in a very compact realization of the frequency and polarization agile feeding network.

Moreover, due to the particular topology of the feeding network, which uses just two switches for selecting among the feeding lines *Lines A-E*, a strong loading effect of the inactive lines is experienced in the two nodes (located at *SW3* and *SW4* common input pin). Therefore, the initial components used for the frequency switchable matching (see Fig. 4.14) need to be adjusted, in order to compensate for the effect of the polarization reconfigurable feeding network in all the four states, since the main source of deviation from the matching condition is given by the open lines, which acts like stubs, showing also a condition dependent on the specific feeding configuration. Actually, as previously explained, the rationale of using just one switch to select the wanted feeding line is based on the possibility to realize the feeding just by employing 0° and 180° lines, which can ideally transmit the input impedance to the end, without any change. However, in reality, the designed ATLs exhibit some losses, which "move" the impedance toward the center of the Smith chart. Moreover, it is noticed that the 0°/180° condition is verified just at one frequency, then also a clockwise transition of the impedance will occur. These considerations can be graphically observed in Fig. 4.31, where the impedance of the *Lines B,D,E* in the *OFF* state of the switch at the *SW4* node are mapped in the Smith chart. In order to do this, each line has been evaluated separately, (i.e. the other lines are disconnected and terminated to 50 Ω load). From Fig. 4.31 it can be noticed that the best case is related to *Line B*, while a consistent deviation from the high impedance point is shown for *Line E* and in particular for*Line D*, where the clockwise transition mapped in the Smith chart is clearly visible.

The integration of the circuital model of the feeding with the antenna in the EM simulator allows to evaluate the complete performance of the antenna. In Fig. 4.32 the simulated reflection coefficients in the EU and US bands for the four polarization

Table 4.2: Values of Components of the Switched ATLs Feeding Network

Lines A, B	**Values**
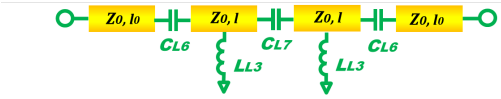	$Z_0 = 50\,\Omega$, $l = 2.5\,mm$ $l_0 = 17\,mm$ $C_{L1} = 22\,pF$, $C_{L2} = 10\,pF$ $L_{L1} = 33\,nH$
Lines C, D	**Values**
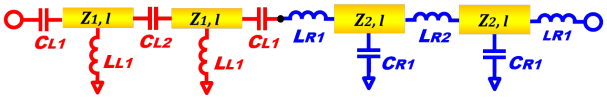	$Z_0 = 50\,\Omega$, $Z_1 = 70.7\,\Omega$ $l = 2.5\,mm$, $C_{L2} = 8.2\,pF$ $C_{L3} = 3.9\,pF$, $L_{L2} = 10\,nH$ $L_{R1} = 3\,nH$, $L_{R2} = 6\,nH$ $C_{R1} = 2.4\,pF$
Line E	**Values**
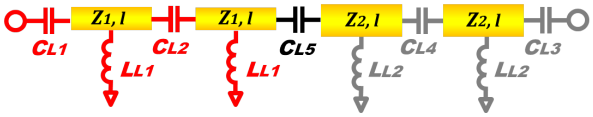	$Z_0 = 50\,\Omega$, $Z_1 = 70.7\,\Omega$ $l = 2.5\,mm$, $C_{L2} = 8.2\,pF$ $C_{L3} = 3.9\,pF$, $L_{L2} = 10\,nH$ $C_{L4} = 3.3\,pF$, $C_{L5} = 5.6\,pF$ $C_{L6} = 2.8\,pF$, $L_{L3} = 15\,nH$
Matching Network	**Values**
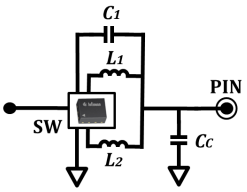	$C_c = 1.2\,pF$ $L_1 = 26\,nH$ $L_2 = 3.9\,nH$ $C_1 = 3.3\,pF$

states are shown. Even if the values of the switchable $L-$type matching network have been adjusted, not all the operating frequencies are matched. Compared to the previous solution, reported in Fig. 4.22, with this design the EU band is fully covered, but the two sub-bands are not matching the EU band completely in all the polarization states. By analyzing the results in Fig. 4.32 with the one reported in Fig. 4.22 (and also Fig. 4.15), it is clearly visible that the first US sub-band has a wider and deeper resonance with respect to the initial cases, but, in contrast, the upper sub-band is matched just in the V_{pol} and 45_{pol} states. This can be explained by the stub effect of the *OPEN* feeding lines, which are introducing a capacitive effect at the junction node, as sown in Fig. 4.31.

Figures 4.33 and 4.34 present the simulated radiation pattern in the four polarization states for the EU band (at frequency 867 MHz). In the displayed cuts, it is recognised that, as expected, the minimum of the gain occurs for the H_{pol} case, with a value of 1 dBi. The other polarizations show a quite stable gain, ranging from

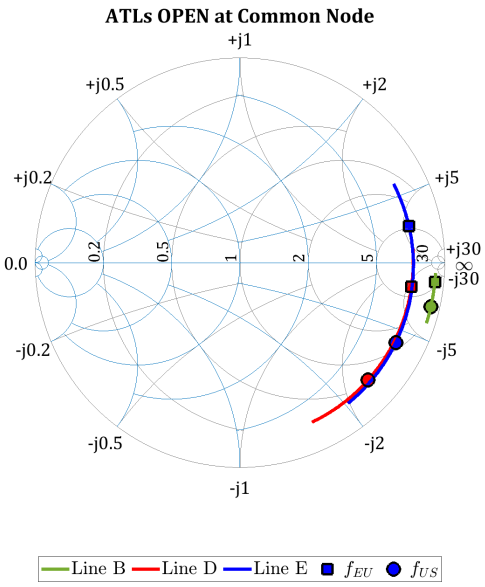

Figure 4.31: Mapping on the Smith chart of *Line B*, *Line D* and *Line E* loaded with the switch C_{OFF}.

1.3 to 1.5 dBi. Moreover, the two diagonal polarizations exhibit a lower cross-polar component, below -25 dBi with the exception of the $H-$plane cut of the 45_{pol} case, which has a maximum of -17.6 dB. For the US band, the 915 MHz center frequency is considered, and it is related to the highest sub-band. Following the analysis and comments already stated for the realized matching reported in Fig. 4.32d, it is expected a low gain for the H_{pol} and -45_{pol} polarization states. This is actually the case shown in Fig. 4.35 and in Fig. 4.36, where a minimum realized gain of 0.5 dBi is measured for the H_{pol}. Because of better matching, the highest gain is found for V_{pol}, with 1.7 dBi. The same condition, measured in relation to the lower US sub-band frequency state, gives a realized gain of approximately 2.4 dBi in both cases. The analysis of the cross-polar component of the electric field shows very good results in the -45_{pol} case, with a value below -38.3 dBi. Surprisingly, the two linear polarizations H_{pol} and V_{pol} show a worse polarization purity with respect to the initial realization using microstrip delay lines (the maximum was found to be -14.3 dBi, measured in the $H-$plane cut for the V_{pol}).

The antenna total efficiency, reported in Fig. 4.37, confirms that the mismatch losses observed in the upper band compromise the functionality of the reconfigurable feeding network. Moreover, an efficiency value slightly lower than the goal limit, set at 50% (for having improvements with respect to the ideal standard CP design), is measured in the EU frequency band. Nevertheless, the potential of the compact switched artificial transmission line is proven by considering the lower US sub-band, where an efficiency of 60% is achieved.

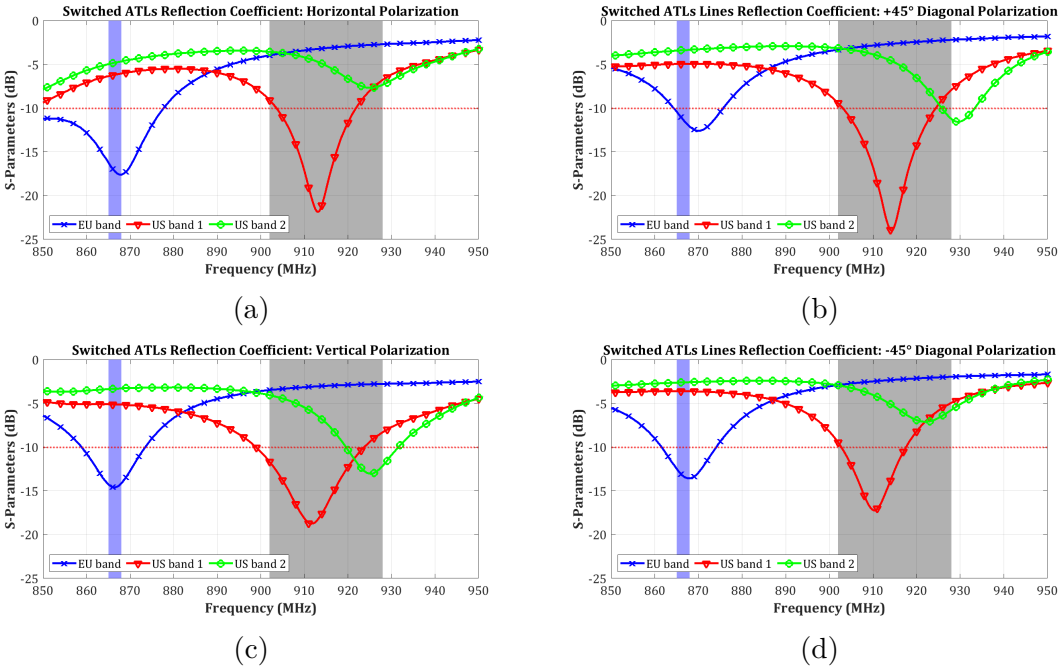

Figure 4.32: Simulated reflection coefficient for the ATL based reconfigurable feeding network antenna system. The frequency states corresponding to the EU band and the two US sub-bands are reported and indicated for reference. The evaluation includes the four polarization:(a) *Horizontal*, (b) *+45°* diagonal, (c) *Vertical* and (d) *-45°* diagonal.

This solution, employing the ATL method for synthesizing the feeding lines brings advantages with respect to the previous case, in terms of compactness and number of switches involved, as demonstrated in Fig. 4.38, where a much more compact design is presented. However, the performance of the proposed structure is not satisfactory, since the frequency coverage is not completely fulfilled and, therefore, the realized gain and total efficiency are reduced in the upper US sub-band.

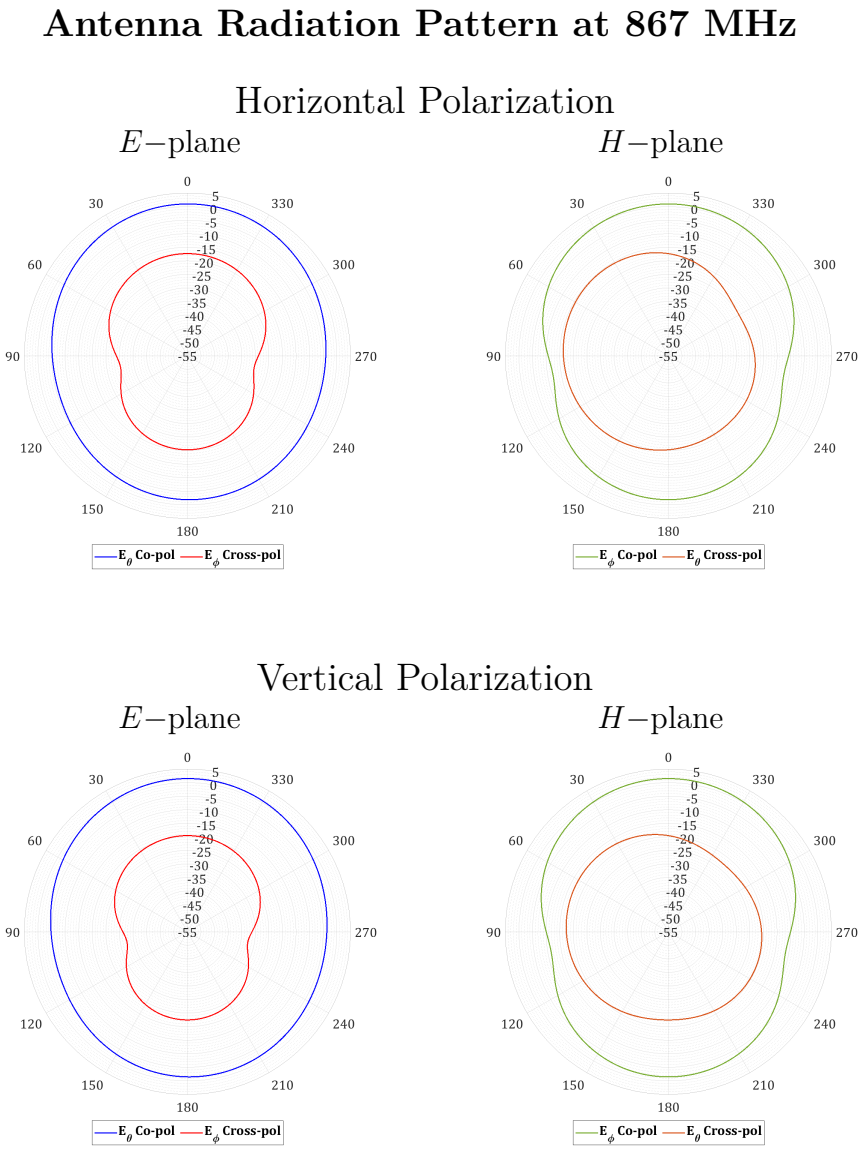

Figure 4.33: Simulated radiation pattern at 867 MHz (related to the EU band) of the modeled suspended patch with the ATL based reconfigurable feeding network antenna system in the *Horizontal* and *Vertical* polarization states. In agreement with the considered polarization, the $E-$plane and $H-$plane components of the electric fields are reported.

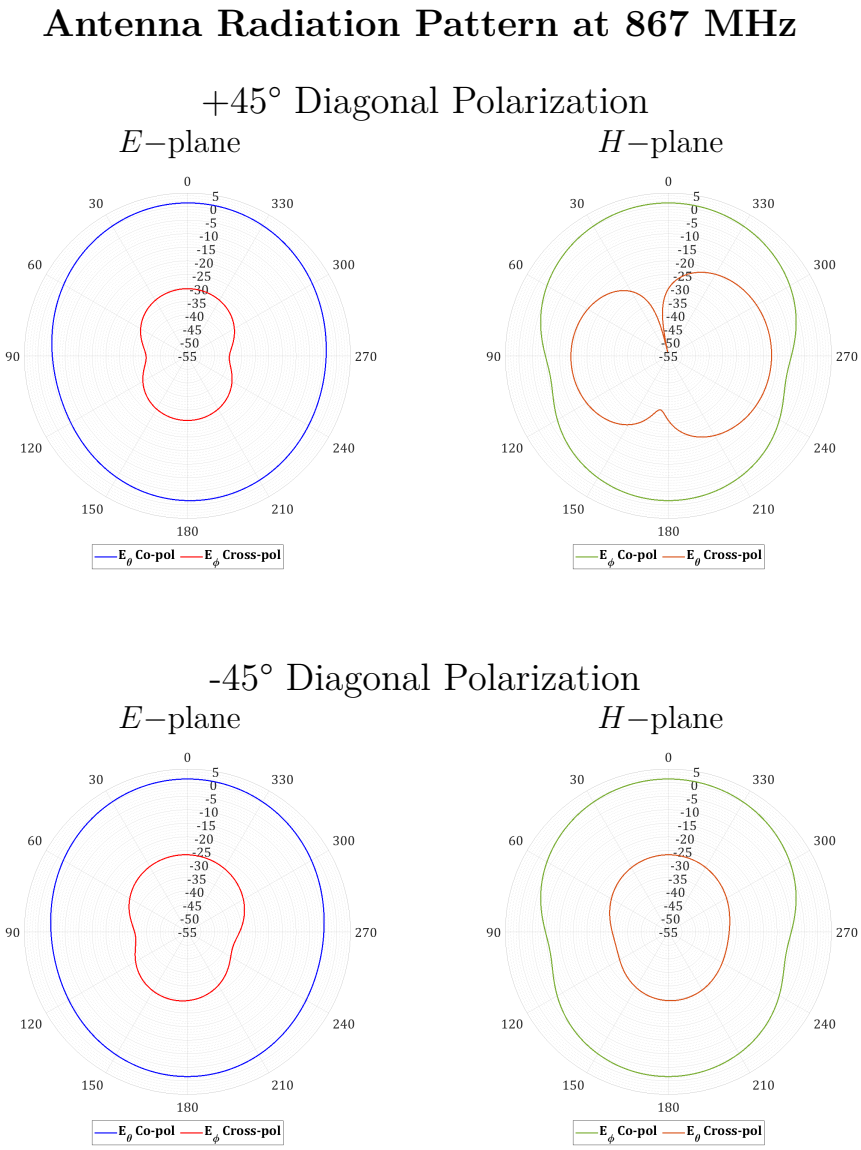

Figure 4.34: Simulated radiation pattern at 867 MHz (related to the EU band) of the modeled suspended patch with the ATL based reconfigurable feeding network antenna system in the two diagonal *+45°* and *-45°* polarization states. In agreement with the considered polarization, the $E-$plane and $H-$plane components of the electric fields are reported.

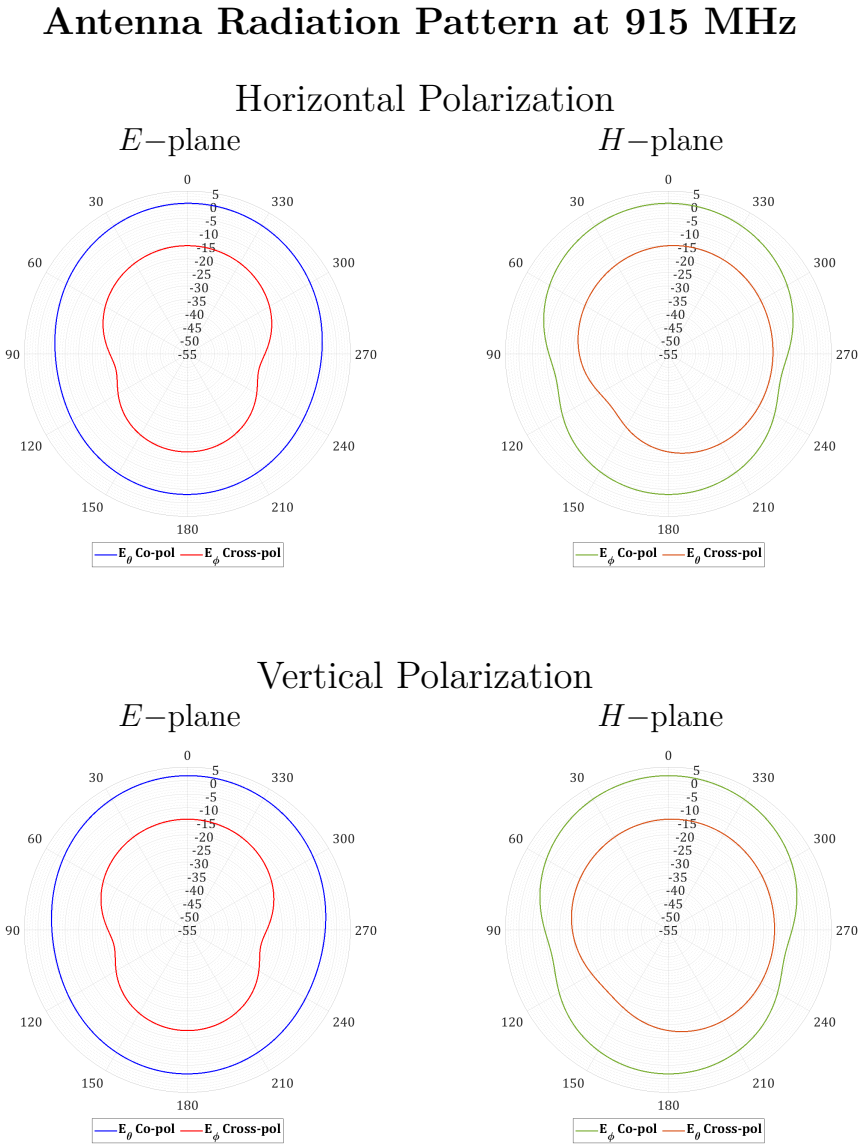

Figure 4.35: Simulated radiation pattern at 915 MHz (related to the upper US band) of the modeled suspended patch with the ATL based reconfigurable feeding network antenna system in the *Horizontal* and *Vertical* polarization states. In agreement with the considered polarization, the $E-$plane and $H-$plane components of the electric fields are reported.

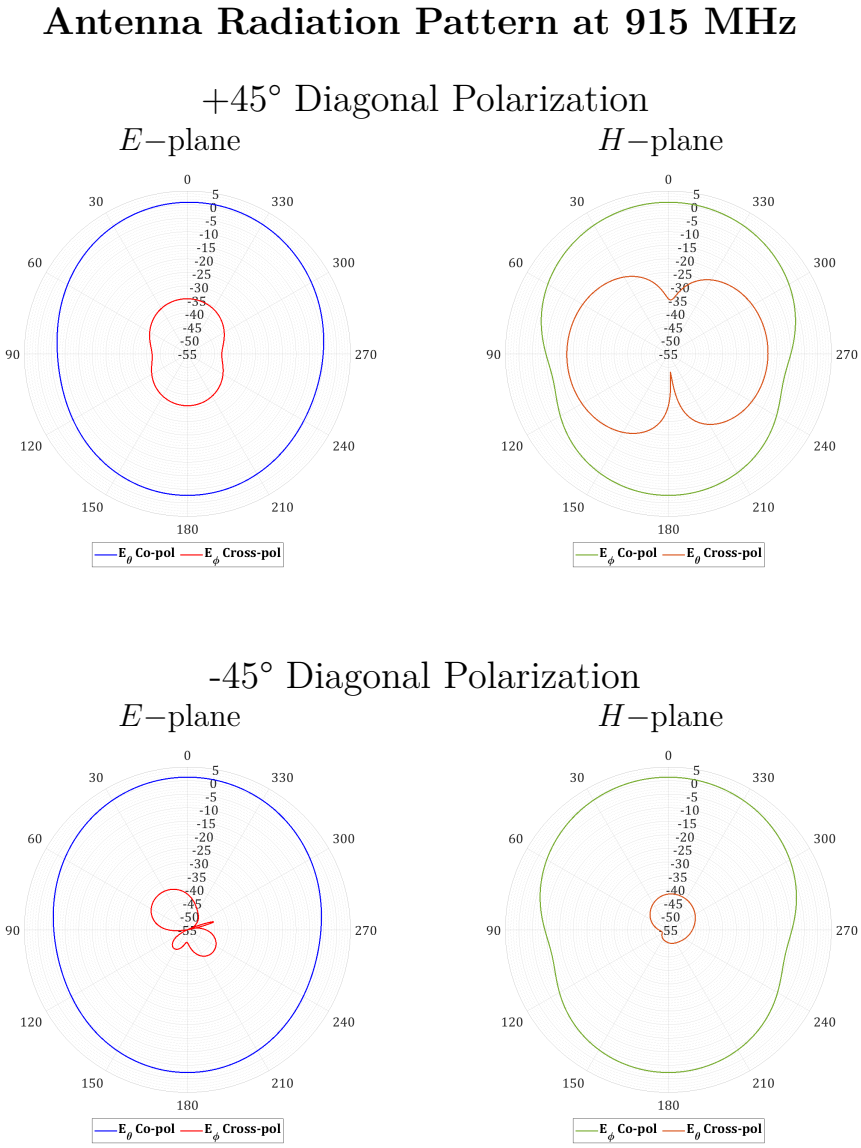

Figure 4.36: Simulated radiation pattern at 915 MHz (related to the upper US band) of the modeled suspended patch with the ATL based reconfigurable feeding network antenna system in the two diagonal *+45°* and *-45°* polarization states. In agreement with the considered polarization, the $E-$plane and $H-$plane components of the electric fields are reported.

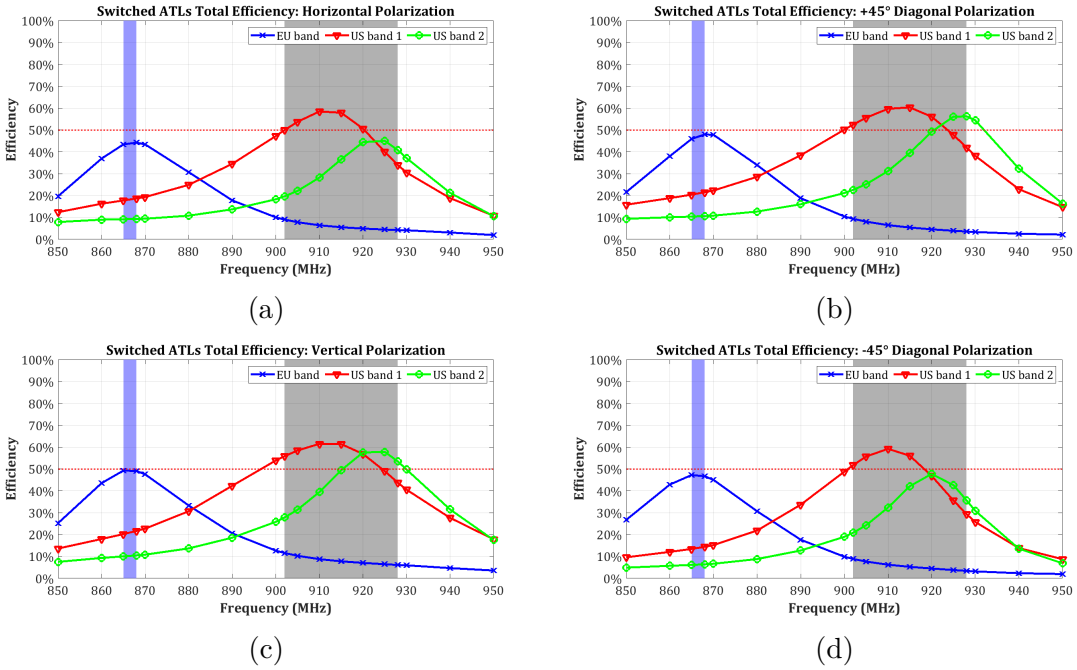

Figure 4.37: Simulated antenna total efficiency for the ATL based reconfigurable feeding antenna system. Frequency switching states are indicated for reference. The evaluation includes the four polarization:(a) *Horizontal*, (b) *+45°* diagonal, (c) *Vertical* and (d) *-45°* diagonal. The 50% limit, related to an ideal antenna with CP approach, is also shown.

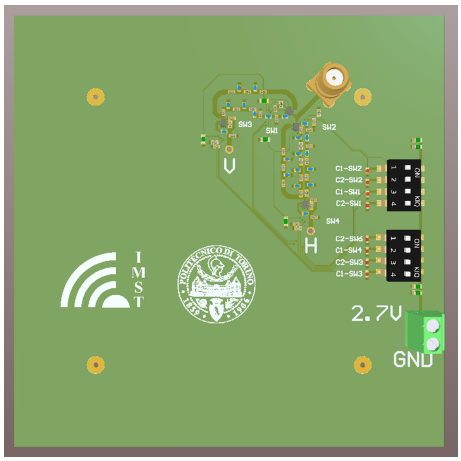

Figure 4.38: Preliminary PCB layout of the proposed reconfigurable feeding network based on ATL allowing frequency and polarization agility to the reduced size patch antenna.

4.5.3 Reconfigurable ATL Based Feeding Network Inspired by Stub Theory

A more elegant design employing the LH and RH artificial transmission lines takes advantage of the addition/subtraction of unit cells for varying the electrical length of the feeding lines, exploiting the same concept described in Sect. 3.4. In the proposed design, a completely different approach is used for fulfilling both frequency and polarization agility, by means of using the well-known procedure for matching a load with a parallel stub. In this way, it is designed a hybrid matching network composed by a series transmission line and lumped components for obtaining the matching condition, instead of the $L-$type matching network previously employed. The rationale of using the stub design instead of the $L-$type matching network is the prospect of having the full flexibility of the type of configuration of the reconfigurable matching network; specifically, the series or shunt topology, as well as the lumped element types (i.e. inductor or capacitors) can be fixed a priori, without being limited or bounded by the antenna impedance that has to be matched. As a matter of fact, it is recognized that this method can be applied to virtually any type of impedance that needs to be matched. Therefore, with this design a more general method to terminate the unused branches is applied, by adding a connection to GND to the switches devoted to frequency reconfigurability (then using a *SHORT* termination, instead of *OPEN*). As a result, a more generic switch can be selected, without being obliged to stick on the special *"all-OFF"* feature of the *BGSA13GN10*. Then, for the purpose of inserting the connection to ground, the *BGSA14GN10* [268] is employed to realize the reconfigurable matching, as it is the *SP4T* version of the already used Infineon switch. Moreover, in the proposed solution the two reconfigurable operations required to switch between the frequency bands and the polarization states can be separated, and they are considered independently during the development. Actually, in the novel concept it is used a series stub to impose an impedance transformation such that the antenna impedance $Z_A = R_A \pm jX_A$ (or equivalently the admittance $Y_A = G_A \pm jB_A$) crosses the unitary resistance/conductance circle (i.e. following the trajectory of the constant $|\Gamma|$ circles), and, then, the switch is used to select the proper component that compensates the reactive part (e.g. reactance $\pm X_A$ or susceptance $\pm B_A$) at the given frequency, using the same procedure extensively described in many books [228, 266]. Furthermore, also the stub length can be adjusted by using a switch, in order to increase or decrease its electrical length by adding/removing ATL sections, and then adapting to the different antenna impedances (related to different frequencies) for establishing the condition of crossing the unitary impedance/admittance circle. In this way, many bands can be matched by using this novel concept. Moreover, it is noticed that by using LH artificial transmission lines, the impedance transition can move from load to generator in counterclockwise direction, in contrast with the classical approach, where the transition is directed clockwise. This

solution gives a great degree of freedom for shortening the electrical length of the series line section. In the new design, only two switches are necessary for realizing the polarization reconfigurability, which are used to vary the electrical length and characteristic impedance of the feeding lines, according to the configuration that is required. In this way, the 50 Ω condition at input is ensured, as well as the feeding with the correct phase at *Pin H* and *Pin V*. By using such a switching system, the same number of switches for selecting among the four polarization are needed, as in the previous case, but in this case it is avoided the mismatch caused by the loading effects at the common nodes (see Fig. 4.31). The complete scheme of the proposed reconfigurable ATL based feeding network inspired by stub theory is depicted in Fig. 4.39.

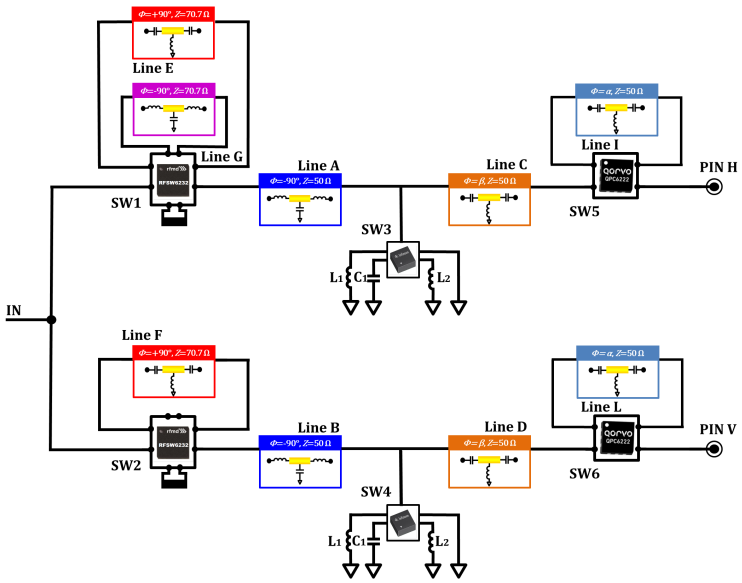

Figure 4.39: Block diagram of the complete reconfigurable ATL based feeding network inspired by stub theory.

In this design, for operating the polarization reconfigurable functionality, a switch from Qorvo (already used in the reconfigurable rat-race design Sect. 3.5) is employed, which is the synchronous $2\times SP3T$ *RFSW6232* [250]. As already mentioned, this component is used to change the feeding line length and impedance at input point, by adding a $\pm 90°$ ATL with characteristic impedance of $50\cdot\sqrt{(2)}\,\Omega$, or instead, to realize a through by shorting the two terminals of the switch for directly connecting the common input with the feed of *Pin H* and *Pin V*. From Fig. 4.39, it is noticed that in the Vertical feeding branch a different type of switch could have been used (e.g. *DPDT* type), however, in this design a full symmetric design is provided, in contrast to the previous solutions. In fact, a different type of switch would have led to amplitude error and to a different phase characteristic (i.e. group

delay) of *Line A* and *Line B*. As already mentioned, the switch *BGSA14GN10* is employed in both branches for switching among the matching components, as well as to realize the termination to the lines that have to be excluded from the feeding. Moreover, the line sections which are essential to accomplish the matching in the EU and US bands (i.e. *Lines C, D, I, L*) are controlled by two Double-Pole Double-Throw transfer switches *QPC6222* [249], used to vary the insertion point of the switches *SW3, SW4* that fulfill the matching, in accordance with the stub theory. Nevertheless, the detailed description of the new frequency reconfigurable method employed here will be performed later in the section.

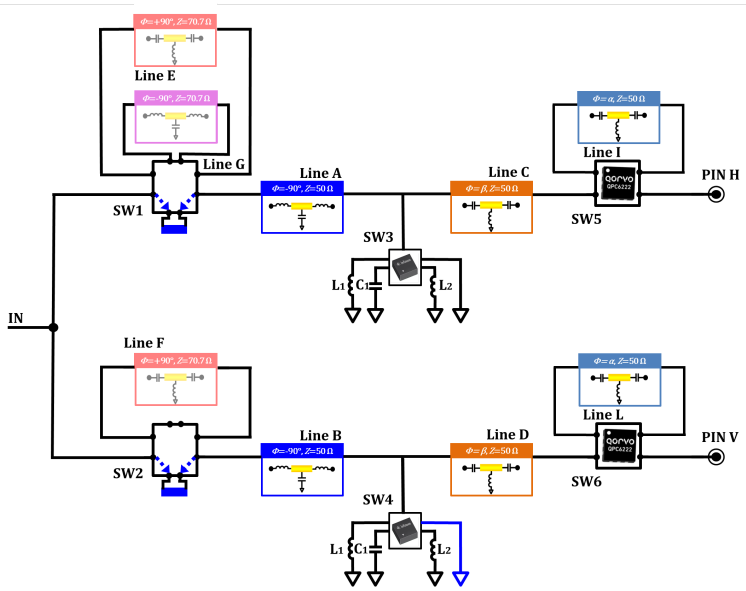

Figure 4.40: Topology of the reconfigurable feeding network for the H_{pol} operation. The lines which are not actively involved are shaded, and the switch operation is illustrated. *SW3*, *SW5*, and *SW6* are set according to the desired frequency state.

At first, the feeding topology in the *Horizontal* polarization case is analyzed. Figure 4.40 illustrates the topology of the feeding network that allows the antenna to radiate in H_{pol}, including also the internal connection of the switches. It is noticed that *SW1* and *SW2* realize a through by an external connection, thus the feeding is composed by two 50 Ω lines named *Line A* and *Line B*. As displayed in Fig. 4.40, the latter ATL is terminated to ground by *SW3*. Moreover, since *Line A* and *Line B* are designed in such a way that the electrical length from the input point and the switches *SW3, SW4* is $\lambda/4$, in this case the *Vertical* feeding branch is equivalent to an *OPEN* at 900 MHz at the $T-$junction splitting point. In order to realize such a condition, the electrical length of the RH-ATL which composes *Line A* and *Line B* have to take into account the phase contribution of the switch in crossing mode (of the same sign). A similar configuration is employed to achieve

the *Vertical* polarization, as can be noticed from Fig. 4.41, where this time *SW3* realizes the *SHORT*, and the *Horizontal* feeding branch is virtually set to *OPEN* at common input by the combination of the *SW3* state and the proper phase attained by *Line A*.

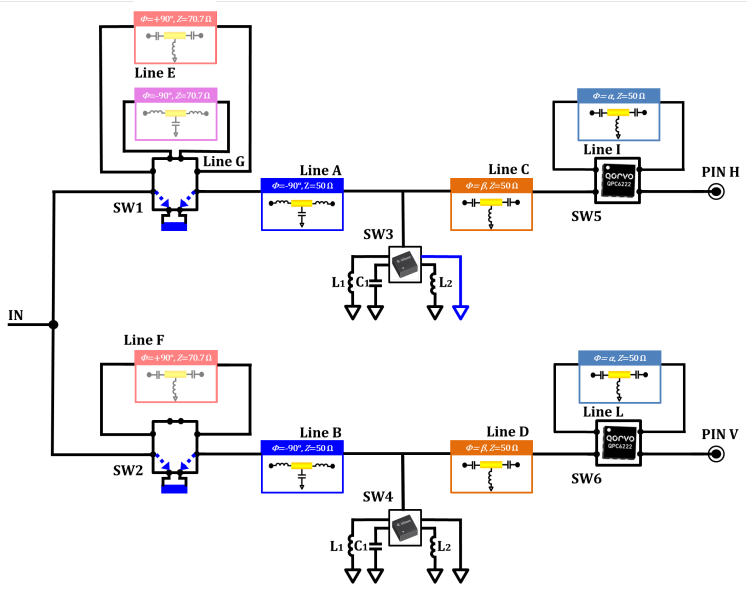

Figure 4.41: Topology of the reconfigurable feeding network for the V_{pol} operation. The lines which are not actively involved are shaded, and the switch operation is illustrated. *SW4*, *SW5*, and *SW6* are set according to the desired frequency state.

The phase equations that specify the two RH-ATLs *Line A* and *Line B* are defined in the following. The phase delay given by the switch is indicated by ϕ_{sw}, while the contributions of the microstrip lines composing both the LH- and RH-ATL unit cells are named ϕ_l^x, where the superscript is related to the characteristic impedance of the artificial transmission line (equal to the Bloch impedance, which is 50 Ω in this case, and therefore ϕ_l^{50} is used). Moreover, for keeping a small form factor of the reconfigurable feeding network, $n = 2$ unit cells are used for all ATLs. Then, the capacitors and inductors composing *Line A* and *Line B* are determined by (4.6):

$$\textbf{Line A, B} \quad \Longrightarrow \quad n\left(-\omega\sqrt{L_{n1}C_{n1}} - \phi_l^{50}\right) - 2\phi_{sw} = -\frac{\pi}{2} \tag{4.6}$$

The achievement of the *45° diagonal* polarization is realized by the simultaneous feeding of *Pin H* and *Pin V*. The aforementioned condition imposes the use of a quarter wave transformer, for achieving the 50 Ω condition at input. Therefore, the feeding network is transformed as in Fig. 4.42, where the two switches *SW1* and *SW2* are used to connect the common input and the -90° RH-ATL sections

with two 70.7 Ω LH-ATLs attaining a phase of +90°, for realizing a net phase of 0° at center frequency (i.e. 900 MHz). The insertion of the +90° LH-ATL sections, named *Line E* and *Line F*, imposes the 50 Ω to 100 Ω impedance transformation required for achieving the matching condition. Moreover, by feeding *Pin H* and *Pin V* with a total phase difference of 0° the diagonal linear polarization 45_{pol} is achieved in a very efficient way, since the two branches are identical. In fact, the choice of alternating the RH- and LH- artificial transmission line section is made on purpose, for "balancing" the group delay.

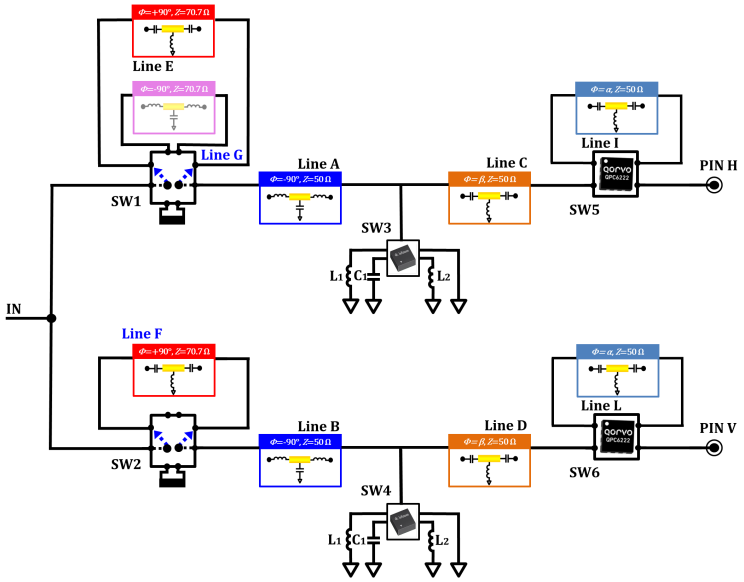

Figure 4.42: Topology of the reconfigurable feeding network for the 45_{pol} operation. The lines which are not actively involved are shaded, and the switch operation is illustrated. *SW3 SW4*, *SW5*, and *SW6* are set according to the desired frequency state.

By keeping the same ATL structure (i.e. $n = 2$ unit cells), and by considering the different delay induced by the transmission lines composing the unit cells (indicated with ϕ_l^{70} in this case), the reactive component of the two LH-ATL *Line E* and *Line F* are calculated from (4.7):

$$\textbf{Line B, C} \quad \Longrightarrow \quad n\left(\frac{1}{\omega\sqrt{L_{p1}C_{p1}}} - \phi_l^{70}\right) = \frac{\pi}{2} \tag{4.7}$$

The approach for obtaining the last polarization state of -45_{pol} is similar to case just discussed: however, a 180° phase difference is required among the feeding *Pin H* and *Pin V*. Thus, as can be noticed from Fig. 4.43, on the *Pin V* feeding branch the configuration of the switch *SW2* is the same as in the case 45_{pol}, while on the

Pin H branch the $2\times SP3T$ switch *SW1* connects *Line G*, which is a -90° phase section realized with RH-ATL. Therefore, the cascade of *Line G* and *Line A* is equal to a -180° ATL line, while as mentioned before the series of *Line F* and *Line B* gives a net phase of 0°, which imposes the phase difference at the two feeding points *Pin H* and *Pin V* to be equal to 180°, as requested from the polarization theory of the patch antenna.

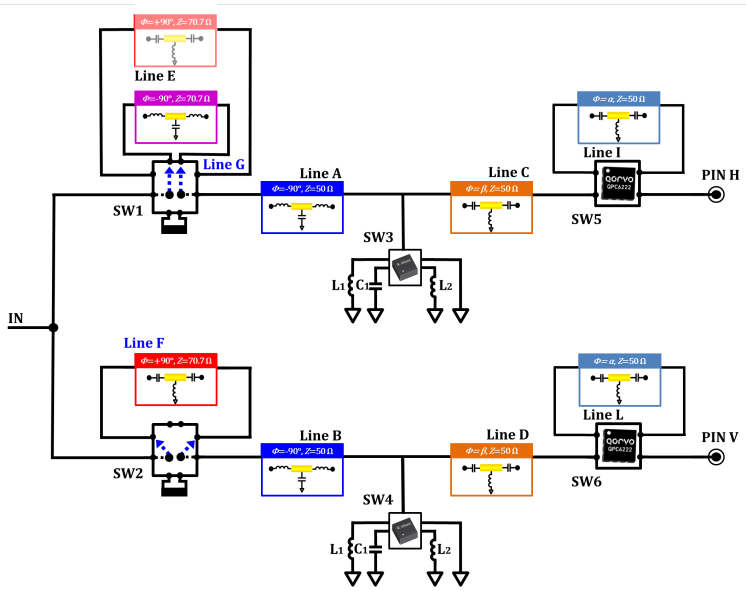

Figure 4.43: Topology of the reconfigurable feeding network for the -45$_{pol}$ operation. The lines which are not actively involved are shaded, and the switch operation is illustrated. *SW3 SW4*, *SW5*, and *SW6* are set according to the desired frequency state.

The complete analytical definition of *Line G* can be promptly found by imposing the phase condition in (4.8), applying the same method as for the other cases:

$$\textbf{Line G} \quad \Longrightarrow \quad n\left(-\omega\sqrt{L_{n2}C_{n2}}-\phi_l^{70}\right)=-\frac{\pi}{2} \tag{4.8}$$

The frequency reconfigurability solution, which characterizes the implementation of the novel feeding network type, is analyzed in the following. At first, it is considered the method for obtaining the matching of the EU band, by referring on Fig. 4.44, in which the procedure for matching the normalized input impedance $z_A = r_A \pm jx_A$ at the EU center frequency f_{EU}, corresponding to the normalized admittance $y_A = 1/z_A = g_A \pm jb_A$, is illustrated. The procedure follows the well known steps required for a single stub matching, where, in first place, it is found the electrical length of the transmission line which provides the intersection to the unitary resistance and conductance circles by following the constant $|\Gamma|$ trajectory.

This line connecting the load (i.e. the antenna input) to the generator (i.e. the feeding network, in this case), with electrical length θ_{EU}, gives the location at which the stub has to be inserted. As previously discusses, a 50 Ω LH-ATL having negative electrical length $-\theta_{EU}$ is exploited for achieving the double advantage of employing shorter lines and enhance bandwidth, thus introducing the counterclockwise transition depicted in Fig. 4.44. For being consistent with the notation used so far for analytically described ATLs, it is defined the phase attained as the negative of the electrical length $\varphi_{EU} = -\theta_{EU}$. In reality, the solution is not unique, since there are four possible points in which the $|\Gamma|$ trajectory intersects the $r = 1$ and $g = 1$ circles, referring to the impedance or admittance Smith charts respectively, at which corresponds to four possible matching configurations (inductor/capacitor in series/shunt topology). In this special design, since the solutions that are of interest are concerning shunt components, the admittance transitions crossing the $g = 1$ circle are considered in the definition of the series line. Therefore, the procedure following the consideration mentioned so far is depicted in the Smith chart in Fig. 4.44a. As can be recognized from Fig. 4.44a, starting from the initial input impedance/admittance $y_A(f_{EU}) = 1/z_A(f_{EU})$ of the UHF RFID patch antenna, the LH-ATL section attaining the phase φ_{EU} transforms the initial admittance $y_A(f_{EU})$ in $y_A^I(f_{EU}) = 1 \pm jb_A$, characterized by the real part equal to $g = 1$. At this stage, instead of placing the stub, the reactive part is compensated by the insertion of the switchable matching component, represented in this case as the shunt capacitor C_m.

In order to match the US band, the same concept is applied. However, it has to be considered the admittance transformation applied in the previous step to achieve the condition $y_A(f_{EU}) = 1 \pm jb_A(f_{EU})$, that locate $y_A(f_{US})$ in an intermediate position, which does not fulfill the requirement. This situation is clarified in Fig. 4.45a, where the line previously used for matching the EU band, attaining a phase φ_{EU}, introduces the new impedance point $y_A^I(f_{US})$. Therefore, a switching element is needed to restore the location of $y_A^I(f_{US})$ to the constant conductance circle, at the point $y_A^{II}(f_{US})$, by adding an LH-ATL section attaining the phase φ_{US}. Finally, the inductance L_m is used to compensate the susceptance and perform the perfect match at frequency f_{US}, as depicted in Fig. 4.45b.

The value of φ_{EU} and φ_{US} can be determined graphically or analytically; in this design it is adopted the second method. It is known from transmission line theory that the generic normalized impedance $z_A = r_A \pm jx_A$ is transformed to z_A^I after the introduction of a line specified by the phase φ:

$$z_A^I = \frac{z_A + j\tan(-\varphi)}{1 + jz_A\tan(-\varphi)} = \frac{(r_A + jx_A) + j\tan(-\varphi)}{1 + j(r_A + jx_A)\tan(-\varphi)} \tag{4.9}$$

where in (4.9) r_A and x_A are the resistance and reactance normalized to $Z_0 = 50\Omega$, which is the characteristic impedance of the line and of the designed system. For imposing in (4.9) the condition $g = 1$, it is used the well known equivalence

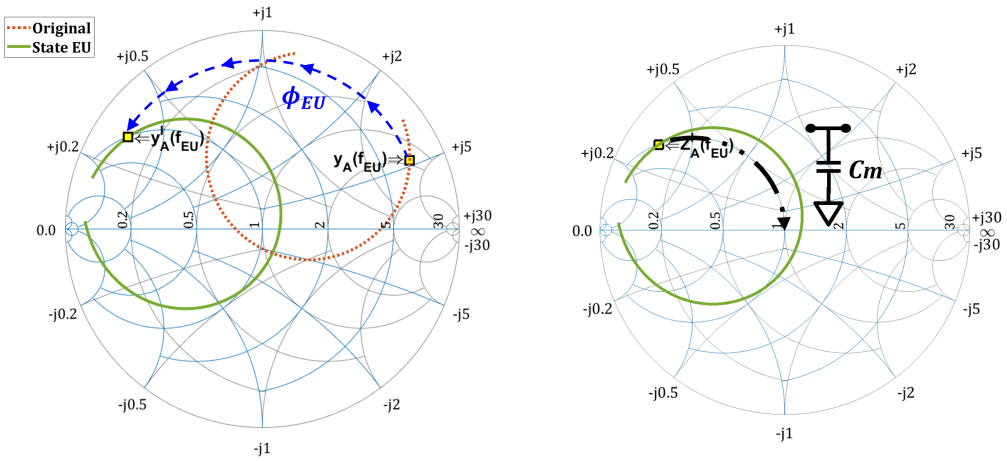

(a) (b)

Figure 4.44: Smith chart representation of the two steps required for matching the EU band: in (a) a series transmission line attaining a phase φ_{EU} imposes a rotation to the antenna input admittance $y_A^I(f_{US}) = 1/z_A^I(f_{US})$ up to the constant conductance circle $g = 1$; in (b) the shunt capacitor C_m perfectly match the impedance $y_A^I(f_{EU})$.

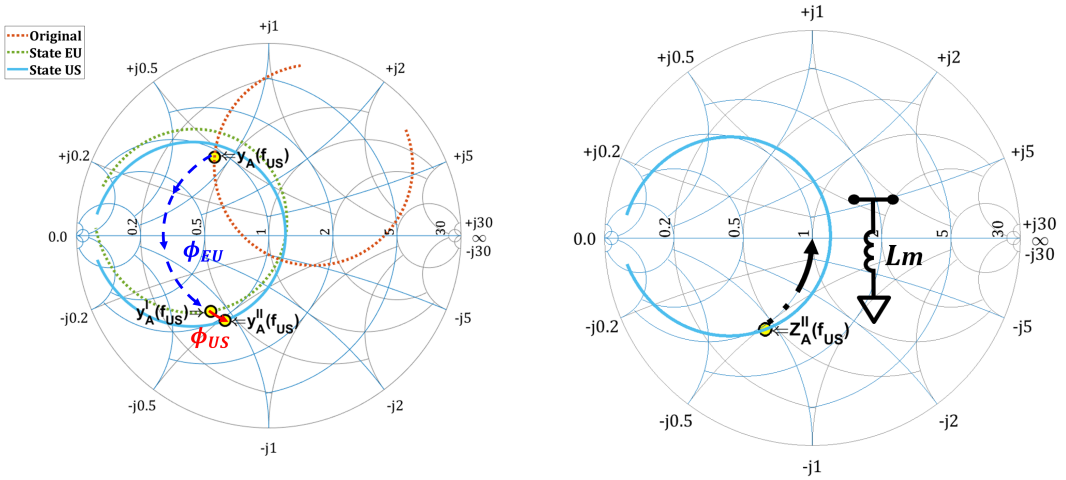

(a) (b)

Figure 4.45: Smith chart representation of the two steps required for matching the US band: in (a) a series transmission line attaining a phase φ_{US} is added to the previous line used to match the EU band, realizing the phase φ_{EU}, in order for $y_A^I(f_{US}) = 1/z_A^I(f_{US})$ to reach the constant conductance circle $g = 1$; (b) the shunt inductor L_m perfectly match the admittance $y_A^{II}(f_{EU})$.

$y_A^I = 1/z_A^I = 1 + jb_A^I$. Therefore, by separating the real and imaginary parts, and considering just the first one, it is obtained (4.10), in which it is also defined the variable $t = \tan -\varphi$:

$$g = 1 = \frac{r_A\,(1+t^2)}{r_A^2 + (x_A + t)^2} \tag{4.10}$$

After some easy math, it is found a quadratic expression (4.11), function of the variable t:

$$(r_A - 1)t^2 - 2x_A t + (r_A - r_A^2 - x_A^2) = 0 \tag{4.11}$$

The resulted φ is found from t, roots of (4.11), that is $\varphi = -\arctan(t)$, and by taking the positive solutions (corresponding to the LH-ATL positive phase contribution). Clearly, the procedure for the calculation is the same for the EU and US frequency bands, being careful to refer z_A and φ to the correct center frequency f_{EU} or f_{US}. Actually, for being compliant with the notation used in 4.45a, for the US case the total phase needed is expressed by $\varphi = \varphi_{EU}|_{f_{US}} + \varphi_{US}$, since the reconfigurable matching is made in two steps. This also leads to the conclusion that the phase that has to be added, namely φ_{US}, is found as the difference of the phases obtained from the application of (4.11) at f_{US} and the value φ_{EU} evaluated in the frequency f_{US} (i.e. $\varphi_{US} = \varphi - \varphi_{EU}|_{f_{US}}$). This point will be clarified next, where all the components of the frequency reconfigurable feeding network will be analyzed. Moreover, it is noticed that the characteristic impedance of the line, here defined as $Z_0 = 50\,\Omega$, could have been used to modify the impedance transition of the input impedance z_A to a new set of z_A^{III}, ideally bringing to the simultaneous fulfillment of the condition $g = 1$ for both the EU and US cases. However, in this design it has been chosen the more general case employing two states for setting the correct matching. As first attempt, in order to demonstrate the validity of the method described so far, the analytical solutions is directly employed for calculating the phases of the LH-ATL to be inserted. By the application of (4.11), the approximate values of $\varphi_{EU} = 60°$ and $\varphi_{US} = 58°$ are calculated starting from the two initial impedances $z_A(f_{EU}) = 1.77 + j3.76\ \Omega$ and $z_A(f_{US}) = 0.42 + j0.44\ \Omega$ for the two center frequencies $f_{EU} = 867$ MHz and $f_{US} = 915$ MHz, obtained from the antenna simulation. This results seem in contrast with what is shown in Fig. 4.45a, since the theoretical calculation demonstrate that $\varphi_{US} < \varphi_{EU}$. This is explained by the fact that that the switch is introducing a phase delay, which is counted once for the EU frequency band matching, while is giving twice the delay in the US frequency state, as shown in Fig. 4.46. In fact, it can be noticed that in Fig. 4.46a the *DPDT* switch realizes a through, while in Fig. 4.46b it uses a crossing mode to connect with *Line I*.

Therefore, the results obtained by the application of (4.11) can not be directly used in the definition of both types of LH artificial transmission lines *Line C* and

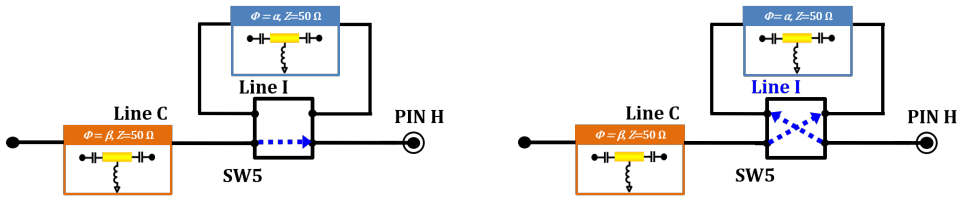

Figure 4.46: Configuration of the line section calculated using the stub matching theory for the Horizontal branch (Vertical branch is identical). In (a) EU band switch topology and (b) US band switch topology.

Line I (and similarly to *Line D* and *Line L*), as defined in Fig. 4.39. Actually, the procedure can be applied only for the first switching state (i.e. for matching the EU band), thus using the phase value of $\varphi_{EU} = 60°$ in (4.12) to calculate the inductor and capacitors composing the specific LH unit cell, setting the phase equation in the same way as for all the ATLs defined so far. Moreover, just one cell is used (namely $m = 1$) for a more compact design of the feeding branches.

$$\textbf{Line C, D} \quad \Longrightarrow \quad m\left(\frac{1}{\omega(f_{EU})\sqrt{L_{p2}C_{p2}}} - \phi_l^{50} f_{EU})\right) - \phi_{sw}(f_{EU}) = \varphi_{EU} \tag{4.12}$$

Nevertheless, if the same approach is used also for the US band, a conspicuous phase error is later found by simulation. The reason is given by the presence of the switches and the lines *Lines C,D*, which are contributing not only with the phase, but they also introduce losses that substantially modify the final φ_{US} value. A more precise definition of φ_{US} is then found by using in (4.11) not the initial impedance $Z_A(f_{US})$, but the one defined as $Z_A^I(f_{US})$ in 4.45a, therefore leading to the condition illustrated in the figure. This example prove that the all the contributions that modify the impedance matching have to be taken into account, to avoid the incurring of unrefined errors, as already mentioned in this chapter. Finally, the single unit cell $m = 1$ composing the lines *Line I* and *Line L* is specified by the appropriate phase condition reported in (4.13):

$$\textbf{Line I, L} \quad \Longrightarrow \quad m\left(\frac{1}{\omega(f_{US})\sqrt{L_{p3}C_{p3}}} - \phi_l^{50} f_{US})\right) - \phi_{sw}(f_{US}) = \varphi_{US} \tag{4.13}$$

After the application of this procedure, the matching components have been defined by means of circuit simulation, employing ADS. As previously done, the $S-$parameters of the switches and the detailed model of the *muRata* components are included. More in detail, inductors *LQW15* and capacitors *GRM15* are used in both the definition of the matching network and the artificial transmission lines. As second step, the model of the feeding network, defined for each of the frequency and

polarization states, has been inserted in the Empire 3-D model of the suspended patch antenna, for the complete characterization of the system performance. Then, in Fig. 4.47 are reported the very good matching results obtained by this approach. By first analyzing the EU frequency band, it is noticed that the matching is better than -14 dB in the H_{pol}, V_{pol} and -45$_{pol}$ cases, while a slightly worse matching is achieved in the 45$_{pol}$ state, due to the impedance shift described in Sect. 4.4.1. In the US frequency band, it is observed that the bandwidth is almost completely covered by the lower state (i.e. US band 1), with the only exception of the -45$_{pol}$ case. This result is directly related to the type of condition applied at the beginning, concerning the location of y_A in the constant conductance and resistance circles. In fact, it is noticed that the chosen condition allows to map almost all $|S_{11}|$ of the antenna in proximity of the $g = 1$ circle, as can be recognized in Figs 4.44b, 4.45b. Moreover, this condition has also the practical advantage of employing the switch in shunt configuration. For this reason, just by imposing the normalized real part of the impedance/admittance equal to one (i.e. $r = 1$ or $g = 1$) at a single frequency, all the band is well matched with just one shunt component. This is verified for the H_{pol} and V_{pol} polarization states because the are not affected by the impedance shift, described in Sect. 4.4.1. In Table 4.3 are listed the components which are composing the frequency and polarization reconfigurable feeding network inspired by stub theory.

Table 4.3: Values of Components of the Reconfigurable Stub Like Feeding

Lines A, B	**Values**	**Lines C, D**	**Values**
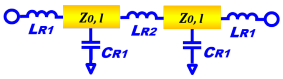	$Z_0 = 50\ \Omega$, $l = 2.5\ mm$ $L_{R1} = 2.7\ nH$ $L_{R2} = 5.6\ nH$ $C_{R1} = 2\ pF$	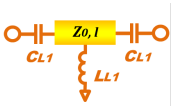	$Z_0 = 50\ \Omega$, $l = 2.5\ mm$ $C_{L1} = 5.6\ pF$ $L_{L1} = 9\ nH$
Lines E, F	**Values**	**Line G**	**Values**
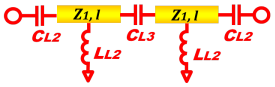	$Z_1 = 70.7\ \Omega$, $l = 2.5\ mm$ $C_{L2} = 5.6\ pF$ $C_{L3} = 2.7\ pF$ $L_{L2} = 15\ nH$	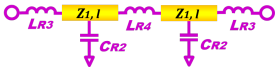	$Z_1 = 70.7\ \Omega$, $l = 2.5\ mm$ $L_{R3} = 4.7\ nH$ $L_{R4} = 9\ nH$ $C_{R2} = 1.6\ pF$
Lines I, L	**Values**	**Matching**	**Values**
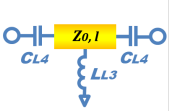	$Z_0 = 50\ \Omega$ $l = 2.5\ mm$ $C_{L4} = 9.5\ pF$ $L_{L3} = 13\ nH$	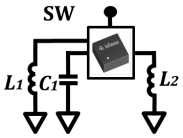	$C_1 = 7.5\ pF$ $L_1 = 15\ nH$ $L_2 = 8.2\ nH$

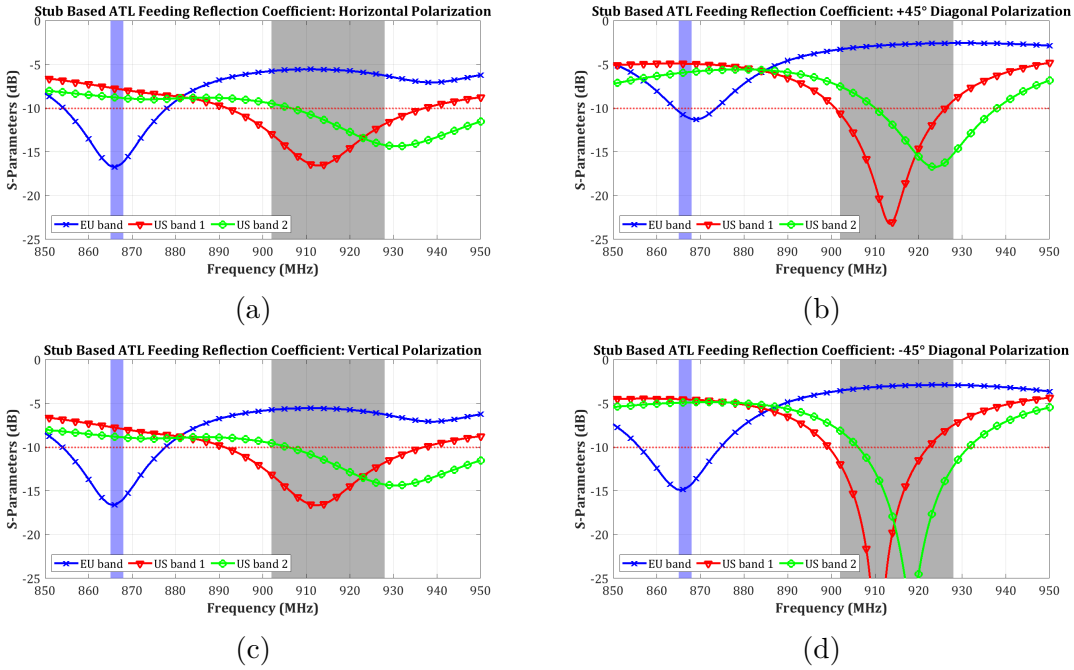

Figure 4.47: Simulated reflection coefficient for the reconfigurable feeding network antenna system based on ATLs and inspired by stub theory. The frequency states corresponding to the EU band and the two US sub-bands are reported and indicated for reference. The evaluation includes the four polarization: (a) *Horizontal*, (b) *+45°* diagonal, (c) *Vertical* and (d) *-45°* diagonal.

The total gain for the reconfigurable antenna system based on switchable ATLs is first analyzed in the EU frequency state for the four polarization cases, reported in Figs. 4.48, 4.49. The choice of keeping a fully symmetrical design demonstrates its effectiveness for the 45_{pol} and -45_{pol}, where the maximum cross-polar component is approximately -20 dB in the $H-$plane cut of the 45_{pol} case. Nevertheless, for the 45_{pol} case, the outstanding cross-polar values of -46 dB is detected in the $E-$plane. However, this solution shows a drawback related to the maximum realized gain, since the simulated values are in the range -0.3 dBi to -0.9 dBi.

The simulated radiation pattern at 915 MHz, displayed in Fig. 4.50 and Fig. 4.51, follows the consideration already mentioned for the EU band case. Interestingly, the cross-polarization achieved in the -45_{pol} case is improved, setting this parameter below -30 dB. Moreover, the total gain increased, with a maximum of 2.1 dBi related to the -45_{pol} case, while in the other polarization states it is found in the range 1.5 ± 0.1 dB.

Although this solution leads to a very flexible and effective solution regarding the matching capability, it has a remarkable drawback due to the high number of switches involved, which are also placed in series configuration, causing direct

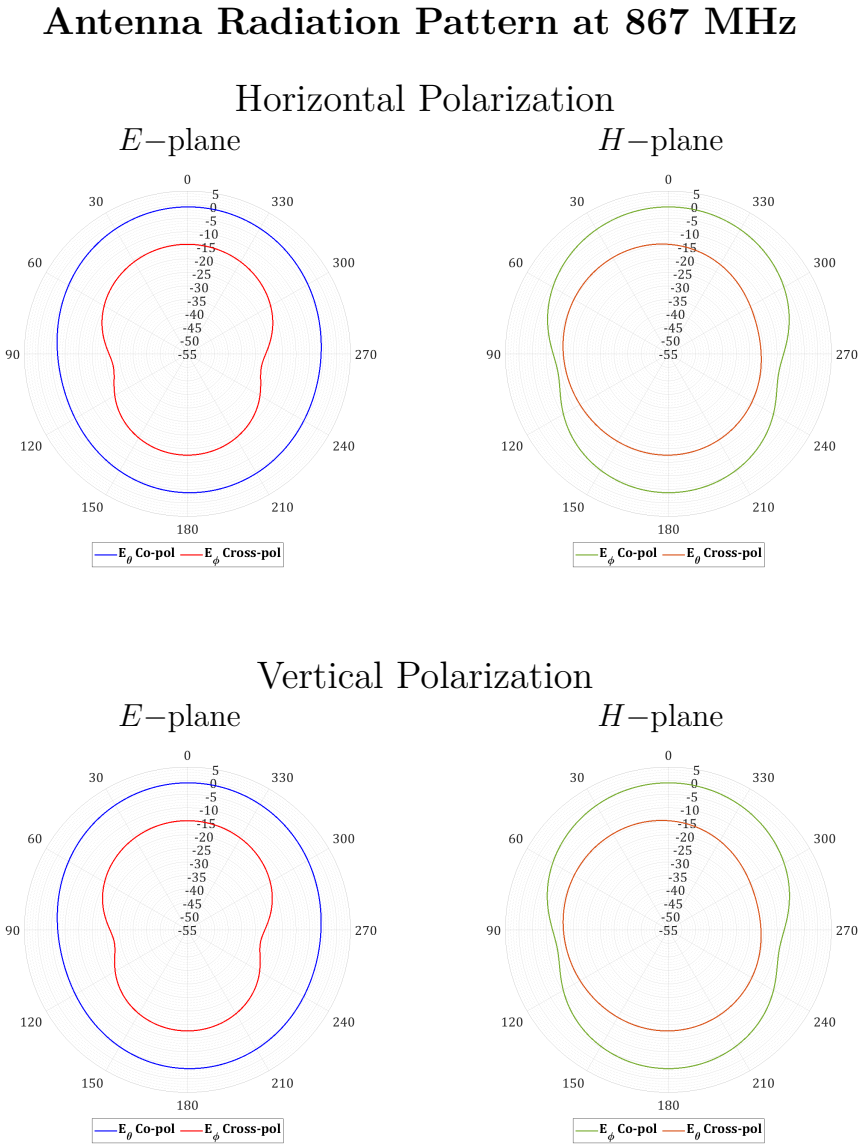

Figure 4.48: Simulated radiation pattern at 867 MHz (related to the EU band) of the modeled suspended patch with reconfigurable feeding network antenna system based on ATLs and inspired by stub theory in the *Horizontal* and *Vertical* polarization states. In agreement with the considered polarization, the $E-$plane and $H-$plane components of the electric fields are reported.

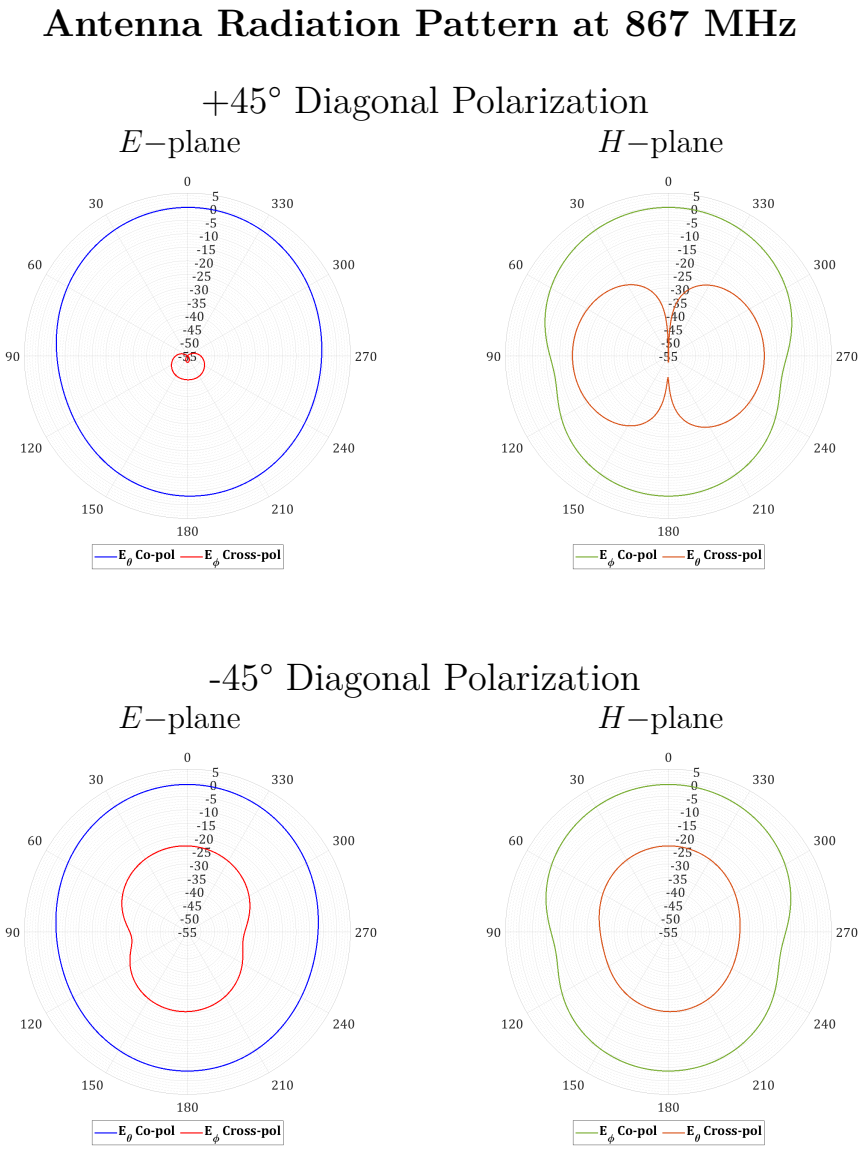

Figure 4.49: Simulated radiation pattern at 867 MHz (related to the EU band) of the modeled suspended patch with reconfigurable feeding network antenna system based on ATLs and inspired by stub theory in the two diagonal *+45°* and *-45°* polarization states. In agreement with the considered polarization, the $E-$plane and $H-$plane components of the electric fields are reported.

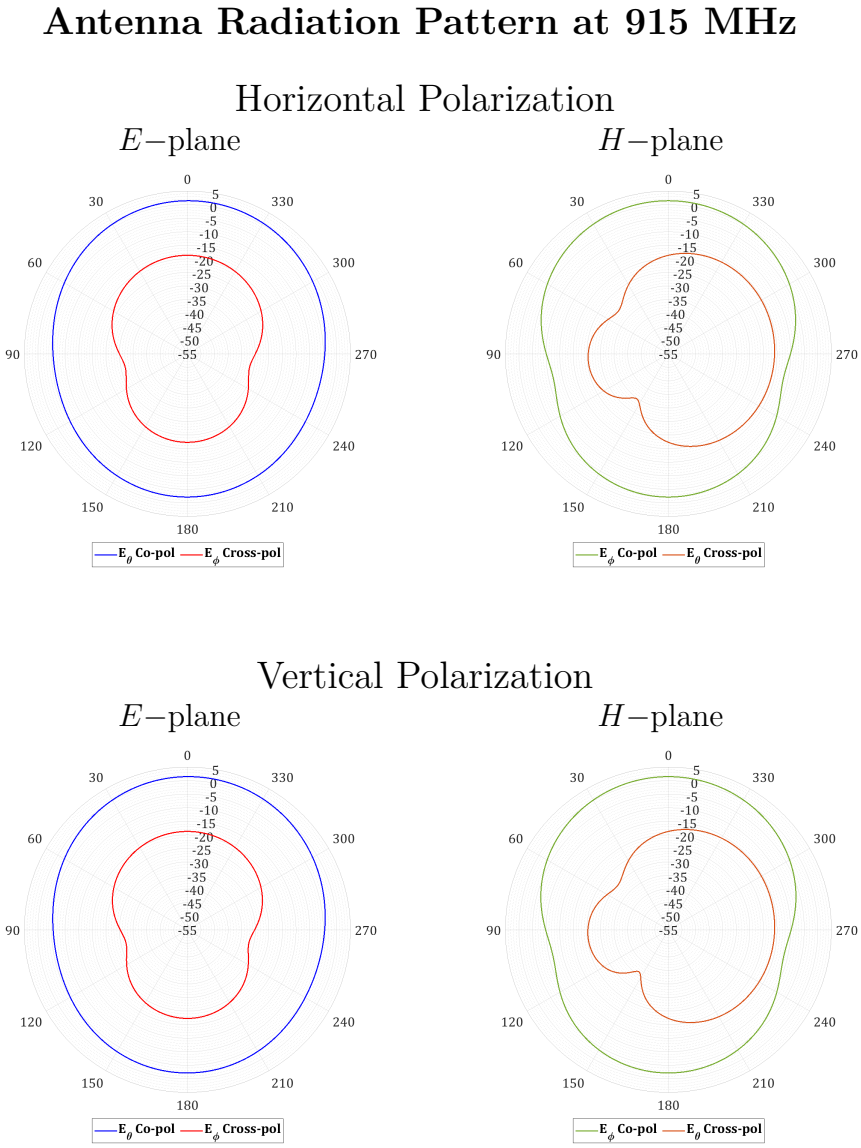

Figure 4.50: Simulated radiation pattern at 915 MHz (related to the upper US band) of the modeled suspended patch with the reconfigurable feeding network antenna system based on ATLs and inspired by stub theory, in the *Horizontal* and *Vertical* polarization states. In agreement with the considered polarization, the $E-$plane and $H-$plane components of the electric fields are reported.

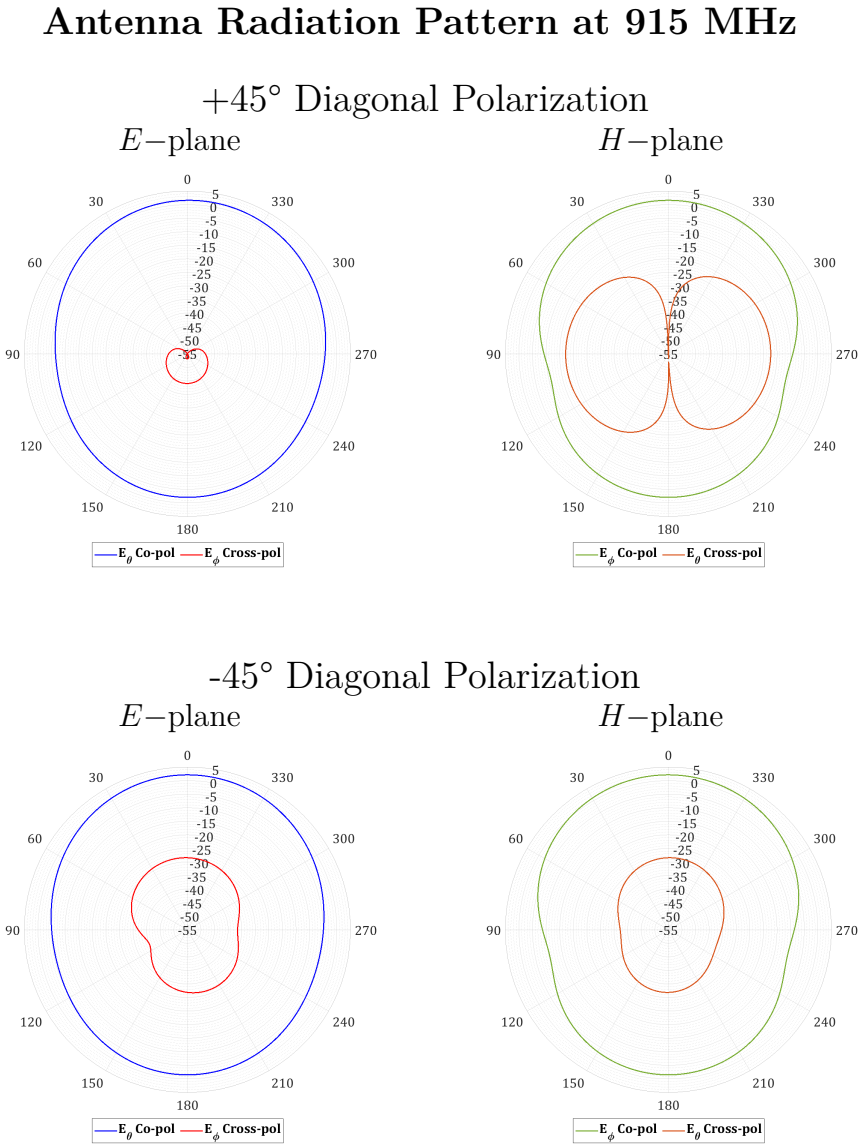

Figure 4.51: Simulated radiation pattern at 915 MHz (related to the upper US band) of the modeled suspended patch with the reconfigurable feeding network antenna system based on ATLs and inspired by stub theory, in the two diagonal *+45°* and *-45°* polarization states. In agreement with the considered polarization, the $E-$plane and $H-$plane components of the electric fields are reported.

losses. In fact, by considering the switching states illustrated in Figures 4.46b and 4.40 – 4.43, the losses for each series switch have to be counted twice. The losses of the feeding lines are added to this source of efficiency reduction. From ADS, it is estimated that the maximum losses are about 1.85 dB at 868 MHz, and this explains the low total efficiency level which is seen in almost all cases, where the 50% limit that was set as goal for this design, is reached only for small portions of the US band.

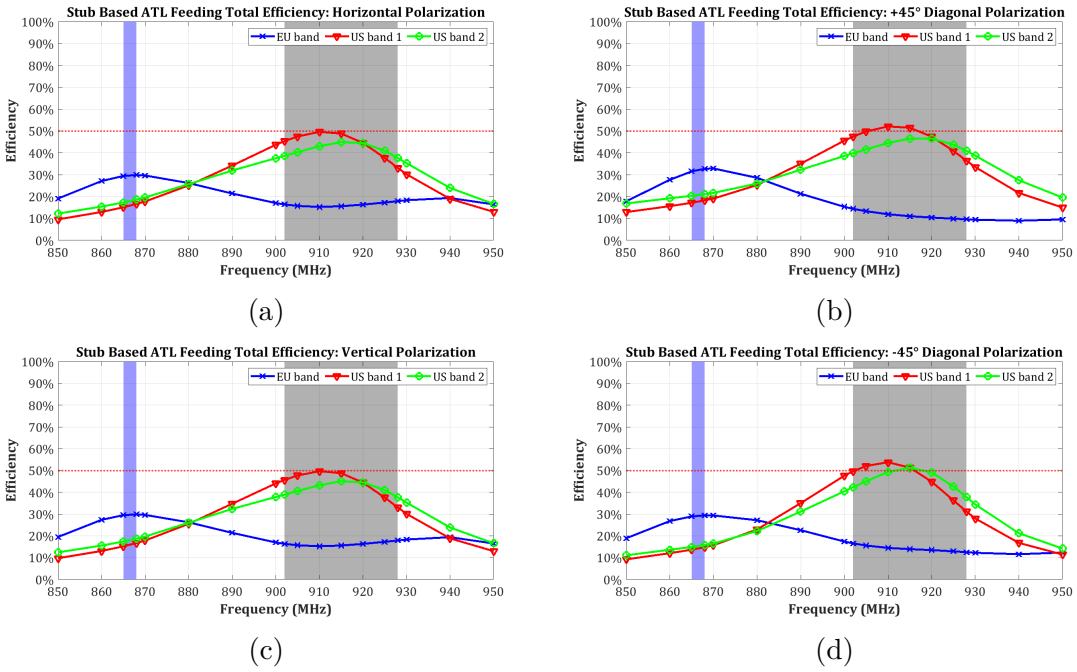

Figure 4.52: Simulated antenna total efficiency for the reconfigurable feeding network antenna system based on ATLs and inspired by stub theory. Frequency switching states are indicated for reference. The evaluation includes the four polarization:(a) *Horizontal*, (b) *+45°* diagonal, (c) *Vertical* and (d) *-45°* diagonal. The 50% limit, related to an ideal antenna with CP approach, is also shown.

4.5.4 Optimized ATL Based Feeding Network

The solutions presented so far are using many switches to accomplish both the frequency and polarization reconfigurability. Here, a new optimized design is proposed, using only three switches for independently change polarizations and frequency bands while keeping a compact structure. The optimized design is based on the structure reported in Sect. 4.5.2, where the flexibility on synthesizing the transmission lines given by ATL technique is exploited to create a compact and switch efficient topology. Moreover, it is exploited the same concept of disabling either *Pin H* and *Pin V* by realizing a *SHORT* termination, as previously done. The block scheme of the novel reconfigurable feeding network type is shown in Fig. 4.53. The feeding network in Fig. 4.53 makes use of a *SP3T* switch for selecting among three different feeding lines, with proper length and characteristic impedance. The switch *BGSA13GN10* is used here because of its low R_{ON} in the active path and its low C_{OFF} of the unused terminals. Therefore, also in the proposed configuration the good similarity to the ideal *OPEN* of the inactive path is exploited together with ATLs in order to reduce the number of switches, as will be discussed in detail in the following.

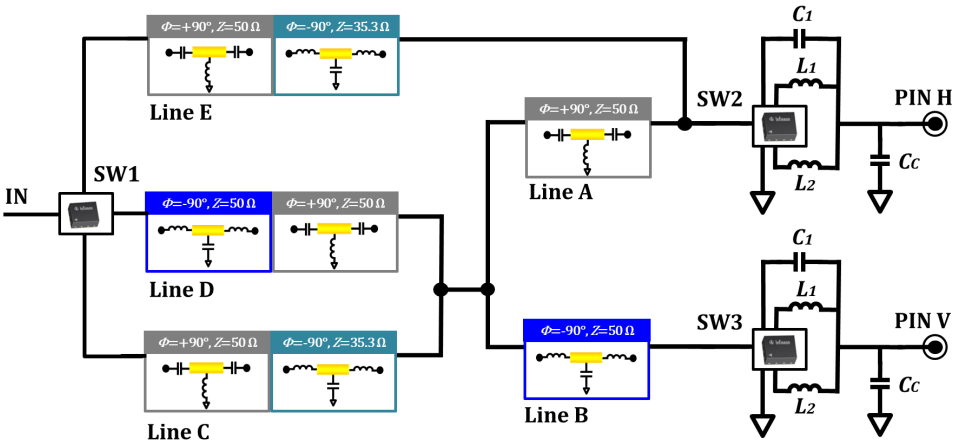

Figure 4.53: Topology of the optimized reconfigurable feeding network employing just three switches and ATLs for fulfilling frequency and polarization agility independently.

As can be noticed from Fig. 4.53, *SW1* is acting as a node that selects among three feeding lines, named *Line C*, *Line D* and *Line E*, which are all characterized by having a total electrical length of 0° at 900 MHz (center frequency). In this way, at the opposite side of the lines, the *OPEN* condition is transferred, and there is no need to use a switch to decouple the lines which are connected to the same node. This approach has already been used in the development of the feeding network in Sect. 4.5.2, however, in the present design, all the lines are

composed by both LH and RH ATL sections with same phase: therefore, the group delay is the same in all cases (i.e. same phase characteristic over frequency). The frequency reconfigurability is performed as previously described, by adopting an $L-$type feeding network, composed by the switch in series configuration. However, in this case, it is introduced the connection to ground, that is used as termination for the unused polarization feeding branches (i.e. as depicted in Fig. 4.53 for *SW2* and *SW3*). In order to accomplish for the switching of the matching components and the imposition of the *SHORT* termination, the *SP4T* switch *BGSA14GN10* from Infineon [268] is employed. Therefore, *SW2* and *SW3* are able to select the desired frequency band by switching to L_1 for matching the EU band, while L_2 and C_1 match the two US sub-bands. It is remarked that the frequency band can be selected independently, since its selection does not affect the polarization agility controls.

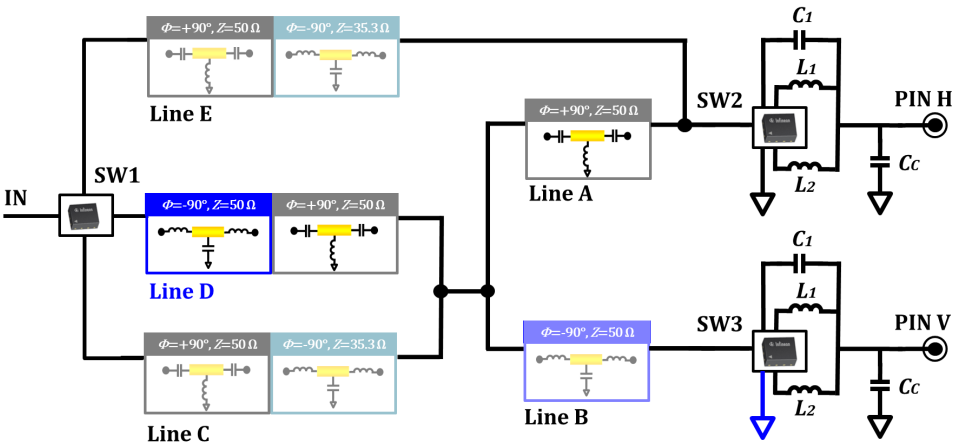

Figure 4.54: Topology of the feeding network for the H_{pol} operation. The selected line is marked in blue, while the lines which are not actively involved are shaded.

Nevertheless, the two switches devoted to frequency reconfigurabilty play a role on the polarization agility when H_{pol} or V_{pol} are required. The mentioned operation is depicted in Fig. 4.54, which illustrates the configuration for the *Horizontal* polarization state, where *SW3* is terminating *Line B* in a *SHORT*, and *SW2* is set accordingly to match the required frequency band. As can be recognized from Fig. 4.54, *Line B* is a 50 Ω RH type artificial transmission line attaining a phase of -90°, and for this reason the *SHORT* condition at its antenna feeding termination imply an *OPEN* condition at its opposite end, thus virtually disconnecting the *Pin V* branch. Therefore, *Pin H* is fed by the cascade of *Line A* and *Line D*, that is selected by *SW1*. More in detail, *Line A* represents the dual version of *Line B*, being a 50 Ω LH-ATL with 90° phase attained. Similarly, *Line D* is composed by an RH-ATL section attaining a phase of -90° and a LH-ATL section realizing the

same phase amount, but with opposite sign. Then, the cascade of the LH-ATL and RH-ATL is composing a 50 Ω transmission line attaining 0° phase at center frequency, set at approximately 900 MHz. Concerning *Line C* and *Line E*, they are offering the *OPEN* condition of the unused terminal of the switch (or more precisely its C_{OFF}) to the feeding nodes, with the effect of being disconnected. However, a loading effect is expected to the *SW2* node due to the line losses and phase inaccuracy.

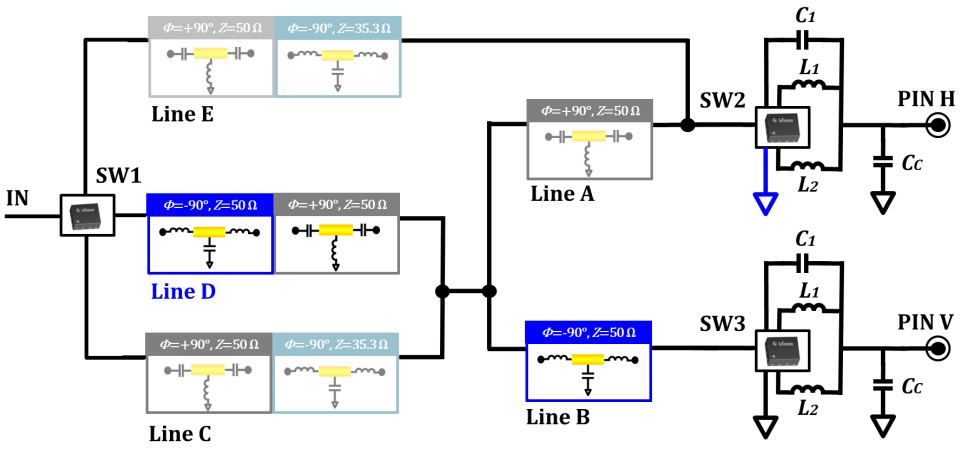

Figure 4.55: Topology of the feeding network for the V_{pol} operation. The selected line is marked in blue, while the lines which are not actively involved are shaded.

The configuration that generates the *Vertical* polarization shares the same configuration as the *Horizontal* one. As can be noticed from 4.55, here *Line B* is feeding *Pin V* through *Line B*, while *Line A* is terminated to a *SHORT*, realized by *SW2*. Again, *Line A* is virtually disconnected from the active parts of the feeding network. In this configuration, *SW3* can select the frequency band to be matched without any interference on the polarization state.

In the other two polarization cases, *SW2* and *SW3* are devoted only to the frequency reconfiguration, and *SW1* selects either 45_{pol} or -45_{pol} polarizations. In the following, Fig. 4.56 is considered for the analysis of the reconfigurable network that generates the *45° diagonal* polarization. As already mentioned, for the achievement of the 45_{pol}, both *Pin H* and *Pin V* have to be fed with the same phase, or equivalently with 0° phase difference. Therefore, the equal phase feeding is fulfilled by directly connecting *Pin H* and *Pin V* with the series of *Line A* and *Line B*: as described before, these lines have both a characteristic impedance of 50 Ω and they attain a phase of +90° and -90°, respectively (because they are realized with LH and RH ATLs). As a result, the input signal is fed to *Pin H* through *Line E*, enabled by *SW1* and, consequently, *Pin V* is fed with the same phase difference through the 0° line composed by the two ATL *Line A* and *Line B* which

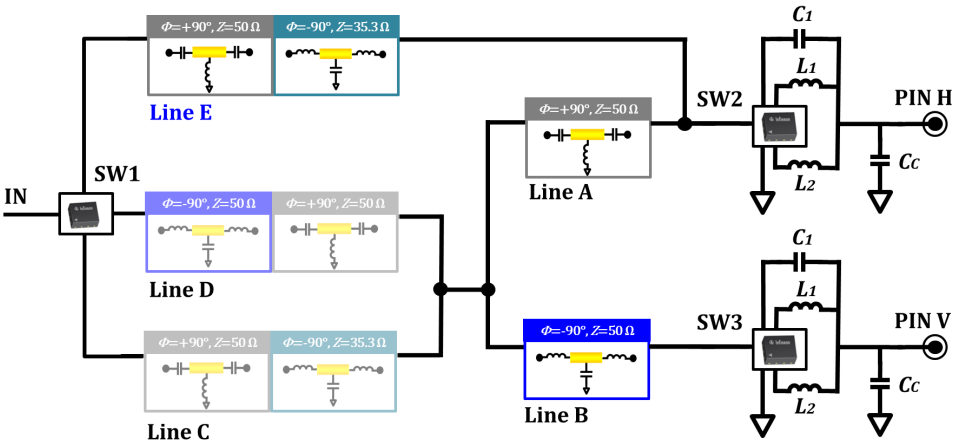

Figure 4.56: Topology of the feeding network for the 45_{pol} operation. The selected line is marked in blue, while the lines which are not actively involved are shaded.

are performing phase canceling. This is achieved also because *Line D* and *Line C* have a total length of 0° and they are terminated to an *OPEN*, thus being virtually disconnected in the joint connection point between *Line A* and *Line B*. Moreover, *Line E* is realized as a 0° line composed by a -90° RH-ATL section with characteristic impedance $50/\sqrt{2}$ (i.e. $\sim 35\ \Omega$) for ensuring the transformation to 50 Ω. This is necessary since the parallel arrangement of the two feeding pins, both with characteristic impedance of 50 Ω, sets the impedance at *Line E* feeding terminal to 25 Ω. Then, the -90° phase attained by the $\lambda/4$ transformer is compensated by a 50 Ω LH-ATL section in series.

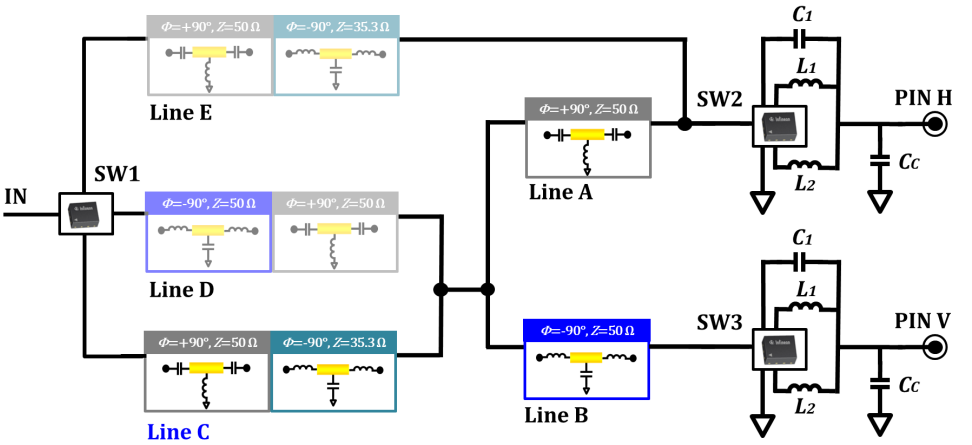

Figure 4.57: Topology of the feeding network for the -45_{pol} operation. The selected line is marked in blue, while the lines which are not actively involved are shaded.

The last configuration is shown in Fig. 4.57, which realizes the -45$_{pol}$ polarization state. The *-45° diagonal* polarization is achieved by feeding the two pins with 180° phase difference, and this condition is easily obtained by feeding the patch antenna in the junction between *Line A* and *Line B*. Therefore, *Pin H* is fed by a +90° LH-ATL section and *Pin V* is fed by -90° RH ATL section, thus obtaining a total phase difference of 180° at the two feeding points. Since *Line A* and *Line B* have a characteristic impedance of 50 Ω, *Line C* is constructed in the same way as *Line E*, thus performing impedance transformation in order to provide matching at the feeding point.

The analytical formulas that specify the loading elements composing the RH and LH artificial transmission lines involved in the polarization reconfigurability described so far, are obtained by imposing the corresponding phase conditions. For enhancing compactness, the number of unit cells n related to the ATLs is set equal to two in all ATL designs. Moreover, it is remarked that ϕ_l^x refers to the phase contribution of the transmission line, where the subscript x is named in accordance with the characteristic impedance of the line which is considered. The two lines connecting the feeding pins *Pin H* and *Pin V* (i.e *Line A* and *Line B* respectively), are defined by (4.14) and (4.15).

$$\textbf{Line A} \quad \Longrightarrow \quad n\left(\frac{1}{\omega\sqrt{L_{p1}C_{p1}}} - \phi_l^{50}\right) = \frac{\pi}{2} \tag{4.14}$$

$$\textbf{Line B} \quad \Longrightarrow \quad n\left(-\omega\sqrt{L_{n1}C_{n1}} - \phi_l^{50}\right) = -\frac{\pi}{2} \tag{4.15}$$

As already mentioned, *Lines C,D,E* are composed by two distinct LH- and RH- sections, indicated with I and II, differing for phase and/or characteristics impedance, as clarified in (4.16) and (4.17):

$$\textbf{Line C, E} \begin{cases} Z_{LH}^{I} = 50\,\Omega & \Longrightarrow n\left(\dfrac{1}{\omega\sqrt{L_{p2}C_{p2}}} - \phi_l^{50}\right) = \dfrac{\pi}{2} \\ Z_{RH}^{II} \approx 35.35\,\Omega & \Longrightarrow n\left(-\omega\sqrt{L_{n2}C_{n2}} - \phi_l^{35}\right) = -\dfrac{\pi}{2} \end{cases} \tag{4.16}$$

$$\textbf{Line D} \begin{cases} Z_{RH}^{I} = 50\,\Omega & \Longrightarrow n\left(-\omega\sqrt{L_{n3}C_{n3}} - \phi_l^{50}\right) = -\dfrac{\pi}{2} \\ Z_{LH}^{II} = 50\,\Omega & \Longrightarrow n\left(\dfrac{1}{\omega\sqrt{L_{p3}C_{p3}}} - \phi_l^{50}\right) = \dfrac{\pi}{2} \end{cases} \tag{4.17}$$

As can be notice also from Fig. 4.53, *Line D* is composed by the same LH-ATL and RH-ATL which are specified as *Line A* and *Line B*, while *Lines C,E* contains

also the *Line B* section as 50 Ω part. However, for completeness, the phase equations necessary to specify all the ATLs used in the reconfigurable feeding network are reported. In the following, the simulated reflection coefficient of the complete reconfigurable antenna in the four states is reported in Fig. 4.58. This results are obtained by first setting the proper circuital model, developed in ADS, and inserting the $S-$parameters of the switches and the components used (i.e. *LQW15* and *GJM15* from *muRata*). The final results are then obtained by including the circuital simulation in the full-wave model of the complete reconfigurable antenna, and evaluating the antenna performance in each reconfigurable state. It is noticed that some tuning of the four element composing the $L-$type matching network was necessary, due to the approximation of the *OPEN* states at the nodes involving *Line C,D* and *Line E*. The calculated and optimized components are reported in Table 4.4, where the complete definition of the ATL based feeding lines is displayed.

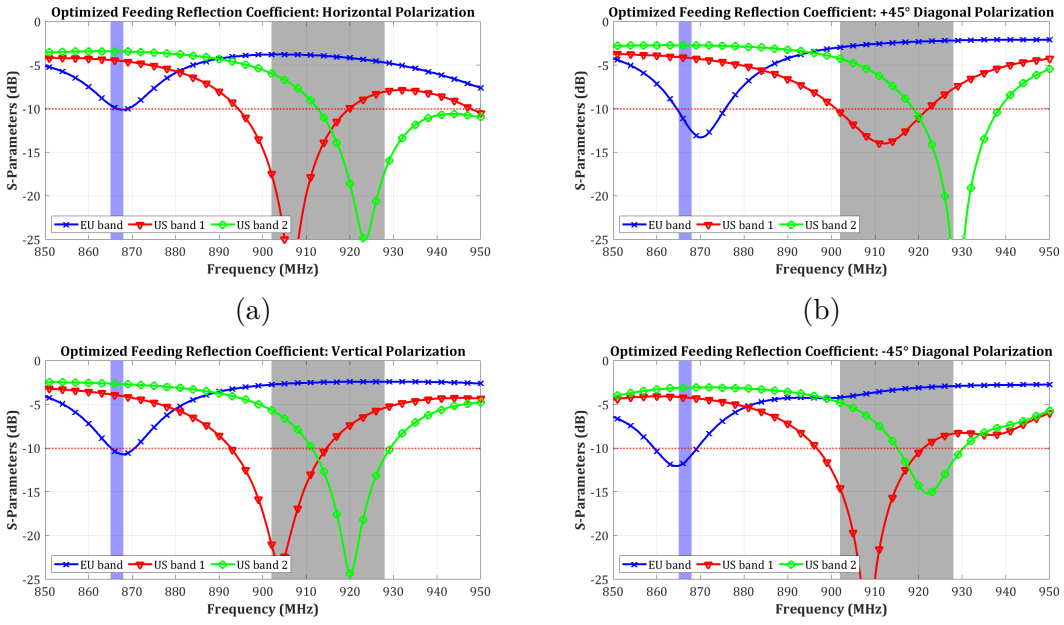

Figure 4.58: Simulated reflection coefficient for the optimized reconfigurable feeding network antenna system. The frequency states corresponding to the EU band and the two US sub-bands are reported and indicated for reference. The evaluation includes the four polarization: (a) *Horizontal*, (b) *+45°* diagonal, (c) *Vertical* and (d) *-45°* diagonal.

As can be noticed from Fig. 4.53, the matching of the two US sub-bands is completely fulfilled, where also a nice overlapping of the US band 1 and band 2 can be noticed for all the four polarization states. Regarding the EU band, the matching is slightly above the target limit of -10 dB for the singular feedings

Table 4.4: Values of Components of the Optimized Reconfigurable Feeding

Line A	**Values**
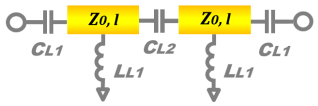	$Z_0 = 50\,\Omega$ $l = 2.5\,mm$ $C_{L1} = 8.2\,pF$ $C_{L2} = 3.9\,pF$ $L_{L1} = 10\,nH$
Line B	**Values**
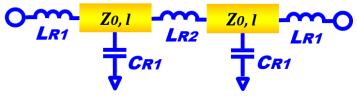	$Z_0 = 50\,\Omega$ $l = 2.5\,mm$ $L_{R1} = 3\,nH$ $L_{R2} = 6\,nH$ $C_{R1} = 2.4\,pF$
Lines C, E	**Values**
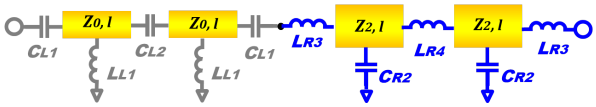	$Z_0 = 50\,\Omega,\ Z_2 = 35\,\Omega$ $l = 2.5\,mm,\ C_{L1} = 8.2\,pF$ $C_{L2} = 3.9\,pF,\ L_{L1} = 10\,nH$ $L_{R3} = 2.2\,nH,\ L_{R4} = 3.9\,nH$ $C_{R1} = 3.3\,pF$
Line D	**Values**
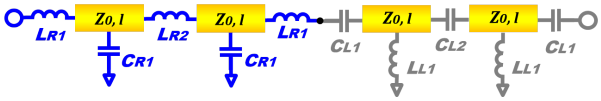	$Z_0 = 50\,\Omega,\ l = 2.5\,mm$ $C_{L1} = 8.2\,pF,\ C_{L2} = 3.9\,pF$ $L_{L1} = 10\,nH$ $L_{R1} = 3\,nH,\ L_{R2} = 6\,nH$ $C_{R1} = 2.4\,pF$
Matching Network	**Values**
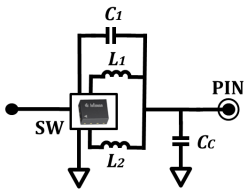	$C_c = 1.2\,pF$ $L_1 = 26\,nH$ $L_2 = 2\,nH$ $C_1 = 2.5\,pF$

condition H_{pol}, which represents the worst case scenario since it is affected by *Line E* terminated into C_{OFF} (*OFF* capacitance of the switch). However, the worst case regarding matching is found at 865 MHz, with a reflection coefficient of -9.6 dB. The effect of the impedance shift described in Sect. 4.4.1 when the two feeding points are simultaneously excited is clearly visible in 4.58b and 4.58d, where the minimum of the resonance is located in opposite directions with respect to the EU center band. Moreover, by considering the US band, the best matching conditions

are swapped from the 45_{pol} in relation to the -45_{pol} state. Finally, the radiation patterns of the reconfigurable feeding network employing just three switches for the full frequency and polarization agility is assessed. The gain at 867 MHz is shown in Fig. 4.59 and Fig. 4.60, where the considered cuts are taken accordingly to the specified polarization. The maximum total gain is achieved in the 45_{pol}, where the simulated value of 1.6 dBi is detected; while the worst case is related to H_{pol}, with 0.5 dBi, caused by the mismatch already mentioned in the analysis of the reflection coefficient. Moreover, the cross-polar component is very low in the -45_{pol} case, below -30 dB, while for all other cases is below -17 dB.

Similarly, it is analyzed the total gain in the upper frequency band, displayed in Fig. 4.61 and in Fig. 4.62. Also in this case, the lowest gain is found for the H_{pol} case. However, the 45_{pol} shows a strong reduction, with a value of 1.2 dBi, while the cross-polar component is also increased, with a value of -10 dB in the $H-$plane. Reminding that the 45_{pol} condition is realized by exploiting the cascade of *Line A* (attaining 90° phase advance) and *Line B* (attaining -90° phase delay), this negative effect is probably due to the loading effect of the *Lines C,D* at the common node. Moreover, also the losses due to the *Line A – Line B* paths are causing an amplitude mismatch between*Pin H* and *Pin V*. Nevertheless, the other polarization states shows a good polarization purity, with values of cross-polar component below -18 dB.

Finally, the total efficiency is reported in Fig. 4.63 for all the reconfigurable feeding states. As already discovered from the description of the $S-$parameters and antenna gain, the lowest efficiency is related to the EU band in the H_{pol} case. The target 50% efficiency is not met at this frequency band, while better performance is achieved in the upper US band, where the efficiency limit related to the polarization mismatch of an ideal CP antenna and a linear tag is outmatched in the V_{pol}, 45_{pol} and -45_{pol} polarization states, while in the H_{pol} case the efficiency is slightly lower, with minimum at 42%.

This solution has shown good results, in relation to the compact form factor and the minimum number of switches used to realize both frequency and polarization agility. The limitations are related to the feeding lines which are loaded by the *OFF* capacitance of the switch responsible for the polarization agility, that causes "stub" effects at the nodes, thus modifying the phase and amplitude relation between the two antenna feeding points. However, this is a promising architecture for realizing a full reconfigurable antenna employing a smart switch-saving method.

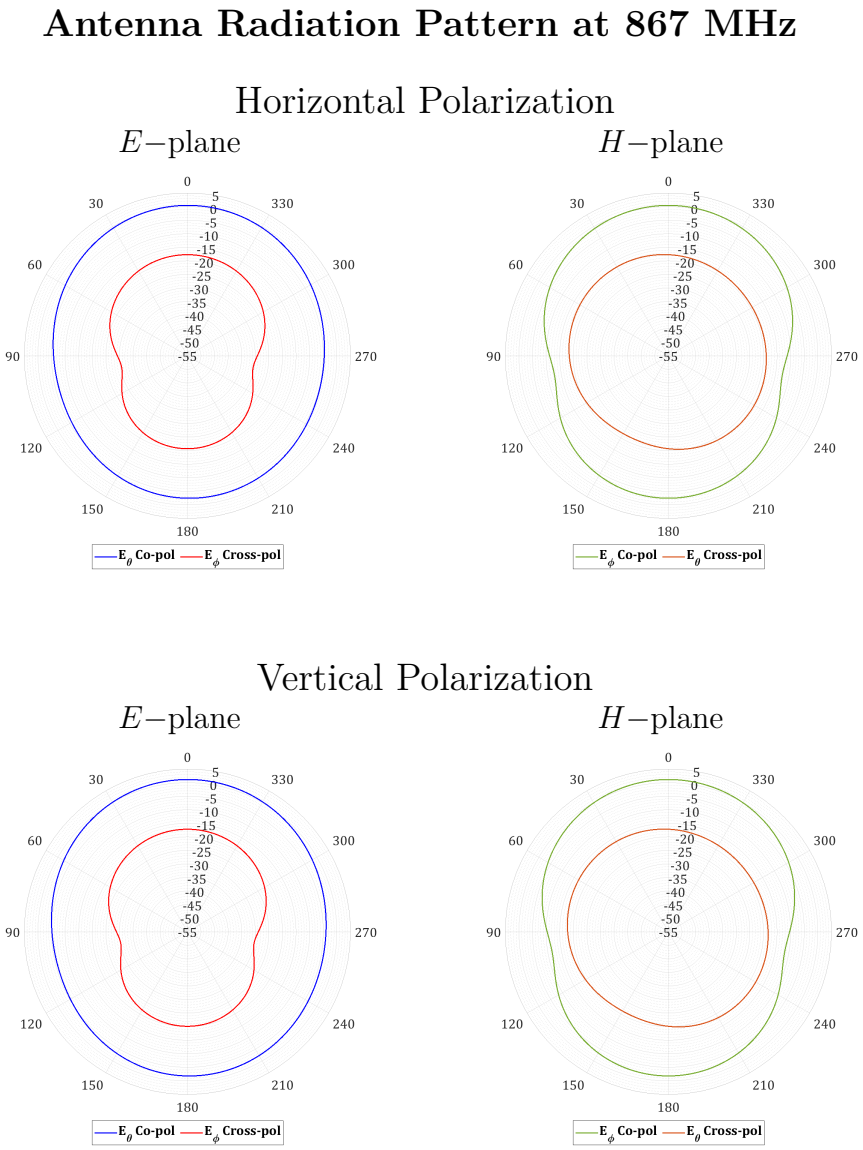

Figure 4.59: Simulated radiation pattern at 867 MHz (related to the EU band) of the modeled suspended patch with the optimized feeding network antenna system, in the *Horizontal* and *Vertical* polarization states. In agreement with the considered polarization, the $E-$plane and $H-$plane components of the electric fields are reported.

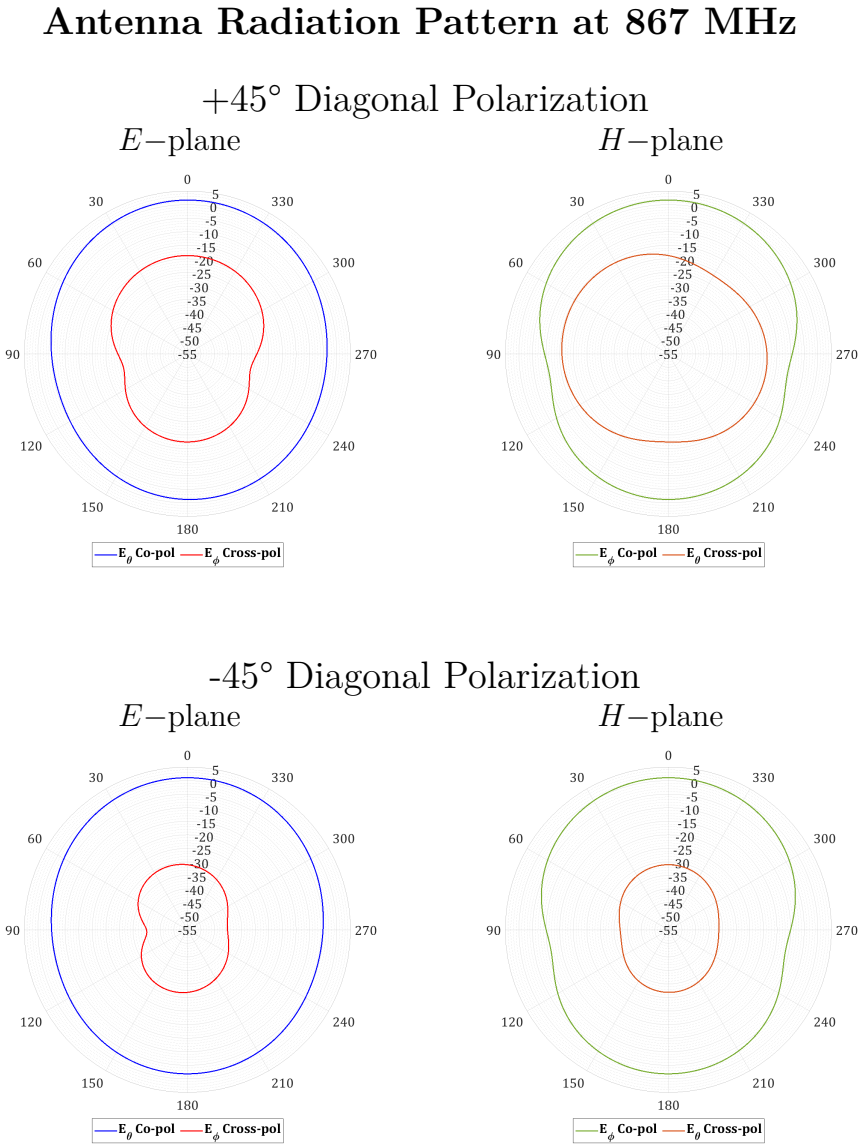

Figure 4.60: Simulated radiation pattern at 867 MHz (related to the EU band) of the modeled suspended patch with the optimized feeding network antenna system, in the two diagonal *+45°* and *-45°* polarization states. In agreement with the considered polarization, the $E-$plane and $H-$plane components of the electric fields are reported.

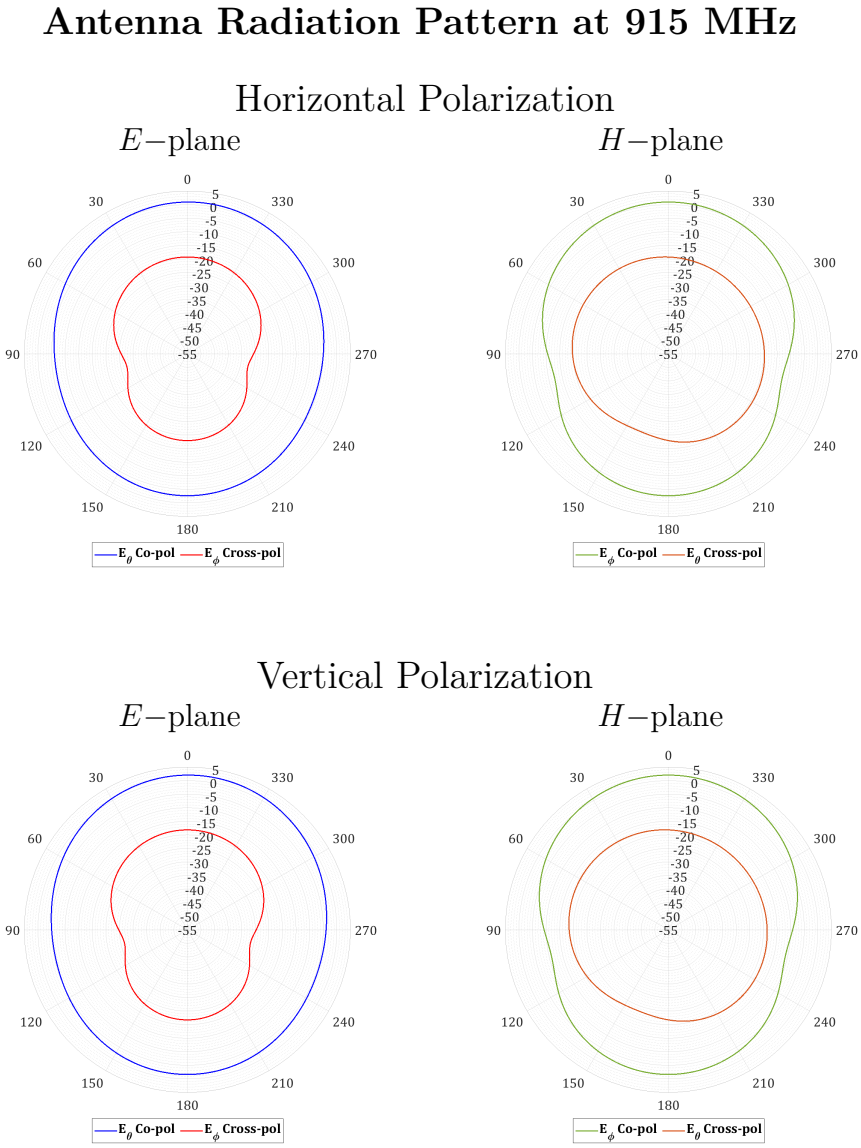

Figure 4.61: Simulated radiation pattern at 915 MHz (related to the upper US band) of the modeled suspended patch with the optimized feeding network antenna system, in the *Horizontal* and *Vertical* polarization states. In agreement with the considered polarization, the $E-$plane and $H-$plane components of the electric fields are reported.

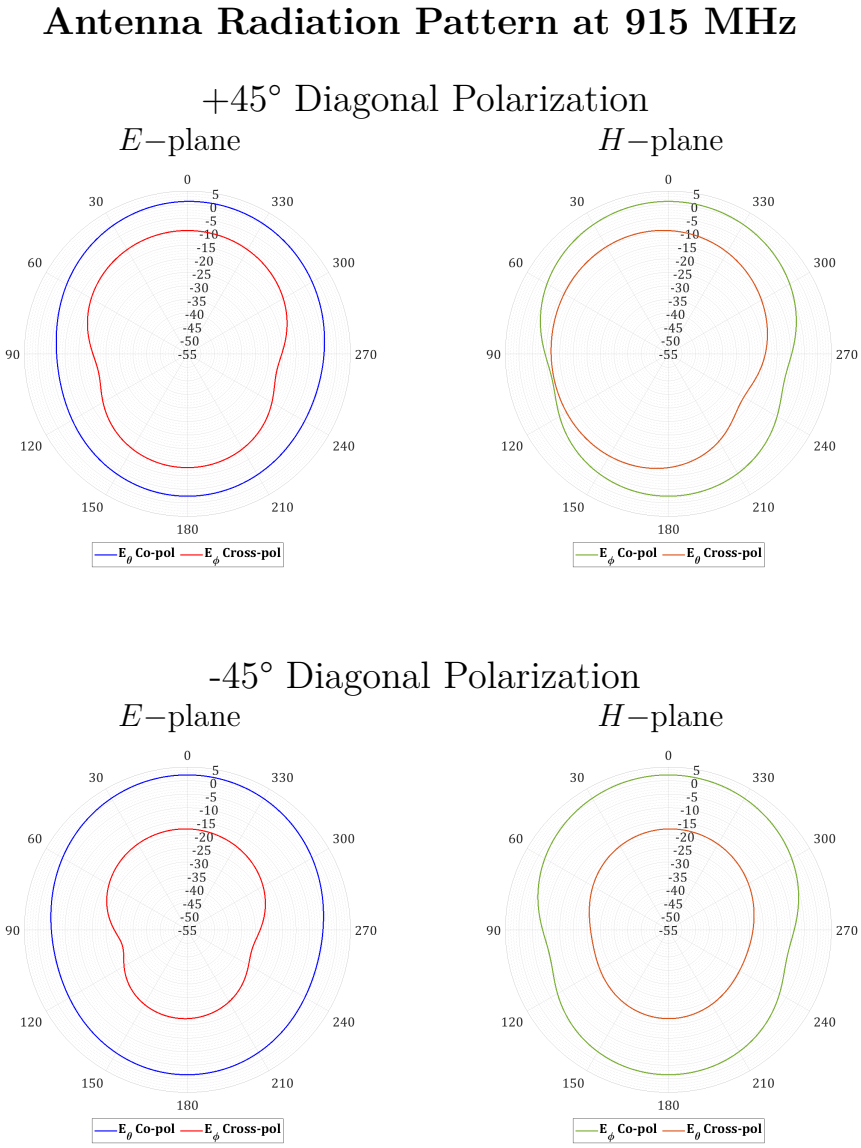

Figure 4.62: Simulated radiation pattern at 915 MHz (related to the upper US band) of the modeled suspended patch with the optimized feeding network antenna system, in the two diagonal *+45°* and *-45°* polarization states. In agreement with the considered polarization, the $E-$plane and $H-$plane components of the electric fields are reported.

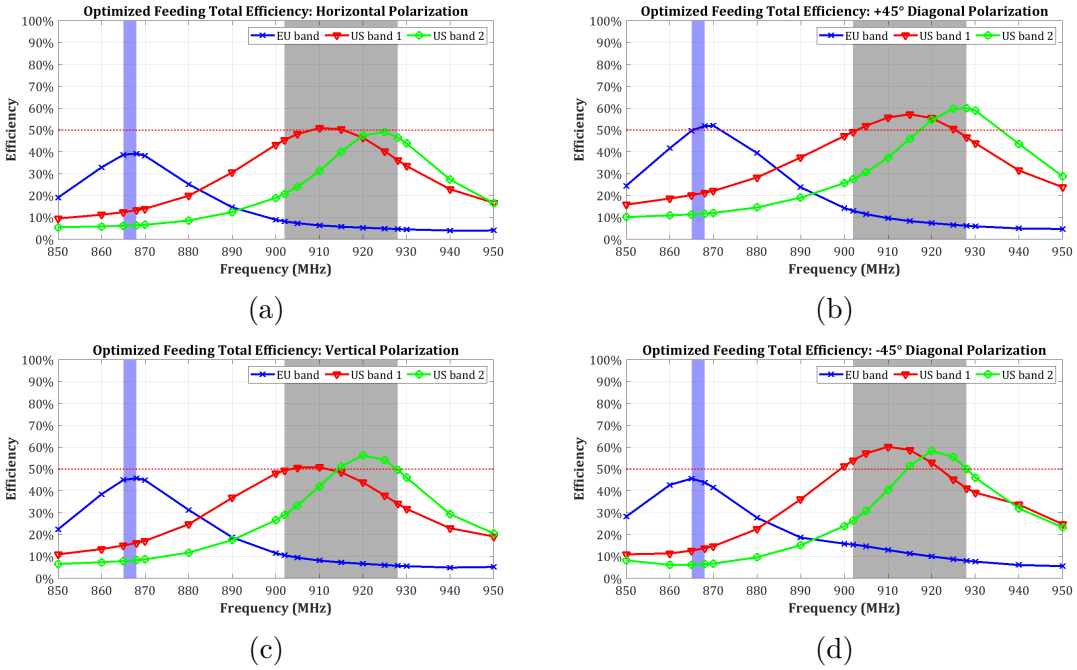

Figure 4.63: Simulated antenna total efficiency for the optimized reconfigurable feeding network antenna system. Frequency switching states are indicated for reference. The evaluation includes the four polarization: (a) *Horizontal*, (b) *+45°* diagonal, (c) *Vertical* and (d) *-45°* diagonal. The 50% limit, related to an ideal antenna with CP approach, is also shown.

4.5.5 Fully Reconfigurable Rat-race Coupler as Feeding Network

All the feeding solutions described so far are based on a simple $T-$junction power divider, which represents a simple structure in which reconfigurability can be applied in a relatively easy way. However, this approach is not the best regarding performance: it is well know from literature (e.g. [228]) that the $T-$junction divider cannot be designed simultaneously lossless, matched and reciprocal. Therefore, there is a poor isolation between the two output ports, and the reflection coefficient looking from one of the two outputs is theoretically limited to -6 dB. The solution to avoid such an ineffective condition is to adopt one of the well known couplers that can fulfill the power division and simultaneously guarantee the isolation and matching condition at its outputs (e.g. branch line coupler, Wilkinson divider, Lange coupler etc.). For the purpose of this design, only the couplers which are suitable to be realized in planar microstrip line technology are considered. The utilization of this kind of coupler to produce polarization reconfigurability has already been proposed in literature, by designing reconfigurable feeding networks employing

several couplers (e.g. [264]), resulting in an electrically large implementation. Here, the goal is to provide a compact solution, that can be easily integrated in a more complex system and, then, only one coupler is employed for fulfilling the reconfigurable feeding network. Therefore, for the purpose of realizing the two diagonal polarizations 45_{pol} and -45_{pol}, the best choice is found to be the rat-race coupler, which has the special feature of realizing an in-phase and out-of-phase configurations [228]. However, the application of reconfigurability to this coupler introduces a level of complexity which is higher compared to the solutions already presented in this chapter, especially considering the optimized design described in Sect. 4.5.4. Nevertheless, a complete reconfigurable rat-race coupler has been designed to fulfill the four polarization states and the switchable $L-$type matching network already described in Sect. 4.5.4, for ensuring an interchangeability of various components. For the same purpose, a connection to ground (i.e. *SHORT* termination) realized by these switches is used to terminate the unused feeding pin. The topology of the novel reconfigurable rat-race coupler is reported in Fig. 4.64. The rat-race is realized with a proper combination of LH and RH artificial transmission lines, in order to remove the long 270° branch and obtaining a compact and efficient structure (please refer to Sect. 3.2). By analysing the conceptual design in Fig. 4.64, it becomes clear that the switching mechanism employed for reconfiguring the coupler is the variation of ATL length and characteristic impedance by adding/removing line sections (same concept used in Sect. 4.5.3 and in Sect. 3.4). Therefore, two Infineon *BGSA14GN10* are responsible for the frequency reconfigurability and feeding termination, while two synchronous $2\times SP3T$ and one *DPDT* from Qorvo, namely *RFSW6232* and *QPC6222* respectively, are employed for achieving the polarization reconfigurability.

At first, the *45° polarization* is analyzed, which is achieved by feeding the rat-race coupler in the in-phase configuration. From Fig. 4.65, it is recognized that the rat-race coupler is realized with three $50 \cdot \sqrt{2}\ \Omega$ LH-ATLs attaining a phase of +90° (i.e. *Line A*, *Line B* and *Line C*), and one RH-ATL with phase -90° (i.e. *Line D*) with the same characteristic impedance. Figure 4.65 shows that this circuital topology is realized just employing *SW3*, *SW4* and *SW5* as through (i.e. no further ATL are added). It is observed that an external connection is used to short circuit the two pins of the switch *RFSW6232*, thus realizing a through, while for the *QPC6222* this is realized internally. It is easy to recognize that, with the described configuration, *Pin H* and *Pin V* are excited with equal phase and amplitude, thus fulfilling the required task.

In the in-phase configuration of the rat-race coupler, three different definition for the artificial transmission lines are involved. According to Fig. 4.65, the most obvious distinction is related to the ATL type, either LH-ATL or RH-ATL. In the analytical analysis of all the ATLs, the delay of the transmission lines included in the ATL unit cells (with length 2.5 mm) are referred as the term ϕ_l. The second distinction is related to the phase contribution of the switches (indicated with ϕ_{sw}),

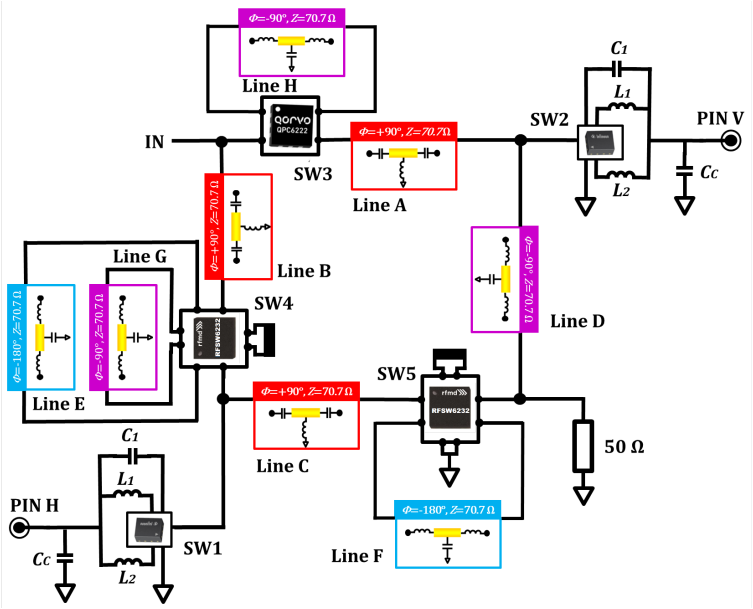

Figure 4.64: Topology of the fully reconfigurable feeding network based on rat-race coupler.

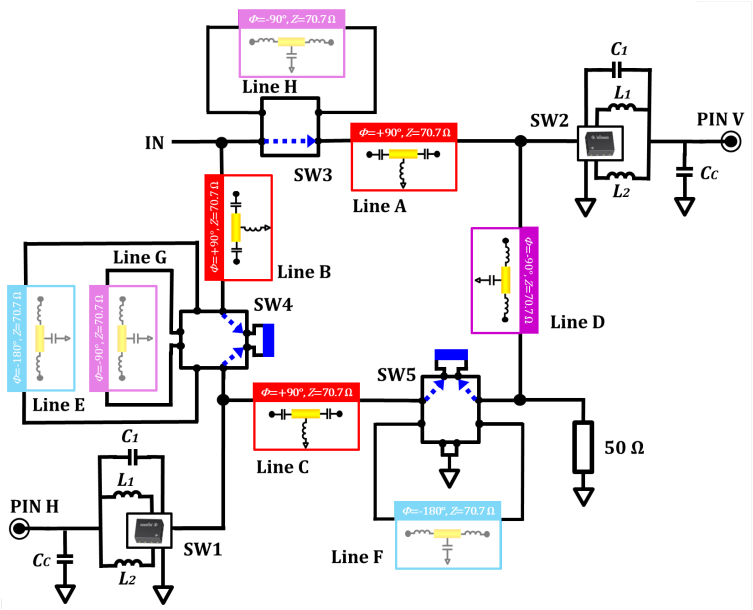

Figure 4.65: Topology of the feeding network for the 45_{pol} operation. The lines which are not actively involved are shaded, and the switch operation is illustrated.

which is added in the $\pm 90°$ phase expressions. Therefore, following this analysis, the three equations that specify the composition of the four branches of the rat-race are reported. More in detail, (4.18) is used to calculate the inductor and

capacitors loading *Line A*, by considering the sum of $n = 2$ LH unit cell and the single contribution of the switch *SW3*, and by finally imposing the 90° condition. Similarly, *Line B* and *Line C* are expressed by (4.19), where the double phase contribution of the $2 \times SP3T$ switches *SW4* and *SW5* are taken into account. Finally, *Line D* is composed just by $n = 2$ RH unit cells, and then the equality to -90° is simply written in (4.20).

$$\textbf{Line A} \quad \Longrightarrow \quad n\left(\frac{1}{\omega\sqrt{L_{p1}C_{p1}}} - \phi_l\right) - \phi_{sw} = \frac{\pi}{2} \tag{4.18}$$

$$\textbf{Line B, C} \quad \Longrightarrow \quad n\left(\frac{1}{\omega\sqrt{L_{p2}C_{p2}}} - \phi_l\right) - 2\phi_{sw} = \frac{\pi}{2} \tag{4.19}$$

$$\textbf{Line D} \quad \Longrightarrow \quad n\left(-\omega\sqrt{L_{n1}C_{n1}} - \phi_l\right) = -\frac{\pi}{2} \tag{4.20}$$

For the evaluation of the performance of the coupler, a complete circuital simulation in ADS is performed, employing the $S-$parameters of the switches and of the *muRata* inductors (*LQW15*) and capacitors (*GRM15*) used in the realization of the ATLs. The $S-$parameters of the realized rat-race coupler in the in-phase configuration are shown in Fig. 4.66, together with the phase and amplitude difference of $S-$parameters at the two outputs *Port 2* and *Port 3* (corresponding to *Pin H* and *Pin V* respectively). From Fig. 4.66a, it can be noticed that the reflection coefficients at *Port 2* and *Port 3*, related to antenna feeds, are better than -18 dB, while at the input (i.e. *Port 1*) it is below -30 dB. The isolation between *Pin H* and *Pin V* is 25 dB with the new solution, while the maximum losses in the frequency range of interest are detected to be equal to 0.9 dB, mostly due to the transition toward the switches. The latter aspect represents the main cause of amplitude mismatch, reported in Fig. 4.66b, since the four branches have three different switch configurations (i.e. through realized with one transition, through realized with two transitions and no switch involved). However, it is remarked that the phase error is very low with this solution, with a maximum of 2.5° at 865 MHz.

The -45_{pol} is obtained by feeding the rat-race coupler in the out-of-phase configuration. By referring to the structure in Fig. 4.65, for having the 180° phase difference at the coupler´s output, the input should be located in the place where the 50 Ω termination is (i.e. in the junction point between *Line C* and *Line D*), and vice versa. This is not possible to realize in practice, and therefore through the switches *SW4* and *SW5* are employed to add to *Line B* and *Line C* an RH-ATL sections with characteristic impedance of $\sim 70.7\,\Omega$, attaining a total phase of -180°. As a result, the sum of the +90° phase of *Line B* (LH-ATL type) with the -180° of *Line E* (RH-ATL type) is equivalent to a line with total phase of -90°. Exactly the same procedure is applied with *Line C* and *Line F*. The novel configuration, illustrated in Fig. 4.67, reports a rat-race coupler composed by a +90° branch

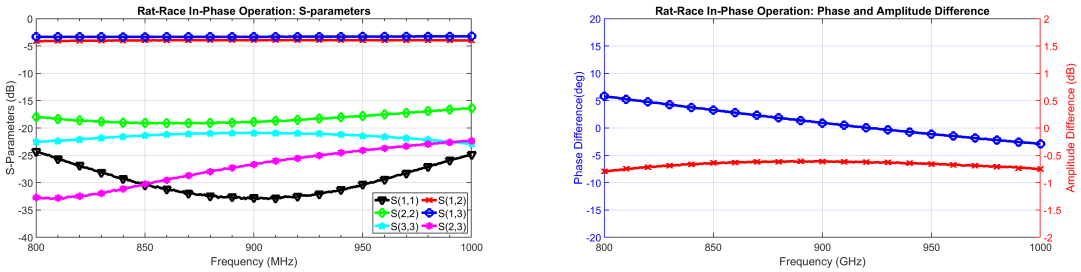

(a) (b)

Figure 4.66: Simulated results of the reconfigurable rat-race coupler for the in-phase configuration related to the 45_{pol} operation (a)$S-$parameters and (b) amplitude and phase difference.

(i.e. *Line A*) and three -90° branches, which are *Line D* and the two combinations *Line B*+*Line E* and *Line C*+*Line F*. No changes in electrical length are applied to *Line A* and *Line D* at this stage. With the coupler reconfigured in out-of-phase operation, as shown in Fig. 4.67, it is now possible to feed *Pin H* and *Pin V* with 180° phase difference.

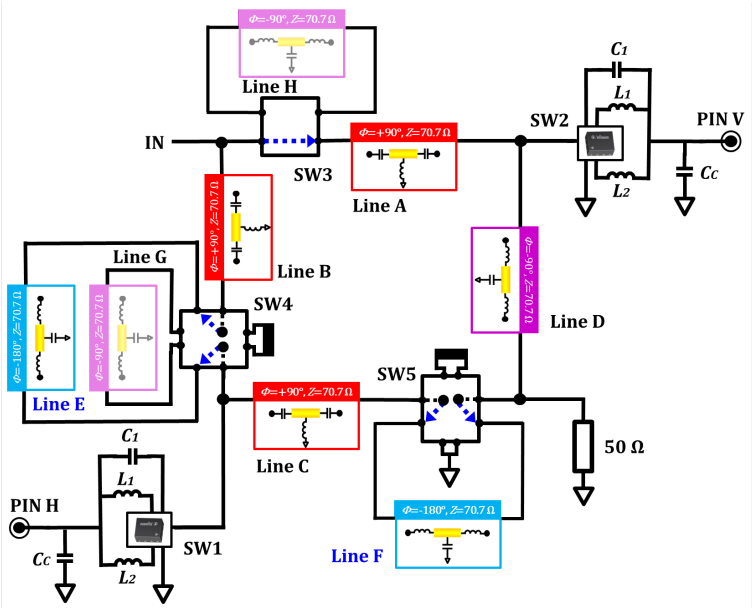

Figure 4.67: Topology of the feeding network for the -45_{pol} operation. The lines which are not actively involved are shaded, and the switch operation is illustrated.

The proposed reconfiguration, although not straightforward to understand, represents the most efficient way to change the operation of the rat-race coupler from in-phase to out-of-phase just employing two switches, without any modification of

the inputs and outputs. The two 180° delay lines *Line E* and *Line F*, which are placed in series to *Line B* and *Line C* respectively, are both composed by $n = 2$ unit cells, as specified by (4.21):

$$\textbf{Line E, F} \quad \Longrightarrow \quad n\left(-\omega\sqrt{L_{n2}C_{n2}} - \phi_l\right) = -\pi \tag{4.21}$$

The performance of the reconfigured coupler is reported in Fig. 4.68, by considering the $S-$parameters and the phase and amplitude difference at the two outputs (*Port 2* is related to *Pin H* and *Port 3* to *Pin V*). Even if the $S-$parameters shown in Fig. 4.66a demonstrate a good functionality in the overall operating band of the out-of-phase configuration of the rat-race, with maxim return loss and insertion loss of 17.5 dB and 1.3 dB respectively, the amplitude difference in Fig. 4.68b is increased with respect to the in-phase configuration by approximately 0.4 dB, due to the losses introduced by *Line E* and *Line F*. Moreover, the phase error is strongly dependent on frequency, showing a steep variation in the frequency range of interest. This effect is given by the construction of the -90° branch, realized as the cascade of a 90° LH-ATL and one -180° RH-ATL. It is noticed that for this special case the use of a phase balancing term, as adopted in Sect. 3.4, would have led to an extremely high contribution for compensating the required group delay, and therefore this solution has been considered unpractical for meeting the goal of high compactness.

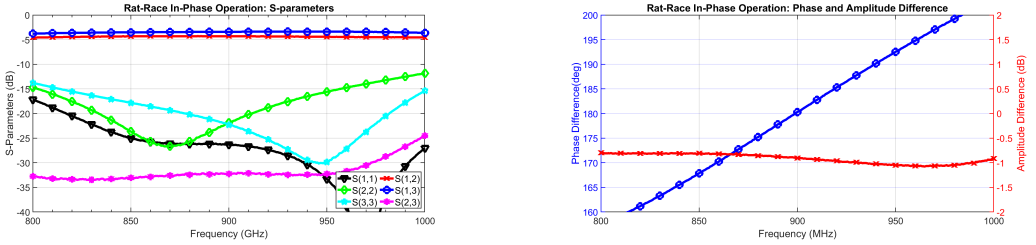

(a) (b)

Figure 4.68: Simulated results of the reconfigurable rat-race coupler for the out-of-phase configuration related to the -45$_{pol}$ operation (a) $S-$parameters and (b) amplitude and phase difference.

However, the coupler is no longer needed when H_{pol} and V_{pol} are required. In these cases, the phase can be arbitrary and the isolation is no more a parameter of interest, since only one of *Pin H* or*Pin V* is excited. There are two main concerns that have to be solved to reconfigure the rat-race coupler as a single feeding line. The first is related to the way to "break" the ring and isolate the two lines, feeding either *Pin H* or *Pin V*: this is given by *SW5* which provides a direct connection to ground. By this operation, *Line C* and *Line D* are terminated in a *SHORT*, and due to their ±90° electrical length, at the connection with *SW1* and *SW2*,

they act like an *OPEN*. It is noticed that with this configuration not only *Line C* and *Line D* are virtually disconnected, but also the 50 Ω termination is excluded from the active structure, since it is placed in parallel to a *SHORT*. The second problem that has to be solved is related to the characteristic impedance of the lines connecting *Pin H* and *Pin V*. Taking advantage of the relatively narrowband range of frequencies involved, and by targeting a solution which employs the minimum number of switches, line sections superimposed to *Line A* and *Line B* are again exploited to realize 0° lines. Since *Line A* and *Line B* are both $50 \cdot \sqrt{2}\ \Omega$ LH artificial transmission lines attaining a phase of +90°, for achieving the 0° condition an RH-ATL with the same characteristic impedance and with opposite phase (i.e. -90°) has to be placed in series. The described case is reported in Fig. 4.69 for the *Horizontal* polarization, where *SW5* selects the $50 \cdot \sqrt{2}\ \Omega$ *Line G* to compensate for the phase of *Line B*, and realizes the 0° line. Moreover *SW2* terminates *Pin V* through a *SHORT*, and it is again exploited the *SHORT* to *OPEN* transformation given by the +90° branch, which is performed by *Line A*. The phase expression (4.22) for *Line G* is simply found by equating the contribution of $n = 2$ RH unit cells to -90°, required to realize the 0° line.

$$\textbf{Line G} \quad \Longrightarrow \quad n\left(-\omega\sqrt{L_{n3}C_{n3}} - \phi_l\right) = -\frac{\pi}{2} \tag{4.22}$$

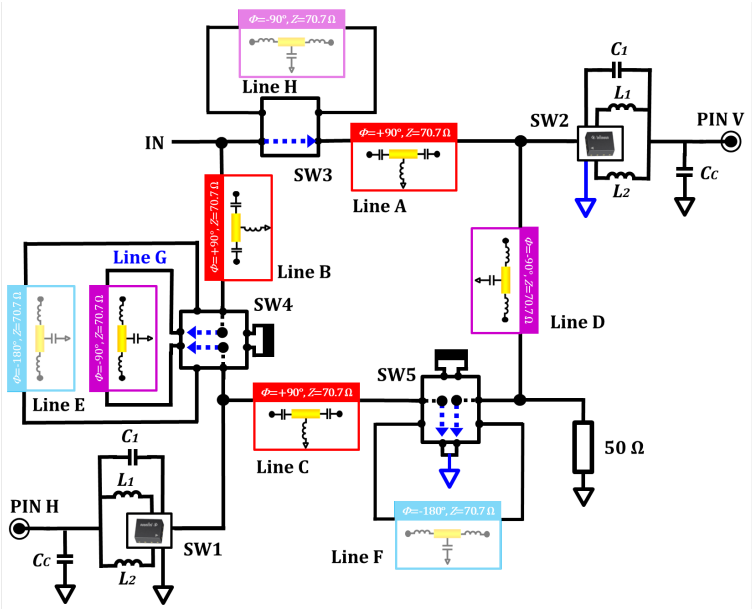

Figure 4.69: Topology of the feeding network for the H_{pol} operation. The lines which are not actively involved are shaded, and the switch operation is illustrated.

Conversely, *SW1* is connected to ground for excluding *Pin H* and *Line B* (through the $\lambda/4$ transformer) in order to obtain the proper excitation for the

Vertical polarization. In this case, *SW3* connects the input and *Line A* with *Line H*, which is the same type as *Line G*. The latter configuration is illustrated in Fig. 4.70.

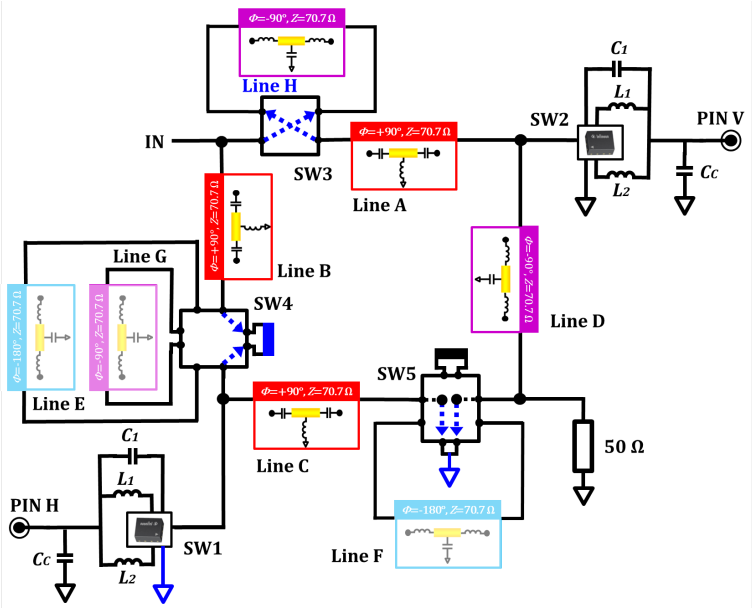

Figure 4.70: Topology of the feeding network for the V_{pol} operation. The lines which are not actively involved are shaded, and the switch operation is illustrated.

However, the phase condition for *Line H* differs from the one written for *Line G*, because of the phase contribution ϕ_{sw} of *SW3*, as can be noticed in (4.23).

$$\textbf{Line H} \quad \Longrightarrow \quad n\left(-\omega\sqrt{L_{n4}C_{n4}} - \phi_l\right) - \phi_{sw} = -\frac{\pi}{2} \tag{4.23}$$

In Table 4.5 are summarized the values of the components loading the artificial transmission lines composing the fully reconfigurable rat-race based reconfigurable feeding network. The matching components, already listed in Fig. 4.14, are also included for clarity.

Moreover, it is noticed that with this type of reconfigurable feeding network there is theoretically no need to tune the matching components composing the frequency agile switching network, and using the values originally calculated without the polarization reconfigurable network, which are specified in 4.3. Therefore, Fig. 4.71 shows the reflection coefficient of the complete system including the patch antenna and the rat-race based feeding network, employing the initial matching network definition. The results displayed in Fig. 4.71 show that both the EU and US bands are well matched, with the exception of the 45_{pol}, reported in Fig. 4.71b, where it can be observed that in the EU band the -10 dB is not met for the complete

Table 4.5: Values of Components Loading the RH-ATLs and LH-ATLs

Line A	**Values**	**Lines B, C**	**Values**
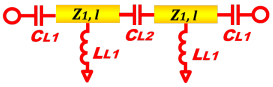	$Z_1 = 70.7\ \Omega$, $l = 2.5\ mm$ $C_{L1} = 5.1\ pF$ $C_{L2} = 2.5\ pF$ $L_{L1} = 14\ nH$	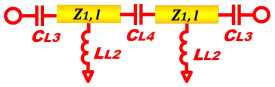	$Z_1 = 70.7\ \Omega$, $l = 2.5\ mm$ $C_{L3} = 5\ pF$ $C_{L4} = 2.7\ pF$ $L_{L2} = 13\ nH$
Lines D, G	**Values**	**Lines E, F**	**Values**
	$Z_1 = 70.7\ \Omega$, $l = 2.5\ mm$ $L_{R1} = 4.7\ nH$ $L_{R2} = 9.5\ nH$ $C_{R1} = 1.6\ pF$	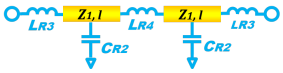	$Z_1 = 70.7\ \Omega$, $l = 2.5\ mm$ $L_{R3} = 8.2\ nH$ $L_{R4} = 18\ nH$ $C_{R2} = 3.2\ pF$
Line H	**Values**	**Matching**	**Values**
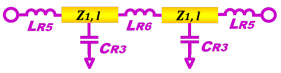	$Z_1 = 70.7\ \Omega$ $l = 2.5\ mm$ $L_{R5} = 3.9\ nH$ $L_{R6} = 8.2\ nH$ $C_{R3} = 1.6\ pF$	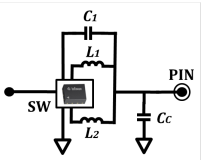	$C_c = 1.2\ pF$ $L_1 = 26\ nH$ $L_2 = 3.9\ nH$ $C_1 = 3.3\ pF$

band, and a maximum reflection coefficient of -9.7 dB is measured from the full-wave simulation performed in the full wave simulation solver. Moreover, differently from the ideal case, the reflection coefficients relative to the H_{pol} and V_{pol} are not coincident, due to the asymmetry of the feeding method applied in the two cases. It is remarked that a slight tuning of the common capacitor C_c (reported in all Figures 4.64 – 4.70), can lead to a complete fulfillment of the matching requirements.

After having completely specified the reconfigurable feeding network, the antenna gain and the polarization purity are evaluated in the *xz* and *yz* cuts, according to the axes definition in Fig. 4.7. Considering first the EU band, reported in Fig. 4.72 and Fig. 4.73, at 867 MHz the minimum of the gain is detected for the *Vertical* polarization, equal to 1 dBi, while the maximum of 1.7 dBi is found for the *45° diagonal* polarization (i.e. corresponding to the in-phase rat-race coupler). The cross-polar components evaluation show good results, well below -15 dBi, with the exception of the -45_{pol}, where the simulated value of -13.2 dB is measured. This is related to the phase error displayed in Fig. 4.68b, which has the worst case scenario in relation to the out-of-phase configuration of the reconfigurable rat-race coupler. It can be recognized from Figs. 4.74, 4.75 that better results are achieved in the US frequency bands, where the minimum value of the gain found for the V_{pol} is increased to approximately 2.1 dB, while the best case related to the -45_{pol}

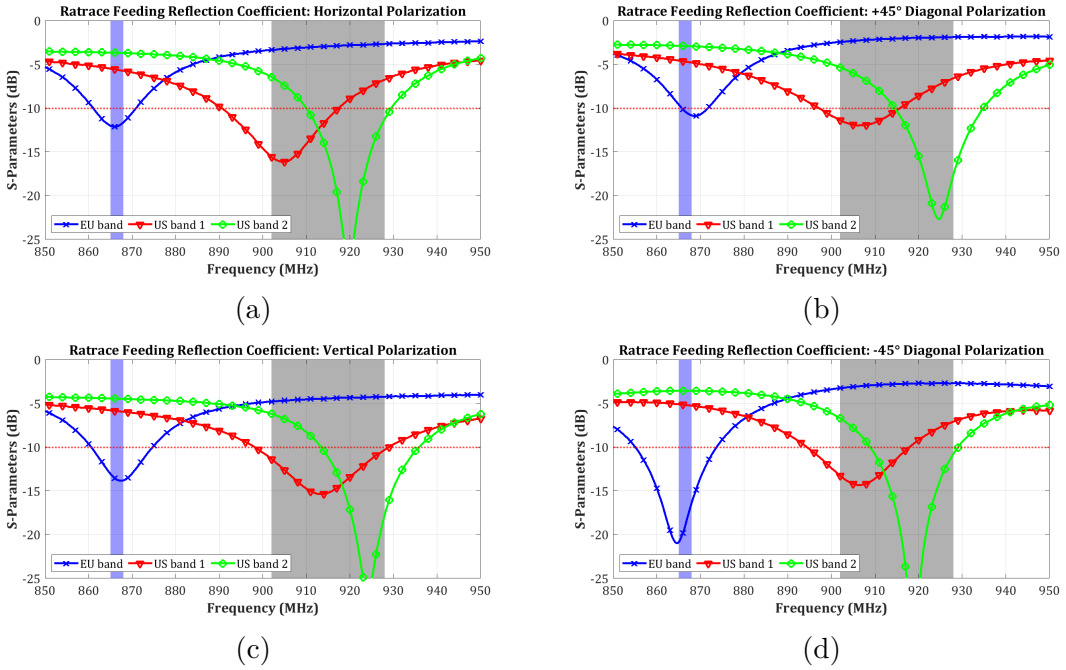

Figure 4.71: Simulated reflection coefficient for the full reconfigurable rat-race feeding network antenna system. The frequency states corresponding to the EU band and the two US sub-bands are reported and indicated for reference. The evaluation includes the four polarization: (a) *Horizontal*, (b) *+45°* diagonal, (c) *Vertical* and (d) *-45°* diagonal.

polarization shows a realized gain of 2.9 dB. In this frequency band the polarization purity is increased, with a maximum cross-polar component well below -15 dBi. It is observed that, at this frequency, the cross-polar component in the -45$_{pol}$ state is below -20 dBi, which demonstrates that the phase error displayed in Fig. 4.68b does not compromise the functionality of the reconfigurable antenna.

Finally, the total radiated efficiency displayed in Fig. 4.76 shows that the 50% target efficiency is exceeded in almost all configurations, except for the EU frequency tuning of the *Horizontal* and *Vertical* polarizations, which are slightly below the desired level. This is due to the losses introduced by the virtual disconnection of the unused feeding pin, realized through *SHORTS*. As already noticed, the produced *SHORT* termination is not ideal, due to the equivalent resistance of the switch used for the connection (i.e. R_{ON}) and because of the phase spread and losses of the ATLs, which lead to a "short stub" effect. Clearly, another limitation of the maximum efficiency is given by the switches, which also contribute to ohmic losses. However, in the two US sub-bands the efficiency is well above the theoretical limit of an ideal CP based UHF RFID reader antennas, thus demonstrating a direct improvement compared to standard applications. Similarly to the comment

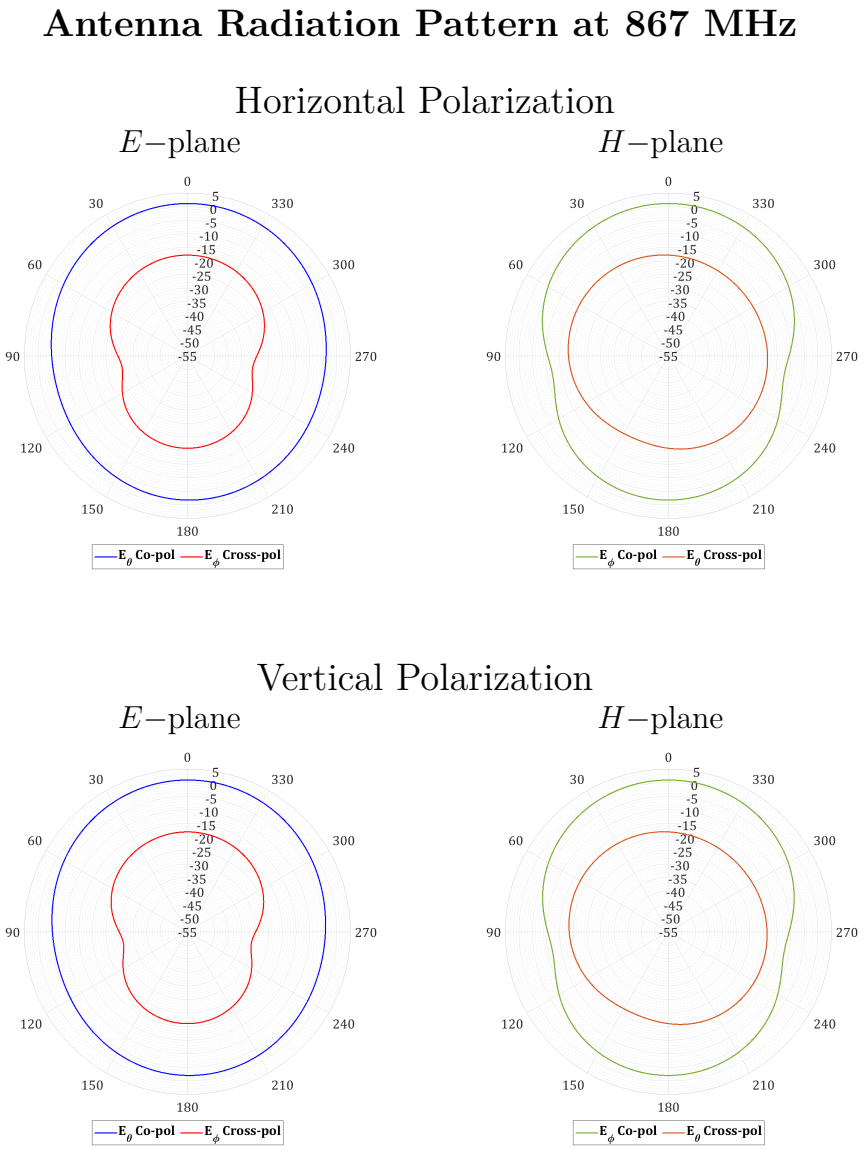

Figure 4.72: Simulated radiation pattern at 867 MHz (related to the EU band) of the modeled suspended patch with the full reconfigurable rat-race feeding network antenna system, in the *Horizontal* and *Vertical* polarization states. In agreement with the considered polarization, the $E-$plane and $H-$plane components of the electric fields are reported.

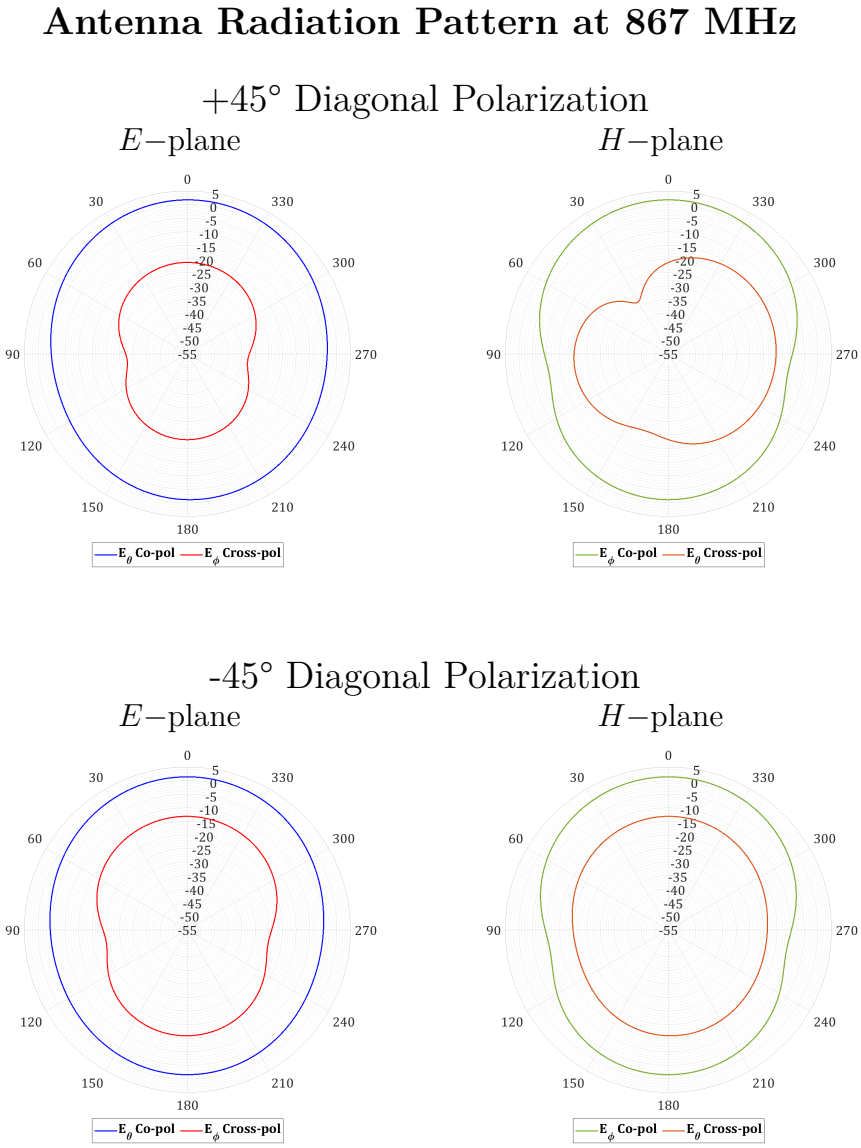

Figure 4.73: Simulated radiation pattern at 867 MHz (related to the EU band) of the modeled suspended patch with the full reconfigurable rat-race feeding network antenna system, in the two diagonal *+45°* and *-45°* polarization states. In agreement with the considered polarization, the $E-$plane and $H-$plane components of the electric fields are reported.

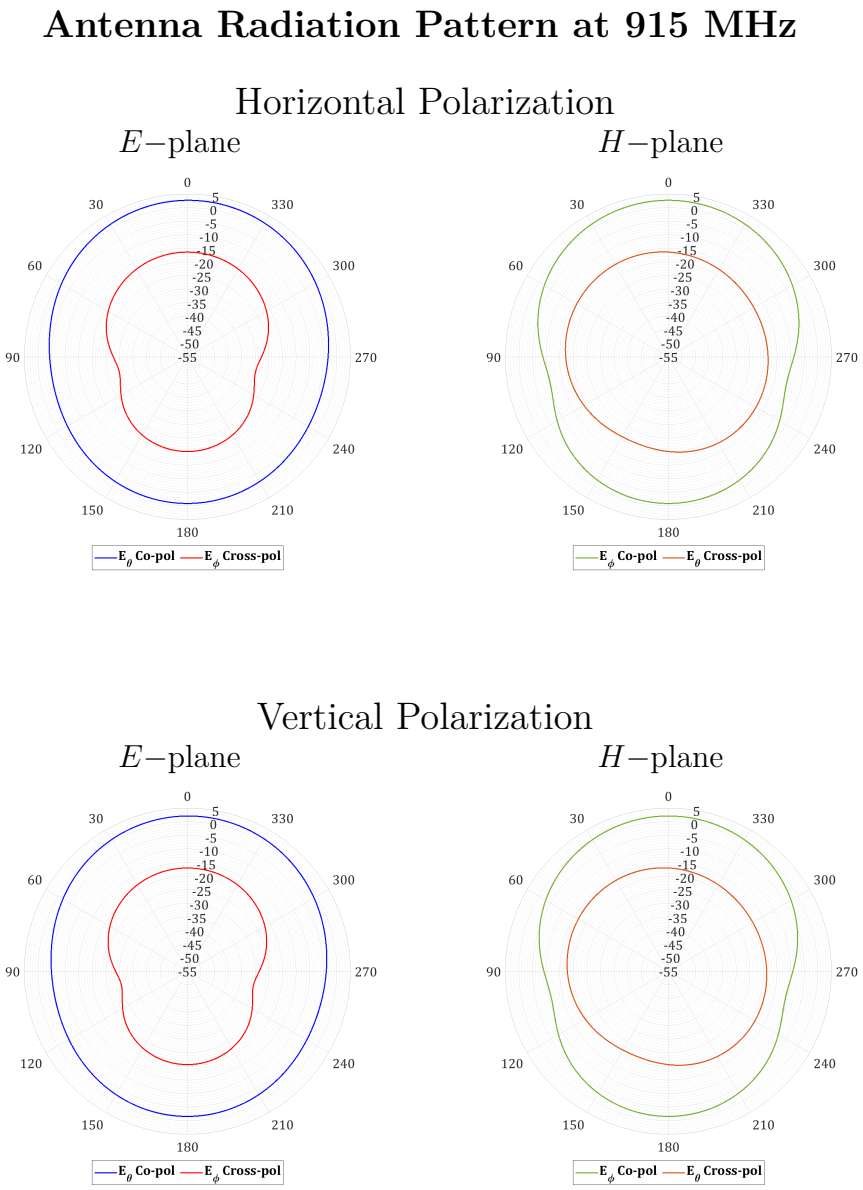

Figure 4.74: Simulated radiation pattern at 915 MHz (related to the upper US band) of the modeled suspended patch with the full reconfigurable rat-race feeding network antenna system, in the *Horizontal* and *Vertical* polarization states. In agreement with the considered polarization, the $E-$plane and $H-$plane components of the electric fields are reported.

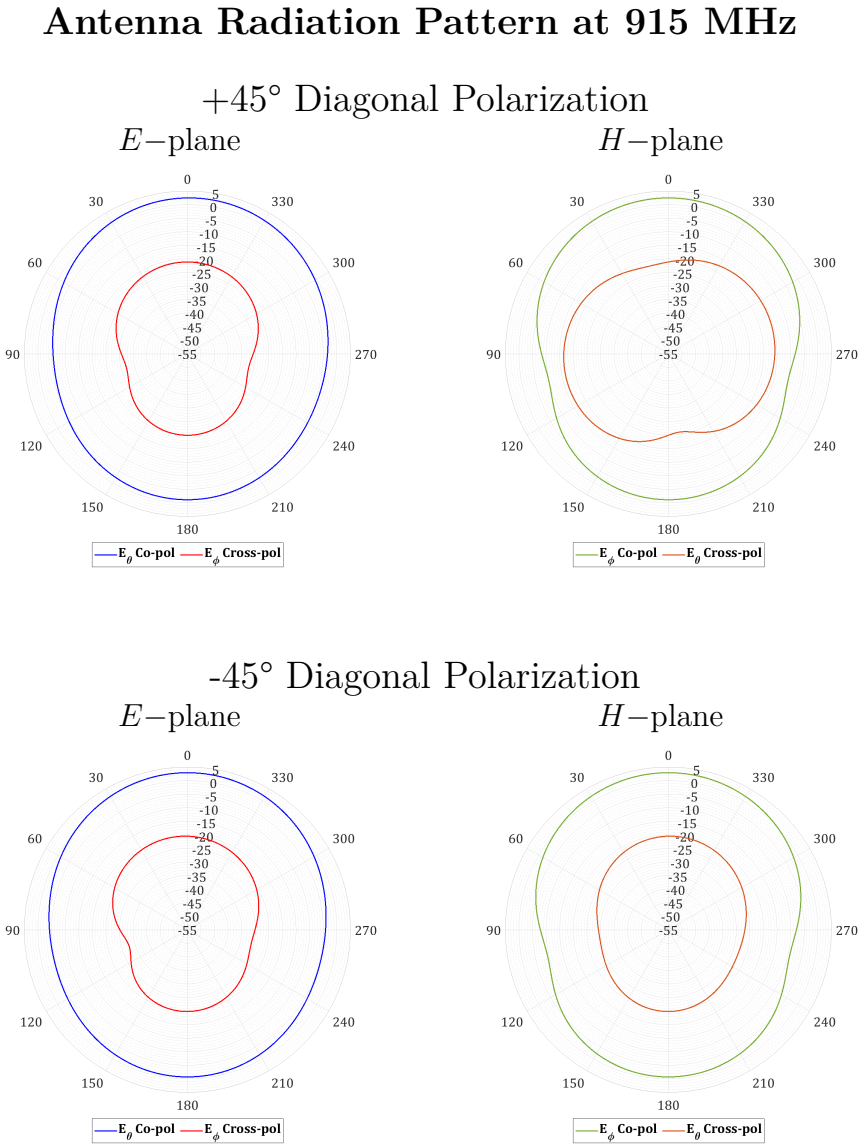

Figure 4.75: Simulated radiation pattern at 915 MHz (related to the upper US band) of the modeled suspended patch with the full reconfigurable rat-race feeding network antenna system, in the two diagonal *+45°* and *-45°* polarization states. In agreement with the considered polarization, the $E-$plane and $H-$plane components of the electric fields are reported.

reported in Sect. 3.5.2, also in this case the use of 50 Ω switches, imposed by available technology, contributes to increase the overall losses of the reconfigurable the rat-race coupler. In fact, the employing of 75 Ω switches would lead to a more optimized and less lossy design. Moreover, it is noticed that in this design the goal of designing a compact reconfigurable feeding network was set, however, by using more unit cells for constructing the ATL based branches of the rat-race, a more precise phase accuracy can be obtained (see [242]).

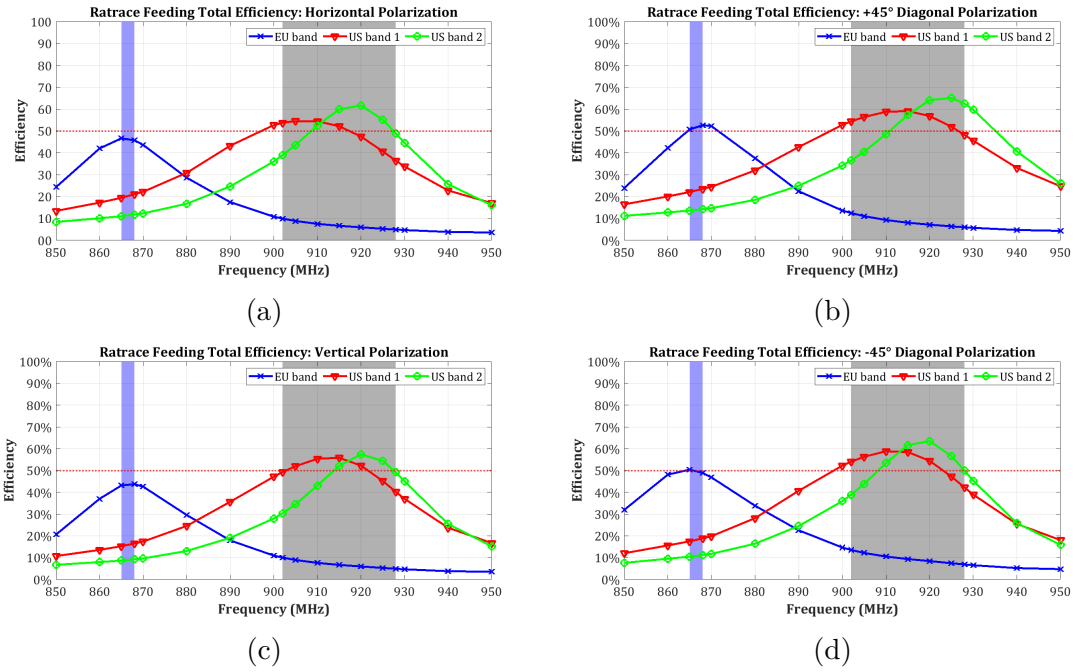

Figure 4.76: Simulated antenna total efficiency for the full reconfigurable rat-race feeding network antenna system. Frequency switching states are indicated for reference. The evaluation includes the four polarization: (a) *Horizontal*, (b) *+45°* diagonal, (c) *Vertical* and (d) *-45°* diagonal. The 50% limit, related to an ideal antenna with CP approach, is also drawn.

4.6 Comparison of Frequency and Polarization Reconfigurable Antennas Performance

Finally, a comparison between the five frequency and polarization reconfigurable feeding networks is here reported. In Table 4.6 the overall performance, distinguished in the EU and US bands, of the five solutions are shown. It is remarked that the goal of Table 4.6 is to give an insight of the most important parameters, which are considered in heterogeneous way across the four polarization states (i.e.

Table 4.6: Frequency and Polarization Reconfigurable Solutions Comparison

	Switched Lines	**Switched ATLs**	**Stub Like Feeding**	**Optimized Feeding**	**Rat-race Based**
Switches	6	4	6	3	5
Area (mm^2)	2552	792	480*	400*	400*
Return Loss Min. (dB)			**EU band**		
	8.7	10.5	10.4	9.6	9.7
			US band		
	9.7	5.8	10.8	10.6	10.5
Peak Gain (dBi)			**EU band**		
	2.1	1.5	-0.3	1.1	1.7
			US band		
	3.2	1.8	2.1	2.0	2.9
Cross-pol. Max (dBi)			**EU band**		
	-17.1	-15.5	-14.7	-15.4	-13.2
			US band		
	-14.7	-14.8	-15.9	-11.9	-15.7
Efficiency Range (%)			**EU band**		
	52.5–55.9	43.4–49.1	28.9–32.7	38.6–51.9	43.6–52.7
			US band		
	53.6–68.3	35.7–61.5	37.7–53.8	49.3–60.1	49.2–65.1

(*) Estimated from ATL unit cells length and switches dimensions.

the maximum and minimum values may refer to different polarization states), and not to fully characterize the solutions. In other words, it has been chosen to give to the reader a clear view of which are the limitations and benefits over the different solutions, without fully reporting the cases in the four polarization state over the two frequency bands.

The first distinction among the described solutions concerns the number of switches. The reconfigurable feeding lines which employs more switches are the switched delay lines and the stub like feeding lines, which requires six switches. However, very different aspect are enhanced in the two design (e.g. efficiency and peak gain is higher with the switched line approach, while a very good matching is achieved with the stub inspired feeding). On the other hand, the optimized version is capable of performing the two reconfigurable operations with fairly good performance with only three switches. By taking into account just the frequency band reconfiguration, the best performance are achieved by the stub like feeding network, which exhibits a very wide matching due to its peculiar matching concept. However, the two band coverage was almost fully achieved in all polarization states for all the solutions, with just small deviation to the targeted limit of -10 dB.

The exception is represented by the switched ATLs, where in two polarization states the resulted matching was poor, due to the non idealities of the *OPEN* termination achieved with the switch. Conversely, considering just the polarization purity achieved with the reconfigurable feeding networks, the best solution for the EU band is represented by the switched lines design, while the stub like feeding is the one with less cross coupling in the US band. However, this are worst cases, mostly related to the $H-$plane, and by reviewing the simulated radiated patterns very low cross polar levels can be found in almost all cases, in particular for the stub inspired solution, where the maximum value of -46 dBi was achieved in $E-$plane. The rat-race based feeding and the switched line reconfigurable network are the ones that can achieve the higher antenna gain, and they also exhibit the best total efficiency. Considering these aspects, also the optimized feeding show good performance, in both the EU and US frequency bands. In contrast, the stub like feeding network and the switched ATLs solution reveal an excessive efficiency and gain loss, due to the component losses of the line (stub inspired feeding) or by a poor matching (switched ATLs design). Nevertheless, an important parameters that was not extensively discussed, but it is reported in Table 4.6, is the PCB area required for the development of the reconfigurable feeding networks. For the solution employing switchable delay lines, the measured PCB are was found to be $58 \times 44\, mm^2$. The solution based on the same switchable lines concept, but employing ATLs, improved the form factor by almost 50%, requiring only $33 \times 24\, mm^2$. For the other three solutions, an estimation can be made, by considering the length of each ATL unit cell and the size of the CMOS switches. The most compact solutions should be the optimized and the rat-race based feeding network, which need a $20 \times 20\, mm^2$ square area to be implemented on the PCB. The last reconfigurable feeding network, which is inspired by stub theory, is expected to be slightly more space consuming, with $24 \times 20\, mm^2$. Among the numbers which are reported in Table 4.6, it can be comment that the rat-race based feeding can provide isolation among the two antenna feeding points, and no further tuning is needed for the reconfigurable matching network, whose design can be then decouple from the polarization feeding network. Moreover, the stub inspired solution provides a high degree of flexibility in the matching topology to be used, in contrast with the other solutions.

4.7 Conclusion and Perspectives

In this chapter, it has been discussed a method to exploit reconfigurability to enhance compactness, communication efficiency and multiple standard compliance of a UHF RFID antenna for reader application. According to the initial goal of designing an uncomplicated and flexible structure, the suspended patch antenna

as radiating element was selected, demonstrating also an efficient method to reduce its form factor by increasing its equivalent electrical length through the use distributed end capacitors. From this basis, five different concepts for achieving frequency and polarization reconfigurability has been developed, selectively matching the EU and US bands while switching among four different linear polarizations (in 45° steps) independently. In particular, the latter operation allows to theoretically reduce the polarization mismatch of the reader-tag communication process from 3 dB to 0.7 dB, considering as reference the circular polarized approach which is commonly used in UHF RFID application. This aspect is more critical in the UHF RFID application, due to the backscattering nature of the communication involved. Moreover, in all the investigated solutions CMOS switches are employed, instead of more popular components, as for instance PIN diodes, for being fully compliant with the power ratings requirement imposed by the UHF RFID standards. The results are obtained by a combination of circuital and full-wave simulation process, for characterizing the five different approaches. The proposed solutions are presenting interesting results, as for instance the possibility to use just three switches for operating both frequency and polarization reconfigurability, or instead to a use fully symmetric feeding network inspired by matching stub theory, which gives full flexibility on the type of matching topology to be used and demonstrate some potential of achieving extremely low cross-polarization levels. In addition, a full reconfigurable rat-race coupler was developed to cover the four polarization states, capable to modify its structure to operate in the in-phase or out-of-phase configurations, as well as to act as a single feeding line to deal with the two single feeding cases. Promising results concerning the fulfillment of the matching condition in all frequency/polarization states have been observed, as well as good results concerning polarization purity, where in most of the cases a cross-polarization ratio of 20 dB was achieved. The use of artificial transmission lines ensures that the proposed solutions employing this technology are very compact, and that they can be easily integrated in an UHF RFID system application.

Further investigation has to be carried for improving the total efficiency, thus exploiting the full potential of this approach. An improvement on the components used, as well as the application of a novel type of reconfigurable matching architecture, reducing the initial efficiency loss of 13% – 18% is needed. Finally; it is remarked that the concepts developed here can be in general applied to other antenna topologies and different frequency bands. Moreover, the same theoretical concepts and analysis developed here can be adapted to different applications, operating in higher frequency bands, by replacing the artificial transmission lines with other suitable technologies (e.g. using smart materials).

Chapter 5

Conclusions and Pespectives

In the applied research activity described in this thesis, the reconfigurability technique is applied to three significant examples, which also represents some more general issues that are currently subjects of investigation by the scientific community. As a matter of fact, great effort is requested to the RF and Microwave designers in order to introduce new solutions and technologies for satisfying the increasing demand of connected devices and wireless sensors. The requested innovation is directed not only on the advance of performance or the overcoming of complications related to the adoption of new standards (e.g. wider bandwidth, higher frequency), but also on the miniaturization and integration of multiple standards and feature in a single device. In the presented scenario, reconfigurable antennas and systems have an enormous potential to identify new solutions for both the aforementioned problems due to their capability to improve systems performance and efficiency, as well as to introduce flexibility and better integration by delivering the same throughput as a multi-antenna system. These aspects have been demonstrated also in this research work, where reconfigurability is used to increase the performance and overcome the scan limitation of a 24 GHz phased array employing a Rotman lens as beamformer (Chapter 2). In the development of the reconfigurable beamforming feeding it has also been considered the further complication of managing a high number of inputs, in contrast with the majority of the solutions that can be found in literature. The frequency agility concept described in Chapter 3, applied to the rat-race coupler, has identified the best technology to realize the desired reconfigurability and, in addition, to design the most compact coupler version that can be found in literature for the center frequency of 900 MHz. In the realized design, it has been recognized that the introduction of active components has to be considered not only in the circuital simulations, but also in a previous phase by revising the theory of artificial transmission lines for including the switching components in the calculation. By the combination of the ATL theory and the reconfigurability concept, a quite wide band behaviour is obtained, despite the very compact form

factor. In the last chapter (i.e. Chapter 4), presenting a study of various realization of switchable feeding networks, reconfigurabilty is used for greatly optimized the design of a UHF RFID reader antenna, by obtaining a unique antenna design for the EU and US regional standards though frequency agility, while the application of the switchable feeding network for select a specific polarization, lead to an increased total efficiency of the complete reader-TAG RFID system, reducing the polarization mismatch loss to 3 dB to maximum 0.7 dB, in comparison with a commonly used circular polarized antenna approach. The theoretical 50% gain in polarization efficiency could enable the design of a very compact but uncomplicated definition of the radiating element. Several techniques to realize the reconfigurable feeding network have been proposed, each of them focused on the improvement of a specific aspect (e.g. minimum number of switches, tuning flexibility, isolation at feeding points). Nevertheless, although reconfigurability proposes very promising concepts and solutions, it also exhibits some notable drawbacks that cannot be ignored, since they are the main limitation of the widespread use of this technology. In fact, the application of reconfigurability introduces a more complex design and development phase, due to the usage of active components, which requires controls and power supply, as well as a preliminary analysis and characterization of the components to be integrated in the system. Especially for antenna designers, these aspect transform the design of a passive device to a complex system, in which are combined electromagnetic theory, digital and analog circuits concepts. Therefore, aspects like power consumption, RF power rating and EMC arises and introduce critical constraints in the design. It is noticed that the successful application of reconfigurability in a real application is strongly related to the considerations of all the aspects involving the system functionality, instead of focusing only on the regular RF/Microwave design constraints. For the same reason, CMOS switches are adopted for the UHF RFID reader application in Chapter 4, in contrast with some designs found in literature which adopt reconfigurable elements that are not compliant with the maximum power rating. Moreover, in general, the multitude of active states leads sometimes to problems due to the non-uniform performance of the reconfigurable device, and also to a more complex development and validation phase since all the single cases have to be fully analysed, resulting in much more effort needed in the design with respect to a standard fixed performance device.

Indeed, the integration with active components imposes to develop new methods to reduce the decrease in efficiency, which is strongly dependent on the active element. Similarly, the tunability is also a function of the method used to apply reconfigurability, and the capability of the switching components to introduce the required modification of the desired characteristic. Therefore, the results achievable with the application of reconfigurability are determined by the performance of the elements used to achieve the tuning function. As an example, in the design of the miniaturized and reconfigurable rat-race coupler in Chapter 3, the use

of 50 Ω switches in the lines with characteristic impedance of $\sim$ 70 Ω was forced, since there were no switch available that satisfy the design requirements (i.e. 75 Ω switches in $DPDT$ and $2 \times SPDT$ configuration). Despite the described drawbacks, that require further investigations and researches, the reconfigurable antennas and systems will be fundamental in the future applications to fulfill the modern requirements. Actually, two main uses are forecast for this type of solutions, one involving the integration of multiple standards in electrically small devices, mostly operating in the sub-6 GHz frequency domain, while the second research branch for reconfigurabilty will focus on the advance and performance expansion of mm-wave and terahertz range devices, where the design complexity and high cost of components, related to the extremely high frequency regime, force to reduce the number of antenna element and to apply smart methods to overcome the limitations of the system. In the first case, the reconfigurability principle will be supported by the development of semiconductor-based switching devices, with improved performance and tunability. In fact, the semiconductor industry is constantly integrating new features on the chips, while reducing form factor and losses, in order to support the demand of multi-functional and multi-operation devices. In the second case, involving mm-waves and low Terahertz frequency ranges, the tunable and phase change materials (e.g GeTe and Graphene based switches) represent a promising solution to introduce flexibility on devices characterized by a wavelength of few millimeters (or even less), which would be otherwise impossible with discrete components. As concluding remark, from the analysis reported in this thesis, much effort on the research is asked not only to antenna designers, but also to the semiconductor and material scientists, for creating the necessary technology that can be uses to face the future challenges. As a consequence, this aspect redefine the role of the antenna and RF/microwave designer, that is requested to have a multi-disciplinary background in order to deal with the multiple technologies and techniques in use.

Appendix A

Phase Balancing Term Calculation

In Fig. A.1 are reported the two reconfigurable branches and switches in both f_1 and f_2 configurations. For calculating the values of inductor L and capacitors C composing the $T-$type unit cells of both LH-ATLs and RH-ATLs, reported in Fig. 3.1, all the phase contributions have to be considered and added (with correct sign), and the equality to $\pm 90°$ imposed.

Beside the two lumped components, the other single elements which are contributing to the total phase of the branch are the transmission lines sections and the switch, attaining a phase $\phi_l = -\beta_l(f_x)\, l_l = \omega_1\sqrt{\mathcal{LC}}l_l$ and $\phi_s = -\beta_s(f_x)\, l_s = \omega_1\sqrt{\mathcal{LC}}l_s$ respectively, where β_l and β_s are the corresponding phase constants (calculated at frequency f_x), $\mathcal{L}$, $\mathcal{C}$ are the distributed capacitance and inductance of a 50 Ω line (used also to model the switch) and, finally, l_l, l_s are the relative physical lengths. For a clearer view of the different phase terms which are composing the reconfigurable branches of the rat-race coupler, all the single contribution types are listed in Table A.1, where in particular the phase contribution of the two ATLs unit cell types are decomposed in the purely RH/LH lumped circuital part and the distribute part given by the microstrip line. Moreover, the phase contributions of the switches are reported in both the transmission and crossing configurations.

Then, by considering the phase elements described so far, and by defining the two angular frequencies $\omega_1 = 2\pi f_1$ and $\omega_2 = 2\pi f_2$, the phase contributions of the four unit cells are reported in (A.1) – (A.4), where the subscript refers to the frequency band (i.e. f_1 or f_2) while the superscript refers to the branch, indicating with "+" the +90° branch and with "−" the -90° branch. With the purpose of finding the derivatives with respect to ω of the phase equations, the single cell phase contribution is expressed in terms of angular frequency.

$$\varphi_1^+(f_1) = \frac{1}{\omega_1\sqrt{L_{p1}C_{p1}}} - \omega_1\sqrt{\mathcal{LC}}l_l \tag{A.1}$$

$$\varphi_2^+(f_2) = \frac{1}{\omega_2\sqrt{L_{p2}C_{p2}}} - \omega_2\sqrt{\mathcal{LC}}l_l \tag{A.2}$$

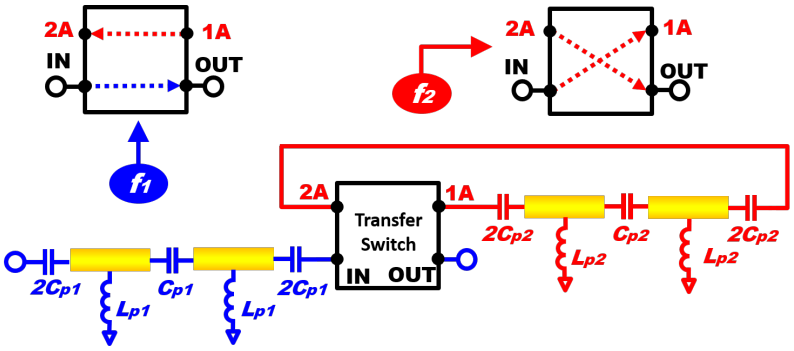

(a)

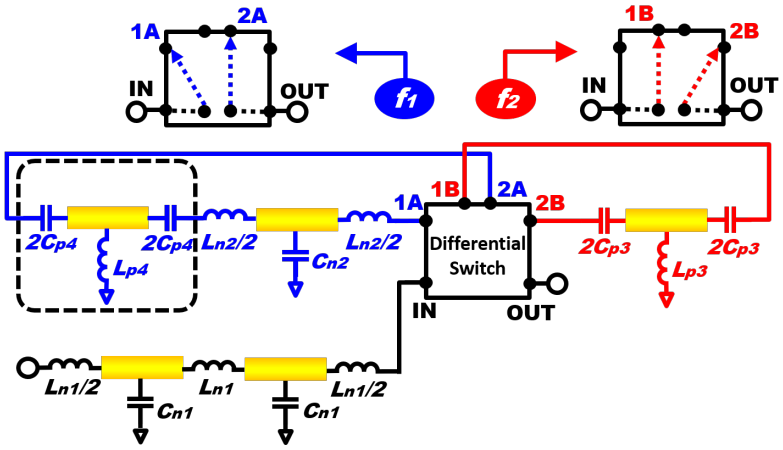

(b)

Figure A.1: Both the frequency agile +90° and -90° branches in both configurations are reported, including the identifier of each component.

$$\varphi_1^-(f_1) = -\left[\omega_1\sqrt{L_{n2}C_{n2}} + \omega_1\sqrt{\mathcal{LC}}l_l\right] \tag{A.3}$$

$$\varphi_2^-(f_2) = -\left[\sqrt{L_{n1}C_{n1}} + \omega_2\sqrt{\mathcal{LC}}l_l\right] \tag{A.4}$$

In the same way, the two phase balancing terms are also defined, that are applied at the -90° branch in both f_1 and f_2 configuration, as reported in Fig. A.1b:

$$\varphi_1^C(f_1) = \frac{1}{\omega_1\sqrt{L_{p4}C_{p4}}} - \omega_1\sqrt{\mathcal{LC}}l_l \tag{A.5}$$

$$\varphi_2^C(f_2) = \frac{1}{\omega_2\sqrt{L_{p3}C_{p3}}} - \omega_2\sqrt{\mathcal{LC}}l_l \tag{A.6}$$

For the calculation of the Phase Balancing Terms, it is first considered the case of the two branches in the highest center frequency f_2, which represents the worst

Table A.1: List of Phase Terms Composing the RH-ATLs and LH-ATLs

Left Handed ATL Unit Cell			
Discrete LH Line	Phase Term	Transmission Line	Phase Term
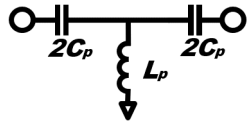	$\phi_{LH} = \dfrac{1}{\omega\sqrt{L_p C_p}}$		$\phi_l = -\omega\sqrt{\mathcal{LC}}l_l$
Right Handed ATL Unit Cell			
Discrete RH Line	Phase Term	Transmission Line	Phase Term
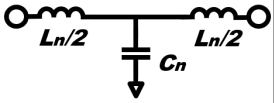	$\phi_{RH} = -\omega\sqrt{L_n C_n}$		$\phi_l = -\omega\sqrt{\mathcal{LC}}l_l$
Switch Configurations			
Switch Transfer	Phase Term	Switch Crossing	Phase Term
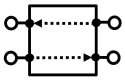	$\phi_s^1 = -\omega\sqrt{\mathcal{LC}}l_s$	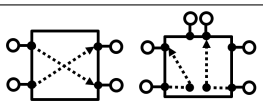	$\phi_s^2 = -2\omega\sqrt{\mathcal{LC}}l_s$

case for this application. As discussed in Sect. 3.4.1 the total sum of the phase contributions for the +90° branch at frequency f_2, needed to write the +90° phase condition and indicated here as Ψ_2^+, is calculated by multiplying the number of LH-ATL unit cells n and m_1, relative to the fixed and switchable ATL sections, with the corresponding phase contribution, expressed in (A.1) and (A.2), and by adding the phase delay of the switch (two times because it is operating in crossing mode):

$$\begin{aligned}\Psi_2^+ = n\left(\frac{1}{\omega_2\sqrt{L_{p1}C_{p1}}} - \omega_2\sqrt{\mathcal{LC}}l_l\right) - 2\omega_2\sqrt{\mathcal{LC}}l_s \\ +m_1\left(\frac{1}{\omega_2\sqrt{L_{p2}C_{p2}}} - \omega_2\sqrt{\mathcal{LC}}l_l\right) = \frac{\pi}{2}\end{aligned} \tag{A.7}$$

Similarly, the phase condition Ψ_2^- is written for the -90° branch at frequency f_2 (occurrence of switch equal to two in this branch), by adding n RH-ATL unit cells (phase attained for each cell expressed in (A.4)) and m_2 PBT unit cells, specified

in (A.6):

$$\Psi_2^- = n\left(-\omega_2\sqrt{\mathcal{LC}}l_l - \omega_2\sqrt{L_{n1}C_{n1}}\right) - 2\omega_2\sqrt{\mathcal{LC}}l_s + m_2\left(-\omega_2\sqrt{\mathcal{LC}}l_l + \frac{1}{\omega_2\sqrt{L_{p3}C_{p3}}}\right) = -\frac{\pi}{2} \tag{A.8}$$

In order to have the same phase characteristic, the phase derivatives of Ψ_2^+ and Ψ_2^- with respect to ω_2 have to be equal (at frequency f_2). Therefore, the derivatives $\frac{d\Psi_2^+}{d\omega_2}$ $\frac{d\Psi_2^-}{d\omega_2}$ of (A.7) and (A.8), respectively, are calculated.

$$\frac{d\Psi_2^+}{d\omega_2} = n\left(-\sqrt{\mathcal{LC}}l_l - \frac{1}{{\omega_2}^2\sqrt{L_{p1}C_{p1}}}\right) - 2\sqrt{\mathcal{LC}}l_s + m_1\left(-\sqrt{\mathcal{LC}}l_l - \frac{1}{{\omega_2}^2\sqrt{L_{p2}C_{p2}}}\right) \tag{A.9}$$

$$\frac{d\Psi_2^-}{d\omega_2} = n\left(-\sqrt{\mathcal{LC}}l_l - \sqrt{L_{n1}C_{n1}}\right) - 2\sqrt{\mathcal{LC}}l_s - m_2\left(\sqrt{\mathcal{LC}}l_l + \frac{1}{{\omega_2}^2\sqrt{L_{p3}C_{p3}}}\right) \tag{A.10}$$

For calculating the PBT for the highest frequency band f_2, indicated as $\varphi_2^C(f_2)$ the equality between the derivatives (A.9) and (A.10) has to be set:

$$\frac{d\Psi_2^+}{d\omega_2} = \frac{d\Psi_2^-}{d\omega_2} \Longrightarrow n\left(-\sqrt{LC}l_l - \frac{1}{{\omega_2}^2\sqrt{L_{p1}C_{p1}}}\right) - 2\sqrt{\mathcal{LC}}l_s + m_1\left(-\sqrt{LC}l_l - \frac{1}{{\omega_2}^2\sqrt{L_{p2}C_{p2}}}\right) = n\left(-\sqrt{\mathcal{LC}}l_l - \sqrt{L_{n1}C_{n1}}\right) - 2\sqrt{\mathcal{LC}}l_s + m_2\left(-\sqrt{\mathcal{LC}}l_l - \frac{1}{{\omega_2}^2\sqrt{L_{p3}C_{p3}}}\right) \tag{A.11}$$

Equation (A.7) and (A.8) can be rearranged, gathering the LH and RH terms which are dependent on lumped components, such that:

$$\frac{n}{\omega_2\sqrt{L_{p1}C_{p1}}} + \frac{m_1}{\omega_2\sqrt{L_{p2}C_{p2}}} = \frac{\pi}{2} + 2\omega_2\sqrt{\mathcal{LC}}l_s + n\omega_2\sqrt{\mathcal{LC}}l_l + m_1\omega_2\sqrt{\mathcal{LC}}l_l \tag{A.12}$$

$$n\omega_2\sqrt{L_{n1}C_{n1}} = \frac{m_2}{\omega_2\sqrt{L_{p3}C_{p3}}} + \frac{\pi}{2} - n\omega_2\sqrt{LC}l_l - 2\omega_2\sqrt{\mathcal{LC}}l_s - m_2\omega_2\sqrt{LC}l_l \tag{A.13}$$

Taking (A.11) and inserting (A.12) in the term $\frac{1}{\omega_2}\left(\frac{n}{\omega_2\sqrt{L_{p1}C_{p1}}} + \frac{m_1}{\omega_2\sqrt{L_{p2}C_{p2}}}\right)$

and (A.13) in the terms $\frac{1}{\omega_2}\left(n\omega_2\sqrt{L_{n1}C_{n1}}\right)$, it is obtained:

$$\begin{aligned}\frac{1}{\omega_2}\left(\frac{\pi}{2}+2\omega_2\sqrt{\mathcal{LC}}l_s+n\omega_2\sqrt{\mathcal{LC}}l_l+m_1\omega_2\sqrt{\mathcal{LC}}l_l\right)+m_1\sqrt{\mathcal{LC}}l_l+2\sqrt{\mathcal{LC}}l_s=\\ \frac{1}{\omega_2}\left(\frac{m_2}{\omega_2\sqrt{L_{p3}C_{p3}}}+\frac{\pi}{2}-n\omega_2\sqrt{\mathcal{LC}}l_l-2\omega_2\sqrt{\mathcal{LC}}l_s-m_2\omega_2\sqrt{\mathcal{LC}}l_l\right)\\ +2\sqrt{\mathcal{LC}}l_s+m_2\sqrt{LC}l_l+\frac{m_2}{{\omega_2}^2\sqrt{L_{p3}C_{p3}}}\end{aligned} \tag{A.14}$$

At this point,the ratio with L_{p3} and C_{p3} in (A.14) is expressed in terms of constants, which will sum up, finding that the condition for the phase derivative balancing imposed to the metamaterial unit cells (in terms of L_{p3} and C_{p3}) is:

$$2\frac{m_2}{{\omega_2}^2\sqrt{L_{p3}C_{p3}}}=4\sqrt{\mathcal{LC}}l_s+2m_1\sqrt{\mathcal{LC}}l_l+2n\sqrt{\mathcal{LC}}l_l \tag{A.15}$$

Which corresponds to the total phase contribution required to balancing the phase of:

$$\frac{m_2}{\omega_2\sqrt{L_{p3}C_{p3}}}=2\omega_2\sqrt{\mathcal{LC}}l_s+(m_1+n)\,\omega_2\sqrt{\mathcal{LC}}l_l \tag{A.16}$$

From the latter equation it is clear that an electrically small switch on the +90° branch and lines hosting the components on the metamaterial unit cell require less amount of phase for balancing the derivatives.

The phase contribution for the phase balancing term φ_1^C in the f_1 case is found with a similar procedure. At first, the two phase conditions Ψ_1^+ for the +90° and -90° cases are written as sum of n LH-ATL unit cells, and taking into account the delay of the switch:

$$\Psi_1^+=n\left(\frac{1}{\omega_2\sqrt{L_{p1}C_{p1}}}-\omega_2\sqrt{\mathcal{LC}}l_l\right)-2\omega_2\sqrt{\mathcal{LC}}l_s=\frac{\pi}{2} \tag{A.17}$$

Then, the phase conditions Ψ_1^- is found adding for n and m_3 RH-ATL unit cells, including also m_4 LH-ATL unit cells for the PBT term and considering the occurrence of switch equal to two:

$$\begin{aligned}\Psi_1^-=n\left(-\omega_1\sqrt{\mathcal{LC}}l_l-\omega_1\sqrt{L_{n1}C_{n1}}\right)+m_3\left(-\omega_1\sqrt{\mathcal{LC}}l_l-\omega_1\sqrt{L_{n2}C_{n2}}\right)\\ -2\omega_1\sqrt{\mathcal{LC}}l_s+m_4\left(-\omega_1\sqrt{\mathcal{LC}}l_l+\frac{1}{{\omega_2}^2\sqrt{L_{p3}C_{p3}}}\right)=-\frac{\pi}{2}\end{aligned} \tag{A.18}$$

The derivatives with respect to ω_1 of (A.17) and (A.18) are then calculated for imposing the condition on the phase:

$$\frac{d\Psi_1^+}{d\omega_1} = n\left(-\sqrt{\mathcal{LC}}l_l - \frac{1}{{\omega_1}^2\sqrt{L_{p1}C_{p1}}}\right) - \sqrt{\mathcal{LC}}l_s \tag{A.19}$$

$$\begin{aligned}\frac{d\Psi_1^-}{d\omega_1} = n\left(-\sqrt{\mathcal{LC}}l_l - \sqrt{L_{n1}C_{n1}}\right) - 2\sqrt{\mathcal{LC}}l_s + m_3\left(-\sqrt{\mathcal{LC}}l_l - \sqrt{L_{n2}C_{n2}}\right) \\ -m_4\left(\sqrt{\mathcal{LC}}l_l + \frac{1}{{\omega_1}^2\sqrt{L_{p4}C_{p4}}}\right)\end{aligned} \tag{A.20}$$

In order to have the same derivative for the positive and negative phase contributions, the following condition have to be satisfied at frequency f_1:

$$\begin{aligned}\frac{d\Psi_2^+}{d\omega_2} = \frac{d\Psi_2^-}{d\omega_2} \Longrightarrow n\left(-\sqrt{\mathcal{LC}}l_l - \frac{1}{{\omega_1}^2\sqrt{L_{p1}C_{p1}}}\right) - \sqrt{\mathcal{LC}}l_s = \\ n\left(-\sqrt{\mathcal{LC}}l_l - \sqrt{L_{n1}C_{n1}}\right) - 2\sqrt{\mathcal{LC}}l_s + m_3\left(-\sqrt{\mathcal{LC}}l_l - \sqrt{L_{n2}C_{n2}}\right) \\ +m_4\left(-\sqrt{\mathcal{LC}}l_l - \frac{1}{{\omega_1}^2\sqrt{L_{p4}C_{p4}}}\right)\end{aligned} \tag{A.21}$$

Expanding and changing the sign of the equation (A.21) it is found:

$$\begin{aligned}n\sqrt{\mathcal{LC}}l_l + \frac{n}{{\omega_1}^2\sqrt{L_{p1}C_{p1}}} + \omega_1\sqrt{\mathcal{LC}}l_s = n\sqrt{\mathcal{LC}}l_l + n\sqrt{L_{n1}C_{n1}} + \omega_1\sqrt{\mathcal{LC}}l_s \\ +m_3\sqrt{LC}l_l + m_3\sqrt{L_{n2}C_{n2}} + m_4\sqrt{\mathcal{LC}}l_l + m_4\frac{1}{{\omega_1}^2\sqrt{L_{p4}C_{p4}}}\end{aligned} \tag{A.22}$$

As in the case of f_2 frequency band, (A.1) and (A.3) are rearranged such that:

$$\frac{n}{\omega_1\sqrt{L_{p1}C_{p1}}} = \frac{\pi}{2} + \omega_1\sqrt{\mathcal{LC}}l_s + n\omega_1\sqrt{LC}l_l \tag{A.23}$$

$$\begin{aligned}n\omega_1\sqrt{L_{n1}C_{n1}} + m_3\omega_1\sqrt{L_{n2}C_{n2}} = \frac{m_4}{\omega_1\sqrt{L_{p4}C_{p4}}} + \frac{\pi}{2} - n\omega_1\sqrt{\mathcal{LC}}l_l \\ -2\sqrt{\mathcal{LC}}l_s - m_3\omega_1\sqrt{\mathcal{LC}}l_l - m_4\omega_1\sqrt{LC}l_l\end{aligned} \tag{A.24}$$

Again in the calculated (A.21), (A.23) is substituted in $\frac{1}{\omega_1}\left(\frac{n}{\omega_1\sqrt{L_{p1}C_{p1}}}\right)$; and

(A.24) in $\frac{1}{\omega_1}\left(n\omega_1\sqrt{L_{n1}C_{n1}}+m_3\omega_1\sqrt{L_{n2}C_{n2}}\right)$:

$$\frac{1}{\omega_1}\left(\frac{\pi}{2}+\omega_1\sqrt{\mathcal{LC}}l_s+n\omega_1\sqrt{\mathcal{LC}}l_l\right)+\omega_1\sqrt{\mathcal{LC}}l_s=$$
$$\frac{1}{\omega_1}\left(\frac{m_4}{\omega_1\sqrt{L_{p4}C_{p4}}}+\frac{\pi}{2}-n\omega_1\sqrt{\mathcal{LC}}l_l-2\sqrt{\mathcal{LC}}l_s-m_3\omega_1\sqrt{\mathcal{LC}}l_l-m_4\omega_1\sqrt{\mathcal{LC}}l_l\right)$$
$$+2\sqrt{\mathcal{LC}}l_s+m_3\sqrt{\mathcal{LC}}l_l+m_4\sqrt{\mathcal{LC}}l_l+m_4\frac{1}{{\omega_1}^2\sqrt{L_{p4}C_{p4}}} \tag{A.25}$$

Terms in (A.25) will cancel out, while the other sum up, obtaining the final expression for the determination of the lumped components needed to be inserted in the PBT LH-ATL unit cells for equalizing the phase characteristic at f_1:

$$\begin{aligned} 2\sqrt{\mathcal{LC}}l_s+n\sqrt{\mathcal{LC}}l_l &= -n\sqrt{\mathcal{LC}}l_l+m_4\frac{2}{{\omega_1}^2\sqrt{L_{p4}C_{p4}}} \\ \Longrightarrow \frac{m_4}{{\omega_1}^2\sqrt{L_{p4}C_{p4}}} &= \sqrt{\mathcal{LC}}l_s+n\sqrt{\mathcal{LC}}l_l \end{aligned} \tag{A.26}$$

Equation (A.26) shows that in this case the phase balancing term $\varphi_1^C(f_1)$ is only dependent on the switch and the number and length of transmission lines sections used in the fixed part of the two branches.

Bibliography

[1] M. Agiwal, A. Roy, and N. Saxena. «Next Generation 5G Wireless Networks: A Comprehensive Survey». In: *IEEE Communications Surveys Tutorials* 18.3 (2016), pp. 1617–1655. ISSN: 2373-745X. DOI: 10.1109/COMST.2016.2532458.

[2] Qorvo. *Wi-Fi Equipment Front-End Solutions*. 2019.

[3] Ovidiu Vermesan and Peter Friess. «Internet of Things: Converging Technologies for Smart Environments and Integrated Ecosystems». In: (2013).

[4] Marie Chan et al. «Smart wearable systems: Current status and future challenges». In: *Artificial Intelligence in Medicine* 56.3 (2012), pp. 137–156.

[5] Constantine A Balanis. *Antenna theory: analysis and design*. Wiley-Interscience, 2005.

[6] D. Wang and C. H. Chan. «Multiband Antenna for WiFi and WiGig Communications». In: *IEEE Antennas and Wireless Propagation Letters* 15 (2016), pp. 309–312.

[7] W. Lee et al. «Low-Profile Multiband Ferrite Antenna for Telematics Applications». In: *IEEE Transactions on Magnetics* 52.7 (July 2016), pp. 1–4.

[8] D. Guo et al. «A Multiband Dual-Polarized Omnidirectional Antenna for Indoor Wireless Communication Systems». In: *IEEE Antennas and Wireless Propagation Letters* 16 (2017), pp. 290–293. ISSN: 1548-5757. DOI: 10.1109/LAWP.2016.2573840.

[9] Y. F. Cao, S. W. Cheung, and T. I. Yuk. «A Multiband Slot Antenna for GPS/WiMAX/WLAN Systems». In: *IEEE Transactions on Antennas and Propagation* 63.3 (Mar. 2015), pp. 952–958. ISSN: 1558-2221. DOI: 10.1109/TAP.2015.2389219.

[10] A. Alexiou and M. Haardt. «Smart antenna technologies for future wireless systems: trends and challenges». In: *IEEE Communications Magazine* 42.9 (Sept. 2004), pp. 90–97. ISSN: 1558-1896. DOI: 10.1109/MCOM.2004.1336725.

[11] Y. Rahmat-Samii and A. C. Densmore. «Technology Trends and Challenges of Antennas for Satellite Communication Systems». In: *IEEE Transactions on Antennas and Propagation* 63.4 (Apr. 2015), pp. 1191–1204. ISSN: 1558-2221. DOI: 10.1109/TAP.2014.2366784.

[12] S. Borisov and A. Shishlov. «Antennas for Satcom-on-the-Move, Review». In: *2014 International Conference on Engineering and Telecommunication*. Nov. 2014, pp. 3–7. DOI: 10.1109/EnT.2014.12.

[13] J. T. Bernhard. *Reconfigurable Antennas*. 2007.

[14] D. Caratelli N. Haider and A. G. Yarovoy. «Recent Developments in Reconfigurable and Multiband Antenna Technology». In: *International Journal of Antennas and Propagation* Article ID 869170 (2013), pp. 1–14.

[15] J. Costantine et al. «Reconfigurable Antennas: Design and Applications». In: *Proceedings of the IEEE* 103.3 (Mar. 2015), pp. 424–437. ISSN: 1558-2256. DOI: 10.1109/JPROC.2015.2396000.

[16] C. G. Christodoulou et al. «Reconfigurable Antennas for Wireless and Space Applications». In: *Proceedings of the IEEE* 100.7 (July 2012), pp. 2250–2261. ISSN: 1558-2256.

[17] Y. J. Guo et al. «Advances in Reconfigurable Antenna Systems Facilitated by Innovative Technologies». In: *IEEE Access* 6 (2018), pp. 5780–5794. ISSN: 2169-3536. DOI: 10.1109/ACCESS.2017.2789199.

[18] S. Ciccia, G. Giordanengo, and G. Vecchi. «Energy Efficiency in IoT Networks: Integration of Reconfigurable Antennas in Ultra Low-Power Radio Platforms Based on System-on-Chip». In: *IEEE Internet of Things Journal* 6.4 (Aug. 2019), pp. 6800–6810. ISSN: 2372-2541. DOI: 10.1109/JIOT.2019.2911557.

[19] J. I. Cairó et al. «Reconfigurable System for Wireless Power Transfer (WPT) and Near Field Communications (NFC)». In: *IEEE Journal of Radio Frequency Identification* 1.4 (Dec. 2017), pp. 253–259. ISSN: 2469-729X. DOI: 10.1109/JRFID.2018.2801120.

[20] Y. Dong et al. «Dual-Band Reconfigurable Terahertz Patch Antenna With Graphene-Stack-Based Backing Cavity». In: *IEEE Antennas and Wireless Propagation Letters* 15 (2016), pp. 1541–1544. ISSN: 1548-5757. DOI: 10.1109/LAWP.2016.2533018.

[21] O. D. Gurbuz and G. M. Rebeiz. «A 1.6–2.3-GHz RF MEMS Reconfigurable Quadrature Coupler and Its Application to a 360° Reflective-Type Phase Shifter». In: *IEEE Transactions on Microwave Theory and Techniques* 63.2 (Feb. 2015), pp. 414–421. ISSN: 1557-9670. DOI: 10.1109/TMTT.2014.2379258.

[22] B. You et al. «A High-Selectivity Tunable Dual-Band Bandpass Filter Using Stub-Loaded Stepped-Impedance Resonators». In: *IEEE Microwave and Wireless Components Letters* 24.11 (Nov. 2014), pp. 736–738. ISSN: 1558-1764. DOI: 10.1109/LMWC.2014.2348322.

[23] Y. Cho and G. M. Rebeiz. «0.7–1.0-GHz Reconfigurable Bandpass-to-Bandstop Filter With Selectable 2- and 4-Pole Responses». In: *IEEE Transactions on Microwave Theory and Techniques* 62.11 (Nov. 2014), pp. 2626–2632. ISSN: 1557-9670. DOI: 10.1109/TMTT.2014.2359645.

[24] T. Lee, J. Laurin, and K. Wu. «Reconfigurable Filter for Bandpass-to-Absorptive Bandstop Responses». In: *IEEE Access* 8 (2020), pp. 6484–6495. ISSN: 2169-3536. DOI: 10.1109/ACCESS.2019.2963710.

[25] H. Jeong and S. Lim. «Broadband Frequency Reconfigurable Metamaterial Absorber using Switchable Ground Plane». In: *2018 IEEE International Symposium on Antennas and Propagation USNC/URSI National Radio Science Meeting*. July 2018, pp. 2325–2326. DOI: 10.1109/APUSNCURSINRSM.2018.8608635.

[26] F. N. Ayoub et al. «Frequency-tunable patch array using highly anisotropic liquid crystal». In: *2014 IEEE Antennas and Propagation Society International Symposium (APSURSI)*. July 2014, pp. 1664–1665. DOI: 10.1109/APS.2014.6905158.

[27] Jeremiah Turpin et al. «Reconfigurable and Tunable Metamaterials: A Review of the Theory and Applications». In: *International Journal of Antennas and Propagation* 2014 (May 2014), pp. 1–18. DOI: 10.1155/2014/429837.

[28] D. Rodrigo, L. Jofre, and B. A. Cetiner. «Circular Beam-Steering Reconfigurable Antenna With Liquid Metal Parasitics». In: *IEEE Transactions on Antennas and Propagation* 60.4 (Apr. 2012), pp. 1796–1802. ISSN: 1558-2221. DOI: 10.1109/TAP.2012.2186235.

[29] R. A. Liyakath, A. Takshi, and G. Mumcu. «Multilayer Stretchable Conductors on Polymer Substrates for Conformal and Reconfigurable Antennas». In: *IEEE Antennas and Wireless Propagation Letters* 12 (2013), pp. 603–606. ISSN: 1548-5757. DOI: 10.1109/LAWP.2013.2260123.

[30] A. Mehdipour et al. «Mechanically reconfigurable antennas using an anisotropic carbon-fibre composite ground». In: *IET Microwaves, Antennas Propagation* 7.13 (Oct. 2013), pp. 1055–1063. ISSN: 1751-8733. DOI: 10.1049/iet-map.2013.0115.

[31] J. Costantine et al. «Reconfigurable antenna system with a movable ground plane for cognitive radio». In: *IET Microwaves, Antennas Propagation* 8.11 (Aug. 2014), pp. 858–863. ISSN: 1751-8733. DOI: 10.1049/iet-map.2013.0605.

[32] J. T. Bernhard, E. Kiely, and G. Washington. «A smart mechanically actuated two-layer electromagnetically coupled microstrip antenna with variable frequency, bandwidth, and antenna gain». In: *IEEE Transactions on Antennas and Propagation* 49.4 (Apr. 2001), pp. 597–601. ISSN: 1558-2221. DOI: 10.1109/8.923320.

[33] S. J. Mazlouman et al. «Pattern reconfigurable square ring patch antenna actuated by hemispherical dielectric elastomer». In: *Electronics Letters* 47.3 (Feb. 2011), pp. 164–165. ISSN: 0013-5194. DOI: 10.1049/el.2010.3585.

[34] A. Jouade et al. «Mechanically Pattern-Reconfigurable Bended Horn Antenna for High-Power Applications». In: *IEEE Antennas and Wireless Propagation Letters* 16 (2017), pp. 457–460. ISSN: 1548-5757. DOI: 10.1109/LAWP.2016.2583203.

[35] A. Dey and G. Mumcu. «Microfluidically controlled metalized plate based frequency reconfigurable monopole for high power RF applications». In: *2015 IEEE International Symposium on Antennas and Propagation USNC/URSI National Radio Science Meeting*. July 2015, pp. 2299–2300. DOI: 10.1109/APS.2015.7305538.

[36] K. Daheshpour et al. «Pattern reconfigurable antenna based on moving V-shaped parasitic elements actuated by dielectric elastomer». In: *Electronics Letters* 46.13 (June 2010), pp. 886–888. ISSN: 0013-5194. DOI: 10.1049/el.2010.0862.

[37] Y. Tawk et al. «Implementation of a Cognitive Radio Front-End Using Rotatable Controlled Reconfigurable Antennas». In: *IEEE Transactions on Antennas and Propagation* 59.5 (May 2011), pp. 1773–1778. ISSN: 1558-2221. DOI: 10.1109/TAP.2011.2122239.

[38] G. Ruvio, M. J. Ammann, and Z. N. Chen. «Wideband Reconfigurable Rolled Planar Monopole Antenna». In: *IEEE Transactions on Antennas and Propagation* 55.6 (June 2007), pp. 1760–1767. ISSN: 1558-2221. DOI: 10.1109/TAP.2007.898575.

[39] J. -. Langer et al. «Micromachined reconfigurable out-of-plane microstrip patch antenna using plastic deformation magnetic actuation». In: *IEEE Microwave and Wireless Components Letters* 13.3 (Mar. 2003), pp. 120–122. ISSN: 1558-1764. DOI: 10.1109/LMWC.2003.810123.

[40] J. M. Zendejas et al. «Magnetic MEMS reconfigurable frequency-selective surfaces». In: *Journal of Microelectromechanical Systems* 15.3 (June 2006), pp. 613–623. ISSN: 1941-0158. DOI: 10.1109/JMEMS.2005.863704.

[41] Y. Kim et al. «60-GHz Full MEMS Antenna Platform Mechanically Driven by Magnetic Actuator». In: *IEEE Transactions on Industrial Electronics* 58.10 (Oct. 2011), pp. 4830–4836. ISSN: 1557-9948. DOI: 10.1109/TIE.2011.2114317.

[42] J. Gibson and S. V. Georgakopoulos. «Reconfigurable antenna using shape memory polymers». In: *2016 IEEE International Symposium on Antennas and Propagation (APSURSI)*. June 2016, pp. 1673–1674. DOI: 10.1109/APS.2016.7696543.

[43] S. V. Georgakopoulos. «Reconfigurable Origami Antennas». In: *2019 International Applied Computational Electromagnetics Society Symposium (ACES)*. Apr. 2019, pp. 1–2.

[44] Y. Tawk, J. Costantine, and C. G. Christodoulou. «A Varactor-Based Reconfigurable Filtenna». In: *IEEE Antennas and Wireless Propagation Letters* 11 (2012), pp. 716–719. ISSN: 1548-5757. DOI: 10.1109/LAWP.2012.2204850.

[45] B. A. Cetiner et al. «RF MEMS Integrated Frequency Reconfigurable Annular Slot Antenna». In: *IEEE Transactions on Antennas and Propagation* 58.3 (Mar. 2010), pp. 626–632. ISSN: 1558-2221. DOI: 10.1109/TAP.2009.2039300.

[46] E. Erdil et al. «Frequency Tunable Microstrip Patch Antenna Using RF MEMS Technology». In: *IEEE Transactions on Antennas and Propagation* 55.4 (Apr. 2007), pp. 1193–1196. ISSN: 1558-2221. DOI: 10.1109/TAP.2007.893426.

[47] G. H. Huff and J. T. Bernhard. «Integration of packaged RF MEMS switches with radiation pattern reconfigurable square spiral microstrip antennas». In: *IEEE Transactions on Antennas and Propagation* 54.2 (Feb. 2006), pp. 464–469. ISSN: 1558-2221. DOI: 10.1109/TAP.2005.863409.

[48] S. Nikolaou et al. «UWB Elliptical Monopoles With a Reconfigurable Band Notch Using MEMS Switches Actuated Without Bias Lines». In: *IEEE Transactions on Antennas and Propagation* 57.8 (Aug. 2009), pp. 2242–2251. ISSN: 1558-2221. DOI: 10.1109/TAP.2009.2024450.

[49] O. D. Gurbuz and G. M. Rebeiz. «A 1.6–2.3-GHz RF MEMS Reconfigurable Quadrature Coupler and Its Application to a 360° Reflective-Type Phase Shifter». In: *IEEE Transactions on Microwave Theory and Techniques* 63.2 (Feb. 2015), pp. 414–421. ISSN: 1557-9670. DOI: 10.1109/TMTT.2014.2379258.

[50] Y. Shim et al. «An integrated RF MEMS tunable filter». In: *2012 IEEE 25th International Conference on Micro Electro Mechanical Systems (MEMS)*. Jan. 2012, pp. 15–18. DOI: 10.1109/MEMSYS.2012.6170082.

[51] A. K. Horestani et al. «Reconfigurable and Tunable S-Shaped Split-Ring Resonators and Application in Band-Notched UWB Antennas». In: *IEEE Transactions on Antennas and Propagation* 64.9 (Sept. 2016), pp. 3766–3776. ISSN: 1558-2221. DOI: 10.1109/TAP.2016.2585183.

[52] M. Tang et al. «Compact, Frequency-Reconfigurable Filtenna With Sharply Defined Wideband and Continuously Tunable Narrowband States». In: *IEEE Transactions on Antennas and Propagation* 65.10 (Oct. 2017), pp. 5026–5034. ISSN: 1558-2221. DOI: 10.1109/TAP.2017.2736535.

[53] L. Hinsz and B. D. Braaten. «A Frequency Reconfigurable Transmitter Antenna With Autonomous Switching Capabilities». In: *IEEE Transactions on Antennas and Propagation* 62.7 (July 2014), pp. 3809–3813. ISSN: 1558-2221. DOI: 10.1109/TAP.2014.2316298.

[54] S. Zhang et al. «A pattern reconfigurable microstrip parasitic array». In: *IEEE Transactions on Antennas and Propagation* 52.10 (Oct. 2004), pp. 2773–2776. ISSN: 1558-2221. DOI: 10.1109/TAP.2004.834372.

[55] J. Row and C. Tsai. «Pattern Reconfigurable Antenna Array With Circular Polarization». In: *IEEE Transactions on Antennas and Propagation* 64.4 (Apr. 2016), pp. 1525–1530. ISSN: 1558-2221. DOI: 10.1109/TAP.2016.2522467.

[56] L. Ji et al. «A Reconfigurable Partially Reflective Surface (PRS) Antenna for Beam Steering». In: *IEEE Transactions on Antennas and Propagation* 63.6 (June 2015), pp. 2387–2395. ISSN: 1558-2221. DOI: 10.1109/TAP.2015.2412143.

[57] W. Lin, H. Wong, and R. W. Ziolkowski. «Circularly Polarized Antenna With Reconfigurable Broadside and Conical Beams Facilitated by a Mode Switchable Feed Network». In: *IEEE Transactions on Antennas and Propagation* 66.2 (Feb. 2018), pp. 996–1001. ISSN: 1558-2221. DOI: 10.1109/TAP.2017.2784452.

[58] D. Rodrigo et al. «Pixel reconfigurable antennas: Towards low-complexity full reconfiguration». In: *2016 10th European Conference on Antennas and Propagation (EuCAP)*. Apr. 2016, pp. 1–5. DOI: 10.1109/EuCAP.2016.7481208.

[59] C. Gu et al. «Frequency-reconfigurable pattern-steerable antenna using active frequency selective surface». In: *12th European Conference on Antennas and Propagation (EuCAP 2018)*. Apr. 2018, pp. 1–5. DOI: 10.1049/cp.2018.0881.

[60] W. Jeong et al. «Tunable Band-notched Ultra Wideband (UWB) Planar Monopole Antennas Using Varactor». In: *2008 38th European Microwave Conference*. Oct. 2008, pp. 266–268. DOI: 10.1109/EUMC.2008.4751439.

[61] M. Tang et al. «Compact, Frequency-Reconfigurable Filtenna With Sharply Defined Wideband and Continuously Tunable Narrowband States». In: *IEEE Transactions on Antennas and Propagation* 65.10 (Oct. 2017), pp. 5026–5034. ISSN: 1558-2221. DOI: 10.1109/TAP.2017.2736535.

[62] F. Costa et al. «An active AMC ground plane for tunable low-profile antennas». In: *2008 IEEE Antennas and Propagation Society International Symposium*. July 2008, pp. 1–4. DOI: 10.1109/APS.2008.4619192.

[63] P. Qin et al. «A Reconfigurable Antenna With Frequency and Polarization Agility». In: *IEEE Antennas and Wireless Propagation Letters* 10 (2011), pp. 1373–1376. ISSN: 1548-5757. DOI: 10.1109/LAWP.2011.2178226.

[64] Z. Wen, M. Tang, and R. W. Ziolkowski. «Band- and frequency-reconfigurable circularly polarised filtenna for cognitive radio applications». In: *IET Microwaves, Antennas Propagation* 13.7 (2019), pp. 1003–1008. ISSN: 1751-8733. DOI: 10.1049/iet-map.2018.5963.

[65] W. Hu et al. «Design and Measurement of Reconfigurable Millimeter Wave Reflectarray Cells With Nematic Liquid Crystal». In: *IEEE Transactions on Antennas and Propagation* 56.10 (Oct. 2008), pp. 3112–3117. ISSN: 1558-2221. DOI: 10.1109/TAP.2008.929460.

[66] A. Tamayo-Domínguez, J. Fernández-González, and M. Sierra-Castañer. «Additive Manufacturing and Liquid Crystals for New Millimeter-Wave Devices». In: *2018 IEEE MTT-S Latin America Microwave Conference (LAMC 2018)*. Dec. 2018, pp. 1–3. DOI: 10.1109/LAMC.2018.8699025.

[67] S. Foo. «Liquid-crystal-tunable metasurface antennas». In: *2017 11th European Conference on Antennas and Propagation (EUCAP)*. Mar. 2017, pp. 3026–3030. DOI: 10.23919/EuCAP.2017.7928122.

[68] R. Reese et al. «A Millimeter-Wave Beam-Steering Lens Antenna With Reconfigurable Aperture Using Liquid Crystal». In: *IEEE Transactions on Antennas and Propagation* 67.8 (Aug. 2019), pp. 5313–5324. ISSN: 1558-2221. DOI: 10.1109/TAP.2019.2918474.

[69] M. A. Christou, N. C. Papanicolaou, and A. C. Polycarpou. «A nematic liquid crystal tunable patch antenna». In: *The 8th European Conference on Antennas and Propagation (EuCAP 2014)*. Apr. 2014, pp. 1875–1878. DOI: 10.1109/EuCAP.2014.6902162.

[70] Z. Chen et al. «UHF tunable compact antennas on Co2Z hexaferrite substrate with 2.5/1 tunable frequency range». In: *2015 IEEE International Symposium on Antennas and Propagation USNC/URSI National Radio Science Meeting*. July 2015, pp. 2287–2288. DOI: 10.1109/APS.2015.7305532.

[71] M. F. Iskander et al. «Design of a low-cost 2-D beam-steering antenna using ferroelectric material and CTS technology». In: *IEEE Transactions on Microwave Theory and Techniques* 49.5 (May 2001), pp. 1000–1003. ISSN: 1557-9670. DOI: 10.1109/22.920163.

[72] H. Mosallaei and K. Sarabandi. «Magneto-dielectrics in electromagnetics: concept and applications». In: *IEEE Transactions on Antennas and Propagation* 52.6 (June 2004), pp. 1558–1567. ISSN: 1558-2221. DOI: 10.1109/TAP.2004.829413.

[73] L. Tan et al. «Magnetically Tunable Ferrite Loaded SIW Antenna». In: *IEEE Antennas and Wireless Propagation Letters* 12 (2013), pp. 273–275. ISSN: 1548-5757. DOI: 10.1109/LAWP.2013.2248113.

[74] W. Hu et al. «Liquid-crystal-based reflectarray antenna with electronically switchable monopulse patterns». In: *Electronics Letters* 43.14 (July 2007). ISSN: 0013-5194. DOI: 10.1049/el:20071098.

[75] T. Zervos et al. «Patch antenna with polarization agility using ferrimagnetic materials». In: *2009 Loughborough Antennas Propagation Conference*. Nov. 2009, pp. 541–544. DOI: 10.1109/LAPC.2009.5352431.

[76] M. Durán-Sindreu et al. «Electrically tunable composite right/left handed transmission-line based on open resonators and Barium-Stronium-Titanate thick films». In: *2011 IEEE MTT-S International Microwave Symposium*. June 2011, pp. 1–4. DOI: 10.1109/MWSYM.2011.5972754.

[77] M. Al Ahmad et al. «Investigations of Indium Tin Oxide—Barium Strontium Titanate–Indium Tin Oxide Heterostructure for Tunability». In: *IEEE Microwave and Wireless Components Letters* 18.6 (June 2008), pp. 398–400. ISSN: 1558-1764. DOI: 10.1109/LMWC.2008.922631.

[78] Z. Su et al. «Additively Manufactured Frequency/Radiation Pattern Reconfigurable Antenna Based on Monolithically Printed VO2 Switch». In: *2019 13th European Conference on Antennas and Propagation (EuCAP)*. Mar. 2019, pp. 1–4.

[79] Z. Su et al. «Fully Printed VO2 Switch Based Reconfigurable PIFA / T-shaped Monopole Antenna». In: *2018 18th International Symposium on Antenna Technology and Applied Electromagnetics (ANTEM)*. Aug. 2018, pp. 1–2. DOI: 10.1109/ANTEM.2018.8572855.

[80] V. Sanphuang et al. «Bandwidth reconfigurable THz filter employing phase-change material». In: *2015 IEEE International Symposium on Antennas and Propagation USNC/URSI National Radio Science Meeting*. July 2015, pp. 2289–2290. DOI: 10.1109/APS.2015.7305533.

[81] Y. Dong et al. «Dual-Band Reconfigurable Terahertz Patch Antenna With Graphene-Stack-Based Backing Cavity». In: *IEEE Antennas and Wireless Propagation Letters* 15 (2016), pp. 1541–1544. ISSN: 1548-5757. DOI: 10.1109/LAWP.2016.2533018.

[82] X. Zhang et al. «Graphene reconfigurable coplanar waveguide (CPW)-fed circular slot antenna». In: *2015 IEEE International Symposium on Antennas and Propagation USNC/URSI National Radio Science Meeting*. July 2015, pp. 2293–2294.

[83] D. N. Elsheakh. «Frequency Reconfigurable and Radiation Pattern Steering of Monopole Antenna Based on Graphene Pads». In: *2019 IEEE-APS Topical Conference on Antennas and Propagation in Wireless Communications (APWC)*. Sept. 2019, pp. 436–440. DOI: 10.1109/APWC.2019.8870446.

[84] A. Bhadauria and S. Sharma. «Optically controlled reflection type RF phase shifter using rat-race coupler on silicon substrate». In: *2016 3rd International Conference on Devices, Circuits and Systems (ICDCS)*. Mar. 2016, pp. 319–321. DOI: 10.1109/ICDCSyst.2016.7570610.

[85] D. Patron, A. S. Daryoush, and K. R. Dandekar. «Optical Control of Reconfigurable Antennas and Application to a Novel Pattern-Reconfigurable Planar Design». In: *Journal of Lightwave Technology* 32.20 (Oct. 2014), pp. 3394–3402. ISSN: 1558-2213. DOI: 10.1109/JLT.2014.2321406.

[86] C. J. Panagamuwa, A. Chauraya, and J. C. Vardaxoglou. «Frequency and beam reconfigurable antenna using photoconducting switches». In: *IEEE Transactions on Antennas and Propagation* 54.2 (Feb. 2006), pp. 449–454. ISSN: 1558-2221. DOI: 10.1109/TAP.2005.863393.

[87] S. H. Zheng, X. Liu, and M. M. Tentzeris. «Optically controlled reconfigurable band-notched UWB antenna for cognitive radio systems». In: *Electronics Letters* 50.21 (Oct. 2014), pp. 1502–1504. ISSN: 0013-5194. DOI: 10.1049/el.2014.2226.

[88] I. F. da Costa et al. «Optically Controlled Reconfigurable Antenna Array for mm-Wave Applications». In: *IEEE Antennas and Wireless Propagation Letters* 16 (2017), pp. 2142–2145. ISSN: 1548-5757. DOI: 10.1109/LAWP.2017.2700284.

[89] N. El-Hinnawy et al. «12.5 THz Fco GeTe Inline Phase-Change Switch Technology for Reconfigurable RF and Switching Applications». In: *2014 IEEE Compound Semiconductor Integrated Circuit Symposium (CSICS)*. Oct. 2014, pp. 1–3. DOI: 10.1109/CSICS.2014.6978522.

[90] A. Crunteanu et al. «Optical switching of GeTe phase change materials for high-frequency applications». In: *2017 IEEE MTT-S International Microwave Workshop Series on Advanced Materials and Processes for RF and THz Applications (IMWS-AMP)*. Sept. 2017, pp. 1–3. DOI: 10.1109/IMWS-AMP.2017.8247379.

[91] L. Huitema et al. «Optical switching of GeTe phase change material: Application to a frequency agile millimeter-waves patch antenna». In: *12th European Conference on Antennas and Propagation (EuCAP 2018)*. Apr. 2018, pp. 1–5. DOI: 10.1049/cp.2018.0888.

[92] J. Costantine et al. «Reducing Redundancies in Reconfigurable Antenna Structures Using Graph Models». In: *IEEE Transactions on Antennas and Propagation* 59.3 (Mar. 2011), pp. 793–801. ISSN: 1558-2221. DOI: 10.1109/TAP.2010.2103005.

[93] J. Costantine et al. «Analyzing the Complexity and Reliability of Switch-Frequency-Reconfigurable Antennas Using Graph Models». In: *IEEE Transactions on Antennas and Propagation* 60.2 (Feb. 2012), pp. 811–820. ISSN: 1558-2221. DOI: 10.1109/TAP.2011.2173104.

[94] J. Costantine et al. «Applying graph models and Neural Networks on reconfigurable antennas for cognitive radio applications». In: *2011 IEEE-APS Topical Conference on Antennas and Propagation in Wireless Communications*. Sept. 2011, pp. 909–912. DOI: 10.1109/APWC.2011.6046815.

[95] J. Kovitz and Y. Rahmat-Samii. «Micro-actuated pixel patch antenna design using particle swarm optimization». In: *2011 IEEE International Symposium on Antennas and Propagation (APSURSI)*. July 2011, pp. 2415–2418. DOI: 10.1109/APS.2011.5997009.

[96] S. Arianos et al. «Automated Design and Experimental Validation of a Reconfigurable, Board-Mounted Compact Antenna». In: *IEEE Antennas and Wireless Propagation Letters* 16 (2017), pp. 589–592. ISSN: 1548-5757. DOI: 10.1109/LAWP.2016.2591326.

[97] S. Somarith, K. Hyunseong, and L. Sungjoon. «Frequency Reconfigurable and Miniaturized Substrate Integrated Waveguide Interdigital Capacitor (SIW-IDC) Antenna». In: *IEEE Transactions on Antennas and Propagation* 62.3 (Mar. 2014), pp. 1039–1045. ISSN: 1558-2221. DOI: 10.1109/TAP.2013.2281662.

[98] L. Hinsz and B. D. Braaten. «A Frequency Reconfigurable Transmitter Antenna With Autonomous Switching Capabilities». In: *IEEE Transactions on Antennas and Propagation* 62.7 (July 2014), pp. 3809–3813. ISSN: 1558-2221. DOI: 10.1109/TAP.2014.2316298.

[99] Songnan Yang et al. «Frequency-Reconfigurable Antennas for Multiradio Wireless Platforms». In: *IEEE Microwave Magazine* 10.1 (Feb. 2009), pp. 66–83. ISSN: 1557-9581. DOI: 10.1109/MMM.2008.930677.

[100] J. Cho, C. W. Jung, and K. Kim. «Frequency-reconfigurable two-port antenna for mobile phone operating over multiple service bands». In: *Electronics Letters* 45.20 (Sept. 2009), pp. 1009–1011. ISSN: 0013-5194. DOI: 10.1049/el.2009.1378.

[101] Y. Cai, Y. J. Guo, and T. S. Bird. «A Frequency Reconfigurable Printed Yagi-Uda Dipole Antenna for Cognitive Radio Applications». In: *IEEE Transactions on Antennas and Propagation* 60.6 (June 2012), pp. 2905–2912. ISSN: 1558-2221. DOI: 10.1109/TAP.2012.2194654.

[102] S. Chen, Q. Chu, and N. Shinohara. «A bandwidth reconfigurable planar antenna for WLAN/WiMAX applications». In: *2016 Asia-Pacific Microwave Conference (APMC)*. Dec. 2016, pp. 1–3. DOI: 10.1109/APMC.2016.7931467.

[103] S. Chen, Q. Chu, and N. Shinohara. «A bandwidth reconfigurable planar antenna for WLAN/WiMAX applications». In: *2016 Asia-Pacific Microwave Conference (APMC)*. Dec. 2016, pp. 1–3. DOI: 10.1109/APMC.2016.7931467.

[104] Y. Tawk, J. Costantine, and C. G. Christodoulou. «Cognitive-radio and antenna functionalities: A tutorial [Wireless Corner]». In: *IEEE Antennas and Propagation Magazine* 56.1 (Feb. 2014), pp. 231–243. ISSN: 1558-4143. DOI: 10.1109/MAP.2014.6821791.

[105] A. K. Horestani et al. «Reconfigurable and Tunable S-Shaped Split-Ring Resonators and Application in Band-Notched UWB Antennas». In: *IEEE Transactions on Antennas and Propagation* 64.9 (Sept. 2016), pp. 3766–3776. ISSN: 1558-2221. DOI: 10.1109/TAP.2016.2585183.

[106] R. J. Langley, H. Lee, and K. L. Ford. «Independent multiband tuning using an active AMC». In: *2011 IEEE-APS Topical Conference on Antennas and Propagation in Wireless Communications*. Sept. 2011, pp. 576–579. DOI: 10.1109/APWC.2011.6046784.

[107] R. Hussain and M. S. Sharawi. «A Cognitive Radio Reconfigurable MIMO and Sensing Antenna System». In: *IEEE Antennas and Wireless Propagation Letters* 14 (2015), pp. 257–260. ISSN: 1548-5757. DOI: 10.1109/LAWP.2014.2361450.

[108] P. Qin, F. Wei, and Y. J. Guo. «A Wideband-to-Narrowband Tunable Antenna Using A Reconfigurable Filter». In: *IEEE Transactions on Antennas and Propagation* 63.5 (May 2015), pp. 2282–2285. ISSN: 1558-2221. DOI: 10.1109/TAP.2015.2402295.

[109] S. Kingsly et al. «Multiband Reconfigurable Filtering Monopole Antenna for Cognitive Radio Applications». In: *IEEE Antennas and Wireless Propagation Letters* 17.8 (Aug. 2018), pp. 1416–1420. ISSN: 1548-5757. DOI: 10.1109/LAWP.2018.2848702.

[110] M. Tang et al. «Compact, Frequency-Reconfigurable Filtenna With Sharply Defined Wideband and Continuously Tunable Narrowband States». In: *IEEE Transactions on Antennas and Propagation* 65.10 (Oct. 2017), pp. 5026–5034. ISSN: 1558-2221. DOI: 10.1109/TAP.2017.2736535.

[111] W. Tu. «Switchable Microstrip Bandpass Filters With Reconfigurable On-State Frequency Responses». In: *IEEE Microwave and Wireless Components Letters* 20.5 (May 2010), pp. 259–261. ISSN: 1558-1764. DOI: 10.1109/LMWC.2010.2045581.

[112] J. Lee, E. J. Naglich, and W. J. Chappell. «Frequency Response Control in Frequency-Tunable Bandstop Filters». In: *IEEE Microwave and Wireless Components Letters* 20.12 (Dec. 2010), pp. 669–671. ISSN: 1558-1764. DOI: 10.1109/LMWC.2010.2080669.

[113] S. Arain et al. «Reconfigurable Bandwidth Bandpass Filter With Enhanced Out-of-Band Rejection Using π -Section-Loaded Ring Resonator». In: *IEEE Microwave and Wireless Components Letters* 28.1 (Jan. 2018), pp. 28–30. ISSN: 1558-1764. DOI: 10.1109/LMWC.2017.2776212.

[114] C. Arnold, J. Parlebas, and T. Zwick. «Reconfigurable Waveguide Filter with Variable Bandwidth and Center Frequency». In: *IEEE Transactions on Microwave Theory and Techniques* 62.8 (Aug. 2014), pp. 1663–1670. ISSN: 1557-9670. DOI: 10.1109/TMTT.2014.2332298.

[115] X. Bi et al. «Design of Notched-Wideband Bandpass Filters With Reconfigurable Bandwidth Based on Terminated Cross-Shaped Resonators». In: *IEEE Access* 8 (2020), pp. 37416–37427. ISSN: 2169-3536. DOI: 10.1109/ACCESS.2020.2975379.

[116] G. Chaudhary, Y. Jeong, and J. Lim. «Harmonic Suppressed Dual-Band Bandpass Filters With Tunable Passbands». In: *IEEE Transactions on Microwave Theory and Techniques* 60.7 (July 2012), pp. 2115–2123. ISSN: 1557-9670. DOI: 10.1109/TMTT.2012.2197020.

[117] B. You et al. «A High-Selectivity Tunable Dual-Band Bandpass Filter Using Stub-Loaded Stepped-Impedance Resonators». In: *IEEE Microwave and Wireless Components Letters* 24.11 (Nov. 2014), pp. 736–738. ISSN: 1558-1764. DOI: 10.1109/LMWC.2014.2348322.

[118] S. Genovesi, A. D. Candia, and A. Monorchio. «Compact and Low Profile Frequency Agile Antenna for Multistandard Wireless Communication Systems». In: *IEEE Transactions on Antennas and Propagation* 62.3 (Mar. 2014), pp. 1019–1026. ISSN: 1558-2221. DOI: 10.1109/TAP.2013.2272731.

[119] C. Sun et al. «A Compact Frequency-Reconfigurable Patch Antenna for Beidou (COMPASS) Navigation System». In: *IEEE Antennas and Wireless Propagation Letters* 13 (2014), pp. 967–970. ISSN: 1548-5757. DOI: 10.1109/LAWP.2014.2322754.

[120] L. Ge and K. Luk. «Frequency-Reconfigurable Low-Profile Circular Monopolar Patch Antenna». In: *IEEE Transactions on Antennas and Propagation* 62.7 (July 2014), pp. 3443–3449. ISSN: 1558-2221. DOI: 10.1109/TAP.2014.2318077.

[121] N. Nguyen-Trong, A. Piotrowski, and C. Fumeaux. «A Frequency-Reconfigurable Dual-Band Low-Profile Monopolar Antenna». In: *IEEE Transactions on Antennas and Propagation* 65.7 (July 2017), pp. 3336–3343. ISSN: 1558-2221. DOI: 10.1109/TAP.2017.2702664.

[122] P. Qin et al. «Frequency Reconfigurable Quasi-Yagi Folded Dipole Antenna». In: *IEEE Transactions on Antennas and Propagation* 58.8 (Aug. 2010), pp. 2742–2747. ISSN: 1558-2221. DOI: 10.1109/TAP.2010.2050455.

[123] C. Chiu et al. «Frequency-Reconfigurable Pixel Slot Antenna». In: *IEEE Transactions on Antennas and Propagation* 60.10 (Oct. 2012), pp. 4921–4924. ISSN: 1558-2221. DOI: 10.1109/TAP.2012.2207334.

[124] E. Erdil et al. «Frequency Tunable Microstrip Patch Antenna Using RF MEMS Technology». In: *IEEE Transactions on Antennas and Propagation* 55.4 (Apr. 2007), pp. 1193–1196. ISSN: 1558-2221. DOI: 10.1109/TAP.2007.893426.

[125] M. U. Memon and S. Lim. «Frequency-Tunable Compact Antenna Using Quarter-Mode Substrate Integrated Waveguide». In: *IEEE Antennas and Wireless Propagation Letters* 14 (2015), pp. 1606–1609. ISSN: 1548-5757. DOI: 10.1109/LAWP.2015.2413945.

[126] S. Missaoui, S. Missaoui, and M. Kaddour. «Tunable microstrip patch antenna based on liquid crystals». In: *2016 XXIst International Seminar/-Workshop on Direct and Inverse Problems of Electromagnetic and Acoustic Wave Theory (DIPED)*. Sept. 2016, pp. 88–91. DOI: 10.1109/DIPED.2016.7772222.

[127] G. Xu et al. «Differential Probe Fed Liquid Crystal-Based Frequency Tunable Circular Ring Patch Antenna». In: *IEEE Access* 6 (2018), pp. 3051–3058. ISSN: 2169-3536.

[128] H. Wong et al. «Multi-Polarization Reconfigurable Antenna for Wireless Biomedical System». In: *IEEE Transactions on Biomedical Circuits and Systems* 11.3 (June 2017), pp. 652–660. ISSN: 1940-9990. DOI: 10.1109/TBCAS.2016.2636872.

[129] W. Lin and H. Wong. «Multipolarization-Reconfigurable Circular Patch Antenna With L-Shaped Probes». In: *IEEE Antennas and Wireless Propagation Letters* 16 (2017), pp. 1549–1552. ISSN: 1548-5757. DOI: 10.1109/LAWP.2017.2648862.

[130] T. J. Jung et al. «Circular/Linear Polarization Reconfigurable Antenna on Simplified RF-MEMS Packaging Platform in K-Band». In: *IEEE Transactions on Antennas and Propagation* 60.11 (Nov. 2012), pp. 5039–5045. ISSN: 1558-2221. DOI: 10.1109/TAP.2012.2207662.

[131] C. T. Rodenbeck, Ming-Yi Li, and Kai Chang. «Circular-polarized reconfigurable grating antenna for low-cost Millimeter-wave beam-steering». In: *IEEE Transactions on Antennas and Propagation* 52.10 (Oct. 2004), pp. 2759–2764. ISSN: 1558-2221. DOI: 10.1109/TAP.2004.834367.

[132] B. A. Cetiner et al. «A MIMO System With Multifunctional Reconfigurable Antennas». In: *IEEE Antennas and Wireless Propagation Letters* 5 (2006), pp. 463–466. ISSN: 1548-5757. DOI: 10.1109/LAWP.2006.885171.

[133] F. Wu and K. M. Luk. «Wideband Tri-Polarization Reconfigurable Magneto-Electric Dipole Antenna». In: *IEEE Transactions on Antennas and Propagation* 65.4 (Apr. 2017), pp. 1633–1641. ISSN: 1558-2221. DOI: 10.1109/TAP.2017.2670521.

[134] W. Lin et al. «Reconfigurable, Wideband, Low-Profile, Circularly Polarized Antenna and Array Enabled by an Artificial Magnetic Conductor Ground». In: *IEEE Transactions on Antennas and Propagation* 66.3 (Mar. 2018), pp. 1564–1569. ISSN: 1558-2221. DOI: 10.1109/TAP.2018.2790437.

[135] K. Tong and J. Huang. «New Proximity Coupled Feeding Method for Reconfigurable Circularly Polarized Microstrip Ring Antennas». In: *IEEE Transactions on Antennas and Propagation* 56.7 (July 2008), pp. 1860–1866. ISSN: 1558-2221. DOI: 10.1109/TAP.2008.924736.

[136] K. X. Wang and H. Wong. «A Reconfigurable CP/LP Antenna With Cross-Probe Feed». In: *IEEE Antennas and Wireless Propagation Letters* 16 (2017), pp. 669–672. ISSN: 1548-5757. DOI: 10.1109/LAWP.2016.2598248.

[137] K. M. Mak et al. «Polarization Reconfigurable Circular Patch Antenna With a C-Shaped». In: *IEEE Transactions on Antennas and Propagation* 65.3 (Mar. 2017), pp. 1388–1392. ISSN: 1558-2221. DOI: 10.1109/TAP.2016.2640141.

[138] S. Chen et al. «A Multi-linear Polarization Reconfigurable Unidirectional Patch Antenna». In: *IEEE Transactions on Antennas and Propagation* 65.8 (Aug. 2017), pp. 4299–4304. ISSN: 1558-2221. DOI: 10.1109/TAP.2017.2712185.

[139] H. H. Tran et al. «Wideband and Multipolarization Reconfigurable Crossed Bowtie Dipole Antenna». In: *IEEE Transactions on Antennas and Propagation* 65.12 (Dec. 2017), pp. 6968–6975. ISSN: 1558-2221. DOI: 10.1109/TAP.2017.2766439.

[140] M. N. Osman et al. «Polarization reconfigurable patch antenna through modification of feeding network». In: *2014 International Symposium on Antennas and Propagation Conference Proceedings*. Dec. 2014, pp. 323–324.

[141] W. Lin and H. Wong. «Wideband Circular-Polarization Reconfigurable Antenna With L-Shaped Feeding Probes». In: *IEEE Antennas and Wireless Propagation Letters* 16 (2017), pp. 2114–2117. ISSN: 1548-5757.

[142] D. Seo et al. «A Quadruple-Polarization Reconfigurable Feeding Network for UAV RF Sensing Antenna». In: *IEEE Microwave and Wireless Components Letters* 29.3 (Mar. 2019), pp. 183–185. ISSN: 1558-1764. DOI: 10.1109/LMWC.2019.2897479.

[143] C. Gu et al. «Compact Smart Antenna With Electronic Beam-Switching and Reconfigurable Polarizations». In: *IEEE Transactions on Antennas and Propagation* 63.12 (Dec. 2015), pp. 5325–5333. ISSN: 1558-2221. DOI: 10.1109/TAP.2015.2490239.

[144] W. Yang et al. «A Polarization-Reconfigurable Dipole Antenna Using Polarization Rotation AMC Structure». In: *IEEE Transactions on Antennas and Propagation* 63.12 (Dec. 2015), pp. 5305–5315. ISSN: 1558-2221. DOI: 10.1109/TAP.2015.2490250.

[145] H. L. Zhu et al. «Design of Polarization Reconfigurable Antenna Using Metasurface». In: *IEEE Transactions on Antennas and Propagation* 62.6 (June 2014), pp. 2891–2898. ISSN: 1558-2221. DOI: 10.1109/TAP.2014.2310209.

[146] L. Ji et al. «A Wideband Polarization Reconfigurable Antenna With Partially Reflective Surface». In: *IEEE Transactions on Antennas and Propagation* 64.10 (Oct. 2016), pp. 4534–4538. ISSN: 1558-2221. DOI: 10.1109/TAP.2016.2593716.

[147] W. Lin and H. Wong. «Polarization Reconfigurable Wheel-Shaped Antenna With Conical-Beam Radiation Pattern». In: *IEEE Transactions on Antennas and Propagation* 63.2 (Feb. 2015), pp. 491–499. ISSN: 1558-2221. DOI: 10.1109/TAP.2014.2381263.

[148] P. Qin, Y. J. Guo, and C. Ding. «A Dual-Band Polarization Reconfigurable Antenna for WLAN Systems». In: *IEEE Transactions on Antennas and Propagation* 61.11 (Nov. 2013), pp. 5706–5713. ISSN: 1558-2221. DOI: 10.1109/TAP.2013.2279219.

[149] P. Qin et al. «A Reconfigurable Antenna With Frequency and Polarization Agility». In: *IEEE Antennas and Wireless Propagation Letters* 10 (2011), pp. 1373–1376. ISSN: 1548-5757. DOI: 10.1109/LAWP.2011.2178226.

[150] S. V. S. Nair and M. J. Ammann. «Reconfigurable Antenna With Elevation and Azimuth Beam Switching». In: *IEEE Antennas and Wireless Propagation Letters* 9 (2010), pp. 367–370. ISSN: 1548-5757. DOI: 10.1109/LAWP.2010.2049332.

[151] L. Ge, K. M. Luk, and S. Chen. «360° Beam-Steering Reconfigurable Wideband Substrate Integrated Waveguide Horn Antenna». In: *IEEE Transactions on Antennas and Propagation* 64.12 (Dec. 2016), pp. 5005–5011. ISSN: 1558-2221. DOI: 10.1109/TAP.2016.2617820.

[152] Z. Lu, X. Yang, and G. Tan. «A Wideband Printed Tapered-Slot Antenna With Pattern Reconfigurability». In: *IEEE Antennas and Wireless Propagation Letters* 13 (2014), pp. 1613–1616. ISSN: 1548-5757. DOI: 10.1109/LAWP.2014.2342737.

[153] G. Yang et al. «Pattern Reconfigurable Microstrip Antenna With Multidirectional Beam for Wireless Communication». In: *IEEE Transactions on Antennas and Propagation* 67.3 (Mar. 2019), pp. 1910–1915. ISSN: 1558-2221. DOI: 10.1109/TAP.2018.2885230.

[154] A. Pal et al. «A Twelve-Beam Steering Low-Profile Patch Antenna With Shorting Vias for Vehicular Applications». In: *IEEE Transactions on Antennas and Propagation* 65.8 (Aug. 2017), pp. 3905–3912. ISSN: 1558-2221. DOI: 10.1109/TAP.2017.2715367.

[155] L. Zhang, Q. Wu, and T. A. Denidni. «Electronically Radiation Pattern Steerable Antennas Using Active Frequency Selective Surfaces». In: *IEEE Transactions on Antennas and Propagation* 61.12 (Dec. 2013), pp. 6000–6007. ISSN: 1558-2221. DOI: 10.1109/TAP.2013.2282921.

[156] B. A. Cetiner et al. «Multifunctional reconfigurable MEMS integrated antennas for adaptive MIMO systems». In: *IEEE Communications Magazine* 42.12 (Dec. 2004), pp. 62–70. ISSN: 1558-1896. DOI: 10.1109/MCOM.2004.1367557.

[157] D. Piazza et al. «Design and Evaluation of a Reconfigurable Antenna Array for MIMO Systems». In: *IEEE Transactions on Antennas and Propagation* 56.3 (Mar. 2008), pp. 869–881. ISSN: 1558-2221. DOI: 10.1109/TAP.2008.916908.

[158] N. H. Chamok et al. «High-Gain Pattern Reconfigurable MIMO Antenna Array for Wireless Handheld Terminals». In: *IEEE Transactions on Antennas and Propagation* 64.10 (Oct. 2016), pp. 4306–4315. ISSN: 1558-2221. DOI: 10.1109/TAP.2016.2598201.

[159] G. Jin et al. «A Simple Planar Pattern-Reconfigurable Antenna Based on Arc Dipoles». In: *IEEE Antennas and Wireless Propagation Letters* 17.9 (Sept. 2018), pp. 1664–1668. ISSN: 1548-5757. DOI: 10.1109/LAWP.2018.2862624.

[160] S. Yong and J. T. Bernhard. «A Pattern Reconfigurable Null Scanning Antenna». In: *IEEE Transactions on Antennas and Propagation* 60.10 (Oct. 2012), pp. 4538–4544. ISSN: 1558-2221. DOI: 10.1109/TAP.2012.2207336.

[161] R. Mehmood and J. W. Wallace. «MIMO Capacity Enhancement Using Parasitic Reconfigurable Aperture Antennas (RECAPs)». In: *IEEE Transactions on Antennas and Propagation* 60.2 (Feb. 2012), pp. 665–673. ISSN: 1558-2221. DOI: 10.1109/TAP.2011.2173445.

[162] T. Aboufoul et al. «Pattern-Reconfigurable Planar Circular Ultra-Wideband Monopole Antenna». In: *IEEE Transactions on Antennas and Propagation* 61.10 (Oct. 2013), pp. 4973–4980. ISSN: 1558-2221. DOI: 10.1109/TAP.2013.2274262.

[163] L. Akhoondzadeh-Asl, J. J. Laurin, and A. Mirkamali. «A Novel Low-Profile Monopole Antenna With Beam Switching Capabilities». In: *IEEE Transactions on Antennas and Propagation* 62.3 (Mar. 2014), pp. 1212–1220. ISSN: 1558-2221. DOI: 10.1109/TAP.2013.2295215.

[164] P. Qin, Y. J. Guo, and C. Ding. «A Beam Switching Quasi-Yagi Dipole Antenna». In: *IEEE Transactions on Antennas and Propagation* 61.10 (Oct. 2013), pp. 4891–4899. ISSN: 1558-2221. DOI: 10.1109/TAP.2013.2274635.

[165] C. Kittiyanpunya and M. Krairiksh. «A Four-Beam Pattern Reconfigurable Yagi-Uda Antenna». In: *IEEE Transactions on Antennas and Propagation* 61.12 (Dec. 2013), pp. 6210–6214. ISSN: 1558-2221. DOI: 10.1109/TAP.2013.2282914.

[166] S. -. Shi and W. -. Ding. «Radiation pattern reconfigurable microstrip antenna for WiMAX application». In: *Electronics Letters* 51.9 (2015), pp. 662–664. ISSN: 0013-5194. DOI: 10.1049/el.2015.0568.

[167] M. Z. M. Nor et al. «Dual-Band, Switched-Beam, Reconfigurable Antenna for WLAN Applications». In: *IEEE Antennas and Wireless Propagation Letters* 12 (2013), pp. 1500–1503. ISSN: 1548-5757. DOI: 10.1109/LAWP.2013.2289919.

[168] S. Ha and C. W. Jung. «Reconfigurable Beam Steering Using a Microstrip Patch Antenna With a U-Slot for Wearable Fabric Applications». In: *IEEE Antennas and Wireless Propagation Letters* 10 (2011), pp. 1228–1231. ISSN: 1548-5757. DOI: 10.1109/LAWP.2011.2174022.

[169] A. Edalati and T. A. Denidni. «High-Gain Reconfigurable Sectoral Antenna Using an Active Cylindrical FSS Structure». In: *IEEE Transactions on Antennas and Propagation* 59.7 (July 2011), pp. 2464–2472. ISSN: 1558-2221. DOI: 10.1109/TAP.2011.2152327.

[170] S. M. Mahmood and T. A. Denidni. «Pattern-Reconfigurable Antenna Using a Switchable Frequency Selective Surface With Improved Bandwidth». In: *IEEE Antennas and Wireless Propagation Letters* 15 (2016), pp. 1148–1151. ISSN: 1548-5757. DOI: 10.1109/LAWP.2015.2496501.

[171] L. Ji et al. «A Reconfigurable Partially Reflective Surface (PRS) Antenna for Beam Steering». In: *IEEE Transactions on Antennas and Propagation* 63.6 (June 2015), pp. 2387–2395. ISSN: 1558-2221. DOI: 10.1109/TAP.2015.2412143.

[172] A. R. Weily, T. S. Bird, and Y. J. Guo. «A Reconfigurable High-Gain Partially Reflecting Surface Antenna». In: *IEEE Transactions on Antennas and Propagation* 56.11 (Nov. 2008), pp. 3382–3390. ISSN: 1558-2221. DOI: 10.1109/TAP.2008.2005538.

[173] Z. Li et al. «A Beam-Steering Reconfigurable Antenna for WLAN Applications». In: *IEEE Transactions on Antennas and Propagation* 63.1 (Jan. 2015), pp. 24–32. ISSN: 1558-2221. DOI: 10.1109/TAP.2014.2367500.

[174] P. Lotfi, S. Soltani, and R. D. Murch. «Printed Endfire Beam-Steerable Pixel Antenna». In: *IEEE Transactions on Antennas and Propagation* 65.8 (Aug. 2017), pp. 3913–3923. ISSN: 1558-2221. DOI: 10.1109/TAP.2017.2716399.

[175] S. Wu and T. Ma. «A Wideband Slotted Bow-Tie Antenna With Reconfigurable CPW-to-Slotline Transition for Pattern Diversity». In: *IEEE Transactions on Antennas and Propagation* 56.2 (Feb. 2008), pp. 327–334. ISSN: 1558-2221. DOI: 10.1109/TAP.2007.915454.

[176] A. Narbudowicz, M. J. Ammann, and D. Heberling. «Switchless Reconfigurable Antenna With 360° Steering». In: *IEEE Antennas and Wireless Propagation Letters* 15 (2016), pp. 1689–1692. ISSN: 1548-5757. DOI: 10.1109/LAWP.2016.2524199.

[177] Chang won Jung et al. «Reconfigurable scan-beam single-arm spiral antenna integrated with RF-MEMS switches». In: *IEEE Transactions on Antennas and Propagation* 54.2 (Feb. 2006), pp. 455–463. ISSN: 1558-2221. DOI: 10.1109/TAP.2005.863407.

[178] I. Lim and S. Lim. «Monopole-Like and Boresight Pattern Reconfigurable Antenna». In: *IEEE Transactions on Antennas and Propagation* 61.12 (Dec. 2013), pp. 5854–5859. ISSN: 1558-2221. DOI: 10.1109/TAP.2013.2283926.

[179] A. Narbudowicz, X. Bao, and M. J. Ammann. «Omnidirectional microstrip patch antenna with reconfigurable pattern and polarisation». In: *IET Microwaves, Antennas Propagation* 8.11 (Aug. 2014), pp. 872–877. ISSN: 1751-8733. DOI: 10.1049/iet-map.2013.0665.

[180] W. Lin, H. Wong, and R. W. Ziolkowski. «Circularly Polarized Antenna With Reconfigurable Broadside and Conical Beams Facilitated by a Mode Switchable Feed Network». In: *IEEE Transactions on Antennas and Propagation* 66.2 (Feb. 2018), pp. 996–1001. ISSN: 1558-2221. DOI: 10.1109/TAP.2017.2784452.

[181] W. Lin and H. Wong. «Polarization Reconfigurable Wheel-Shaped Antenna With Conical-Beam Radiation Pattern». In: *IEEE Transactions on Antennas and Propagation* 63.2 (Feb. 2015), pp. 491–499. ISSN: 1558-2221. DOI: 10.1109/TAP.2014.2381263.

[182] A. Chen et al. «A design of radiation pattern and polarization reconfigurable antenna using metasurface». In: *2017 IEEE Asia Pacific Microwave Conference (APMC)*. Nov. 2017, pp. 108–111. DOI: 10.1109/APMC.2017.8251389.

[183] X. Yi, L. Huitema, and H. Wong. «Polarization and Pattern Reconfigurable Cuboid Quadrifilar Helical Antenna». In: *IEEE Transactions on Antennas and Propagation* 66.6 (June 2018), pp. 2707–2715. ISSN: 1558-2221. DOI: 10.1109/TAP.2018.2816785.

[184] Symeon Nikolaou et al. «Pattern and frequency reconfigurable annular slot antenna using PIN diodes». In: *IEEE Transactions on Antennas and Propagation* 54.2 (Feb. 2006), pp. 439–448. ISSN: 1558-2221.

[185] M. Ye and P. Gao. «Back-to-back F semicircular antenna with frequency and pattern reconfigurability». In: *Electronics Letters* 51.25 (2015), pp. 2073–2074. ISSN: 0013-5194. DOI: 10.1049/el.2015.3029.

[186] Nghia Nguyen Trong, Leonard Hall, and Christophe Fumeaux. «A dual-band dual-pattern frequency-reconfigurable antenna». In: *Microwave and Optical Technology Letters* 59 (Aug. 2017), pp. 2710–2715. DOI: 10.1002/mop.30815.

[187] D. Rodrigo, J. Romeu, and L. Jofre. «Interference rejection using frequency and pattern reconfigurable antennas». In: *Proceedings of the 2012 IEEE International Symposium on Antennas and Propagation*. July 2012, pp. 1–2. DOI: 10.1109/APS.2012.6347994.

[188] J. Perruisseau-Carrier. «Versatile reconfiguration of radiation patterns, frequency and polarization: A discussion on the potential of controllable reflectarrays for software-defined and cognitive radio systems». In: *2010 IEEE International Microwave Workshop Series on RF Front-ends for Software Defined and Cognitive Radio Solutions (IMWS)*. Feb. 2010, pp. 1–4. DOI: 10.1109/IMWS.2010.5440982.

[189] D. V. Niture, P. A. Govind, and S. P. Mahajan. «Frequency and polarisation reconfigurable square ring antenna for wireless application». In: *2016 IEEE Region 10 Conference (TENCON)*. Nov. 2016, pp. 1302–1306. DOI: 10.1109/TENCON.2016.7848223.

[190] M. S. Kumar and Y. K. Choukiker. «Frequency and polarization reconfigurable antenna using BLC feed network». In: *2017 IEEE International Conference on Antenna Innovations Modern Technologies for Ground, Aircraft and Satellite Applications (iAIM)*. Nov. 2017, pp. 1–4. DOI: 10.1109/IAIM.2017.8402550.

[191] M. A. Rahman, E. Nishiyama, and I. Toyoda. «A frequency diversity reconfigurable antenna with circular polarization switching capability». In: *2017 IEEE International Symposium on Antennas and Propagation USNC/URSI National Radio Science Meeting*. July 2017, pp. 1367–1368. DOI: 10.1109/APUSNCURSINRSM.2017.8072726.

[192] D. V. Niture, P. A. Govind, and S. P. Mahajan. «Frequency and polarisation reconfigurable square ring antenna for wireless application». In: *2016 IEEE Region 10 Conference (TENCON)*. Nov. 2016, pp. 1302–1306. DOI: 10.1109/TENCON.2016.7848223.

[193] B. Liang et al. «A Frequency and Polarization Reconfigurable Circularly Polarized Antenna Using Active EBG Structure for Satellite Navigation». In: *IEEE Transactions on Antennas and Propagation* 63.1 (Jan. 2015), pp. 33–40. ISSN: 1558-2221. DOI: 10.1109/TAP.2014.2367537.

[194] T. S. Rappaport et al. «Millimeter Wave Mobile Communications for 5G Cellular: It Will Work!» In: *IEEE Access* 1 (2013), pp. 335–349. ISSN: 2169-3536. DOI: 10.1109/ACCESS.2013.2260813.

[195] Ching-Yao Chan. «Advancements, prospects, and impacts of automated driving systems». In: *International Journal of Transportation Science and Technology* 6.3 (2017). Safer Road Infrastructure and Operation Management, pp. 208–216. ISSN: 2046-0430. DOI: https://doi.org/10.1016/j.ijtst.2017.07.008. URL: http://www.sciencedirect.com/science/article/pii/S2046043017300035.

[196] E. H. Mujammami, I. Afifi, and A. B. Sebak. «Optimum Wideband High Gain Analog Beamforming Network for 5G Applications». In: *IEEE Access* 7 (2019), pp. 52226–52237. ISSN: 2169-3536. DOI: 10.1109/ACCESS.2019.2912119.

[197] R. Rotman, M. Tur, and L. Yaron. «True Time Delay in Phased Arrays». In: *Proceedings of the IEEE* 104.3 (Mar. 2016), pp. 504–518. ISSN: 1558-2256. DOI: 10.1109/JPROC.2016.2515122.

[198] W. Rotman and R. Turner. «Wide-angle microwave lens for line source applications». In: *IEEE Transactions on Antennas and Propagation* 11.6 (Nov. 1963), pp. 623–632. ISSN: 1558-2221. DOI: 10.1109/TAP.1963.1138114.

[199] J. Ruze. «Wide-Angle Metal-Plate Optics». In: *Proceedings of the IRE* 38.1 (Jan. 1950), pp. 53–59. ISSN: 2162-6634. DOI: 10.1109/JRPROC.1950.232789.

[200] D. H. Archer and M. J. Maybell. «Rotman lens development history at Raytheon Electronic Warfare Systems 1967-1995». In: *2005 IEEE Antennas and Propagation Society International Symposium*. Vol. 2B. July 2005, 31–34 vol. 2B. DOI: 10.1109/APS.2005.1551927.

[201] T. Katagi, S. Mano, and S. Sato. «An improved design method of Rotman lens antennas». In: *IEEE Transactions on Antennas and Propagation* 32.5 (May 1984), pp. 524–527. ISSN: 1558-2221. DOI: 10.1109/TAP.1984.1143353.

[202] R. C. Hansen. «Design trades for Rotman lenses». In: *IEEE Transactions on Antennas and Propagation* 39.4 (Apr. 1991), pp. 464–472. ISSN: 1558-2221. DOI: 10.1109/8.81458.

[203] J. Shelton. «Focusing characteristics of symmetrically configured bootlace lenses». In: *IEEE Transactions on Antennas and Propagation* 26.4 (July 1978), pp. 513–518. ISSN: 1558-2221. DOI: 10.1109/TAP.1978.1141883.

[204] Peter S. Simon. «ANALYSIS AND SYNTHESIS OF ROTMAN LENSES». In: 2004.

[205] E. O. Rausch and A. F. Peterson. «Rotman lens design issues». In: *2005 IEEE Antennas and Propagation Society International Symposium*. Vol. 2B. July 2005, 35–38 vol. 2B. DOI: 10.1109/APS.2005.1551928.

[206] N. J. G. Fonseca. «A Focal Curve Design Method for Rotman Lenses With Wider Angular Scanning Range». In: *IEEE Antennas and Wireless Propagation Letters* 16 (2017), pp. 54–57. ISSN: 1548-5757. DOI: 10.1109/LAWP.2016.2554281.

[207] I. L. F. Filho and M. M. Mosso. «A new concept of microstrip Rotman lens design». In: *2015 SBMO/IEEE MTT-S International Microwave and Optoelectronics Conference (IMOC)*. Nov. 2015, pp. 1–5. DOI: 10.1109/IMOC.2015.7369130.

[208] P. K. Singhal, P. C. Sharma, and R. D. Gupta. «Design and analysis of Rotman type lens using hyperbolic focal arc for wide angle scanning». In: *1999 Asia Pacific Microwave Conference. APMC'99. Microwaves Enter the 21st Century. Conference Proceedings (Cat. No.99TH8473)*. Vol. 3. Nov. 1999, 932–935 vol.3. DOI: 10.1109/APMC.1999.833748.

[209] P. K. Singhal, P. C. Sharma, and R. D. Gupta. «Rotman lens with equal height of array and feed contours». In: *IEEE Transactions on Antennas and Propagation* 51.8 (Aug. 2003), pp. 2048–2056. ISSN: 1558-2221. DOI: 10.1109/TAP.2003.814742.

[210] J. Dong, A. I. Zaghloul, and R. Rotman. «Phase-error performance of multi-focal and non-focal two-dimensional Rotman lens designs». In: *IET Microwaves, Antennas Propagation* 4.12 (Dec. 2010), pp. 2097–2103. ISSN: 1751-8733. DOI: 10.1049/iet-map.2009.0565.

[211] M. Rajabalian and B. Zakeri. «Optimisation and implementation for a non-focal Rotman lens design». In: *IET Microwaves, Antennas Propagation* 9.9 (2015), pp. 982–987. ISSN: 1751-8733. DOI: 10.1049/iet-map.2014.0797.

[212] E. Sbarra et al. «A novel rotman lens in SIW technology». In: *2007 European Radar Conference*. Oct. 2007, pp. 236–239. DOI: 10.1109/EURAD.2007.4404980.

[213] J. Pourahmadazar and T. A. Denidni. «Multi-beam tapered slot antenna array using substrate integrated waveguide Rotman lens». In: *2015 European Radar Conference (EuRAD)*. Sept. 2015, pp. 425–428. DOI: 10.1109/EuRAD.2015.7346328.

[214] K. Tekkouk, M. Ettorre, and R. Sauleau. «SIW Rotman Lens Antenna With Ridged Delay Lines and Reduced Footprint». In: *IEEE Transactions on Microwave Theory and Techniques* 66.6 (June 2018), pp. 3136–3144. ISSN: 1557-9670. DOI: 10.1109/TMTT.2018.2825374.

[215] A. Attaran, R. Rashidzadeh, and A. Kouki. «60 GHz Low Phase Error Rotman Lens Combined With Wideband Microstrip Antenna Array Using LTCC Technology». In: *IEEE Transactions on Antennas and Propagation* 64.12 (Dec. 2016), pp. 5172–5180. ISSN: 1558-2221. DOI: 10.1109/TAP.2016.2618479.

[216] L. Schulwitz and A. Mortazawi. «A New Low Loss Rotman Lens Design for Multibeam Phased Arrays». In: *2006 IEEE MTT-S International Microwave Symposium Digest*. June 2006, pp. 445–448. DOI: 10.1109/MWSYM.2006.249587.

[217] T. K. Vo Dai, T. Nguyen, and O. Kilic. «Compact multi-layer microstrip Rotman lens design using coupling slots to support millimetre wave devices». In: *IET Microwaves, Antennas Propagation* 12.8 (2018), pp. 1260–1265. ISSN: 1751-8733. DOI: 10.1049/iet-map.2017.0817.

[218] F. C. Suárez, D. N. Méndez, and M. Baquero-Escudero. «Rotman lens with Ridge Gap Waveguide technology for millimeter wave applications». In: *2013 7th European Conference on Antennas and Propagation (EuCAP)*. Apr. 2013, pp. 4006–4009.

[219] Sang-Gyu Kim, P. Zepeda, and Kai Chang. «Piezoelectric transducer controlled multiple beam phased array using microstrip Rotman lens». In: *IEEE Microwave and Wireless Components Letters* 15.4 (Apr. 2005), pp. 247–249. ISSN: 1558-1764. DOI: 10.1109/LMWC.2005.845728.

[220] S. Christie et al. «Electronically scanned Rotman lens antenna with liquid crystal phase shifters». In: *Electronics Letters* 49.7 (Mar. 2013), pp. 445–447. ISSN: 0013-5194.

[221] IMST GmbH. *EMPIRE XPU Manual Version 7.71*. Kamp Lintfort, Germany. Aug. 2018.

[222] R. Garg, I. Bahl, and M. Bozzi. *Microstrip Lines and Slotlines, Third Edition*. Microwave & RF. Artech House, 2013. ISBN: 9781608075355. URL: https://books.google.de/books?id=1PQfAgAAQBAJ.

[223] A. M. Abbosh. «Ultra-Wideband Phase Shifters». In: *IEEE Transactions on Microwave Theory and Techniques* 55.9 (Sept. 2007), pp. 1935–1941. ISSN: 1557-9670. DOI: 10.1109/TMTT.2007.904051.

[224] A. M. Abbosh and M. E. Bialkowski. «Design of Compact Directional Couplers for UWB Applications». In: *IEEE Transactions on Microwave Theory and Techniques* 55.2 (Feb. 2007), pp. 189–194. ISSN: 1557-9670. DOI: 10.1109/TMTT.2006.889150.

[225] B. Shuppert. «Microstrip/slotline transitions: modeling and experimental investigation». In: *IEEE Transactions on Microwave Theory and Techniques* 36.8 (Aug. 1988), pp. 1272–1282. ISSN: 1557-9670. DOI: 10.1109/22.3669.

[226] MACOM. *MA4FCP200 Flip chip PIN diode*. Rev. 5.

[227] O. Litschke A. Lauer. *Kompakte Richtantennenanordnung mit Mehrfachnutzung von Strahlerelementen*. DE10 2007 055 534 B4. Aug. 2018.

[228] David M Pozar. *Microwave engineering; 3rd ed.* Wiley, 2005.

[229] H. Xu, G. Wang, and K. Lu. «Microstrip Rat-Race Couplers». In: *IEEE Microwave Magazine* 12.4 (2011), pp. 117–129.

[230] C. Tseng and H. Chen. «Compact Rat-Race Coupler Using Shunt-Stub-Based Artificial Transmission Lines». In: *IEEE Microwave and Wireless Components Letters* 18.11 (2008), pp. 734–736.

[231] H. Ghali and T. A. Moselhy. «Miniaturized fractal rat-race, branch-line, and coupled-line hybrids». In: *IEEE Transactions on Microwave Theory and Techniques* 52.11 (2004), pp. 2513–2520.

[232] W. Chang, C. Liang, and C. Chang. «Slow-Wave Broadside-Coupled Microstrip Lines and Its Application to the Rat-Race Coupler». In: *IEEE Microwave and Wireless Components Letters* 25.6 (2015), pp. 361–363.

[233] J. Selga et al. «Miniaturised and harmonic-suppressed rat-race couplers based on slow-wave transmission lines». In: *IET Microwaves, Antennas Propagation* 13.9 (2019), pp. 1293–1299.

[234] H. Okabe, C. Caloz, and T. Itoh. «A compact enhanced-bandwidth hybrid ring using an artificial lumped-element left-handed transmission-line section». In: *IEEE Transactions on Microwave Theory and Techniques* 52.3 (2004), pp. 798–804.

[235] Y. Cao et al. «A miniaturized 3-db microstrip rat-race coupler using shorted trans-directional coupled lines». In: *2017 Sixth Asia-Pacific Conference on Antennas and Propagation (APCAP)* (2017), pp. 1–3.

[236] T. T. Mo, Q. Xue, and C. H. Chan. «A Broadband Compact Microstrip Rat-Race Hybrid Using a Novel CPW Inverter». In: *IEEE Transactions on Microwave Theory and Techniques* 55.1 (Jan. 2007), pp. 161–167. ISSN: 1557-9670.

[237] L. Chang and T. Ma. «Dual-Mode Branch-Line/Rat-Race Coupler Using Composite Right-/Left-Handed Lines». In: *IEEE Microwave and Wireless Components Letters* 27.5 (2017), pp. 449–451.

[238] L. Cai and K. M. Cheng. «A Novel Design of Dual-Band Rat-Race Coupler With Reconfigurable Power-Dividing Ratio». In: *IEEE Microwave and Wireless Components Letters* 28.1 (2018), pp. 16–18.

[239] C. Chang, Y. Wei, and K. Chin. «Design of dual-band -90°/+90° transmission lines for miniaturized dual-band 1:4 rat-race couplers». In: *2017 IEEE MTT-S International Microwave Symposium (IMS)*. June 2017, pp. 1289–1292. DOI: 10.1109/MWSYM.2017.8058845.

[240] B. Dwivedy, S. K. Behera, and D. Mishra. «Design of a frequency agile rat race coupler». In: *2015 IEEE Applied Electromagnetics Conference (AEMC)*. 2015, pp. 1–2.

[241] X. Tan and F. Lin. «A Novel Rat-Race Coupler With Widely Tunable Frequency». In: *IEEE Transactions on Microwave Theory and Techniques* 67.3 (Mar. 2019), pp. 957–967. ISSN: 1557-9670. DOI: 10.1109/TMTT.2018.2889453.

[242] Marc A. Antoniades. «Microwave Devices and antennas based on negative refractive index transmission line metamaterials». PhD thesis. University of Toronto, Department of Electrical and Computer Engineering, 2009.

[243] Martin Ferran. *Artificial Transmission Lines for RF and Microwave Applications*. John Wiley & Sons, 2015.

[244] T. Shen et al. «Dual-band rat-race coupler design in multilayer LTCC». In: *2010 Asia-Pacific Microwave Conference*. Dec. 2010, pp. 798–801.

[245] T. -. Kim and B. Lee. «Metamaterial-based wideband rat-race hybrid coupler using slow wave lines». In: *IET Microwaves, Antennas Propagation* 4.6 (June 2010), pp. 717–721. ISSN: 1751-8733. DOI: 10.1049/iet-map.2009.0109.

[246] H. Rahmanian, S. H. Sedighy, and M. Khalaj-Amirhosseini. «Using a composite right/left handed transmission line to design a high compact Wilkinson power divider and rate race coupler». In: *6th International Symposium on Telecommunications (IST)*. Nov. 2012, pp. 84–87. DOI: 10.1109/ISTEL.2012.6482960.

[247] G. Siso et al. «Compact Rat-Race Hybrid Coupler Implemented Through Artificial Left Handed and Right Handed Lines». In: *2007 IEEE/MTT-S International Microwave Symposium*. June 2007, pp. 25–28. DOI: 10.1109/MWSYM.2007.380209.

[248] J. Kuo, J. Wu, and Y. Chiou. «Miniaturized Rat Race Coupler With Suppression of Spurious Passband». In: *IEEE Microwave and Wireless Components Letters* 17.1 (Jan. 2007), pp. 46–48.

[249] Qorvo. *QPC6222 datasheet*. 2015.

[250] Qorvo. *RFSW6232 datasheet*. 2015.

[251] J. Wang et al. «Compact slow-wave microstrip rat-race ring coupler». In: *Electronics Letters* 43.2 (2007), pp. 111–113.

[252] K. Finkenzeller. *RFID Handbook: Fundamentals and Applications in Contactless Smart Cards and Identification*. Wiley, 2003. ISBN: 9780470844021.

[253] Xiaolin Jia et al. «RFID technology and its applications in Internet of Things (IoT)». In: *2012 2nd International Conference on Consumer Electronics, Communications and Networks, CECNet 2012 - Proceedings* (Apr. 2012). DOI: 10.1109/CECNet.2012.6201508.

[254] Malte Brettel et al. «How Virtualization, Decentralization and Network Building Change the Manufacturing Landscape: An Industry 4.0 Perspective». In: *International journal of mechanical, aerospace, industrial and mechatronics engineering* 8.1 (2014), pp. 37–44.

[255] Z. Wang et al. «Single-Fed Broadband Circularly Polarized Stacked Patch Antenna With Horizontally Meandered Strip for Universal UHF RFID Applications». In: *IEEE Transactions on Microwave Theory and Techniques* 59.4 (Apr. 2011), pp. 1066–1073. ISSN: 1557-9670. DOI: 10.1109/TMTT.2011.2114010.

[256] Nasimuddin and X. Qing. «Wideband Circularly Polarized UHF RFID Reader Antenna». In: *2018 IEEE International Conference on Service Operations and Logistics, and Informatics (SOLI)*. July 2018, pp. 127–130. DOI: 10.1109/SOLI.2018.8476761.

[257] Y. Pan et al. «Directly-fed single-layer wideband RFID reader antenna». In: *Electronics Letters* 48.11 (May 2012), pp. 607–608. ISSN: 0013-5194. DOI: 10.1049/el.2012.1140.

[258] J. Lu and S. Wang. «Planar Broadband Circularly Polarized Antenna With Square Slot for UHF RFID Reader». In: *IEEE Transactions on Antennas and Propagation* 61.1 (Jan. 2013), pp. 45–53. ISSN: 1558-2221. DOI: 10.1109/TAP.2012.2220103.

[259] J. Li et al. «A Wideband Single-Fed, Circularly-Polarized Patch Antenna With Enhanced Axial Ratio Bandwidth for UHF RFID Reader Applications». In: *IEEE Access* 6 (2018), pp. 55883–55892. ISSN: 2169-3536. DOI: 10.1109/ACCESS.2018.2872692.

[260] J. Yuan et al. «A Compact Low-Profile Ring Antenna With Dual Circular Polarization and Unidirectional Radiation for Use in RFID Readers». In: *IEEE Access* 7 (2019), pp. 128948–128955. ISSN: 2169-3536. DOI: 10.1109/ACCESS.2019.2939271.

[261] A. L. Borja et al. «A Reconfigurable Passive UHF Reader Loop Antenna for Near-Field and Far-Field RFID Applications». In: *IEEE Antennas and Wireless Propagation Letters* 11 (2012), pp. 580–583. ISSN: 1548-5757. DOI: 10.1109/LAWP.2012.2200870.

[262] A. Michel, M. Rodriguez Pino, and P. Nepa. «Reconfigurable Modular Antenna for NF UHF RFID Smart Point Readers». In: *IEEE Transactions on Antennas and Propagation* 65.2 (Feb. 2017), pp. 498–506. ISSN: 1558-2221. DOI: 10.1109/TAP.2016.2640140.

[263] Y. F. C. X. Ding et al. «A polarization reconfigurable RFID reader antenna». In: *2017 IEEE International Symposium on Antennas and Propagation USNC/URSI National Radio Science Meeting*. July 2017, pp. 2213–2214. DOI: 10.1109/APUSNCURSINRSM.2017.8073149.

[264] Y. Tawk and J. Costantine. «A Reconfigurable Wideband Feeding Network for Polarization Diverse Antenna Arrays». In: *2019 IEEE International Symposium on Antennas and Propagation and USNC-URSI Radio Science Meeting*. July 2019, pp. 1153–1154. DOI: 10.1109/APUSNCURSINRSM.2019.8888669.

[265] H. Sun and Z. Pan. «Design of a Quad-Polarization-Agile Antenna Using a Switchable Impedance Converter». In: *IEEE Antennas and Wireless Propagation Letters* 18.2 (Feb. 2019), pp. 269–273. ISSN: 1548-5757. DOI: 10.1109/LAWP.2018.2888843.

[266] Guillermo Gonzalez. *Microwave transistor amplifiers: analysis and design*. Prentice-Hall, 1996.

[267] Infineon Technologies AG. *BGSA13GN10 Datasheet, Single-Pole Triple Throw Antenna Tuning Switch*. 20 January 2016.

[268] Infineon Technologies AG. *BGSA14GN10 Datasheet, Single-Pole Quad Throw Antenna Tuning Switch*. 6 June 2016.

List of Publications

Journal contributions

[J1] E. Tolin, A. Bahr and F. Vipiana, "Miniaturized and Reconfigurable Rat-Race Coupler Based on Artificial Transmission Lines", *IEEE Microwave and Wireless Components Letters*, 25 February 2020.

[J2] E. Tolin, O. Litschke, S. Bruni and F. Vipiana, "Compact Extended Scan Range Antenna Array Based on Rotman Lens", *IEEE Transactions on Antennas and Propagation*, vol. 67, no. 12, pp. 7356-7367, Dec. 2019.

Congress Contributions

[C1] E. Tolin, F. Vipiana, A. Bahr and S. Bruni, " Reduced Size RFID Reader Antenna Based on Reconfigurable Feeding Network Realized with Artificial Transmission Lines", *2020 14th European Conference on Antennas and Propagation (EuCAP)*, Copenhagen, Denmark, 2020.

[C2] E. Tolin, F. Vipiana, S. Bruni and A. Bahr, "Polarization Reconfigurable Patch Antenna for Compact and Low Cost UHF RFID Reader", *2019 IEEE International Conference on RFID Technology and Applications (RFID-TA)*, Pisa, Italy, 2019, pp. 128-130.

[C3] E. Tolin, F. Vipiana, A. Bahr, S. Bruni and W. Simon, "Frequency and Polarization Agile RFID Patch Antenna with Reduced Dimensions", *2019 IEEE International Symposium on Antennas and Propagation and USNC-URSI Radio Science Meeting*, Atlanta, GA, USA, 2019, pp. 1889-1890.

[C4] E. Tolin, O. Litschke, S. Bruni and F. Vipiana, "Compact Design of a 24 GHz Extended Scan Range Rotman Lens Antenna", *2019 13th European Conference on Antennas and Propagation (EuCAP)*, Krakow, Poland, 2019, pp. 1-4.

[C5] E. Tolin, F. Vipiana, O. Litschke and S. Bruni, "Phase Shifters Design for Scan Range Extension of Rotman Lens Beamforming Based Antenna Arrays", *2018 IEEE International Symposium on Antennas and Propagation USNC/URSI National Radio Science Meeting*, Boston, MA, 2018, pp. 2129-2130.

[C6] E. Tolin, O. Litschke and F. Vipiana, "Phase Management for extended scan range antenna arrays based on rotman lens", *12th European Conference on Antennas and Propagation (EuCAP 2018)*, London, 2018, pp. 1-5.

[C7] E. Tolin, O. Litschke, S. Bruni and F. Vipiana, "Innovative Rotman lens setup for extended scan range array antennas", *2017 IEEE-APS Topical Conference on Antennas and Propagation in Wireless Communications (APWC)*, Verona, 2017, pp. 252-255.

[C8] E. Tolin, A. Bahr, M. Geissler and F. Vipiana, "Flexible and cost effective reconfigurable UHF RFID antenna system", *2017 11th European Conference on Antennas and Propagation (EUCAP)*, Paris, 2017, pp. 2037-2040.

Acknowledgements

In the last pages of this thesis I would like to express my gratitude to all the people that, in many ways, helped me to reach this important goal, after three intense years, that so much gave me in terms of technical and human growth. However, I know that it is always difficult to summarize in few lines how important all these people have been through this important life experience, and for sure the list would be also long.

At first, I would like to express my sincere gratitude to Prof. Francesca Vipiana for this opportunity. I will never forget her confidence in me from our first meeting in Torino, helping in my unusual Ph.D. student situation. She has always been an inspiration for continuous improvement, as well as a reference point, not only for technical aspects. I wish also to thank her for being friendly and collaborative, in all these years. Of course, I would also remember with a smile the funny "paper review' with Matilde during EUCAP.

I wish to acknowledge IMST GmbH, and especially Matthias Geissler, for valorizing my passion and my willingness to improve. I really think that IMST, and the ANTEMO group in particular, is one of the best places for this, not only because of high technical level of the projects, but mostly because it is composed by smart and open minded people, which is contributing to establish a pleasant and inspiring environment. A special mention is reserved for Achim Bahr and Oliver Litschke for the technical support and the human qualities that both of you have. With Achim I really enjoyed the fruitful theoretical discussions as well as the funny conversations during the regular coffee-times. I am grateful for the support he always gave me, from small problems and with this thesis, being much more than just a colleague. I thank Oliver for being always an inspiration and for helping me to improve as an antenna designer and as a person. He is demonstrated to be always a friend, except to some Saturday mornings during the football match, when we play on different teams (joking!). I would like to thank all of my colleagues, for the interest and support demonstrated in these years, with special mention on Peter Uhlig and the Technology laboratory, for being always kind, curios about my work and ready to help with my prototypes. Thanks also to Stefan Weitz, for his knowledge and patience in measuring the antennas. I thank also Marta, for sharing with me this "expert student" life in these years. A mention is also reserved to the

"Ausländer" lunch group, for the daily company.

I would like here to thank also the members of the LACE group in LINKS, for being always friendly and make me enjoying working in Torino. I wish I would have more time to spend with you.

Nevertheless, there were not only working days in this Ph.D. period: for this I thank all my friends in Italy, in particular Federico, Marco, Stefano, Paolo, for being always funny as I never left, looking forward for the next gathering and spritz times. I would like to thank also Filippo (Pippo), Giuseppe (Jeppo), Nicola (Panoz) e Alessandro (Berla) for making me feel as I never left the university in Padova, every time we meet.

I take the chance to heartily thank Simona Bruni, because without her friendship, enthusiasm and encouragement I would have never succeed on this experience. I feel myself lucky for having her strong support and motivation day-by-day, enriching me with her advice and helping me through hard times, giving her support in technical problems as well as everyday life struggles.

Simona, grazie per credere in me piú di quanto faccio io stesso.

Beside the academic and professional aspect, I wish to thank her and Massimo for the friendship and help on daily life that you have given to me in all these years, making me feel as part of the family. *Un grazie speciale va anche a Valerio e Leonardo, perchè anche nei giorni piú difficili e stressanti, mi avete regalato un sorriso e un momento di svago.*

Finally, I would like to thank my family, to which this thesis is dedicated. *Grazie non solo per il supporto che mi avete dato in questi anni, ma per la fiducia incondizionata, per avermi motivato sia con le parole che con il vostro esempio di vita a migliorare sempre, ispirandomi giorno per giorno fino al raggiungimento di questo importante obiettivo. Una menzione particolare va a chi ci ha lasciato, ma che sono sicuro sará ugualmente orgoglioso di questo traguardo.*

Grazie a tutti! Thank you all! Herzlichen Dank!

This Ph.D. thesis has been typeset by means of the TEX-system facilities. The typesetting engine was pdfLATEX. The document class was `toptesi`, by Claudio Beccari, with option `tipotesi=scudo`. This class is available in every up-to-date and complete TEX-system installation.